

## **ABSTRACT**

### **NEXT GENERATION DIGITAL VECTOR MAGNETOGRAPH; HIGH CADENCE, PRECISION AND RESOLUTION**

**by  
Thomas J. Spirock**

The first Digital Vector Magnetograph (DVMG) was developed for the Big Bear Solar Observatory. This is a critical instrument for studying the evolution of the magnitude and direction of the magnetic field on the surface of the Sun. The DVMG uses the wavelength shift and Stokes polarization components (I, U, Q & V), of the Ca I line at 610.3 nm resulting from the Zeeman effect, to measure the solar magnetic field.

The DVMG combines three characteristics to properly study the dynamics of solar magnetic fields that have not been readily available in earlier magnetographs. The essential characteristics are high time cadence (1 minute), high spatial resolution (1 arc-sec / pixel) over a large field of view (300 arc-sec x 300 arc-sec) and high quality. Measurements of the longitudinal magnetic field acquired with this cadence have a noise level of ~10 Gauss while measurements of the transverse magnetic field have a noise level of ~100 Gauss. Note that the typical strength of magnetic fields in sunspots is >1000 Gauss. Longitudinal magnetogram noise can be reduced to below 5 Gauss, if the integration time is increased to ~5 min, especially when using post-processing techniques such as image selection and alignment. Vector magnetograms can be obtained and plotted in near real-time to help determine the likelihood that any particular active region will produce a flare and can be obtained at this rate continuously to study the evolution of the vector magnetic field.

DVMG observations have shown that there are rapid changes in the photospheric magnetic field. These findings are contrary to the long-held belief that the photospheric magnetic field is strongly locked in place by solar material and can not change rapidly. The magnitude of the magnetic field of the leading polarity tends to increase while the following polarity tends to decrease, but by a smaller amount. Also, after many flares, the magnetic field tends to become more vertical at locations some distance from neutral line.

**NEXT GENERATION DIGITAL VECTOR  
MAGNETOGRAPH; HIGH CADENCE,  
PRECISION AND RESOLUTION**

**by Thomas J. Spirock**

**Co-advisor: Timothy Chang**

**Co-advisor: Philip Goode**

**A Dissertation  
Submitted to the Faculty of  
New Jersey Institute of Technology  
In Partial Fulfillment of the Requirements for the Degree of  
Doctor of Philosophy in Electrical Engineering**

**Department of Electrical and Computer Engineering**

**May 2005**

**Copyright © 2005 by Thomas J. Spirock**

**ALL RIGHTS RESERVED**



**APPROVAL PAGE**

**NEXT GENERATION DIGITAL VECTOR  
MAGNETOGRAPH; HIGH CADENCE,  
PRECISION AND RESOLUTION**

**Thomas J. Spirock**

---

Dr. Timothy N. Chang, Dissertation Advisor Date  
Associate Professor of Electrical and Computer Engineering, NJIT

---

Dr. Philip R. Goode, Dissertation Advisor Date  
Distinguished Professor of Physics, NJIT

---

Dr. Marek Sosnowski, Committee Member Date  
Professor of Electrical and Computer Engineering, NJIT

---

Dr. Sui-hoi Edwin Hou, Committee Member Date  
Associate Professor of Electrical and Computer Engineering, NJIT

---

Dr. Haimin Wang, Committee Member Date  
Distinguished Professor of Physics, NJIT

## BIOGRAPHICAL SKETCH

**Author:** Thomas J. Spirock  
**Degree:** Doctor of Philosophy  
**Date:** May 2005  
**Date of Birth:** September 8, 1968  
**Place of Birth:** East Orange, New Jersey

### **Undergraduate and Graduate Education:**

- Doctor of Philosophy in Electrical Engineering,  
New Jersey Institute of Technology, Newark, NJ, 2005
- Master of Science in Electrical Engineering,  
New Jersey Institute of Technology, Newark, NJ, 1996
- Bachelor of Science in Electrical Engineering,  
New Jersey Institute of Technology, Newark, NJ, 1993

**Major:** Electrical Engineering

### **Publications:**

- Wang, H., Qiu, J., Jing, J., Spirock, T. J., Yurchyshyn, V., Abramenko, V., Ji, H. & Goode, P. R., 2004, *Astrophysical Journal*, Vol. 605, Issue 2, pp. 931-937.
- Yurchyshyn, V., Wang, H., Abramenko, V., Spirock, T. J. & Krucker, S., 2004, *Astrophysical Journal*, Vol. 605, Issue 1, pp. 546-553.
- Abramenko, V. I., Yurchyshyn, V. B., Wang, H., Spirock, T. J. & Goode, P. R., 2003, *Astrophysical Journal*, Vol. 597, Issue 2, pp. 1135-1144.
- Moon, Y.-J., Wang, H., Spirock, T. J., Goode, P. R. & Park, Y. D. *Solar Physics*, 2003, Vol. 217, Issue 1, pp. 79-94.
- Jing, J., Lee, J., Spirock, T. J., Xu, Y., Wang, H. & Choe, G. S., 2003, *Astrophysical Journal*, Vol. 584, Issue 2, pp. L103-L106.
- Ji, H. S., Wang, H., Spirock, T. J., Qiu, J., Yang, G. & Goode, P. R., 2002, *Solar Physics*, Vol. 211, Issue 1, pp. 221-229.

- Moon, Y.-J., Wang, H., Spirock, T. J. & Park, Y. D., 2002, *Journal of the Korean Astronomical Society*, Vol. 35, no. 3, pp. 143-149.
- Abramenko, V. I., Yurchyshyn, V. B., Wang, H., Spirock, T. J. & Goode, P. R., 2002, *Astrophysical Journal*, Vol. 577, Issue 1, pp. 487-495.
- Wang, H., Spirock, T. J., Qiu, J., Ji, H., Yurchyshyn, V., Moon, Y.-J., Denker, C. & Goode, P. R., 2002, *Astrophysical Journal*, Vol. 576, Issue 1, pp. 497-504.
- Gallagher, P. T., Denker, C., Yurchyshyn, V., Spirock, T., Qiu, J., Wang, H. & Goode, P. R., 2002, *Annales Geophysicae*, Vol. 20, Issue 7, pp. 1105-1115.
- Spirock, T. J., Yurchyshyn, V. B. & Wang, H., 2002, *Astrophysical Journal*, Vol. 572, Issue 2, pp. 1072-1076.
- Chae, J., Martin, S. F., Yun, H. S., Kim, J., Lee, S. Goode, P. R., Spirock, T. & Wang, H., 2001, *Astrophysical Journal*, Vol. 548, Issue 1, pp. 497-507.
- Wang, H., Qiu, J., Denker, C., Spirock, T., Chen, H. & Goode, P. R., 2000, *Astrophysical Journal*, Vol. 542, Issue 2, pp. 1080-1087.
- Chae, J., Denker, C., Spirock, T. J., Wang, H. & Goode, P. R., 2000, *Solar Physics*, Vol. 195, Issue 2, pp. 333-346.
- Wang, H., Denker, C., Spirock, T., Goode, P. R., Yang, S., Marquette, W., Varsik, J., Fear, R. J., Nenow, J. & Dingley, D. D., 1998, *Solar Physics*, Vol. 183, Issue 1, pp. 1-13.
- Wang, H., Spirock, T., Goode, P. R., Lee, C., Zirin, H. & Kosonocky, W., 1998, *Astrophysical Journal* Vol. 495, p. 957.

## TABLE OF CONTENTS

Chapter	Page
1 INTRODUCTION .....	1
1.1 Solar Basics and Space Weather .....	1
1.2 Structure of the Sun and Solar Activity .....	8
1.3 The Zeeman Effect .....	20
1.4 Review of Magnetograph Types .....	30
1.4.1 Full Spectrum Magnetograph .....	30
1.4.2 Spectroheliograph Based Magnetograph .....	31
1.4.3 Filter Based Magnetograph .....	33
1.4.4 Fabry-Perot Based Magnetograph .....	36
1.5 Development of the Solar Magnetograph: The Hale Tower Telescope Magnetograph .....	37
1.6 Initial Attempts to Measure the Magnetic Field of the Sun With Photoelectric Methods .....	42
1.7 The Babcock Photoelectric Magnetograph .....	43
1.8 The Leighton Photographic Subtraction Magnetograph .....	48
1.9 The Big Bear Magnetograph.....	53
2 INSTRUMENTATION .....	59
2.1 Overview of the Instrument .....	62
2.2 Telescope Details and Limitations .....	66
2.3 Image Scale & Light Throughput .....	72
2.4 The Ca I Absorption Line .....	75

**TABLE OF CONTENTS**  
**(Continued)**

<b>Chapter</b>	<b>Page</b>
2.5 The Pre-Filter .....	76
2.6 Polarization Optics .....	78
2.6.1 Review of Mueller Calculus .....	80
2.6.2 Principles of Retarders .....	82
2.6.3 Nematic Liquid Crystal Variable Retarders .....	84
2.6.4 Ferroelectric Variable Retarders .....	88
2.6.5 Three Crystal Optical Layout .....	90
2.6.6 LCVR and FLC Calibration .....	95
2.7 The Birefringent Filter .....	106
2.7.1 Tuning the Birefringent Filter .....	108
2.8 The CCD Camera, Image Capture Board & Instrument Control Program ...	113
2.9 The Weak-Field Approximation .....	116
2.9.1 Introduction .....	116
2.9.2 Brief Overview of the Weak Field Approximation .....	118
2.10 DVMG & Telescope Control Computers and Overall System Schematic .	121
<b>3 OBSERVATIONS AND DATA REDUCTION .....</b>	<b>124</b>
3.1 Acquisition of Dark and Flat Field Frames .....	125
3.2 Target Choice .....	132
3.3 Sample Reduction of Data .....	135
3.3.1 Step 1 - Acquisition of Raw Data .....	135

**TABLE OF CONTENTS**  
(Continued)

<b>Chapter</b>	<b>Page</b>
3.3.2 Step 2 - Application of the Flat Field and Dark Frame Images .....	136
3.3.3 Step 3 - Calculation of the Stokes Parameters.....	138
3.3.4 Step 4 - Longitudinal Magnetogram.....	139
3.3.5 Step 5 - Cross Talk .....	140
3.3.6 Step 6 - Vector Magnetograms .....	148
3.3.7 Step 7 - Converting Vector Magnetic Field into Cartesian Coordinates.....	150
3.3.8 Step 8 – Plot the Vector Magnetograms.....	150
3.3.9 180° Ambiguity in Vectors.....	151
3.3.10 Magnetograms on the Web .....	152
3.4 Archiving the Data .....	154
3.5 Automatic Web Page for Reviewing the Data .....	155
3.6 Evaluation of Data .....	157
3.6.1 Image Sensitivity vs. Number of Integrations .....	157
3.6.2 Image Post-Processing (Alignment and Selection) .....	168
3.7 Sample Longitudinal Magnetograms .....	173
3.7.1 Sample Quiet-Sun Longitudinal Magnetogram .....	174
3.7.2 Sample Active Region Longitudinal Magnetogram .....	177
3.7.3 The Limb (Canopy) Effect .....	180
3.8 Sample Vector Magnetograms .....	183

**TABLE OF CONTENTS**  
(Continued)

<b>Chapter</b>	<b>Page</b>
3.8.1 Test Instrument on a Simple Round Sunspot .....	183
3.8.2 Active Region With a Complicated Magnetic Field .....	185
<b>4 RAPID CHANGES IN THE SOLAR MAGNETIC FIELD .....</b>	<b>189</b>
4.1 Rapid Changes of Magnetic Fields Associated with Six X-Class Flares ....	190
4.1.1 Introduction .....	190
4.1.2 Observations and Data Reduction .....	192
4.1.3 Results .....	194
4.1.4 Summary and Discussion .....	208
4.2 Rapid Changes in the Longitudinal Magnetic Field Related to the 2001 April 2 X20 Flare .....	211
4.2.1 Introduction .....	211
4.2.2 Data and Instrumentation .....	212
4.2.3 Results .....	215
4.2.4 Discussion and Conclusions .....	220
4.3 Magnetic Field, H-Alpha and RHESSI Observations of the 2002 July 23 Gamma-Ray Flare .....	224
4.3.1 Introduction .....	224
4.3.2 Observations .....	226
4.3.3 The Gamma-Ray Flare as seen in Multi-Wavelength Data .....	228
4.3.4 Rapid Changes of the Longitudinal Magnetic Field Associated with the Flare .....	231

**TABLE OF CONTENTS**  
(Continued)

<b>Chapter</b>	<b>Page</b>
4.3.5 Discussion .....	241
<b>5 SOME CURRENT AREAS OF STUDY .....</b>	<b>247</b>
5.1 High Cadence Observations of an Impulsive Flare .....	247
5.1.1 Introduction .....	247
5.1.2 Observations and Data Reduction .....	249
5.1.3 Results .....	250
5.1.4 Discussion .....	269
5.2 Signature of an Avalanche in Solar Flares as Measured by Photospheric Magnetic Fields .....	271
5.2.1 Introduction .....	271
5.2.2 Observations .....	273
5.2.3 Methods .....	276
5.2.4 Data Processing and Results .....	283
5.2.5 Summary and Discussion .....	300
<b>CONCLUSIONS .....</b>	<b>304</b>
6.1 Digital Vector Magnetograph Characterization and Data Quality .....	304
6.2 Testing the DVMG on a Simple Round Sunspot .....	305
6.3 Image Post Processing (Alignment & Selection) .....	306
6.4 Rapid Changes in the Solar Magnetic Field .....	307
6.5 Limitations of Current Observations and Motivation for Improvements ....	308



**TABLE OF CONTENTS**  
**(Continued)**

<b>Chapter</b>	<b>Page</b>
6.5.1 Desired Improvements to Magnetographs in General .....	308
6.5.2 Desired Improvements to the DVMG Specifically .....	308
6.6 Future Instrumentation .....	309
APPENDIX A MUELLER MATRICES.....	312
A.1 Mueller Matrices of Reterders.....	312
A.2 Mueller Matrices of Polarizations of Light.....	313
APPENDIX B TEMPERATURE CONTROL AND OPTICS MOUNTING COMPONENTS .....	315
APPENDIX C CN76000 TEMPERATURE CONTROLLER.....	316
APPENDIX D 100Ω Pt RTD-850 TEMPERATURE PROBE.....	317
APPENDIX E FLEXIBLE SILICON RUBBER FIBERGLASS INSULATED HEATERS.....	318
APPENDIX F USING THE INSTRUMENT.....	319
F.1 Camera Initialization.....	319
F.2 Live Images.....	320
F.3 Instrument Settings.....	321
F.3.1 Edit/Sequene Configuration.....	321
F.3.2 Edit/Display Setting Pull Down Menu.....	329
F.3.3 Edit/Object Type Pull Down Menu.....	330
F.3.4 Edit/Crystal Voltage Pull Down Menu.....	331
F.4 File/Start & File/Acquire Pull Down Menus.....	331

**TABLE OF CONTENTS**  
**(Continued)**

<b>Chapter</b>	<b>Page</b>
F.5 Telescope Control Computer.....	332
REFERENCES.....	334

## TABLE OF CONTENTS

Chapter	Page
1 INTRODUCTION .....	1
1.1 Solar Basics and Space Weather .....	1
1.2 Structure of the Sun and Solar Activity .....	8
1.3 The Zeeman Effect .....	20
1.4 Review of Magnetograph Types .....	30
1.4.1 Full Spectrum Magnetograph .....	30
1.4.2 Spectroheliograph Based Magnetograph .....	31
1.4.3 Filter Based Magnetograph .....	33
1.4.4 Fabry-Perot Based Magnetograph .....	36
1.5 Development of the Solar Magnetograph: The Hale Tower Telescope Magnetograph .....	37
1.6 Initial Attempts to Measure the Magnetic Field of the Sun With Photoelectric Methods .....	42
1.7 The Babcock Photoelectric Magnetograph .....	43
1.8 The Leighton Photographic Subtraction Magnetograph .....	48
1.9 The Big Bear Magnetograph.....	53
2 INSTRUMENTATION .....	59
2.1 Overview of the Instrument .....	62
2.2 Telescope Details and Limitations .....	66
2.3 Image Scale & Light Throughput .....	72
2.4 The Ca I Absorption Line .....	75

**TABLE OF CONTENTS**  
(Continued)

<b>Chapter</b>	<b>Page</b>
2.5 The Pre-Filter .....	76
2.6 Polarization Optics .....	78
2.6.1 Review of Mueller Calculus .....	80
2.6.2 Principles of Retarders .....	82
2.6.3 Nematic Liquid Crystal Variable Retarders .....	84
2.6.4 Ferroelectric Variable Retarders .....	88
2.6.5 Three Crystal Optical Layout .....	90
2.6.6 LCVR and FLC Calibration .....	95
2.7 The Birefringent Filter .....	106
2.7.1 Tuning the Birefringent Filter .....	108
2.8 The CCD Camera, Image Capture Board & Instrument Control Program ...	113
2.9 The Weak-Field Approximation .....	116
2.9.1 Introduction .....	116
2.9.2 Brief Overview of the Weak Field Approximation .....	118
2.10 DVMG & Telescope Control Computers and Overall System Schematic .	121
<b>3 OBSERVATIONS AND DATA REDUCTION .....</b>	<b>124</b>
3.1 Acquisition of Dark and Flat Field Frames .....	125
3.2 Target Choice .....	132
3.3 Sample Reduction of Data .....	135
3.3.1 Step 1 - Acquisition of Raw Data .....	135

**TABLE OF CONTENTS**  
(Continued)

<b>Chapter</b>	<b>Page</b>
3.3.2 Step 2 - Application of the Flat Field and Dark Frame Images .....	136
3.3.3 Step 3 - Calculation of the Stokes Parameters.....	138
3.3.4 Step 4 - Longitudinal Magnetogram.....	139
3.3.5 Step 5 - Cross Talk .....	140
3.3.6 Step 6 - Vector Magnetograms .....	148
3.3.7 Step 7 - Converting Vector Magnetic Field into Cartesian Coordinates.....	150
3.3.8 Step 8 – Plot the Vector Magnetograms.....	150
3.3.9 180° Ambiguity in Vectors.....	151
3.3.10 Magnetograms on the Web .....	152
3.4 Archiving the Data .....	154
3.5 Automatic Web Page for Reviewing the Data .....	155
3.6 Evaluation of Data .....	157
3.6.1 Image Sensitivity vs. Number of Integrations .....	157
3.6.2 Image Post-Processing (Alignment and Selection) .....	168
3.7 Sample Longitudinal Magnetograms .....	173
3.7.1 Sample Quiet-Sun Longitudinal Magnetogram .....	174
3.7.2 Sample Active Region Longitudinal Magnetogram .....	177
3.7.3 The Limb (Canopy) Effect .....	180
3.8 Sample Vector Magnetograms .....	183

**TABLE OF CONTENTS**  
(Continued)

<b>Chapter</b>	<b>Page</b>
3.8.1 Test Instrument on a Simple Round Sunspot .....	183
3.8.2 Active Region With a Complicated Magnetic Field .....	185
<b>4 RAPID CHANGES IN THE SOLAR MAGNETIC FIELD .....</b>	<b>189</b>
4.1 Rapid Changes of Magnetic Fields Associated with Six X-Class Flares ....	190
4.1.1 Introduction .....	190
4.1.2 Observations and Data Reduction .....	192
4.1.3 Results .....	194
4.1.4 Summary and Discussion .....	208
4.2 Rapid Changes in the Longitudinal Magnetic Field Related to the 2001 April 2 X20 Flare .....	211
4.2.1 Introduction .....	211
4.2.2 Data and Instrumentation .....	212
4.2.3 Results .....	215
4.2.4 Discussion and Conclusions .....	220
4.3 Magnetic Field, H-Alpha and RHESSI Observations of the 2002 July 23 Gamma-Ray Flare .....	224
4.3.1 Introduction .....	224
4.3.2 Observations .....	226
4.3.3 The Gamma-Ray Flare as seen in Multi-Wavelength Data .....	228
4.3.4 Rapid Changes of the Longitudinal Magnetic Field Associated with the Flare .....	231

**TABLE OF CONTENTS**  
(Continued)

<b>Chapter</b>	<b>Page</b>
4.3.5 Discussion .....	241
<b>5 SOME CURRENT AREAS OF STUDY .....</b>	<b>247</b>
5.1 High Cadence Observations of an Impulsive Flare .....	247
5.1.1 Introduction .....	247
5.1.2 Observations and Data Reduction .....	249
5.1.3 Results .....	250
5.1.4 Discussion .....	269
5.2 Signature of an Avalanche in Solar Flares as Measured by Photospheric Magnetic Fields .....	271
5.2.1 Introduction .....	271
5.2.2 Observations .....	273
5.2.3 Methods .....	276
5.2.4 Data Processing and Results .....	283
5.2.5 Summary and Discussion .....	300
<b>CONCLUSIONS .....</b>	<b>304</b>
6.1 Digital Vector Magnetograph Characterization and Data Quality .....	304
6.2 Testing the DVMG on a Simple Round Sunspot .....	305
6.3 Image Post Processing (Alignment & Selection) .....	306
6.4 Rapid Changes in the Solar Magnetic Field .....	307
6.5 Limitations of Current Observations and Motivation for Improvements ....	308

**TABLE OF CONTENTS**  
**(Continued)**

<b>Chapter</b>	<b>Page</b>
6.5.1 Desired Improvements to Magnetographs in General .....	308
6.5.2 Desired Improvements to the DVMG Specifically .....	308
6.6 Future Instrumentation .....	309
APPENDIX A MUELLER MATRICES.....	312
A.1 Mueller Matrices of Reterders.....	312
A.2 Mueller Matrices of Polarizations of Light.....	313
APPENDIX B TEMPERATURE CONTROL AND OPTICS MOUNTING COMPONENTS .....	315
APPENDIX C CN76000 TEMPERATURE CONTROLLER.....	316
APPENDIX D 100Ω Pt RTD-850 TEMPERATURE PROBE.....	317
APPENDIX E FLEXIBLE SILICON RUBBER FIBERGLASS INSULATED HEATERS.....	318
APPENDIX F USING THE INSTRUMENT.....	319
F.1 Camera Initialization.....	319
F.2 Live Images.....	320
F.3 Instrument Settings.....	321
F.3.1 Edit/Sequene Configuration.....	321
F.3.2 Edit/Display Setting Pull Down Menu.....	329
F.3.3 Edit/Object Type Pull Down Menu.....	330
F.3.4 Edit/Crystal Voltage Pull Down Menu.....	331
F.4 File/Start & File/Acquire Pull Down Menus.....	331



**TABLE OF CONTENTS**  
**(Continued)**

<b>Chapter</b>	<b>Page</b>
F.5 Telescope Control Computer.....	332
REFERENCES.....	334

## LIST OF FIGURES

<b>Figure</b>		<b>Page</b>
1.1	Examples of near-Earth and Earth-bound systems which can be effected by space weather.....	2
1.2	The solar corona .....	3
1.3	Examples of a solar flare (left), a CME (center) and a coronal hole (right) .....	4
1.4	Structure of the Sun .....	10
1.5	Full-disk white light (left) and full-disk longitudinal magnetogram (right).....	13
1.6	High resolution image of a sunspot.....	14
1.7	The 11 year solar cycle.....	17
1.8	The Maunder Butterfly diagram.....	19
1.9	Portion of the solar spectrum.....	23
1.10	Zeeman's experiment.....	26
1.11	The Zeeman Effect.....	26
1.12	Polarization components of the Zeeman Triplet.....	27
1.13	The Zeeman Effect in a sunspot.....	29
1.14	Basic schematic of a filter based magnetograph.....	33
1.15	Example of a magnetogram from a filter based system.....	35
1.16	The Mt. Wilson 60 Foot Tower Telescope.....	40
1.17	Schematic of the two slits and photomultipliers of the Babcock magnetograph.....	45

**LIST OF FIGURES**  
(Continued)

<b>Figure</b>	<b>Page</b>
1.18 Photograph of the CRT output from the Babcock magnetograph.....	46
1.19 Schematic of the polarization optics and spectrograph slit for the Leighton photographic spectrograph.....	49
1.20 The Leighton photographic subtraction technique.....	50
1.21 Schematic of the original VMG system.....	54
1.22 Saving the magnetograms from the original VMG system.....	55
2.1 Schematic and optical layout of the DVMG.....	64
2.2 Functional block diagram of the DVMG.....	65
2.3 The Big Bear Solar Observatory (BBSO).....	67
2.4 Photo of the telescope assembly at BBSO.....	67
2.5 Optical bench of the 25 cm vacuum-refractor.....	68
2.6 The Ca I absorption line profile.....	75
2.7 The Pre-filter band-pass.....	77
2.8 Orthogonal decomposition of linearly polarized light.....	83
2.9 Orthogonal decomposition of circularly polarized light.....	84
2.10 Schematic & operation of the nematic liquid crystal variable retarders ...	86
2.11 Example of retardance vs. input voltage for the LCVR.....	87
2.12 Typical response time of a LCVR.....	88
2.13 Optical diagram of Step1 of calibrating LCVR <sub>1</sub> .....	97
2.14 Optical diagram of Step 2 of calibrating LCVR <sub>1</sub> .....	97

**LIST OF FIGURES**  
(Continued)

<b>Figure</b>	<b>Page</b>
2.15 Light intensity at the CCD vs. rotation angle of $LP_1$ for Step 2.....	97
2.16 Optical diagram of Step 3 of calibrating $LCVR_1$ .....	98
2.17 Optical diagram of Step 4 of calibrating $LCVR_1$ .....	99
2.18 Typical retardance vs. voltage plot for a $LCVR$ .....	99
2.19 Light intensity at the CCD vs. rotation angle of $LCVR_1$ for Step 5.....	100
2.20 Light intensity at the CCD vs. retardance of $LCVR_1$ for Step 6.....	100
2.21 Optical diagram of Steps 9 & 10 of calibrating $LCVR_1$ .....	101
2.22 Light intensity at the CCD vs. rotation angle of the FLC for Step 3.....	103
2.23 Example of cross talk in a Stokes-Q image.....	104
2.24 Sample vector magnetogram of a simple round sunspot.....	106
2.25 Ca I line profile.....	113
2.26 Block diagram of how the CCD camera, frame grabber board and instrument control program interact.....	114
2.27 Straight-line approximation of the Ca I 610.3 nm absorption line.....	119
2.28 Example of the Zeeman shift in the straight line approximation of the Ca I absorption line.....	120
2.29 General control schematic.....	122
3.1 Sample dark image.....	126
3.2 Sample flat field image.....	128
3.3 Typical flat field images for the individual stokes components.....	132
3.4 Example of the Active Region Monitor (ARM) web page.....	134

**LIST OF FIGURES**  
(Continued)

<b>Figure</b>	<b>Page</b>
3.5 Example of the results of the application of the dark and flat field images to the raw data.....	137
3.6 Sample of Stokes-V, Q & U images.....	138
3.7 Longitudinal magnetogram.....	140
3.8 Schematic of the components of the magnetic field.....	141
3.9 Example of cross-talk.....	145
3.10 Example of a cross-talk scatter plot.....	146
3.11 Example of correction for cross-talk.....	147
3.12 $B_T$ (left) and $\alpha$ (right) images.....	149
3.13 Vector magnetogram.....	150
3.14 Sample of DVMG data on the BBSO Latest Images web page.....	153
3.15 A Sample of the DVMG Data Summary Page for 04Jun16.....	156
3.16 Four quiet-Sun longitudinal magnetograms obtained on 04Jan29.....	158
3.17 The standard-deviation of the portion of the longitudinal magnetogram produced with 1024 total integrations (as shown in Figure 3.16) that was selected by the noise mask vs. the threshold of each noise mask...	161
3.18 2D surface plot of the lower-right magnetogram in Figure 3.16.....	162
3.19 The noise mask (left) and the lower right longitudinal magnetogram from Figure 3.16.....	163
3.20 The standard deviation of a set of longitudinal magnetograms vs. the number of integrations in each image.....	164
3.21 $B_T$ (left images) and $\alpha$ (right images) images for the Stokes-Q (upper set) and Stokes-U (lower set) images.....	166

**LIST OF FIGURES**  
**(Continued)**

<b>Figure</b>	<b>Page</b>
3.22 A plot of the noise (in Gauss) vs. the number of integrations for the idealized Stokes-Q (solid) and idealized Stokes-U (dashed) images....	167
3.23 Plot of the contrast of a set of magnetograms vs. the image number.....	170
3.24 Plot of image translation of a set of magnetograms in arc-sec vs. image number.....	171
3.25 Longitudinal magnetograms not using (left) and using image selection & alignment.....	172
3.26 Power spectra of left (solid) and right (dashed) magnetograms in Figure 3.25.....	173
3.27 Quiet Sun longitudinal magnetogram acquired at 15:57 UT on September 13, 2004.....	176
3.28 Quiet Sun longitudinal magnetogram acquired at 15:57 UT on September 13, 2004.....	176
3.29 610.3 nm intensitygram obtained at 15:57 UT.....	177
3.30 Longitudinal magnetogram of active region NOAA 10652 obtained July 23, 2004.....	178
3.31 610.3 nm intensitygram corresponding to the magnetogram shown in Figure 3.30.....	180
3.32 Example of the Limb (Canopy) Effect.....	182
3.33 610.3 nm intensitygram (left) and vector magnetogram (right) of active region NOAA 10306 on 03Mar12.....	184
3.34 610.3 nm intensitygram (left) and vector magnetogram (right) of active region NOAA 10330 on 03Apr08.....	184
3.35 610.3 nm intensitygram of active region NOAA 10652 on 04Jul24.....	186

**LIST OF FIGURES**  
(Continued)

<b>Figure</b>	<b>Page</b>
3.36	Vector magnetogram of active region NOAA 10652 on 04Jul24..... 187
4.1	Line-of-sight magnetogram (left), white-light (center) and H $\alpha$ images of the 2001 August 25 flare that occurred in AR 9591. The field of view is 190 arc-sec x 190 arc-sec. The box marks the flux calculation area. The H $\alpha$ image shows the morphology of the flare..... 196
4.2	(First panel) Evolution of magnetic flux in AR 9591 on 2001 August 25. The solid line represents the following (positive) flux, while the dashed line represents the leading flux (negative). The thin solid line is the Yohkoh hard X-ray curve in the high-energy channel of HXT. (Second panel) Evolution of transverse field strength. (Third panel) Weighted mean shear angle. (Bottom panel) Mean intensity in the box..... 198
4.3	Sequence of TRACE images showing the 2001 August 25 flare. The new penumbral area is indicated by the arrow. The time of the flare maximum is approximately 16:32 UT..... 199
4.4	Line-of-sight magnetogram (left), white-light (center) and H $\alpha$ images for the flare of 2001 October 19 that occurred in AR 9661. The field-of-view is 120 arc-sec x 120 arc-sec. The box marks the flux calculation area. The H $\alpha$ image shows the morphology of the flare.... 200
4.5	(Top) Evolution of magnetic flux on 2001 October 19. The solid line represents the leading (positive) flux, while the dashed line represents the following (negative) flux. The thin solid line is the Yohkoh hard X-ray curve in the high-energy channel of HXT. The remaining panels are as in Figure 4.2..... 201
4.6	Vector magnetograms of 2001 October 19 of AR 9661. (Left) Magnetic fields before the flare. (Right) Magnetic fields after the flare. Grey scale represents the line-of-sight magnetic field strength, which is also plotted as contours (red as positive, blue as negative). The green arrows indicate the transverse fields. The dark black lines are the magnetic neutral lines where the line-of-sight field is zero..... 203
4.7	(Left) Line-of-sight magnetogram of 2001 April 6 of AR 9415. The box marks the flux calculation area. (Right) TRACE 17.1 nm image during the flare. The field-of-view is 200 arc-sec x 200 arc-sec..... 205

**LIST OF FIGURES**  
(Continued)

<b>Figure</b>	<b>Page</b>
4.8 Evolution of negative (leading polarity, dashed line) and positive (following polarity, thick solid line) magnetic flux in AR 9415 on 2001 April 6. The thin solid line is the Yohkoh/WBS hard X-ray curve.....	206
4.9 Line-of-sight magnetogram (left), white-light (center) and H $\alpha$ images (right) of the 2001 October 22 flare that occurred in AR 9672. The field-of-view is 120 arc-sec x 120 arc-sec. The H $\alpha$ image shows the morphology of the flare.....	207
4.10 Evolution of the line-of-sight magnetic flux in AR 9672 on 2001 October 22. The solid line represents the following (positive) flux, while the dashed line represents the leading (negative) flux. The thin solid line is the Yohkoh hard X-ray curve in the high energy channel of HXT.....	207
4.11 Ca I (left) and H $\alpha$ center-line (right) intensitygram taken during the flare.....	215
4.12 Two sets of Ca I intensitygrams and Stokes-V images from before (top) and after (bottom) the flare.....	217
4.13 Evolution of the magnitude of the positive and negative normalized flux in the region of the flare (solid line) and the control region (dotted line). The bottom panel shows the GOES-8 X-ray flux during the flare.....	219
4.14 Schematic of how the emergence of the magnetic flux inside the limbward penumbra of a negative polarity sunspot can be seen, at the western solar limb, as an increase in the positive polarity field.....	221
4.15 Cross-sectional view of the sunspot, which demonstrates a possible magnetic field configuration that could account for the observed changes. The top panel displays the configuration before the flare, while the bottom panel displays the configuration after. The thick vectors represent the actual magnetic field, while the thin vectors show the line-of-sight component.....	223



**LIST OF FIGURES**  
(Continued)

<b>Figure</b>	<b>Page</b>	
4.16	BBSO H $\alpha$ images of the X4.8 two-ribbon flare on 2002 July 23. The field-of-view is 118 arc-sec x 280 arc-sec. The dashed contours are the corresponding RHESSI X-ray emissions in the energy range of 12 to 20 keV, while the solid contours are for the 100 to 150 keV energy band. The white circle in the right panel shows the position of the 2.223 MeV centroid. North is up and west if to the right.....	228
4.17	(Thin lines) Light curves for 50 – 100, 100 – 300, 800 – 1900, 2218 – 2228 and 2228 – 7000 keV energy bands. (Thick lines) H $\alpha$ light curves for the flare core (top panel) and the for remote brightening (fourth panel).....	230
4.18	MDI positive (top) and negative (bottom) magnetic flux and the RHESSI XRT flux (shaded area in arbitrary units) in the 100 – 150 keV energy range shown as a function of time.....	232
4.19	Two BBSO DVMG vector magnetograms acquired before (July 22 at 22:43 UT, left) and after (July 23 at 0114 UT, right) the 2002 July 23 gamma-ray flare. The backgrounds are longitudinal magnetograms (white/black correspond to $\pm 350$ Gauss). The leading polarity is negative (black). The gray thick contours outline the photospheric-penumbra boundary of the sunspots. The black and white line segments display the transverse magnetic field, while the box and circle mark the areas where the magnetic flux changes were studied in detail. North is up and west is to the right.....	234
4.20	RHESSI data (the same as in Figure 4.16) plotted over two BBSO longitudinal magnetograms (white/black correspond to $\pm 450$ Gauss) acquired before and after the flare. The box and the circle are the same as in Figure 4.19. The cross marks the position of the 2.223 MeV source centroid. North is up and west is to the right.....	237
4.21	BBSO H $\alpha$ center (left) and H $\alpha$ -0.07 nm (right) images obtained ~2 hr before the flare. One of the foot-points of a cold surge, indicated by the arrow, is located at the position of the earlier XRT foot-point and is probably associated with flux emergence. The box and the circle are the same as in Figure 4.19 (see also Figures 4.16 & 4.20).....	239

**LIST OF FIGURES**  
(Continued)

<b>Figure</b>	<b>Page</b>	
4.22	Simulated magnetograms: vertical component, $B_z$ , shown at the center of the solar disk (left) and the longitudinal component of an LFFF calculated with parameter $\alpha = 0.025 \text{ arc-sec}^{-1}$ and $\alpha = 0.001 \text{ arc-sec}^{-1}$ (middle two panels), as seen at the eastern limb. White/black is a magnetic field intensity exceeding $\pm 500$ Gauss. The right panel shows the difference image between the two longitudinal components (black represents areas where the longitudinal component decreased).....	239
5.1	Time profiles of GOES soft X-ray (+), BASTE hard X-ray (solid line), $H\alpha$ line center (dotted line) and $H\alpha$ -0.13 nm (dashed line) emissions of the 1999 August 23 flare. The $H\alpha$ light curves indicate the excess emission, i.e., the flare intensity with the quiet region intensity subtracted and then normalized to the quiet region intensity. The two vertical band in the plot indicate the two intervals of the $H\alpha$ -0.13 nm emission analyzed in the paper and plotted in Figures 5.5 & 5.6.....	251
5.2	Time sequence of $H\alpha$ -0.13 nm (top six panels) and $H\alpha$ line center (bottom six panels) images showing the evolution of the flare. The white boxes in the figures indicate the regions from which $H\alpha$ -0.13 nm light curves were obtained at the three flare kernels and the quiet-Sun region.....	253
5.3	Time sequence of $H\alpha$ -0.13 nm flare emission as shown by contours; the contour levels are 0.05, 0.1, 0.2, 0.4 and 0.8 of the maximum of the emission. The background is the magnetogram obtained right before the flare.....	255
5.4	Time profiles of the flare emission in $H\alpha$ -0.13 nm at three flare kernels (solid line) compared with BASTE hard X-ray emission (dashed line) and GOES soft X-ray 0.1 to 0.8 nm emission (dot-dashed line).....	256
5.5	Comparison of $H\alpha$ -1.3A intensity (thin lines) and hard X-ray flux (thick lines) for three flare kernels during the time interval 18:03:59 to 18:04:06 UT. For the $H\alpha$ emission, both the raw data and a 10 point smoothed curve are plotted.....	259
5.6	Comparison of $H\alpha$ -0.13 nm intensity (thin lines) and hard X-ray flux (thick lines) for three flare kernels during the time interval from 18:04:22 to 18:04:29 UT. For the $H\alpha$ emission, both the raw data and a ten point smoothed curve are plotted.....	262

**LIST OF FIGURES**  
(Continued)

<b>Figure</b>		<b>Page</b>
5.7	Time profiles of H $\alpha$ -0.13 nm flare emission. The ten point smoothed background is subtracted from all of the curves. The top three panels show fluctuations at three flare kernels in the time interval shown in Figure 5.1. The bottom panel shows the variations at K1 in a time interval 40 sec later.....	264
5.8	Power spectra of the fast variations of the H $\alpha$ -0.13 nm emission at the three flare kernels 18:04:22 to 18:04:29 UT.....	265
5.9	Sketch of the magnetic configuration of the flare before and after the reconnection. The background contours show the line-of-sight magnetogram taken before the flare as in Figure 5.3. The solid (dashed) lines indicate the positive (negative) magnetic polarities, and the contour levels are $\pm 20, 50, 100$ & $200$ Gauss.....	268
5.10	Maps of the longitudinal magnetic field of the four active regions under study. Images are scaled with a range of $\pm 500$ Gauss. West is to the right and north is to the top.....	274
5.11	Exponents $\zeta(q)$ of structure functions of order $q$ vs. $q$ , calculated for two magnetograms of NOAA AR 0039. The Kolmororov's straight line K41 corresponding to non-intermittent turbulence is shown with the dotted line. The thin solid line denotes the scaling exponents before the onset of the flare at 20:28 UT (small deviations from the K41 line, low degree of intermittency). The thick solid line shows the scaling exponents during the rising phase of the flare, at 20:57:40 UT (this moment of the maximum $\beta$ is denoted as $t_1$ in Figure 5.17; large deviation from the K41 line, high degree of intermittency).....	277
5.12	Structures of magnetic energy dissipation, $\varepsilon(B_z)$ , shown in arbitrary units, were calculated by using eq. (4) for the magnetograms shown in Figure 5.10.....	281

**LIST OF FIGURES**  
(Continued)

<b>Figure</b>	<b>Page</b>
5.13    Photos of the normalized correlation function, $b(r)$ , of magnetic energy dissipation calculated by using eqs. (5) and (6) for two magnetograms of NOAA AR 9661. The areas under the curves are equal to the correlation length $\lambda$ of the magnetic energy dissipation at two different times. The thick line correspond to the moment of the minimum correlation length near the beginning of the flare (16:19:37 UT). The thin line shows the correlation function when $\lambda$ was at its maximum near the peak of the flare (16:27:04 UT).....	283
5.14    Map of the longitudinal magnetic field for NOAA AR 9661 (left panel, the intensity of the I mage is scaled within a range of $\pm 250$ Gauss), and an $H\alpha$ image of the X1.6 flare (right panel) shown at 16:25:33 UT (also denoted by the arrow in Figure 5.15). The contours enclose the area within an $H\alpha$ intensity twice that of the intensity of the undisturbed chromosphere. The area inside the contours was excluded from the calculation of the $\beta$ and $\lambda$ parameters. West is to the right and north is to the top.....	285
5.15    Time variations of the parameters for the X1.6 flare on 2001 October 19 in NOAA AR 9661: the scaling exponent, $\beta$ (top panel), and the correlation length, $\lambda$ (bottom panel). The thick lines represent the data calculated from the entire magnetogram, whereas the thin solid lines show the data calculated with the individual blocking of the bright $H\alpha$ areas, and the thick dotted lines represent the result of the common blocking of the bright $H\alpha$ ribbons. The arrow indicates the moment at which the magnetogram and $H\alpha$ image used in Figure 5.14 were obtained. The flux of $H\alpha$ emission, in arbitrary units, is shown in the bottom panel by the dash-dotted line. The vertical dotted lines denoted as $t_1$ and $t_2$ are the same as in Figure 5.18.....	286

**LIST OF FIGURES**  
(Continued)

<b>Figure</b>	<b>Page</b>	
5.16	<p>Time variations of the parameters for the M8.4 solar flare on 1998 November 5 in NOAA AR 8375. The upper panel shows the 0.1 to 0.8 nm GOES X-ray flux (thin line), its time derivative (thick line), the H<math>\alpha</math> flux in arbitrary units (dash-dotted line) and the BATSE X-ray flux, in arbitrary units. In the middle panel the relative variations of the contrast, <math>c</math> (diamonds), and total positive F+ (stars) and negative F- (triangles) magnetic flux are plotted. The bottom panel shows the variations of the correlation length (solid lines) and the scaling exponent, <math>\beta</math> (dotted lines). The thin lines are the original values, and the thick lines are their smoothed values. The left vertical dotted line marks the moment of maximum <math>\beta</math>, <math>t_1</math>. The right vertical dotted line indicates the moment when <math>\lambda</math> is maximum, <math>t_2</math>. The time interval between the two vertical lines is defined as <math>T_\lambda</math>, (see text, § 5.4.4).....</p>	289
5.17	<p>Time variations of parameters for the M8.7 flare on 2002 July 26 in NOAA AR 0039. The notations for the top and middle panels are the same as in Figure 5.16. The bottom panel shows the non-smoothed values for the scaling exponent, <math>\beta</math> (dotted line), and correlation length, <math>\lambda</math> (bold solid line), calculated for each magnetogram. The thin solid line in the lower part of the bottom panel shows the values of <math>\beta</math> (left axis) calculated by using the full-disk MDI magnetograms.....</p>	291
5.18	<p>Time variations of parameters for the X1.6 flare on 2001 October 19 in NOAA 9661. The notations are the same as in Figure 5.16.....</p>	294
5.19	<p>Time variations of parameters for the X9.4 flare on 1991 march 22 in NOAA 6555. The notations are the same as in Figure 5.17.....</p>	296
6.1	<p>Vector magnetogram of a simple round sunspot.....</p>	305
6.2	<p>Example of the improvements gained when using image selection and alignment.....</p>	306
F.1	<p>Variation in the seeing, as measured by the contrast, of a sequence of 100 610.3 nm intensitygrams.....</p>	324

## CHAPTER 1

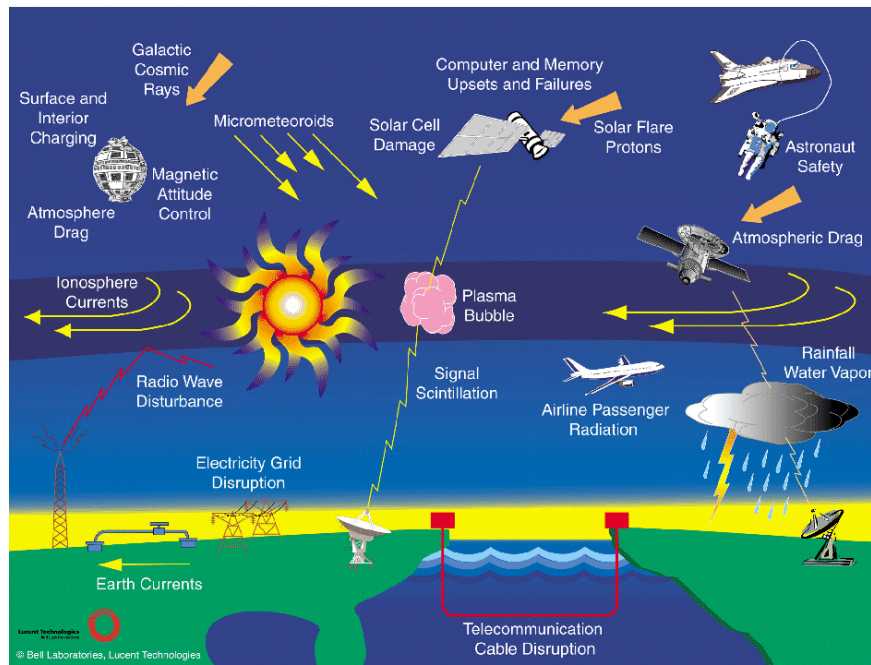
### INTRODUCTION

#### 1.1 Solar Basics and Space Weather

The Sun, a typical main-sequence star, is a self-gravitating hot ball of gas with a radius of  $6.96 \times 10^5$  km., a mass of  $1.99 \times 10^{33}$  grams, a luminosity of  $3.86 \times 10^{33}$  ergs/sec with an age of approximately 4 ½ billion years and is primarily composed of hydrogen and helium. Via nuclear fusion, the Sun converts hydrogen into helium, neutrinos and energy, thus providing the Earth with its life sustaining light. Activity on the Sun, in the form of solar flares, Coronal Mass Ejections (CMEs) and coronal holes, can effect the near-Earth space environment. The term “space weather” specifically refers to the conditions of the near-Earth interplanetary environment which can influence the performance and reliability of space and ground-based systems [1].

Solar flares, CMEs and coronal holes can emit huge bursts of radiation and high-energy particles into interplanetary space, sometimes explosively. These events are ultimately caused by the interaction of very strong magnetic fields (~1000 Gauss) on the surface of the Sun with the material which composes the solar surface and the solar atmosphere. Depending on the direction that these emissions of radiation and high energy particles are emitted, and depending on the configuration of both the interplanetary magnetic field and the magnetic field of the Earth, these high energy emissions can effect the condition of the near-Earth space environment in a way that can significantly, and negatively, effect Earth bound systems and satellites in orbit ([2] is an

excellent comprehensive summary of the various effects that space weather can have on technological and human systems, which will be briefly discussed in the following few paragraphs). Figure 1.1 shows examples of near-Earth and Earth-bound systems which can be effected by space weather (courtesy [3]).

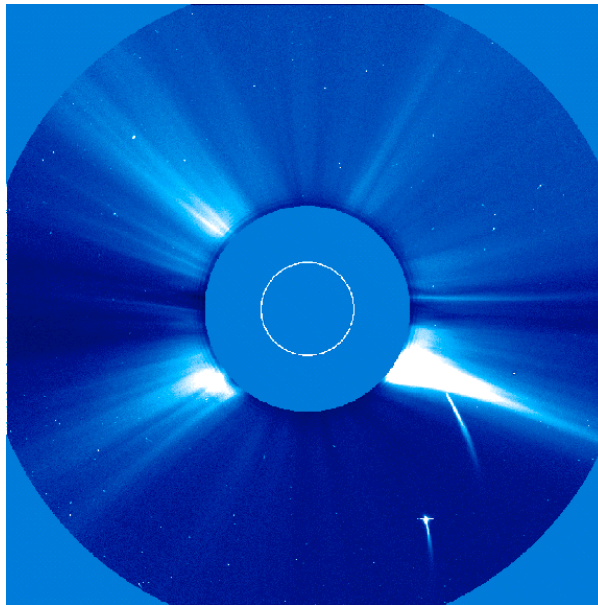


**Figure 1.1** Examples of near-Earth and Earth-bound systems which can be effected by space weather.

The space surrounding the Sun is filled with a tenuous gas, known as the corona, which is made up of charged particles, with a density on the order of a few particles per cubic centimeter. Despite the extremely low density of this plasma, it still exhibits many properties of an ordinary gas, such as pressure and density. The temperature and density of the corona decrease with increasing distance from the Sun. This decrease in temperature and density causes a pressure gradient which is sufficient to overcome the force of the gravity of the Sun and blow the coronal gas away from the Sun. This outflow

of plasma from the Sun is known as the solar wind and constitutes the outer solar atmosphere which extends for many billions of kilometers.

Figure 1.2 shows a Large Angle and Spectromagnetic Coronagraph (LASCO) image from the Solar & Heliospheric Observatory (SOHO) spacecraft. The inner white circle represents the size and location of the Sun while the outer blue circle represents the occulting disk (to avoid saturation of the instrument) of the coronagraph. The bright jet-like features to the lower-right, lower-left and upper-left of the Sun are areas of relatively high particle density due to activity on the solar surface. The two long and thin features to the lower-right of the Sun are sun-grazing comets. (Image courtesy [4].)



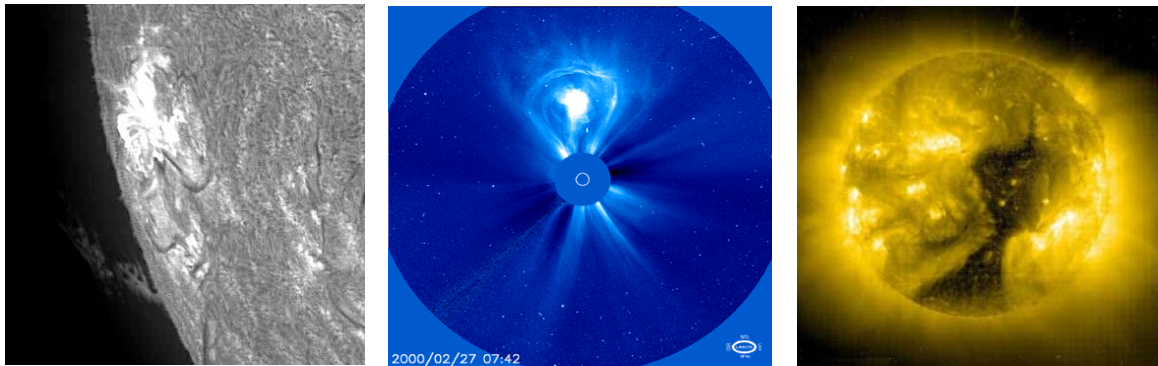
**Figure 1.2** The solar corona.

The solar wind is a continuous stream of charged particles. However, the intensity and speed of the solar wind can be highly variable. This variability in intensity and speed is a direct result of activity on the surface of the Sun, which is driven by the solar



magnetic field. Due to the fact that the plasma of the solar wind is highly electrically conductive, the solar wind can drag the magnetic field of the Sun into interplanetary space. These charged particles, which pass the Earth at hundreds of kilometers per second, and their associated magnetic field, can interact with the magnetic field of the Earth.

Energetic events on the Sun, that can effect the Earth and the near-Earth environment in the short term, can, basically, be divided into three categories: solar flares, CMEs and coronal holes. A solar flare is a rapid rearrangement of the solar magnetic field which releases great amounts of radiation, at all wavelengths, and charged particles [5]. A CME is the ejection of a mass of solar material which carries with it the solar magnetic field into interplanetary space [6] [7] [8]. A coronal hole is a region of open magnetic field in the solar corona. These three events may, or may not, be related to each other depending on the specific circumstances of the state of the solar atmosphere.



**Figure 1.3** Examples of a solar flare (left), a CME (center) and a coronal hole (right).

Figure 1.3 shows examples of a solar flare (left), a CME (center) and a coronal hole (right). The left image is a portion of an H $\alpha$  (626.3 nm) full-disk image from the Big Bear Solar Observatory (BBSO). The flare is the bright region above and slightly to the

left of the center of the image. The center image is from LASCO onboard the SOHO spacecraft. The CME is the light-bulb shaped object above the occulting disk. The right image is from the Extreme Ultra-Violet Imaging Telescope (EIT) onboard the SOHO spacecraft. The coronal hole is the dark object which extends from center-right to the bottom portion of the image. ( $H\alpha$  image courtesy [9]. LASCO and EIT images courtesy [10]).

These events can greatly increase the density and energy of the solar wind [11]. If ejected from the Sun in the path of the Earth, the Earth can be showered with high energy charged particles. These great masses of charged particles can carry with them the very intense, and twisted, remains of the magnetic field from the surface of the Sun. If the direction of the magnetic field, as carried by these charged particles, is orientated in such a direction that it is opposite to the direction of the magnetic field of the Earth the two fields can cancel. This process is known as magnetic reconnection, which weakens the magnetic field of the Earth in the direction of the Sun. The free magnetic energy released during the reconnection of the fields is converted into kinetic energy of the charged particles. The weakening of the magnetic field of the Earth and the high energy of the charged particles of the solar wind allows these charged particles to easily penetrate the magnetic field of the Earth.

These charged particles can have sufficient energy to penetrate the outer reaches of the magnetic field of the Earth. The magnetic field of the Earth tends to deflect the charged particles into regions within approximately  $30^\circ$  of the poles where the field lines converge. These particles can reach the upper atmosphere causing such harmless effects as the northern and southern lights.

However, not all of the effects of these high-energy particles are benign. The bombardment of the upper atmosphere by high-energy particles can cause the atmosphere to heat and expand which increases atmospheric drag on low orbiting satellites. Such particles also represent a significant radiation hazard to astronauts [12] and the avionics and crews of commercial airline flights on polar routes [13]. For example, the passengers and crew on such an airline flight can receive the equivalent of a chest x-ray during a typical storm.

Solar flares also emit great amounts of X-rays and radio noise. In addition to the high-energy particles that collide with the molecules of the atmosphere of the Earth which enhance the ionosphere, this radio noise can interfere with radio communications and GPS based navigation systems [14].

Particles ejected from the Sun during a solar flare or CME can also effect satellites in orbit [15]. Particles with relatively low energies can immerse satellites in a cloud of charged particles which can charge the surface of satellites to negative voltages. These voltages, which can reach 10 kilovolts in a storm, can build up to the point where they can produce sparks which can cause electrical transient signals, which can mimic real signals. These so called “phantom commands” can interfere with real control signals transmitted from control stations on the ground.

Charged particles of moderate energy can penetrate the insulating surface of spacecraft where they can build up a charge to the point that an arc can be formed which can damage the electronics in the spacecraft. This process is known as deep dielectric discharge [16]. High energy protons cause radiation damage to the solar cells that power satellites reducing their efficiency and, thus, the operational lifetime of the satellite. The

charged particles with the highest energy can directly penetrate electronic circuits within satellites and damage memory chips and microprocessors.

The flow of charged particles along the magnetic field lines of the Earth creates strong electric currents that can interfere with the control and pointing systems of satellites and can produce sudden changes in the local magnetic field at the surface of the Earth. These currents can introduce strong torques in satellites, especially in the auroral zone, which can cause uncontrolled tumbling of satellites. These sudden changes in the magnetic field of the Earth near the ground can induce strong currents in electric power grids, causing overloads [17] and the acceleration of corrosion in long pipelines as currents flow between pipe and soil. These currents can also interfere with the testing of microchips which requires the measurements of very low level currents.

Strategies for reducing the impact of space weather events rely, chiefly, on early warning so that satellites can avoid risky maneuvers, astronauts can seek safety, polar commercial airline flights can be rerouted and civilian and military communications can be shifted to methods that are less effected by a space weather event. Commercial and government satellite operators and utility power companies are interested in knowing when a storm is likely to disrupt their service. The goal of space weather research is to be able to predict when a storm is coming with sufficient lead time to make the proper preparations to minimize the effects a storm might have on these systems. In addition, the knowledge gained by the study of the Sun and how solar flares effect the near-Earth space environment can provide engineers the information required so that satellites, and Earth bound systems that can be effected by a space weather event, can be designed to survive the largest expected event over their design lifetime.

Considering the myriad effects that space weather can have on technological systems, it is important that the mechanism which causes storms in space be understood. Since solar flares and CMEs are the primary sources for the high-energy charged particles that can cause a storm, and the fact that solar magnetic field reconnection events are the result of the release of great amounts of energy stored in the magnetic fields on the surface of the Sun which have been highly twisted by the turbulent motions of the solar material, knowing the morphology of the three-dimensional magnetic field, at the surface of the Sun, is of great importance in predicting the probability of solar flares.

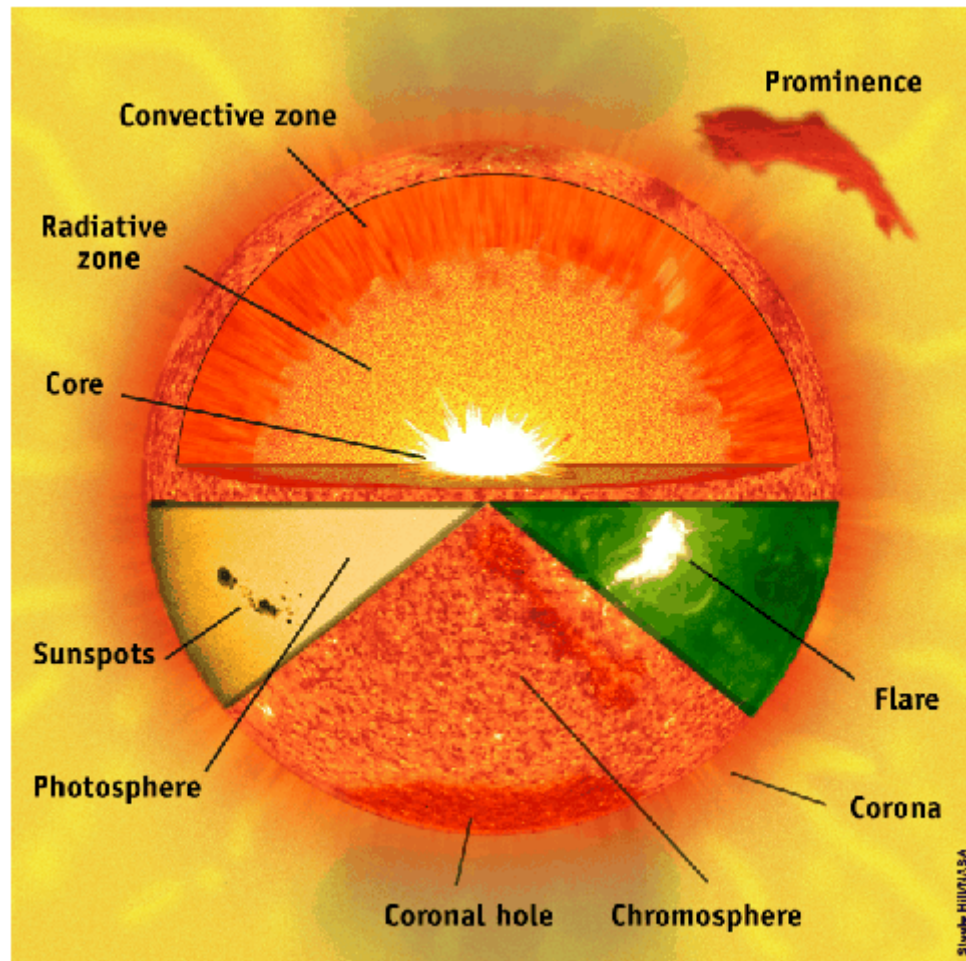
In addition to understanding how the Sun effects the near-Earth environment, detailed observations of the Sun have many other applications. Due to its close proximity to the Earth, the Sun is the only star in the universe that can be studied in high resolution detail. Thus, the Sun can be used as a proxy to test models of stellar structure and evolution. Because of the temperatures and pressures present in the Sun, which are conditions far in excess of that which can be produced in the laboratory, in addition to its very large physical size, the Sun can be used as a unique laboratory to test theories and computer models for studies of atomic, nuclear and plasma physics as well as magnetohydrodynamics.

## **1.2 Structure of the Sun and Solar Activity**

The interior of the Sun can be divided into two distinct regions the radiative zone and the convection zone, each having its own specific physical characteristics as defined by its local temperature, pressure and density. The primary difference between these two regions is the way that energy is transported through each. The inner region of the solar

interior, out to approximately 70% of the radius, is known as the radiative zone, through which energy is transported, over about a million years, by radiative diffusion. The innermost region of the radiative zone, out to approximately 25% of the solar radius, is known as the core and is where the temperature and pressure are sufficiently high to allow the fusion of hydrogen atoms which produces energy, heavier elements and neutrinos. Figure 1.4 shows a cutaway drawing indicating the different regions of the Sun (Courtesy [18]).

Above the radiative zone, and extending to the surface, is the convection zone, where material is transported to the surface, over approximately a month (the so-called dynamical timescale), by turbulent convection. The transition from radiative transfer to convective transfer occurs because the Sun is cool enough at that location that nuclei begin to capture electrons, which gives rise to a sharp opacity gradient that induces a convective instability. Due to the fact that the density near the bottom of the convection zone is on the order of one million times that near the top of the convection zone, only a very small percentage of the material at the bottom of the convection zone would reach the surface within any given month. Furthermore, it would take approximately 100,000 years for the heat currently stored in the convection zone to be radiated away by the luminosity of the Sun (the so-called thermal timescale of the Sun). The photosphere, the top of the convection zone and the visible surface of the Sun, has a temperature of approximately 6000 K and is approximately 500 km thick and is from where virtually all of the visible light from the Sun, known as the solar spectrum, radiates. This region, at the top of the convection zone, emits its energy radiatively because the sharp local density gradient suppresses convection.



**Figure 1.4** Structure of the Sun.

Above the photosphere there are two distinct layers of the solar atmosphere. The inner most region of the atmosphere is known as the chromosphere and extends to a height of approximately 1,500 km above the photosphere. The outer region of the atmosphere is the corona which extends many million of km into space. The Earth, in fact, orbits within the tenuous corona.

The Sun has a general dipole magnetic field on the order of one to two Gauss in the photosphere, as compared to the dipole magnetic field of the Earth which is

approximately  $\frac{1}{2}$  Gauss. It should be noted, however, that the general magnetic field of the Sun does not result from a dipole within the Sun but from the accumulation of many small photospheric magnetic fields, of like polarity, in the polar regions above  $50^\circ$  solar latitude.

The solar plasma has a high electrical conductivity ( $1 \times 10^{-4}$  to 20 ohm/cm) due to the fact that it contains a very high concentration of charge carriers. As the solar plasma moves, relative to the general dipole magnetic field of the Sun, a current is induced in the plasma. By Lenz's law, this current will be in such a direction as to generate a magnetic field that will oppose the motion. Because of the high electrical conductivity of the plasma, and the fact that the characteristic scales on the Sun are so large, the current induced in the plasma, and, thus, the magnetic field generated by the induced current, can persist for a long time. The net result of this effect is that the magnetic field is essentially frozen into the solar plasma. Therefore, not only can the general dipole magnetic field of the Sun effect the motions of the solar plasma but the motions of the solar plasma can literally drag the local magnetic field along with it.

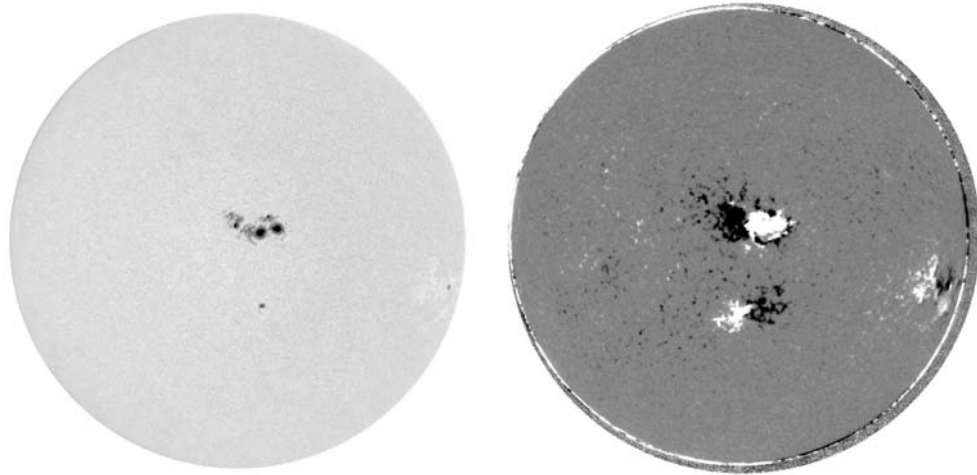
The most obvious manifestation of solar activity are sunspots. sunspots are dark patches on the surface of the Sun which can be from 1,000 km (the smallest pores) to 40,000 km (the largest spots) in diameter, as compared to the Earth which has a diameter of 12,000 km. sunspots usually appear in groups, known as active regions, which form over the course of several days and can last from a few to several weeks. The typical active region can be from 75,000 km to 250,000 km across.

sunspots are always associated with strong photospheric magnetic fields, typically from 1,000 to 3,000 Gauss. The magnetic field is, in general, vertical in the center of the



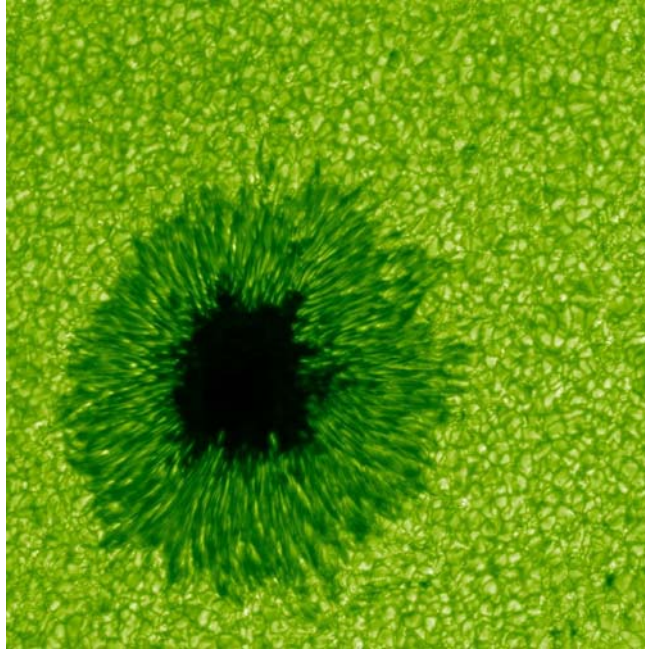
umbra. As the distance from the center of the sunspot increases, the magnetic field becomes weaker and more inclined. The inclination of the magnetic field is typically  $45^\circ$  at the boundary between the umbra and penumbra and very nearly horizontal at the outer edge of the penumbra. The fact that the magnetic field is frozen in the solar plasma enables the strong magnetic field in the sunspot to suppress the convective energy transport from below. The photospheric material in the sunspot cools relative to the unaffected photosphere and, thus, appears darker. In the penumbra, the convective heating from below is not suppressed as efficiently as in the umbra so there is less cooling and the penumbra does not appear as dark as does the umbra.

Figure 1.5 shows two full-disk pictures of the Sun. The left image is taken in white-light with the limb darkening removed (to increase image contrast). A large sunspot group can be seen near the center of the solar disk with a small group below center (south) and a small group near the right (west) limb. The right image is a longitudinal magnetogram. The white regions on the image indicate the magnetic fields on the surface of the Sun that are directed towards the line-of-sight while the black regions indicate to magnetic fields that are directed away from the line-of-sight (the details of magnetograms will be discussed in detail in the following chapters of this work). Note that the locations of the sunspots correspond with the locations of the magnetic fields. (White-light image courtesy [9]. Magnetogram courtesy [19]).



**Figure 1.5** Full-disk (left) and full-disk longitudinal magnetogram (right).

When looked at closely, sunspots typically have two components. The inner, darker region of the sunspot is known as the umbra. The brighter region which surrounds the umbra is known as the penumbra. Sunspots appear darker than the photosphere because of their lower temperature. The intensity of the umbra is on the order of 10% of that of the photosphere. The temperature of the umbra is typically approximately 4000 K as compared that of the photosphere which is approximately 6000 K.



**Figure 1.6** High resolution image of a sunspot.

Figure 1.6 shows a broad-band high resolution white-light image of a sunspot clearly showing the umbra and the penumbra. The features surrounding the sunspot are solar granulation which are the top of the convection zone when no strong magnetic fields are present. The bright inner regions of the granulation are the hot rising solar material while the dark lanes are the slightly cooler descending material. (sunspot image courtesy Denker, C., BBSO, Center for Solar-Terrestrial Research, NJIT).

The earliest recorded sightings of sunspots were made by the Chinese in the 12<sup>th</sup> century B.C. Theophrastus of Athens, a pupil of Aristotle, recorded his observations of a spot on the Sun in the 4<sup>th</sup> century B.C. The Chinese and Peruvian astronomers began to systematically observe and record sunspot observations within a few centuries of Theophrastus. Large groups of sunspots were occasionally viewed, by ancient peoples,

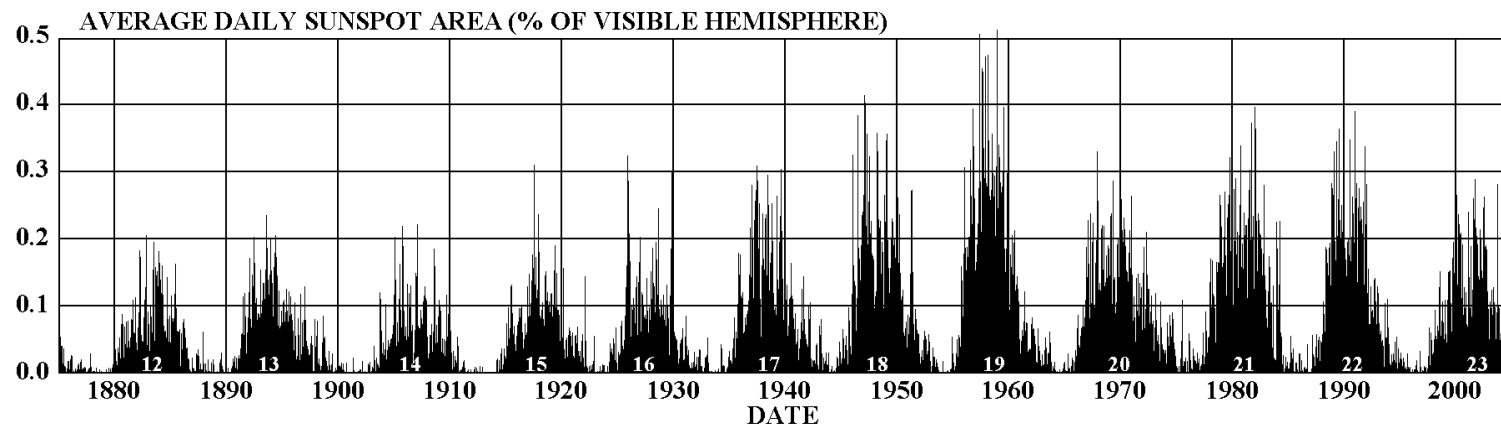
with the naked eye when the Sun was very near the horizon and its intense brightness was substantially dimmed by haze or smoke (The reader is strongly cautioned that atmospheric haze and/or smoke is insufficient to adequately screen the damaging light from the Sun. Viewing the Sun without proper protection is very dangerous and viewing the Sun in this manner should never be attempted). These initial sightings of spots on the Sun were initially attributed to unknown planets crossing between the Earth and the Sun or objects in either the atmosphere of the Sun or the atmosphere of the Earth.

It was not until about 1610 that astronomers were able to study sunspots in detail. At approximately the same time, Galileo Galilei (1564 to 1642) in Italy, Johann Goldsmid (1587 to 1616) in Holland, Christopher Scheiner (1575 to 1650) in Germany and Thomas Harriot (1560 to 1621) in England all began observations of the Sun with the newly invented telescope. It is not necessarily clear as to which man actually was the first to observe sunspots or to determine some of the initial conclusions about the characteristics of the Sun and sunspots.

Galileo and Goldsmid noted that sunspots continually appeared and disappeared, with lifetimes varying from a few days to a few weeks. Within a few years, they tracked longer lived sunspots moving across the solar disk, over a period of about two weeks, from east to west and, thus, surmised that the Sun rotates on its axis over a period of about 27 days and that sunspots must be objects either on or close to the surface of the Sun. This conclusion was solidified when Galileo noticed that a sunspot which appears circular when near the center of the solar disk becomes elongated as it approaches the solar limb due to the foreshortening effect. Both Scheiner and Galileo noted that sunspots do not appear over the entire surface of the Sun but appeared to be confined to latitude

bands within  $\sim 50^\circ$  of the equator. They also noticed that sunspots tended not to be isolated from one another but tended to appear in groups. In addition, they noted that larger, more complex, sunspots have a darker inner region known as the umbra and an outer brighter region known as the penumbra.

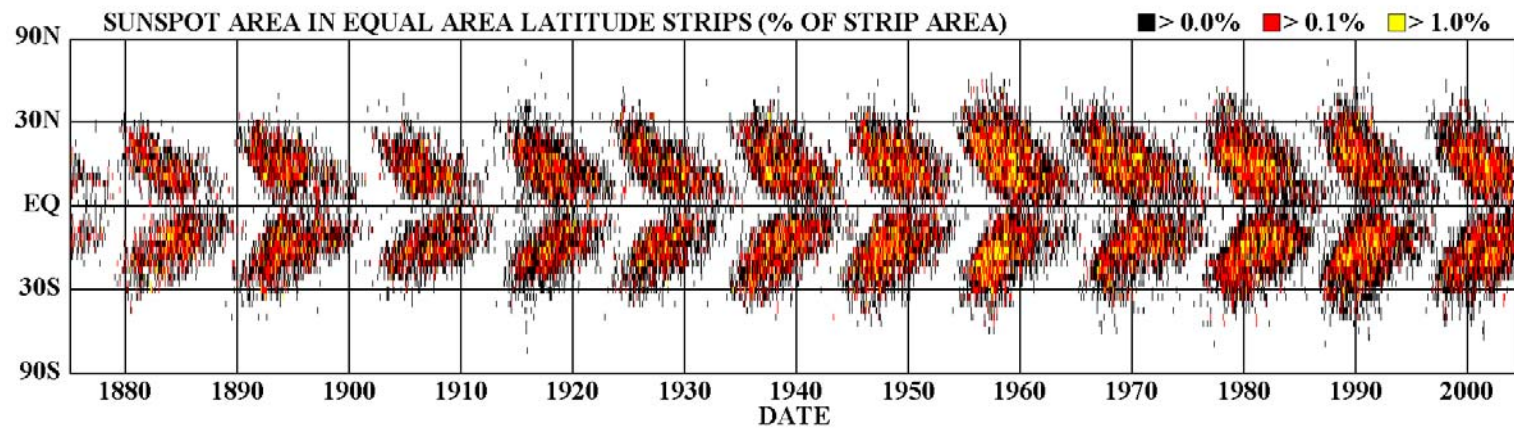
The level of solar activity is not constant over time. The most straightforward way to determine the level of solar activity is to simply count the number of sunspots. The existence of the sunspot cycle was initially recognized in the mid-nineteenth century. Heinrich Schwabe, a German amateur astronomer, suspected that an unidentified planet orbited the Sun within the orbit of Mercury. He surmised that such a planet would eventually transit the solar disk. In an attempt to identify such a planet, he began to carefully observe the Sun, a project which eventually stretched for 43 years. Schwabe recorded the occurrence of sunspots so if his mystery planet made an appearance it might be readily distinguished from the typical spots. While the mystery planet never did appear, by 1843 Schwabe noticed that the number of sunspots seemed to vary periodically with time over the course of about ten years. Using Schwabe's observations as a basis, in 1852 Rudolf Wolf examined sunspot records dating back to the earliest telescopic data of the 17<sup>th</sup> century and was able to determine a more accurate estimate of 11 years as the average length of the solar cycle. This periodicity in the number of sunspots has remained consistent since the first telescopic observations of the Sun, except from 1645 to 1715 during which very few sunspots were observed. It has been determined, however, that the falloff in sunspot observations during this time is due to a real decrease in the solar activity and not due to a lack of observations.



**Figure 1.7** The 11 year solar cycle.

Figure 1.7 shows a plot of the average daily sunspot area as a percentage of the hemisphere of the Sun that is visible from Earth from 1880 to the present. One can easily see the ~11 periodicity (Figure courtesy [20]).

Several years after Schwabe and Wolf discovered the length of the solar cycle, Richard Carrington published his results on his study of the locations of the appearances of new sunspots over time. Carrington noted that, near the beginning of the solar cycle, as defined when the number of sunspots is at a minimum, sunspots tended to appear at high solar latitudes ( $\sim 50^\circ$ ). As the solar cycle progressed, the latitudes where new sunspots appeared gradually decreased until, near the end of the solar cycle, sunspots tended to appear near the solar equator ( $\sim 5^\circ$ ). Sunspots associated with the next solar cycle would then begin to appear again at high solar latitudes. The fact that the solar latitude at which new sunspots appeared is a function of the progress of the solar cycle was later separately confirmed by G. Sporer and W. Maunder. Consequently, this phenomena is known as Sporer's Law and the plot of the latitudes at which sunspots appear with respect to time is known as the Maunder Butterfly diagram.



**Figure 1.8** The Maunder Butterfly diagram.



Figure 1.8 shows the Maunder Butterfly diagram from 1180 to the present. Note that, at the beginning of an specific cycle, sunspots tend to appear at high solar latitudes ( $\sim 30^\circ$ ). The latitudes at which sunspots first appear then migrates towards the solar equator as the cycle progresses. Near the end of the cycle the sunspots tend to appear exclusively near the equator ( $\sim 5^\circ$ ). sunspots which belong to the next cycle then appear once again at the high latitudes (Figure courtesy [20]).

The Sun does not rotate uniformly as a rigid body. The equator of the Sun takes approximately 26 days to complete a full revolution. The rotation rate gradually decreases with increasing latitude to the point where the poles take approximately 37 days to complete a rotation. This effect is known as differential rotation. In addition to the relationship of the latitude at which new sunspots appear with the progress of the solar cycle, Carrington also noted that sunspots at higher latitudes rotated about the solar axis more slowly than those closer to the solar equator. Thus, Carrington discovered the differential rotation of the Sun. It is now known that Sun takes approximately 25 days to complete a rotation at the equator while the time to complete a rotation is approximately 37 days near the pole. As it will be noted shortly, the differential rotation of the Sun is an important factor in the generation of solar activity.

### **1.3 The Zeeman Effect**

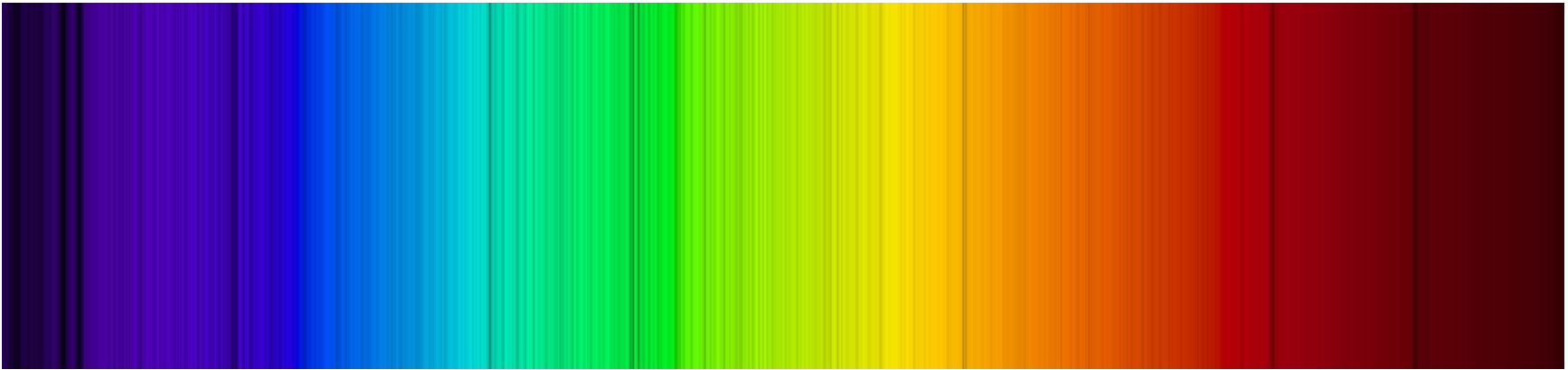
All aspects of astronomy, including studies of the Sun, are both observational as well as experimental. Because astronomical targets are typically located at very great distances from the Earth, these targets can not be sampled directly. Therefore, all information about

any astronomical target of interest must be gleaned solely from the light, both from the total intensity and any spectral details, that is emitted by, or reflected off of, the subject. One example where astronomical observations and laboratory experiments have worked together to glean important information about the Sun is in the determination of the temperature of its visible surface. The distribution of radiation from the photosphere, from which most of the radiation from the Sun emanates, very closely matches the distribution of radiation from a blackbody at approximately 6000 K as determined in the laboratory. Therefore, it is a reasonable conjecture that the opaque gas, which forms the surface of the Sun, is at this temperature.

Another excellent example of the codependence of observation and experimentation, in the science of astronomy, is the discovery of Helium. Helium was first identified spectroscopically in the Sun by J. N. Lockyer in 1868, and confirmed by P. Janssen in 1869. When Lockyer observed a solar flare with his spectroscope, he noticed a yellow line that could not be attributed to any known element. When both Lockyer and Janssen could not reproduce this spectral line that was observed in the solar flare in the laboratory, Lockyer, in 1870, suggested that this new spectral line was the fingerprint of a previously unidentified element. Lockyer named this new element Helium, from the Greek word for the Sun “helios”. Helium was then isolated in the laboratory in 1895 by W. Ramsay. While studying the spectrum of gases given off by the Uranium mineral Clevite, Ramsay noticed a mysterious yellow line which he was unable to attribute to any known element. Lacking a spectroscope with sufficient resolution to properly study the line, Ramsay sent samples of the gas to Lockyer and W. Crookes. Both Lockyer and Crookes confirmed that the new line observed by Ramsay was indeed the

same line that Lockyer had observed in the Sun. Thus confirming that the spectral line first observed by Lockyer in the spectrum of the Sun was the result of a previously unknown element.

The spectrum of the Sun actually contains a forest of absorption lines, first observed by W. H. Wollaston in 1802 and extensively mapped in 1814 by J. von Fraunhofer. The surface of the Sun, which, as previously noted, has a temperature of approximately 6000 K, radiates a continuous spectrum. The absorption lines arise, as was determined by G. Kirchhoff in 1859, from the absorption of light, at specific wavelengths, by atoms in the slightly cooler photosphere just above the solar surface. However, the absorption lines in the spectrum of the Sun are not as narrow as would be expected of absorption lines produced from an isolated atom. Each absorption line, whose shape can be approximated by a gaussian curve, is broadened due to the physical conditions in the solar atmosphere at the location where the line is formed. The local pressure, density, abundance and thermal motion of each particular type of atom in the photosphere, as well as the characteristics of each specific element, all effect the width of the absorption lines. The depth of each particular absorption line is determined by the population of the atom which absorbs light at that specific wavelength. Typically, these lines have a FWHM on the order of 100 mÅ and a center depth intensity from 20% to 60% of that of the continuum. By carefully studying the solar spectrum, and with a knowledge of the specific properties of the atoms found there, one can deduce the local properties of the photosphere.



**Figure 1.9** Portion of the solar spectrum.

Figure 1.9 shows a portion of the solar spectrum from 384 nm to 386 nm. The many dark lines represent specific wavelengths of the solar continuum, emitted from the photosphere, which are absorbed by electron transitions of specific elements in the slightly cooler solar atmosphere (solar spectrum courtesy [21]).

In the history of solar physics, experiments in the laboratory have not exclusively been used to confirm information gained with observations. At times, phenomena first observed in the laboratory were then subsequently used to gain information about the Sun. As briefly stated previously, it is now well known that the Sun has a general bipolar magnetic field. In addition, there are areas on the Sun where the magnetic field becomes very concentrated. These very strong local magnetic fields are the source of solar activity, which was discussed previously. As with all solar phenomena, the information as to whether solar activity is the result of the interaction of strong magnetic fields with the material which composes the Sun is hidden in the solar spectrum. It took a breakthrough in the laboratory to develop the basic methods which solar physicists used to determine that strong magnetic fields were indeed responsible for solar activity.

In 1862, M. Faraday first investigated the effect of a magnetic field on the wavelength of light, and whether the wavelength of light is altered passing through a hot or cold gas that is immersed in a magnetic field. However, due to the insufficient sensitivity of equipment at the time, Faraday was unable to detect any change in wavelength due to the presence of a magnetic field.

Then, in 1897, P. Zeeman detected a change in wavelength in the presence of a magnetic field with the following experiment [22] (Figure 1.10). Sodium vapor was

heated in a clear tube which was placed between the poles of an electro magnet. The light from an arc-lamp was passed through the vapor and observed with a spectroscope. When the electromagnet was not energized the absorption lines of the Sodium doublet appeared as usual. However, when the electromagnet was energized there appeared an immediate broadening of the lines. Thus proving that the wavelength of light absorbed by the Sodium vapor was altered when the vapor was immersed in a magnetic field.

Upon hearing of these results, H. Lorenz suggested that the edges of the broadened absorption lines should be circularly polarized, in opposite directions to each other, when the magnetic field is directed along the line of sight. By means of a quarter wave plate and a linear polarizer, used as the analyzer, Zeeman determined that the edges of the magnetically broadened line were indeed circularly polarized. Theory also indicated that when the magnetic field is directed normal to the line of sight the edges of the magnetically broadened line should be linearly polarized, and parallel, to the direction of the magnetic field and that the center of the magnetically broadened line should be linearly polarized perpendicular to the direction of the magnetic field. Zeeman also determined this to be the case. For the verification and explanation of this phenomena, now known as the Zeeman Effect, Zeeman and Lorenz were awarded the Nobel Prize in 1902.

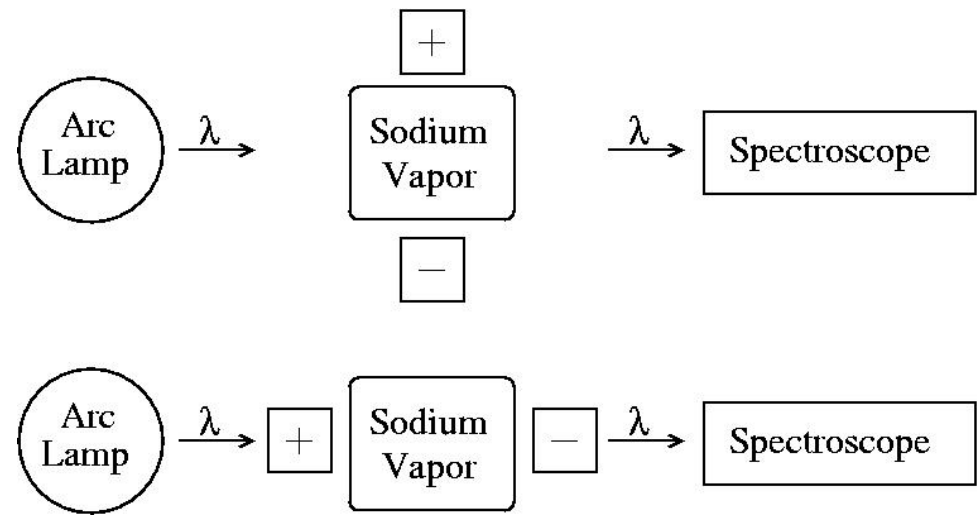


Figure 1.10 Zeeman's experiment.

The specifics of the Zeeman effect, in general, are as follows. The interaction of an external magnetic field with the magnetic moment of electrons in the atoms which produce absorption or emission lines changes the orbital transition energies as the electrons jump between their various orbital levels. Thus, the wavelength and polarization of photons emitted in the presence of a magnetic field is changed relative to photons emitted when not in the presence of a magnetic field (Figure 1.11, courtesy [23]).

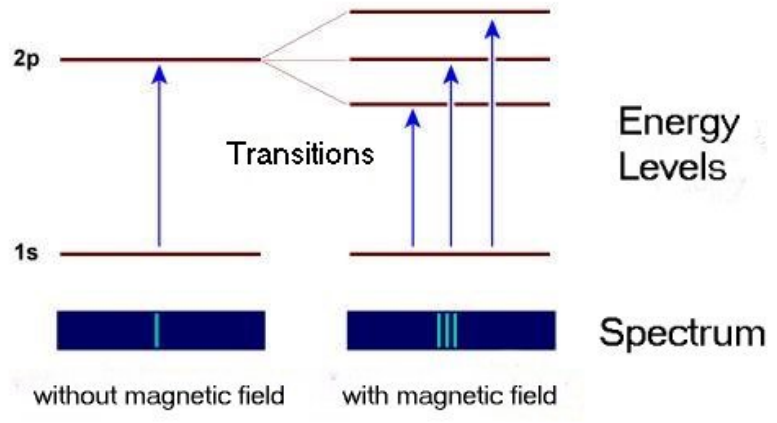
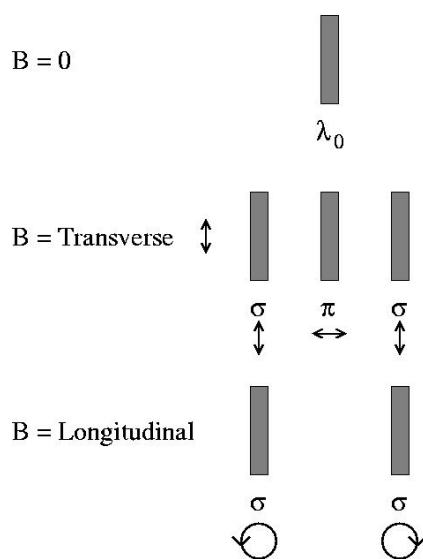


Figure 1.11 The Zeeman Effect.

Specifically, a magnetic field perpendicular to the line of sight (Figure 1.10, upper panel), the transverse component, produces a small change in wavelength,  $\Delta\lambda$ , both towards the red and blue ends of the spectrum, proportional to the strength of the magnetic field. These shifted absorption lines, referred to as the  $\sigma$  components, are linearly polarized perpendicular to the magnetic field. In addition, there is an unshifted absorption line, known as the  $\pi$  component, that is linearly polarized parallel to the magnetic field (Figure 1.11, center panel). In the case where the magnetic field is along the line of sight (Figure 1.10, lower panel), the longitudinal component, there is no unshifted  $\pi$  component of the absorption line and each shifted  $\sigma$  component has opposite circular polarizations (Figure 1.11, lower panel). A field whose inclination is intermediate to these two ideal cases produces a combination of both effects.



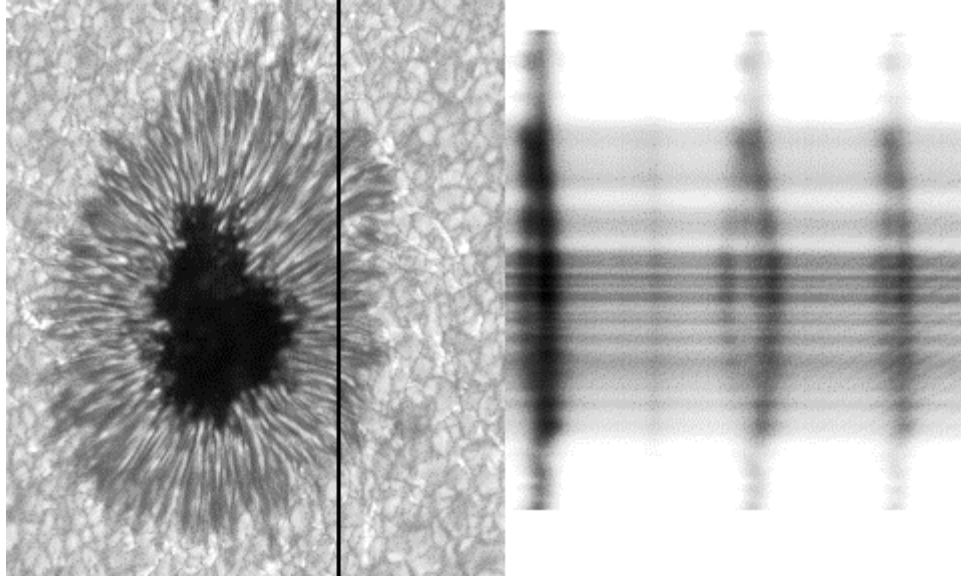
**Figure 1.12** Polarization components of the Zeeman Triplet.



In the case of the solar spectrum, this Zeeman broadening, or, in the case of a very strong magnetic field where the shifted  $\sigma$  components are completely separated from each other, Zeeman splitting, is, in general, quite small when compared to the total width of a typical spectral line in the visible portion of the spectrum for magnetic field strengths that are typically found in the photosphere. In the general, even the relatively strong magnetic fields in a sunspot, typically on the order of 1000 G, only produces a shift in wavelength of a few tens of mÅ. Thus, if it were not for the effect that the oppositely shifted absorption lines are also polarized, each Zeeman component would, typically, be indistinguishable from the other. Therefore, a solar magnetograph is actually a device for measuring the polarization of the light to deduce the solar magnetic field. The conversion of polarization into magnetic field strength is performed during the processing of the data from the instrument.

Zeeman broadening in the solar spectrum was first observed at the Halsted Observatory at Princeton University by C. A. Young [24] and extensively catalogued by W. M. Mitchell [25]. When observing the spectrum of sunspots, where the strongest magnetic fields on the Sun can be found, they noticed that some of the absorption lines appeared broader as compared to the same lines when observed away from the spot. Or, in some cases, the absorption lines were split into two separate components. However, while they noticed the fact that the absorption lines in the solar spectrum were affected by the presence of a sunspot they did not investigate the cause. This task was shortly thereafter taken up by G. E. Hale, working at the Mt. Wilson Solar Observatory in California, using the spectroheliograph of his own invention [26]. However, before discussing the details of how Hale was able to prove that solar activity is caused by

intense magnetic fields, and the subsequent evolution of solar magnetographs up to the present day, the various types of instruments used to study solar magnetic fields will be reviewed.



**Figure 1.13** The Zeeman Effect in a sunspot.

Figure 1.14 shows the Zeeman effect in a sunspot. The left panel is a typical sunspot. The black vertical line shows the location of the entrance slit of the spectrograph. The right panel is the spectra (the x-axis is the wavelength while the y-axis corresponds to the location in the left panel of the entrance slit). Note that there is no Zeeman broadening/splitting in the locations which corresponds to the solar granulation, there is moderate Zeeman broadening in the outer penumbra and Zeeman splitting in areas of the penumbra close to the umbra (where the magnetic field is the strongest) (image courtesy [27]).

## 1.4 Review of Magnetograph Types

Instruments that measure the polarization of light from the Sun, as induced by the Zeeman effect, and subsequently convert those measurements into magnetic field values are referred to as magnetographs. There are four basic types of magnetographs, two based on a spectrograph and one each based on a narrow band filter or a Fabry-Perot filter. As can be seen from this list, each type differs from the other in the way that each instrument obtains the spectral information required to infer the solar magnetic field. Each type of magnetograph has relative advantages and disadvantages to the other. Which type of magnetograph that is to be used will be determined by the specific requirements of the desired observations. In reality, these different types of magnetographs complement each other in that they can each contribute a data set with unique characteristics. Taken as a whole, these different data sets provide a more complete picture of the solar magnetic field than can be provided by data from any individual instrument. Thus, the contributions from each type of instrument are required to fully understand the magnetic fields which drive solar activity. The specific details of the four basic types of magnetographs will be discussed in Chapter 1.5.

### 1.4.1 Full Spectrum Magnetograph

The first type of magnetograph, originally developed by G. E. Hale at the Mt. Wilson Solar Observatory in California [26] & [28] is of the spectrograph type in which the light from the Sun is imaged with a spectrograph, of high dispersion, and the shift in wavelength can, thus, be measured directly and accurately. In an instrument so based, a spectrograph separates white light, from the Sun, into its component spectrum, via a diffraction grating. A optical train, used as polarization analyzers, is used to isolate each

polarized component of the shifted line. The entire spectral line profile, in each polarization state, is thus obtained so the wavelength shift of each polarized component can be measured separately. Also, all of the information about the local magnetic field, in addition to photospheric heating and Doppler motions, for example, provided by the absorption line are preserved. The strength of the magnetic field, in both the longitudinal and transverse directions, can then be precisely determined since the strength of the magnetic field, in each direction, is directly proportional to the shift in wavelength of the appropriately polarized component. The primary disadvantage of a spectrograph based magnetograph is that, for any single observation, only a one dimensional image is produced. Therefore, to produce a two dimensional image of the photospheric magnetic field, many observations, each at an adjacent location to the previous, are required. Thus, the total time to scan a desired region on the Sun can take many minutes and the final two dimensional map of the magnetic field must be reconstructed from each individual one dimensional strip. This aspect of spectrograph based magnetographs can be particularly limiting if weak, small scale magnetic features are being studied or if high time cadence observations are required because these features can evolve significantly over just a few minutes. This type of magnetograph will be henceforth referred to as a “full spectrum” magnetograph for the remainder of this discussion.

#### **1.4.2 Spectroheliograph Based Magnetograph**

The second type of magnetograph, the spectroheliograph based magnetograph, is a modified version of the full spectrum magnetograph. In a spectroheliograph based instrument, an exit slit is used to isolate the wing of the magnetically sensitive spectral line under study. The spectrograph and exit slit, therefore, are set up to function as a

narrow band filter. As with the full spectrum version of the instrument, the spectroheliograph also produces a one-dimensional image. Therefore, the image of the Sun must be scanned across the entrance slit of the spectrograph to produce a two-dimensional image on the detector.

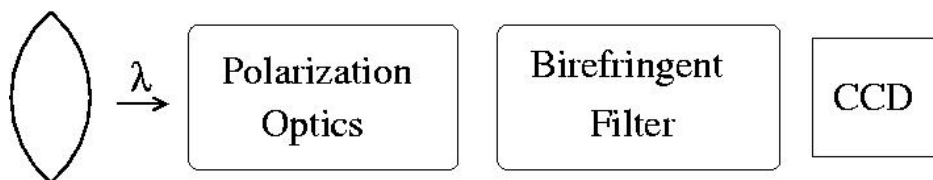
A version of this type of magnetograph was developed by H. W. Babcock and H. D. Babcock [29] & [30] in which they used two exit slits, each positioned in opposite wings of the same magnetically sensitive absorption line. By electronically comparing the relative brightness between the oppositely shifted and oppositely polarized absorption lines, the strength of the magnetic field could be determined.

Another version of the spectroheliograph based magnetograph was also developed by R. B. Leighton [31] where he used a single exit slit to isolate a single wing of a magnetically sensitive absorption line. Polarization optics were set to isolate a single polarization component. The image of the Sun was scanned across the entrance slit of the spectrograph synchronized with the motion of a photographic plate which was scanned across the exit slit. Thus producing a two dimensional monochromatic photograph of an area of the Sun. A second photograph was taken of the same area of the Sun at the other polarization component in the desired set. Due to the very slight shift in wavelength in each polarization state because of the Zeeman effect, the intensity at each point will be slightly different at all locations in the images where a magnetic field is present. This difference in intensity is a function of the strength of the magnetic field at each position in the image. By comparing the difference in brightness between the two photographs, the strength of the magnetic field can thus be inferred. The specifics of both the Babcock & Babcock and the Leighton magnetographs will be discussed shortly.

### 1.4.3 Filter Based Magnetograph

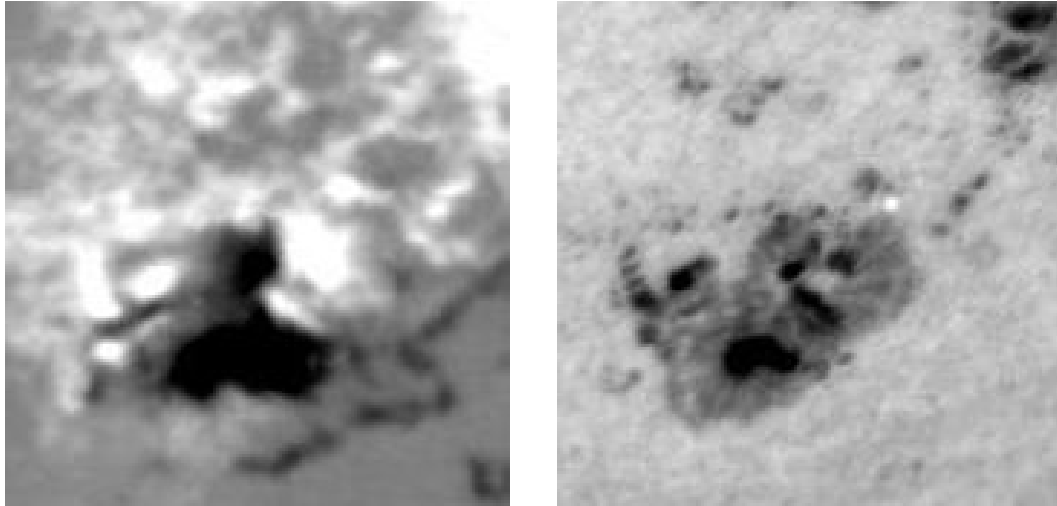
The third type of magnetograph, a version of which was initially developed at Caltech for the Big Bear Solar Observatory by R. C. Smithson and R. B. Leighton [32] is of the filter type. A detailed description of the original instrument can be found in [33]. The Digital Vector Magnetograph at the Big Bear Solar Observatory, the details of which are the ultimate subject of this discussion, is the latest version in the continual evolution of this same instrument.

The basic operation of a filter based solar magnetograph is as follows. The optics of the telescope provides a beam of sunlight, of high focal ratio, to the optical bench where the instrument is mounted. A birefringent filter, with a very narrow bandwidth that is typically on the order of  $1/4 \text{ \AA}$ , isolates the wing of the magnetically sensitive absorption line under study. The Sun is imaged onto an electronic detector. In the case when the absorption line being used lies in the visible portion of the solar spectrum, this detector is typically of the silicon based charged couple device (CCD) type. Polarization optics isolates one of the two desired polarization components of the particular Stokes set of interest. The basic schematic of a filter based magnetograph is shown in Figure 1.14.



**Figure 1.14** Basic schematic of a filter based magnetograph.

The detector takes a single image of that first polarization component and that image is saved in the RAM of the computer which controls the instrument. The polarization optics then isolates the second polarization component. The detector takes a single image of that second polarization component which is also saved in RAM. If there is a magnetic field present, the intensity of the two images, at any individual point, will be slightly different. The process of taking single images of alternating polarization components is repeated and each new image is summed, with its appropriate fellows, to increase the signal to noise ratio to the desired level. When all of the desired images have been integrated in RAM, a magnetogram is produced by displaying the difference between the two integrated polarization images divided by their sum. In the case where the longitudinal magnetic field is of interest, all of the locations in the image where the magnetic field is directed towards the instrument will be positive while all of the locations in the image where the magnetic field is directed away from the instrument will be negative. This magnetogram can then be conveniently displayed where all of the positive values are plotted as shades of white, all of the negative values are plotted as shades of black and the areas where no magnetic field is present is plotted as a uniform gray.



**Figure 1.15** Example of a magnetogram from a filter based system.

Figure 1.15 shows an example of a magnetogram produced by a filter based system (which is ultimately the primary subject of this work). The left image is the longitudinal magnetogram. As stated previously, the white regions are areas on the surface of the Sun where the magnetic field is directed towards the line-of-sight while the black areas are regions where the magnetic field is directed away from the line-of-sight. The right image is a 610.3 nm filtergram of the same area on the Sun (images courtesy BBSO).

A magnetogram thus employed uses the weak field approximation, the details of which will become clear in Chapter 2.9. This is the modern electronic version of the photographic subtraction technique, which will be discussed in detail in Chapter 1.7, developed by R. B. Leighton [31]. The construction of a birefringent filter will be discussed, in detail, in Chapter 2.7. The primary disadvantages of a filter based magnetograph is that the tradeoffs made in order to use the weak field approximation



reduce the sensitivity of the instrument and impose an upper limit on the strength of the magnetic field that can be measured, known as Zeeman saturation. Both of these situations will become evident in the detailed discussion of the weak field approximation which is to follow in Chapter 2.9. This type of magnetograph, however, is specially suited to producing two dimensional vector magnetograms with a high time cadence, typically on the order of one minute. The slight reduction in sensitivity and saturation in magnetic field are considered acceptable tradeoffs to gain the advantage of high time cadence magnetograms.

#### **1.4.4 Fabry-Perot Based Magnetograph**

The fourth, and final, type of magnetograph, a version of which is currently being developed for the Big Bear Solar Observatory's 65 cm vacuum-reflector [34] & [35] is of the Fabry-Perot type. In a Fabry-Perot based magnetograph, a Fabry-Perot filter takes the place of either the spectrograph or the narrow band birefringent filter. The construction and operation of a Fabry-Perot based magnetograph is basically the same as a filter based magnetograph. However, since the Fabry-Perot filter can be quickly, and accurately, tuned in wavelength, the entire profile of the spectral line under study can be obtained. Therefore, a Fabry-Perot based magnetograph can function either as a filter based magnetograph or as a full spectrum magnetograph, depending on the specific observational requirements. Thus, this type of instrument can be considered to be a hybrid of the spectrograph based and filter based magnetographs because the Fabry-Perot filter can allow the instrument to emulate both other types depending on how the Fabry-Perot is employed. If the Fabry-Perot is used to scan the line, the actual absorption line profile can be reconstructed and  $\Delta\lambda$  can be measured directly, as with the spectrograph

based magnetograph. The line information can also be used by the Stokes Inversion method to determine the conditions of the solar atmosphere, such as temperature, density, pressure, etc. Or, if the Fabry-Perot is used as a very narrow band filter, the system will exactly emulate the filter based magnetograph. However, a Fabry-Perot based magnetograph, when used as a filter based magnetograph, would tend to have better accuracy than a magnetograph that uses a Birefringent filter because the band-pass of Fabry-Perot filter tends to be more narrow than Birefringent filters, thus eliminating contamination from the continuum and the line center. The flexibility of Fabry-Perot filters, and the fact this type of filter typically has a much greater light throughput than both spectrographs and narrow band birefringent filters, makes the use of a Fabry-Perot very desirable if the additional technical challenges imposed by their use, which are beyond the scope of this discussion, can be overcome.

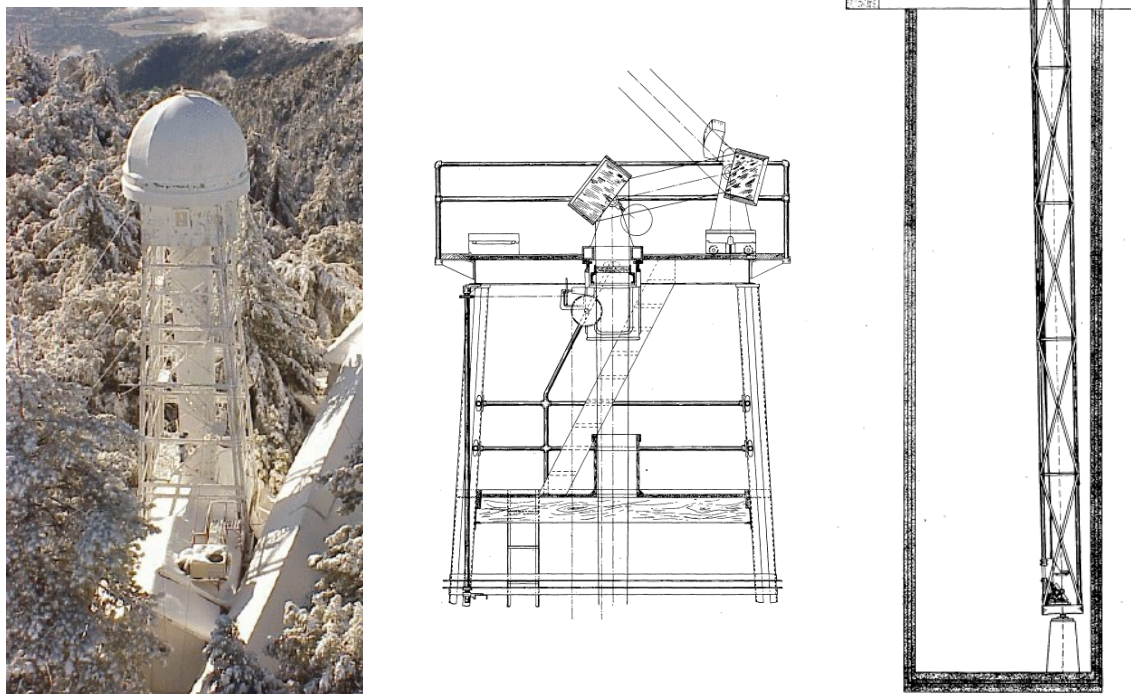
### **1.5 Development of the Solar Magnetograph: The Hale Tower Telescope Magnetograph**

As previously stated, the most obvious manifestation of solar activity are sunspots. G. E. Hale, the founding father of modern solar physics, initially interpreted sunspots as spinning “vortices” of solar material. He believed that charged particles, dragged in continual circular motions by the vortices, generated magnetic fields of sufficient strength to produce the broadening of the solar absorption lines first noticed by Young and Mitchell. With the knowledge of how magnetic fields effect the wavelength and the polarization of light provided by Zeeman and Lorenz, Hale set out to determine if there were indeed very strong magnetic fields coincident with sunspots.

To expand and improve his studies of the Sun, which he had been carrying out for many years at his home in Chicago and at the Yerkes Observatory in Wisconsin, Hale established the Mt. Wilson Solar Observatory in the mountains above Pasadena, CA in the early 1900's. There, Hale constructed several state of the art instruments, each more capable than the last, to study the Sun. Among these were two Tower Telescopes, each containing a large, fixed spectrograph of very high dispersion which would be the foundation of his spectrograph based magnetograph.

The principle of the spectrograph based magnetograph, as used with the then recently completed 60-Foot Tower Telescope at Mt. Wilson [26] & [28] is as follows (Figure 1.16, left image, courtesy [36]). A pair of plane mirrors, mounted in a shelter at the top of the tower used to track the Sun through the day, fed a fixed long focus objective lens (Figure 1.16, center image, from [37]). The advantage of mounting the mirrors at the top of a tower is that poor seeing (distortions in the image caused by turbulence in the atmosphere of the Earth) near ground level, produced by turbulence from solar heating of the ground, may be avoided. The objective lens produced a large image of the Sun in an optics lab near ground level. In the image plane was mounted a slit which allowed a small portion of the solar image to enter a spectrograph, of high dispersion, placed in a deep pit below the tower. Placing the spectrograph in the pit provided an environment for the spectrograph with very high mechanical and temperature stability (Figure 1.16, right image, from [38], p. 208). A spectrum was thus produced of the one dimensional portion of the Sun allowed to enter the spectrograph by the slit. However, to study the physical and temporal details of features on the Sun, whether the features of interest are of magnetic origin or not, it is of great advantage to be able to

produce a two dimensional image of a portion of the Sun at a single wavelength. To accomplish this, Hale added a second slit at the output spectrum which allowed only a very narrow wavelength to pass through. This single wavelength was imaged on to a photographic plate. To construct the two dimensional image on the photographic plate, the image of the Sun was scanned across the first slit by adjusting the rate of the motors which moved the plane mirrors at the top of the tower to track the Sun as it moved across the sky during the course of the day. The photographic plate was scanned across the second slit synchronized with the motion of the solar image across the first slit. Thus building up a two dimensional image of the Sun, at a single wavelength, on the photographic plate. The great advantage, therefore, of the spectroheliograph was that it could easily and quickly produce a two dimensional image of an area of the Sun at a single wavelength.



**Figure 1.16** The Mt. Wilson 60 foot Tower Telescope.

With his newly completed spectroheliograph, Hale set out to determine if the absorption lines that appeared undisturbed when photographed far away from sunspots and were seen to be either broadened or split when photographed inside sunspots exhibited the polarization effects discovered by Zeeman in the laboratory. To test the components of the broadened or split lines from a sunspot for evidence of circular polarization, Hale mounted a  $1/4\lambda$  plate and a linear polarizer, used as the analyzer, before the first slit of the spectrograph. As a reference, part of the Sun far away from a sunspot, where there was no obvious line broadening was used. If the components of the broadened spectral line were circularly polarized, the  $1/4\lambda$  plate would convert the

oppositely circularly polarized components into linear polarizations at right angles to each other. As the linear polarizer is rotated, it would transmit one circular component and then the other. This Hale found to be the case, although neither component was completely blocked partially due to spurious polarization induced by the plane mirrors of the coelostat which fed light to the fixed spectrograph and partially due to the fact that the magnetic field, at the location on the Sun where the observations were made, was not exactly directed in the line of sight resulting in a small linearly polarized component.

If the broadening of the spectral lines were indeed caused by the presence of a magnetic field, this linear polarization should also be detectable both in the displaced spectral lines, which should be linearly polarized and perpendicular to the magnetic field, and as a non-displaced component of the line that is linearly polarized but parallel to the magnetic field. By removing the  $1/4\lambda$  plate and analyzing the light only with the linear polarizer, Hale also found this to be the case. Therefore, Hale's experiments left no doubt that the broadened and/or split absorption lines contained all of the components predicted by the Zeeman Effect.

To further confirm that the observed effects were indeed the result of the light being absorbed by the relatively cool gas of the solar atmosphere when immersed in a magnetic field, A. S. King, a colleague of Hale, redid Zeeman's experiment, with a spectrograph in the laboratories of the Mt. Wilson Solar Observatory of much higher dispersion than available to Zeeman, with elements that produced the same spectral lines as those Hale observed in the spectrum of the Sun [39]. King and Hale found that the results determined in the laboratory matched the results obtained from the Sun to within the error of their measurements. Therefore, Hale proved conclusively that the broadening

and/or splitting of solar absorption lines in sunspots are the result of very strong magnetic fields on the surface of the Sun.

### **1.6 Initial Attempts to Measure the Magnetic Field of the Sun With Photoelectric Methods**

The use of photoelectric methods to map the spectrum of the Sun was initially investigated by T. Dunham, Jr., H. A. Bruck and D. Phil [40] in the early 1930's. They successfully mounted a photomultiplier at the focus of a spectrograph, trained on the Sun. As the solar spectrum was scanned across the photomultiplier, the electrical signal from the photomultiplier, and associated electronics, was detected by the deflections of a galvanometer and recorded on a recording drum. This system would thus produce a plot of intensity vs. wavelength of the solar spectrum.

The first attempts to construct an instrument to detect the magnetic field on the Sun, via the Zeeman effect, using similar photoelectric methods was conducted by Hale and colleagues, also in the early 1930's. The basic method is as follows. A spectrograph, of very high dispersion, is used to image a magnetically sensitive absorption line in the solar spectrum. If there is a magnetic field present, the observed spectrum will consist of the overlapped oppositely circularly polarized components, both slightly shifted in wavelength from the nominal absorption line if no magnetic field was present. The instrument is equipped with polarization and analyzer optics so that both circularly polarized components may be isolated, and imaged, in turn. A second slit is positioned in the wing of the magnetically sensitive absorption line and imaged onto a photomultiplier. Due to the fact that each component of the absorption line is shifted in wavelength, the intensity measured by the photomultiplier will be slightly different for either polarization

state. Thus, for magnetic field strengths that are typically found on the surface of the Sun, the strength of the magnetic field is directly proportional to this difference in intensity.

There were several technical problems, however, that Hale and colleagues were unable to overcome with the equipment available at the time which ultimately led to their failure to detect the magnetic field on the Sun via photoelectric techniques. The shifts in wavelength, for magnetic field strengths that are typically found on the surface of the Sun, are very small. Typically on the order of just a few mÅ in the visible portion of the spectrum. Therefore, the difference in intensity, as measured between both polarization states of the absorption line, is also very small. In addition, due to the fact that the telescope and spectrograph were fixed, light from the Sun must have been directed to the instrument via a set of plane mirrors. A strong linear polarization is imparted onto light whenever there is a reflection off of a mirror at an oblique angle. The amount of this linear polarized bias is a function of the angle of the reflection. In addition, this bias polarization is continually changing as the mirrors track the Sun across the sky. This linear polarization represents a strong and variable bias on the polarization signal in the Sunlight and can easily overwhelm the weak polarization signal caused by the solar magnetic field.

### **1.7 The Babcock Photoelectric Magnetograph**

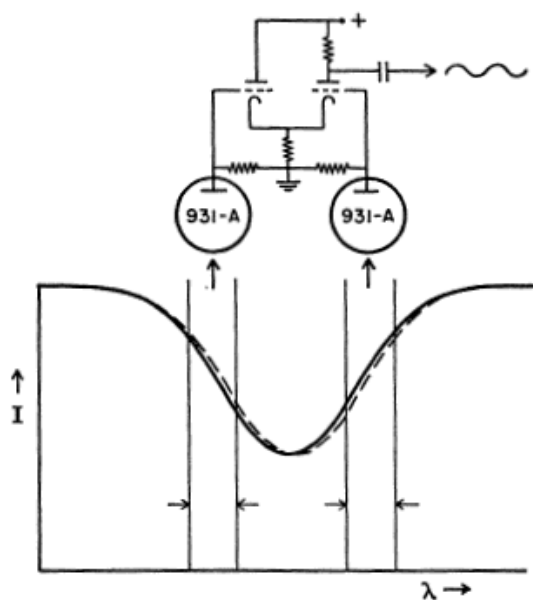
The first successful photoelectric magnetograph was developed by H. W. Babcock and H. D. Babcock [29] & [30] at the Mt. Wilson Solar Observatory in California using a spectrograph of very high dispersion on the 150 foot Tower Telescope [41]. As with the first attempt by Hale, each overlapping circularly polarized component of the longitudinal



Zeeman effect of the magnetically sensitive line under study was individually imaged in sequence. To isolate each individual circularly polarized component, an electro-optic retardation plate, made of ammonium-dihydrogen-phosphate (ADP), followed by a fixed linear polarizer, used as the analyzer, was mounted in the light path before the spectrograph. An alternating voltage, at a rate of 120 Hz, applied to the ADP selected its retardance to be either plus or minus  $1/4\lambda$ . The ADP would thus convert the two oppositely circular polarizations into orthogonal linear polarizations. The rotation of the fixed linear polarizer was calibrated to be parallel to one of the linearly polarized components and would thus pass one component of the longitudinal Zeeman effect and then the other, depending on the state of the ADP.

The spectrograph was of sufficient dispersion that two slits could be positioned, one in each wing, in the profile of the absorption line under study, which, in addition to the natural improvements in technology was the primary improvement over Hale's attempt. The light through each slit was detected with a separate photomultiplier, whose outputs were fed through a difference amplifier and accompanying electronics (Figure 1.17 is from [29], p. 283). The advantage of being able to use the difference signal from two photomultipliers was that any change in the overall intensity of the Sun light, caused by seeing or instrument polarization imparted by the plane mirrors that fed the fixed spectrograph, for example, will be minimized. Because each circularly polarized component of the absorption line is also shifted slightly in wavelength, the intensity of the light measured by the photomultipliers in each state of the ADP would be slightly different. The two slits were positioned near the steepest slopes in each wing of the profile of the absorption line since the minute change in intensity measured by each

photomultiplier, as the ADP selected one polarization state and then the other, would be greatest.

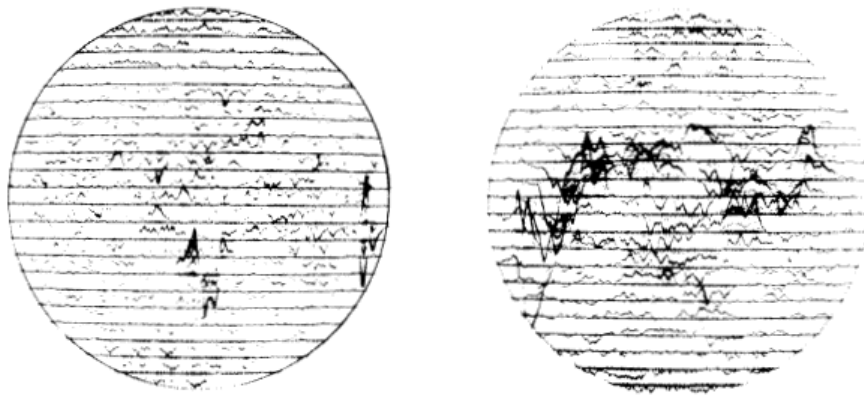


**Figure 1.17** Schematic of the two slits and photomultipliers of the Babcock magnetograph.

The output of the detector was a DC signal whose magnitude was directly proportional to the average strength of the magnetic field, within the linear range of the photomultipliers, in the region of the Sun under study. The resultant magnetic signal was shown by vertical fluctuations on a cathode-ray tube (CRT).

To build up a two dimensional map of the magnetic field, the image of the Sun was scanned, in right ascension (East/West direction), across the slit of the spectrograph. The general position of the trace on the CRT was calibrated to match the location on the solar disk that was being imaged at that moment. Simultaneously, a straight line, corresponding to zero magnetic signal, was also drawn on the CRT. The distance between the horizontal straight lines from successive scans on the CRT was previously determined such that it corresponded to a known magnetic value. The magnitude of the

magnetic field at each point could thus be determined by comparing the vertical deflection of the trace on the CRT to this reference. Because this instrument was specifically designed to study the overall magnetic field of the Sun, which is relatively weak when compared to the magnetic field present in an active region, this vertical reference distance was typically set to be on the order of ten to twenty Gauss (Figure 1.18, from [30], p. 329A).



**Figure 1.18** Photograph of the CRT output from the Babcock magnetograph.

The number of scans in right ascension that were required to map the magnetic field on the entire surface of the Sun depended on the scale of the solar image at the slit of the spectrograph. Since this would typically required many minutes, a camera was conFigured to photograph the CRT as the image was slowly constructed by the trace. Thus, providing a map of the magnetic field on the entire surface of the Sun.

The Babcock magnetograph was designed specifically to study the overall magnetic field of the Sun, the strength of which is just a few Gauss. The optics of the instrument were set up to produce a scale which provided a resolution of approximately

110 arc-sec (the width of the solar disk is approximately 2000 arc-sec). This resolution provided enough light that a single scan could be performed at a reasonable speed and still provide a large enough signal-to-noise ratio that magnetic fields down to one Gauss might be accurately measured. It also provided that sufficiently few scans were required to cover the entire solar surface such that a scan of the entire Sun might be completed in a reasonable time. Typically, nineteen adjacent scans were required to cover the entire surface of the Sun which took approximately one hour.

While this setup would provide information about the global magnetic field of the Sun, the resolution is entirely insufficient to study the details of solar active regions, the largest of which are on the order of 300 arc-sec across. If the size of the solar image, at the slit of the spectrograph, were modified to provide a scale such that small-scale solar features could be studied with sufficient resolution, the resulting decrease in light at the photomultipliers would require that each single scan be conducted much more slowly. In addition, the number of scans required to construct a two-dimensional image covering a sufficient portion of the Sun would also increase accordingly. This process can take many minutes even with modern electronic detection techniques. With the equipment then available to Babcock & Babcock, the process would have taken many, many hours. Thus making the observations of the magnetic fields in active regions impossible.

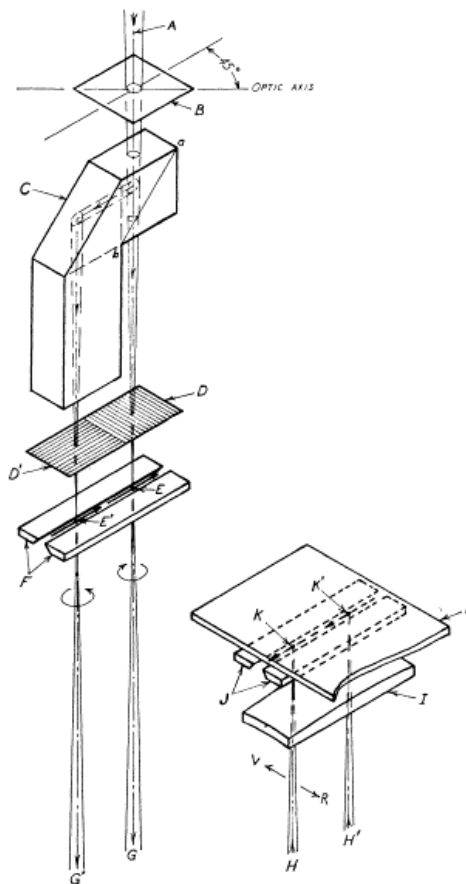
In addition, the morphology of both magnetic and non-magnetic features on the Sun can change in as little as five minutes. Also, environmental changes, such as seeing and the overall transparency of the atmosphere, which can both effect the quality of the measurements of the magnetic fields, can change significantly over a time scale which would be much less than the time required to complete a two-dimensional scan. If the

goal of the observation is to study the magnetic fields at the surface of the Sun with even moderate spatial and temporal resolution the Babcock magnetograph method is simply much too slow.

### **1.8 The Leighton Photographic Subtraction Magnetograph**

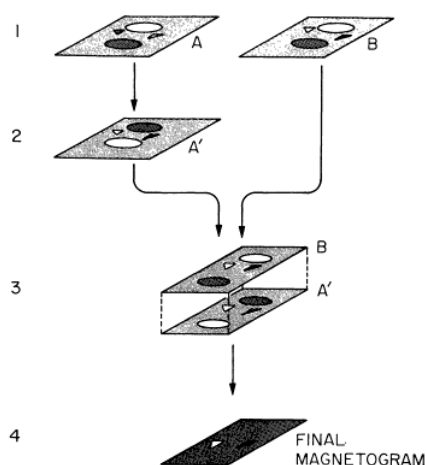
To overcome the limitations of using the Babcock photoelectric magnetograph for studying the magnetic fields on the Sun in detail, R. B. Leighton developed the “photographic subtraction” method [31] using a modified spectroheliograph on the 60 foot Tower Telescope at the Mount Wilson Solar Observatory [42]. The key to Leighton’s innovation is the following. Before the slit of the spectrograph was mounted a  $1/4\lambda$  plate, as in previous spectroheliographs set up to study magnetic fields to convert the circularly polarized light from the longitudinal Zeeman effect into the set of normal linear polarizations. Following the  $1/4\lambda$  plate was a beam splitter which produced two identical side-by-side images at the focal plane of the primary objective. A linear polarizer was mounted in each light path after the beam splitter and before the slit of the spectrograph. One linear polarizer was orientated to pass the right-hand circularly polarized component and the other linear polarizer was orientated to pass the left-hand circularly polarized component. The images then passed through the spectrograph, as usual. A second slit used to isolate the wing of the magnetically sensitive absorption line under study. To build the desired two-dimensional images, the telescope was scanned across the disk of the Sun, as usual. The net result was that two side-by-side images were produced simultaneously on the photographic plate, one of each circular polarization. A

schematic of the polarization optics and spectrograph slit for the Leighton Photographic spectrograph can be seen in Figure 1.19 (from [31], p. 367).



**Figure 1.19** Schematic of the polarization optics and spectrograph slit for the Leighton photographic spectrograph.

In the locations on the photograph where there was zero magnetic signal, the two side-by-side images would be identical. However, in the locations where there was a non-zero magnetic signal, there would be a slight difference in intensity between the images, because of the very slight shift in wavelength of the absorption line if a magnetic field was present, thus producing a difference in the optical density of the resultant photographic negatives of each channel. A positive was then made of one of the images which is then very carefully superimposed on the negative of the other image. A print is then developed using this composite negative. The net result in the final print is that any features that are common to both images are canceled, while any differences are enhanced. The specific details in the development of the negatives and the printing, throughout this process, are kept such that the locations with zero magnetic signal print out to be a uniform middle-gray while regions that exhibit a positive longitudinal magnetic field print lighter and regions that exhibit a negative longitudinal magnetic field print darker. The various steps involved in the Leighton Photographic Subtraction magnetograph are illustrated in Figure 1.20 (from [32], p. 78).



**Figure 1.20** The Leighton photographic subtraction technique.

Because photographic film is a two-dimensional detector, as opposed to a photomultiplier which is basically a single pixel detector, this process has an advantage over the Babcock photoelectric magnetograph in that it can produce a two-dimensional magnetogram with only a single scan of the area on the solar disk under study. Because of the very high resolution inherent in photographic film, solar features of relatively fine details may be discerned. Also, because the right and left-handed polarization components are imaged simultaneously, any variations in light level that are common to both channels will be canceled out.

The net result is that a magnetogram of a sufficiently large area of the surface of the Sun can be constructed in a reasonable time with a suitable resolution. Typically, the Leighton magnetograph was able to produce a magnetogram covering a region on the Sun 350 arc-sec by 600 arc-sec in about six minutes, with a resolution of approximately 1 arc-sec.

The Leighton magnetograph was, of course, not without its problems. Dust and blemishes on the film, both on the original and intermediate plates, accumulated with each step in the process and all appeared in the final image as spurious features. Also, non-uniform plate sensitivity and non-uniform development and printing also incorporated cumulative errors which progressively degraded the final result. These errors decreased the sensitivity of the instrument with the introduction of random background noise.

In addition, it was impossible to exactly align the negative and the positive images. This effect would be most severe at the locations in the image where there was a large gradient in the photographic density, such as at the boundary of a sunspot or at the



solar limb. Further complicating the alignment process, slight defects in the optics of the telescope resulted in the fact that both images were of slightly different scale at different locations in each image. This effect made it impossible to obtain exact alignment over the entire image. The cumulative effect of these errors was that the instrument had a sensitivity of approximately 20 Gauss near the center of the image, where the alignment of the images was the best, with the sensitivity progressively decreasing towards the edges.

Due to the fact that this process required the successive development, printing and careful alignment of photographic plates, it typically took at least a few days before the magnetograms were available. Also, the difficulty and tediousness of this process discouraged the taking of many successive magnetograms which would have enabled the investigation of the dynamics of the morphology of an active region over relatively short time scales.

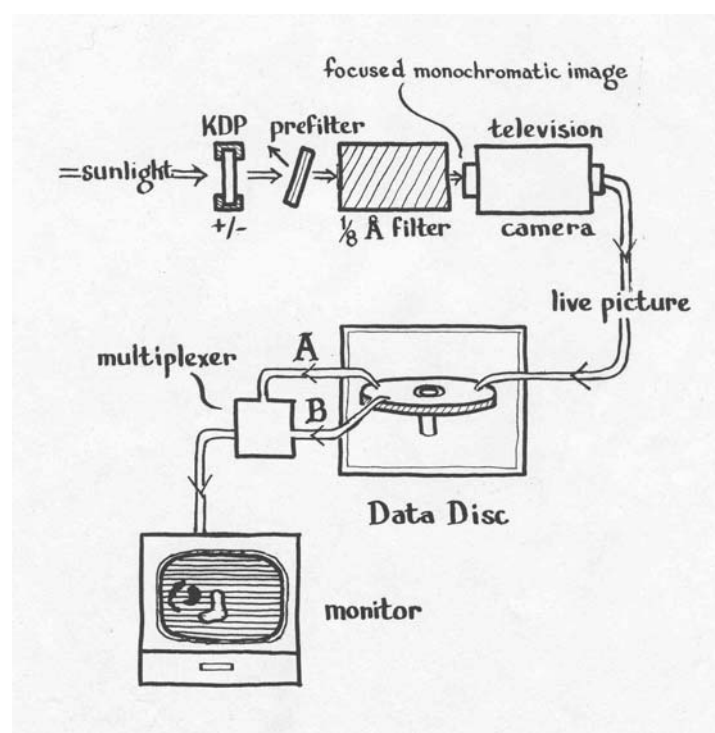
Despite the aforementioned limitations, the Leighton magnetograph was able to obtain magnetograms of sufficiently high scale and sensitivity that the magnetic properties of active regions on the Sun could be studied in detail. In general, the highest quality photographic plates were selected, care was taken in the development, printing and alignment processes and the spurious features, created by blemishes and dust on the photographic plates, were easily recognizable and could, thus, be ignored.

## 1.9 The Big Bear Magnetograph

The magnetograph that was developed for the Big Bear Solar Observatory (BBSO) to satisfy the afore mentioned requirements was initially developed at Caltech by Smithson and Leighton in 1971 [32]. Commonly know of as the Video Magnetograph (VMG), this instrument was tested on campus then moved to BBSO and improved upon by Mosher in 1972 [33]. It has been a part of routine observations at BBSO ever since. Since that time, the instrument has gone through a continual evolution as new and improved cameras, computers, data recording devices and polarization optics have become available. This natural progression has currently culminated in the current form of the instrument, the Digital Vector Magnetograph (DVMG), the details of which are the ultimate goal of this discussion. This evolution will most certainly continue in the near future.

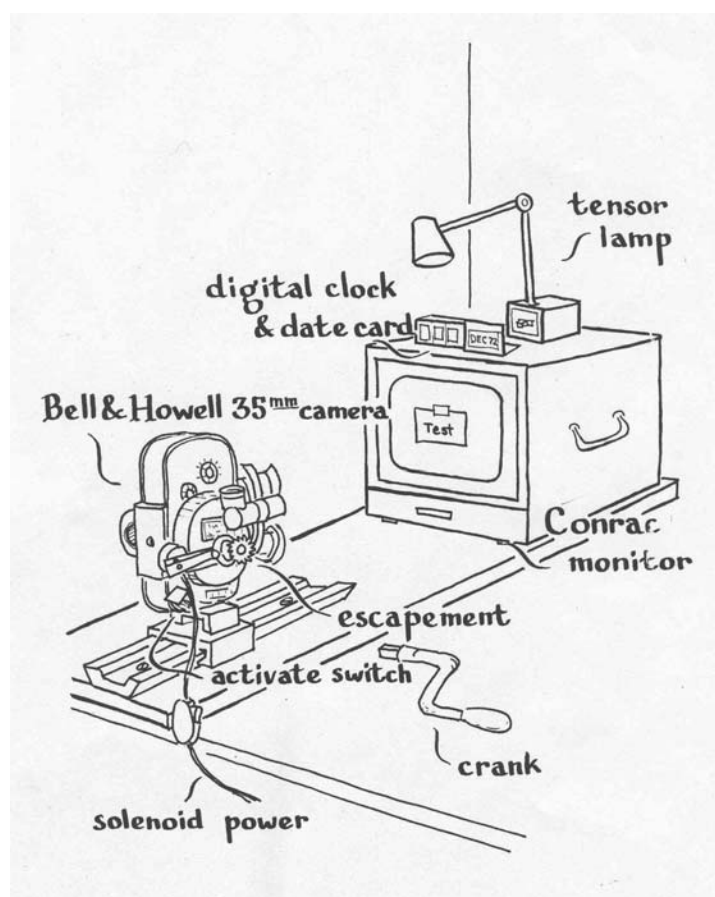
To overcome the problems inherent in the Leighton magnetograph, as was discussed in Chapter 1.9, R. C. Smithson and R. B. Leighton developed the video differential photometer magnetograph, more commonly known of as the Video Magnetograph (VMG) at the California Institute of Technology [32]. This instrument used an electronic equivalent of Leighton's photographic subtraction technique to construct a magnetogram. To simplify the structure of the telescope, so the entire instrument could be mounted on the small refractor on campus, the spectrograph was replaced by an  $1/8 \text{ \AA}$  Lyot filter tuned to the wing of a magnetically sensitive absorption line. Use of a narrow-band filter further simplified the instrument by immediately providing a monochromatic two-dimensional image as opposed to the one-dimensional image as produced by a spectrograph. Thus, scanning the solar image across the instrument, to build up a two-dimensional image, and the reconstruction of the two-

dimensional image was not required. An electro-optic retardation plate, similar to the ADP used in the Leighton photographic subtraction magnetograph, was used to convert the oppositely circularly polarized components into linear polarizations which were subsequently isolated by a linear polarizer, as in the Babcock magnetograph. Since the entire instrument could be mounted on the part of the telescope that tracked the Sun, the set of plane mirrors, used to feed the fixed spectrograph in previously discussed magnetographs, were not required. Thus avoiding the bias signal due to spurious polarization imparted on the signal by the plane mirrors. See Figure 1.21 for a schematic of the original VMG system (from [33], p. 26).



**Figure 1.21** Schematic of the original VMG system.

To keep costs low, standard commercial television equipment was used. The entire process of making a magnetogram was under the control of a patchcord-programmable controller. The state of the electro-optic retardation plate was synchronized with the television detector. A many-track video disk recorder was used to store the images. All video subtraction, averaging, and any other image processing, was done in analog form. The final magnetogram was displayed on a television monitor and photographed with a camera (Figure 1.22 from [33], p. 88).



**Figure 1.22** Saving the magnetograms from the original VMG system.

Since the entire process was automatically controlled, and since the development of only one photograph was required to produce a single magnetogram, the time from the acquisition of the data to the production of a magnetogram was greatly reduced. The relative ease of production encouraged the taking of many sequential magnetograms which enabled the study of the temporal evolution of active regions on the time scales of a few minutes.

Another disadvantage of the Leighton magnetograph was that each individual photographic plate had unique defects and each photographic plate would be developed slightly differently. The VMG avoided this problem in that there is a single electronic detector. Any defects on the optics or the detector, such as dust or a malfunctioning pixel element, will be canceled when the subtraction is performed. Thus, spurious features, caused by these defects, do not appear in the final magnetogram. Only the final photograph of the magnetograph, as displayed on the television screen, was saved.

It was desired at the outset that the instrument have a sensitivity of 1:1000. Since commercial television images typically had a signal-to-noise ratio of 1:300 the sensitivity of individual magnetograms needed to be increased. Since each magnetogram was stored on the many-track video disk, many magnetograms could be averaged to increase the signal-to-noise ratio of the final magnetogram. The signal-to-noise ratio should thus be improved by  $N^{1/2}$  if  $N$  magnetograms are averaged. Unfortunately, the signal to noise ratio of actual magnetograms does not improve exactly by this law. As the total integration time for a single magnetogram increases, the distorting effects of the atmosphere of the Earth blurs the integrated image. Thus washing out small scale features that would otherwise be detected. In addition, solar features are not static. Small scale features on the

Sun remain apparently the same for only a few minutes. Therefore, the magnetograms become smeared by the actual motion of the features as the total integration times becomes longer than the lifetime of the small scale features (the details of this will be presented in detail in Chapter 3.6.2).. Typically, 64 magnetograms were averaged to achieve the desired sensitivity of 0.1%. Approximately 10 seconds were required to record the initial images and another 50 seconds were then required for subtraction and averaging. Thus, a magnetogram could be automatically produced about once a minute.

Since no beam splitter was used, both the right and left-hand polarization images traversed the same optical path. Also, since the left and right-hand polarization images were obtained in sequence very rapidly, the VMG did not suffer from the fact that each image set needed to be aligned. One image simply needed to be subtracted from the other with the analog computer to obtain the difference. Another advantage to the fact that both the left and right-hand polarization images used the same optical path is that each channel had the same scale across the entire image. Therefore, there was perfect alignment across the entire image and spurious features near the edges of sunspots, caused by different scales across the images as in the Leighton magnetograph, were not produced.

As stated previously, this instrument was moved to BBSO and improved upon by Mosher in 1972. Because of the mounting of the telescope at the time, the VMG was mounted on a side bench of the 10 inch vacuum-refractor. A plane mirror was introduced into the light path to divert the light to the instrument. The instrument has subsequently been revised and improved. A description of the various forms of the instrument can be found in [43].

The purpose of the BBSO magnetograph, from its inception, was to study the changes in the morphology of the solar magnetic field with a high cadence. Since filter based magnetographs, even with all of their limitations (many of which will be addressed in the following chapters of this work), are ideally suited for this purpose all of the discussed limitations can be tolerated. In reality, no single instrument can measure the solar magnetic field, over the entire area of an active region, with both high accuracy and high cadence. Therefore, it is not unusual to simultaneously study the solar magnetic field with a variety of coordinated instruments, at multiple locations, from both on the ground and in space, over a variety of wavelengths. The BBSO filter based magnetograph provides one important data set in the overall study of solar magnetic fields.

The remainder of this work will discuss the details of the current variation of the BBSO magnetograph – the Digital Vector Magnetograph (DVMG). Chapter 2 will focus on the construction of the instrument. Chapter 3 will discuss the collection and calibration of the data and the creation of the magnetograms. Results from the instrument will be presented in Chapters 4 and 5. Chapter 5 will also review some future improvements and current magnetogram projects.

## CHAPTER 2

### INSTRUMENTATION

Using Zeeman splitting (Section 1.3), solar magnetographs measure the polarization of light from the Sun. The polarization properties of light can be represented by the Stokes vector:

$$S = \begin{pmatrix} I \\ Q \\ U \\ V \end{pmatrix} \quad (2.1)$$

where  $I$  is the total intensity of the light,  $Q$  is the intensity difference between the horizontal and vertical linearly polarized parameters ( $Q = Q_H - Q_V$ ),  $U$  is the intensity difference between the linearly polarized components that are oriented at  $\pm 45^\circ$  ( $U = U_A - U_B$ ) and  $V$  is the intensity difference between the right and left-handed circularly polarized parameters ( $V = V_R - V_L$ ) (Note that, from this point forward,  $Q$ ,  $U$  &  $V$  will be referred to as the Stokes elements while  $Q_H$ ,  $Q_V$ ,  $U_A$ ,  $U_B$ ,  $V_R$  &  $V_L$  will be referred to as the Stokes components). All polarization characteristics of light can be represented by some combination of the above parameters. From the three polarization measurements ( $Q$ ,  $U$  &  $V$ ), the strength and direction of the magnetic field, at every point in an image, can be reconstructed. Thus, solar magnetographs are actually polarization analyzers, inferring the strength and direction of the magnetic fields on the surface of the Sun by analyzing the polarization of Sunlight.

Since the three polarization elements of the Stokes vector ( $Q$ ,  $U$  &  $V$ ) represent the difference in intensity between their respective polarization components, each individual component ( $Q_H$ ,  $Q_V$ ,  $U_A$ ,  $U_B$ ,  $V_R$  &  $V_L$ ) must be isolated and imaged



separately. To accomplish this task, a series of variable polarization optics is used (Section 2.6). The purpose of the variable polarization optics is to convert the polarization of the component that is to be imaged into linear polarization. The linear polarization is isolated by a linear polarizer, used as an analyzer. Thus, only the desired polarization component will successfully pass through the instrument and be imaged while all other polarization components will be blocked. The specific details and operation of the polarization optics will be discussed in Section 2.6.

The magnetograph at the Big Bear Solar Observatory (BBSO) is of the filter-based type (Sections 1.9). The specific details of the BBSO magnetograph is the subject of the current section. Typically, two types of magnetograms are obtained at the BBSO: longitudinal magnetograms and vector magnetograms. Longitudinal magnetograms yield the line-of-sight magnetic field, requiring only the Stokes-V element. Vector magnetograms, reveal both the line-of-sight and the transverse magnetic field, require the complete Stokes set (Q, U & V). The specific type of magnetogram obtained will depend on the scientific goal of a particular observation.

Studies of the photospheric magnetic field can be divided into two general categories: that of the quiet Sun and that of active regions. Observations of the magnetic fields of the quiet Sun typically require only longitudinal magnetograms while observations of active regions require vector magnetograms

The strength of the measured magnetic fields in quiet Sun regions are typically on the order of a few to a few hundred Gauss, which is much weaker than those found in active regions. Due to their relative weakness, the motion of quiet Sun magnetic fields tend to be dominated by the turbulent motion of the solar plasma in the photosphere,

which sweeps these fields in the lanes between the solar granules. The isolated components of magnetic fields in quiet Sun regions tend to be essentially normal to the solar surface and can be crudely envisioned as vertically floating magnetic “straws”. Because quiet Sun magnetic fields are relatively weak, and tend to be normal to the solar surface, the strength of the transverse components of quiet Sun magnetic fields are also very weak and typically below the sensitivity level of current instruments. Considering these factors, longitudinal magnetograms are considered to be sufficient for the study of quiet Sun magnetic fields.

On the other hand, the strength of magnetic fields in active regions can be several hundred to a few thousand Gauss. At this strength, the magnetic fields tend to dominate the motion of the solar plasma in the photosphere and inhibit the convective motion of the solar material. The magnetic fields are twisted and arrange themselves at any angle relative to the solar surface. Therefore, both longitudinal and transverse magnetograms are required to adequately reconstruct the magnitude and direction of the magnetic fields of active regions. Of course, measuring the fields require a fairly sophisticated device.

A major challenge in the design and construction of astronomical instrumentation is that the requirements of the optical, imaging and other components, and their associated control software, is typically much different than the requirements for such components that can be found in industry. Because astronomical instrumentation is a relatively small part of the market, manufacturers typically do not take the requirements of components for astronomical instrumentation into account when designing their products. This problem tends to be even more pronounced when building instrumentation for solar telescopes because the field of solar astronomy is a minority player in the

astronomical instrumentation field as a whole. Of course, it is possible to order custom components. However, because a production run for a custom component to be used in astronomical instrumentation would typically be a single component, or very few, this tends to make the cost prohibitive and the time scale for delivery unacceptable.

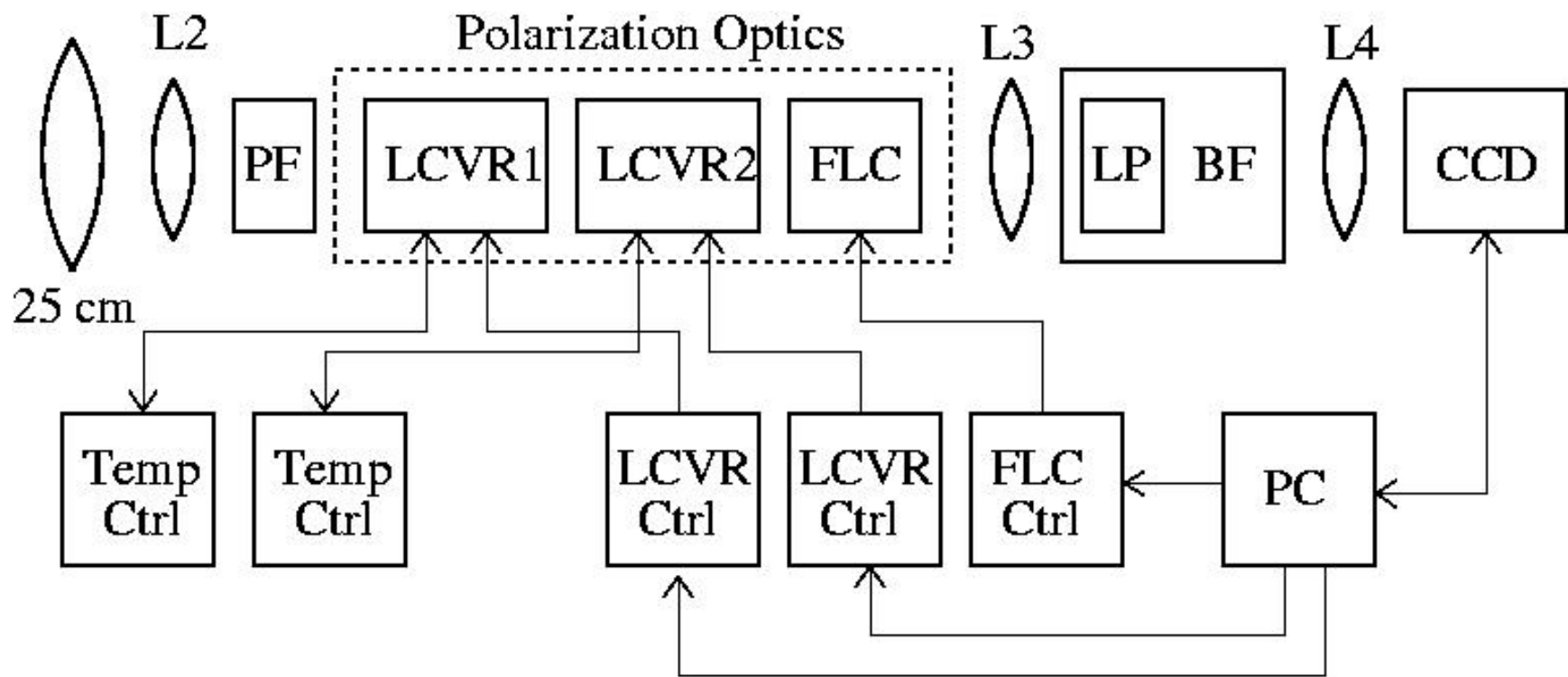
Clearly, the usual way around this problem is for individual astronomical facilities to manufacture custom equipment specifically designed to meet their requirements. However, designing and building a CCD camera, for example, from scratch is typically beyond the capabilities of any astronomical facility.

Therefore, builders of astronomical instrumentation are forced to purchase components, that are available on the market, whose characteristics most closely resemble the ideal for their particular use. The exact design and implementation of the instrument must then be made which both accomplishes the end goal of the instrument and takes advantage of the specific characteristics of each individual component. In this regard, the specific limitations and tradeoffs made will be addressed as each component of the DVMG is discussed, in detail, in the following sections of this section.

## **2.1 Overview of the Instrument**

The DVMG is a filter based magnetograph (Section 1.4.3). Figure 2.1 is a schematic and optical layout while Figure 2.2 is a functional block diagram of the instrument. The basic operation of a filter based solar magnetograph is as follows. The optics of the telescope (labeled 25 cm in Figure 2.1) provide a beam of sunlight, of high focal ratio, to the optical bench where the instrument is mounted. A Birefringent filter (labeled BF in Figure 2.1), with a very narrow bandwidth, that is typically on the order of  $1/4 \text{ \AA}$ , isolates

the wing of the magnetically sensitive absorption line under study. The Sun is imaged onto an electronic detector (labeled CCD in Figures 2.1 & 2.2). In the case when the absorption line being used lies in the visible portion of the solar spectrum, this detector is typically of the silicon based charged couple device (CCD) type. Polarization optics (labeled LCVR<sub>1</sub>, LCVR<sub>2</sub>, FLC in Figures 2.1 & 2.2 and LP in Figure 2.1) isolates one of the two desired polarization components of the particular Stokes set of interest. The detector takes a single image of that first polarization component and that image is saved in the RAM of the computer which controls the instrument. The polarization optics then isolate the second polarization component. The detector takes a single image of that second polarization component which is also saved in RAM. If there is a magnetic field present, the intensity of the two images, at any individual point, will be slightly different (as will be discussed in Section 2.9). The process of taking single images, of alternating polarization components, is repeated and each new image is summed, with its appropriate fellows, to increase the signal to noise ratio to the desired level. When the number of images required to reach the desire signal-to-noise ratio have been integrated in RAM, a magnetogram is produced by displaying the difference between the two integrated polarization images divided by their sum.



**Figure 2.1** Schematic and optical layout of the DVMG.

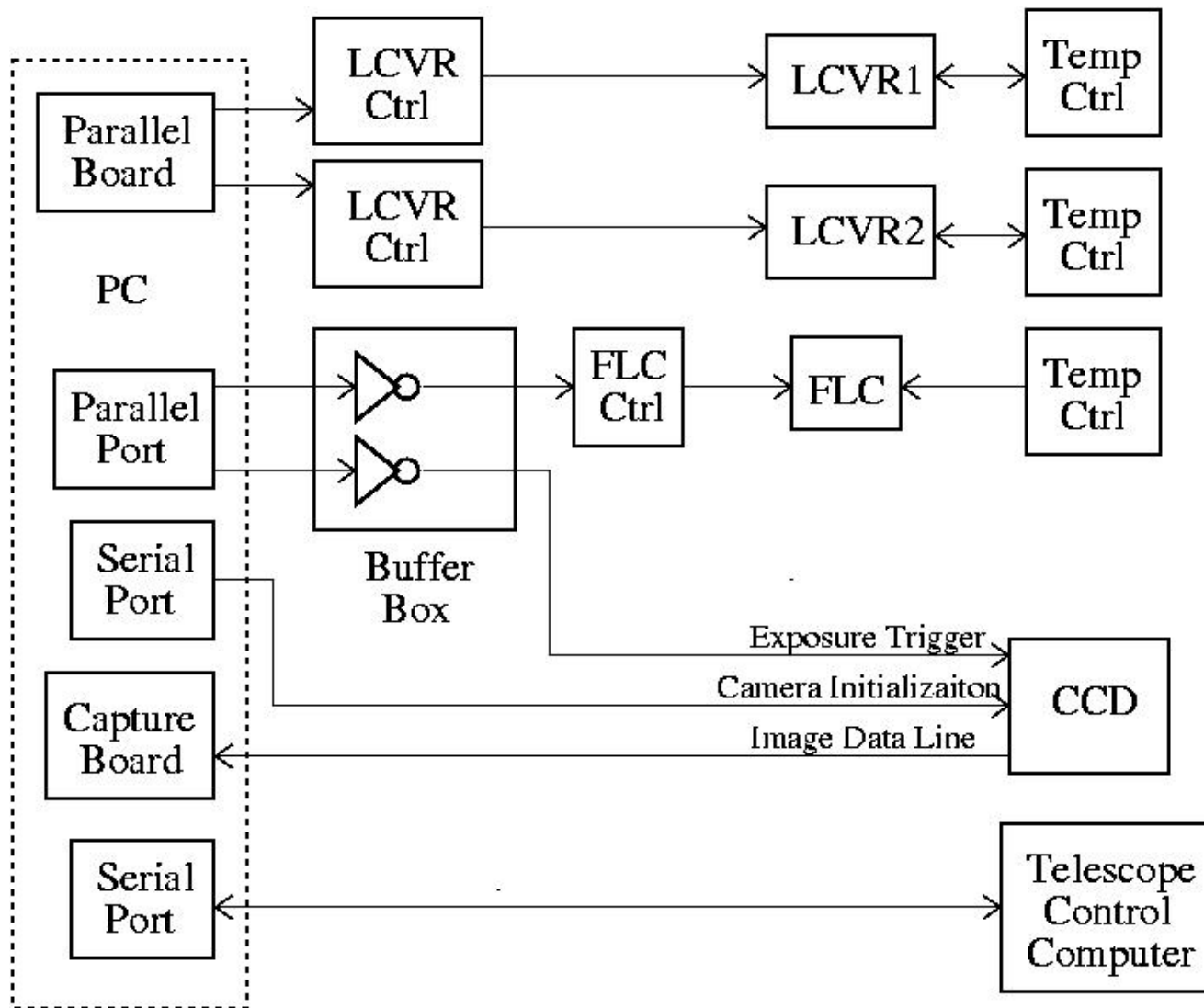


Figure 2.2 Functional block diagram of the DVMG.

For example, in the case when quiet Sun magnetic fields are being studied, where only the longitudinal magnetic field is required (as previously discussed), all of the locations in the image where the magnetic field is directed toward the instrument will be positive while all of the locations in the image where the magnetic field is directed away from the instrument will be negative. This magnetogram can then be conveniently displayed where all of the positive values are plotted as shades of white, all of the negative values are plotted as shades of black and the areas where no magnetic field is present is plotted as a uniform gray (Figure 1.15, Section 1).

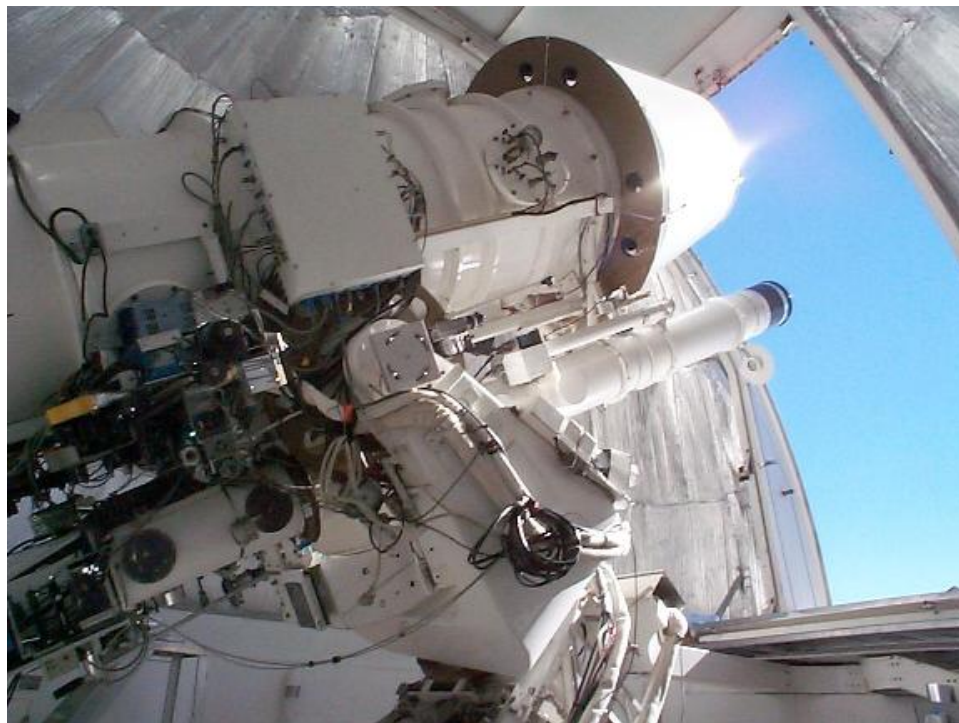
The specific details of the telescope will now be discussed, each element of the instrument, as shown in the schematic diagram, and the computers which control both the telescope and the DVMG.

## **2.2 Telescope Details and Limitations**

There are three primary telescopes at the BBSO (Figure 2.3). The 65 cm vacuum-reflector and the 25 cm and 20 cm refractors. Both the 65 cm vacuum-reflector and the 25 cm refractor are configured as high-resolution telescopes, thus only imaging a small portion of the solar disk. Specifically, the 65 cm vacuum-reflector has a useable field-of-view of approximately 100 arc-sec while the 25 cm refractor has a useable field of view of approximately 300 arc-sec (one arc-sec is equivalent to 725km on the Sun). The 20 cm refractor is configured to operate as a full-disk instrument. The three primary telescopes can be seen in Figure 2.4.



**Figure 2.3** The Big Bear Solar Observatory (BBSO).



**Figure 2.4** Photo of the telescope assembly at BBSO.





**Figure 2.5** Optical bench of the 25 cm vacuum-refractor.

The 65 cm vacuum-reflector is mounted on an equatorial fork-mount. In an equatorial type mounting, only the right-ascension axis (the axis parallel to the rotation axis of the Earth) needs to be rotated to track an object across the sky as the Earth rotates. Both the 25 cm and 20 cm refractors are mounted piggy-back onto the 65 cm vacuum-reflector. However, each piggybacked telescope has an independent guider so that the 65 cm vacuum-reflector and the 25 cm refractor can be pointed at, and accurately track, different areas on the solar disk. The 20 cm refractor also has an independent guider so that the 65 cm vacuum-reflector need not be pointed at the center of the Sun to maintain proper alignment of the image of the Sun on the detector of the full-disk telescope.

The DVMG is mounted on the 25 cm refractor. There are three optical benches on this telescope (Figure 2.5). Each bench has a unique instrument controlled by a separate computer. Light is directed to each bench by a computer controlled mirror assembly (inside the black metal box slightly above the center of Figure 2.5). The DVMG is mounted on the center bench, with a straight-through light path, to avoid affecting the polarization of the light by reflection, which can greatly complicate the measurements of the solar magnetic field as was discussed in the introduction. The two side benches image the same area on the Sun, one in H $\alpha$  (656.3 nm) and the other in Ca II K (393.3 nm), at the same scale (0.6 arc-sec/pixel, as does the magnetograph). The DVMG and the two instruments on the side benches can be used in any desired sequence to fulfill the requirements of the observations carried out at that time.

As briefly discussed in the introduction, while mounting a magnetograph on the moving telescope has the great advantage of avoiding spurious polarization imparted by reflection from mirrors, it does have several disadvantages. Mainly, the space available to

contain the instrument tends to be much more limited when the instrument is installed on the telescope as opposed to being mounted on a stationary optical table. Specifically, the space available, on the center optical bench of the 25 cm refractor, along the direction of the light path is 90 cm, while the cross sectional area is approximately 25 cm x 25 cm. The entire instrument must be contained in this space, including the birefringent filter (the large silver rectangular shaped box at the center of Figure 2.5), which is, by far, the largest single component at 35 cm in length. This is a much more limited space than the stationary optics table in the Coude' room below the telescope, which measures 2 m x 4 m, where available space for instrumentation tends to be much less of a limitation.

A second disadvantage is that it is absolutely required that the temperature of the air immediately surrounding the telescope be as close as possible to the temperature of the air outside the observatory building to avoid the degradation of the solar image imparted by turbulent air currents. The aperture through which light reaches the telescope (see Figure 2.4) is, of course, closed during times which the telescope is not in operation and/or during times of inclement weather. However, it must be open during observations. Not only to allow light to reach the telescope but also to allow the outside air to properly mix with the air in the vicinity of the telescope. For example, if the air temperature outside the observatory building is  $-7^{\circ}$  C ( $20^{\circ}$  F) then the air temperature immediately surrounding the telescope, and any instrumentation mounted thereon, should also be  $-7^{\circ}$  C. This presents challenges because many components used in astronomical instrumentation are fragile and demand a much more benign environment, thus requiring protection from the outside environment and accurate temperature control.

It must be kept in mind that filters and polarization optics must not only be kept at a constant temperature, but a clear optical path must also be maintained. Also, adjustments must be made, from time to time, in the alignment and rotation of filters and polarization optics without disturbing their operating temperature. This requirement for strict temperature control, of certain components, conspires with the very limited space available for the instrument to create difficulties and limitations in the design of the instrument.

Another disadvantage of mounting an instrument on the telescope is that of telescope flexure. The telescope must track the Sun across the sky to compensate for the rotation of the Earth. As it does so, the gravity vector is continually changing. Thus, the slight bending of the mounting, the telescope proper and the optical benches also changes with time. This problem manifests itself most notably in that a set of flat-fields taken early in the day, for example, will not completely correct for dust and dirt on the optics and non-uniformities in the light path in images that are taken later in the day. An obvious solution to this problem would be to take several flat field images through the day. Unfortunately, the time required to take flat field images for the DVMG is much greater than other instruments. Specifically, it typically takes at least 15 minutes to take a flat field sequence for the DVMG, not to mention the significant computing time required to generate the flat field files after the data is acquired. While taking several flat field sequences through the day would more precisely account for optical non-uniformities, the time required to acquire the flat fields would be a significant fraction of the observing time. Therefore, only one set of flat field images are typically taken per day. In actual practice, flat field images taken at the start of an observing day do indeed remove most of

the non-uniformities in the optical path even in images taken several hours after the flat fields are acquired. However, if it is determined that higher quality flat fields are required for the observing run during any particular day, the observer can schedule time for additional flat fields. The specific creation and use of flat fields for the DVMG will be discussed, in detail, in Section 3.5.

### **2.3 Image Scale and Light Throughput**

In modern solar instrumentation, image scale is defined as the amount of the solar surface that is imaged onto a single pixel of the CCD camera (black cube protruding from the white box near bottom-center of Figure 2.5). This value is stated in arc-sec / pixel. The actual image scale that is used is a compromise between three competing factors – image resolution, signal level of an individual exposure and the apparent size of a typical large active region on the Sun.

The resolution (diffraction limit) of a telescope can be defined by:

$$r = 1.22 \lambda / d \quad (2.2)$$

where  $r$  is the resolution in radians,  $\lambda$  is the wavelength of light of the spectral line being used and  $d$  is the diameter of the objective. Using 610 nm for the wavelength of light and  $2.5 \times 10^8$  nm (25 cm) for the diameter of the objective yields a resolution of  $3.0 \times 10^{-6}$  radians or 0.6 arc-sec. Thus, the Nyquist sampling rate would be 0.30 arc-sec / pixel to completely record all of the detail that the telescope is capable of resolving.

While the specific details of the CCD camera used on the DVMG will be discussed in detail in Section 2.7 below, some characteristics of the camera will be

introduced here for the purpose of the current discussion. The signal level of an individual exposure is a function of the number of photons reaching the detector per second, the quantum efficiency of the detector and the exposure time. Once a specific camera has been chosen for use on a specific instrument the amount of light reaching the detector and the quantum efficiency characteristics of the camera can not be changed. Therefore, the only way to adjust the signal level of a single exposure is to adjust the exposure time. To fully take advantage of the 12-bit capability of the CCD camera used on the DVMG the exposure time must be long enough to approximately fill the electronic wells of the pixels.

It has already been noted that the light throughput of the instrument is very low due to the light throughput characteristics of the individual optical components used. Because the Sun is so bright, and the fact that the instrument is mounted on a telescope whose primary objective is 25 cm in diameter, it might appear that the instrument is provided with more than enough light. In actuality this is not the case. First, the fact that a linear polarizer (LP in Figure 2.1) must be used to isolate the individual Stokes parameters reduces the light level by 50%. Then, each optical and polarization component reduces the total light level in the pass-band, in turn.

The pre-filter (PF in Figure 2.1) has a transmission, in the pass-band, of approximately 80%. The three polarizers (LCVR<sub>1</sub>, LCVR<sub>2</sub> & FLC in Figures 2.1 & 2.2) each has a transmission of approximately 90%. The birefringent filter (BF in Figures 2.1 & 2.2) has a transmission of approximately 2% in the pass-band. Finally, the CCD camera (CCD in Figures 2.1 & 2.2) has a quantum efficiency of approximately 15% at the operating wavelength of the instrument (610 nm). The next result is that less than

$1/1000^{\text{th}}$  of the light that enters the telescope, in the pass-band of the instrument, is actually detected by the CCD camera.

Finally, the apparent size of a typical large active region on the Sun must be taken into account. In general, it is desired to be able to image an entire active region in a single frame without repositioning the telescope. The largest active regions on the Sun can be on the order of 400 arc-sec across. It is thus desired to set the scale to at least approximately image a region on the Sun of that size on the detector.

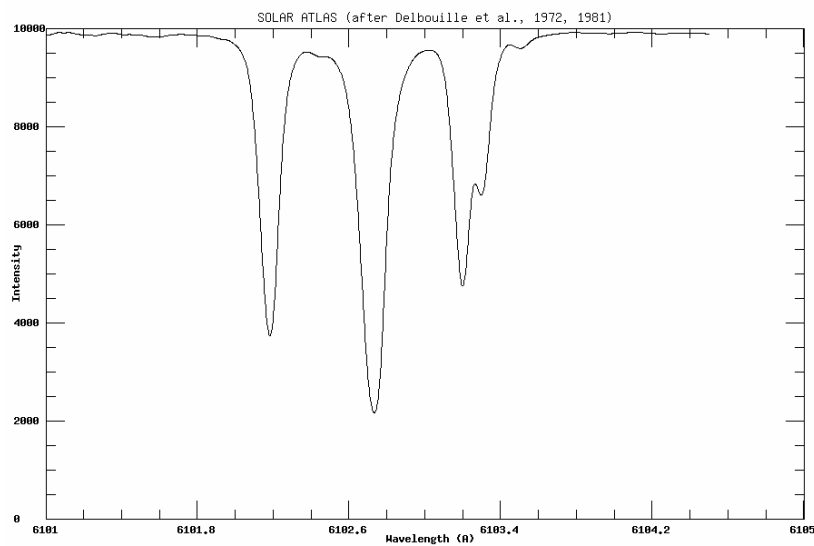
It must be noted that it is always desired to use the shortest exposure time possible to minimize the distorting effects of the atmosphere of the Earth. These three aspects (image resolution, signal level and the apparent size of an active region on the Sun) tend to compete against the desire to record all of the detail that the telescope is capable of resolving. The detector has  $1024 \times 1024$  pixels. The camera is always used in the  $2 \times 2$  binning mode producing an effective array of  $512 \times 512$  pixels. By summing the light from four adjacent pixels, the exposure is thus reduced by an equivalent amount, but sacrificing image resolution.

Taking all of these factors into account, the optics of the 25 cm refractor were designed to provide a scale at the focal plane of approximately 20 arc-sec / mm. The exact image scale is easily adjusted by a zoom-lens (L4 in Figure 2.1, black cylinder just below the birefringent filter in Figure 2.5) which produces the final image on the detector. By reducing the image scale from the Nyquist rate, to concentrate more light on each individual pixel, the exposure can be shortened to a reasonable time. The size of each image pixel, after binning, is  $28 \mu\text{m} \times 28 \mu\text{m}$ . The exposure used is 120 ms. The net result is an image scale of 0.6 arc-sec / pixel producing an image that is 300 arc-sec

across on the detector. This is a good compromise between resolution, signal level of an individual exposure and the apparent size of a typical large active region. If the scale were to be set to the Nyquist sampling rate of 0.25 arc-sec / pixel, the image would only be 130 arc-sec across, which is smaller than a mid-side active region. Also, the exposure to acquire the same signal level of an individual frame would increase to 700 ms allowing the distortions caused by the atmosphere of the Earth to degrade the image.

## 2.4 The Ca I Absorption Line

The absorption line used by the DVMG is the magnetically sensitive Ca I line at 610.273 nm, the center line of the Calcium triplet in that region of the solar spectrum. A plot of the Calcium triplet is shown in Figure 2.6 (courtesy [44]). The line has a center depth of 22% of the continuum intensity, a FWHM of 0.015 nm and a Lande` g-factor of 2.



**Figure 2.6** The Ca I absorption line profile.



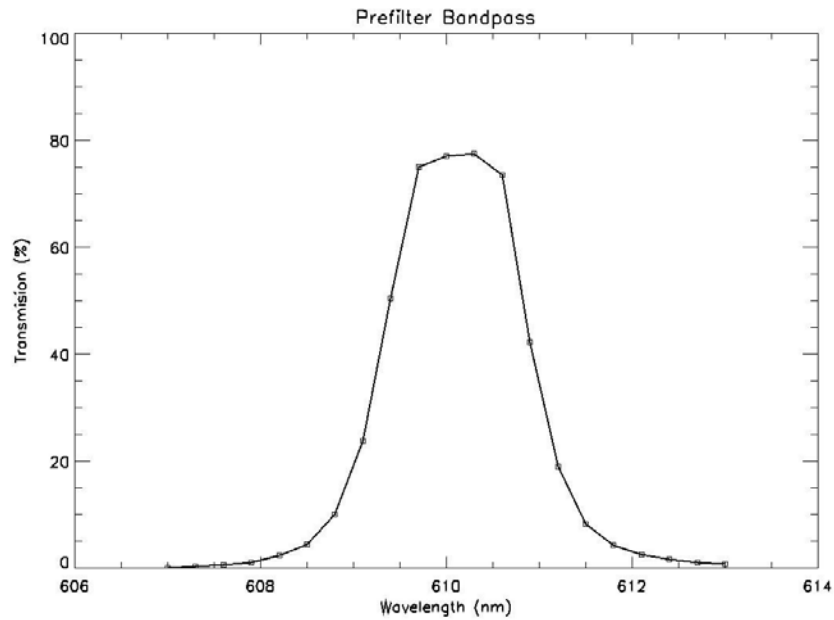
The narrowness of this line, when compared to the 0.025 nm band-pass of the birefringent filter, is the source of some loss of sensitivity in magnetic field measurements. This loss of sensitivity arises from the fact that, when the filter is tuned to the center of the blue wing of the Ca I line, there is some leakage from the continuum on the blue side of the filter and from the line center and some of the red wing of the line on the red side of the filter. This situation is, unfortunately, unavoidable when using a typical birefringent filter. Birefringent filters with band-passes that are narrower than 0.025 nm are very rare and very expensive. In addition, birefringent filters intrinsically have a very poor light throughput in the band-pass. The specifics of birefringent filters will be discussed in Section 2.7.

The only solution to this problem is to use a Fabry-Perot' filter, which, typically, has a band-pass on the order of 0.01 nm or less. However, the use of a Fabry-Perot' on a moving telescope in an outside environment presents its own unique set of challenges, as previously discussed (Section 2.2),. This is most certainly an option in a future upgrade of this instrument (Section 6.5).

## **2.5 The Pre-Filter**

The purpose of the pre-filter (PF in Figure 2.1) is to suppress the side-bands of the birefringent filter (Section 2.7), which are a natural consequence of the design of that specific type of narrow-band filter, and to block ultra-violet light which can damage the ferroelectric liquid crystal  $\frac{1}{4}\lambda$  plate (Section 2.6.4). The pre-filter for the instrument, from Barr Associates in Cambridge, MA, has a central wavelength of 610.1 nm, a band-

width of 1.4 nm and a transmission of approximately 75%. A plot of the transmission curve for the pre-filter is shown in Figure 2.7.



**Figure 2.7** The Pre-filter band-pass.

It was important to obtain a pre-filter with the highest transmission reasonably possible to maximize the light throughput of the instrument. This was especially important due to the fact that the birefringent filter has a very low transmission in its band-pass (Section 2.7) and the CCD detector has a relatively low quantum efficiency (Section 2.8). The transmission of the birefringent filter and the quantum efficiency of the CCD detector will be discussed in the appropriate sections below.

## 2.6 Polarization Optics

As discussed in the opening paragraphs of Chapter 2, a solar magnetograph determines the magnetic field on the Sun by measuring the polarization of sunlight. By measuring the polarization components of the Stokes vector (Q, U & V), one can infer the strength and direction of the solar magnetic where:  $Q = Q_H - Q_V$ ,  $U = U_A - U_B$  and  $V = V_R - V_L$ . The incoming light from the Sun contains a mixture of these polarization components. The purpose of the polarization optics (LCVR<sub>1</sub>, LCVR<sub>2</sub>, FLC & LP in Figures 2.1 & 2.2) is to isolate the individual Stokes components (Q<sub>H</sub>, Q<sub>V</sub>, U<sub>A</sub>, U<sub>B</sub>, V<sub>R</sub> & V<sub>L</sub>), so each may be imaged separately, and the Stokes elements determined from the equations above. The Stokes components are isolated using the following steps.

Step 1: Stokes Parameter Selection - The first step in isolating the Stokes components is to determine which Stokes element is to be measured (Q, U or V) and to then convert the appropriate Stokes components into a set of orthogonal linear polarizations that are aligned with the linear polarizer that is used to isolate each polarization component. (In the case of the DVMG, the Q components arrive at the instrument as a set of orthogonal linear polarizations already in the correct orientation and need not be converted from their original form.) The two Liquid Crystal Variable Retarders act as the Stokes parameter selectors. The details of exactly how the two Liquid Crystal Variable Retarders accomplish this task will be discussed, in detail, in Section 2.6.

Step 2: Stokes Component Selection – Once the set of Stokes components of interest are converted into orthogonal linear polarizations, the particular Stokes component that is to be imaged must be aligned parallel to the linear polarizer that will

isolate the component. This is accomplished by the Ferroelectric Liquid Crystal. For each set of Stokes components ( $Q_H/Q_V$ ,  $U_A/U_B$  &  $V_R/V_L$ ) one component ( $Q_H$ ,  $U_A$  &  $V_R$ , depending on which Stokes parameter has been selected in Step 1) is already parallel with the isolation linear polarizer when the light immerges from the Stokes parameter selection optics (Step 1). Therefore, these three components need not be changed. However, their counterparts ( $Q_V$ ,  $U_B$  &  $V_L$ ) immerge from the Stokes parameter selection optics rotated  $90^\circ$  to the isolation linear polarizer. Therefore, these three components must be rotated to be parallel with the isolation linear polarizer. Again, the details of exactly how the Ferroelectric Liquid Crystal accomplishes this task will be discussed in Section 2.6.

Step 3: Stokes Component Isolation – The purpose of the Stokes Parameter Selector (Step 1) and the Stokes Component Selector (Step 2) was to convert the polarization of the particular Stokes component that is to be imaged into a linear polarization that is parallel to the linear polarizer (LP in Figure 2.1). Therefore, the linear polarizer will only pass one of the six Stokes components, which will be imaged by the CCD detector. Since each pair of Stokes parameters immerges from the Stokes Parameter Selector as orthogonal linear polarizations, the partner of the individual Stokes component that is being imaged at any particular time is blocked by the linear polarizer. The four Stokes components that are used to create the two Stokes parameters that are not to be imaged at that particular time will be either circularly polarized or linearly polarized  $\pm 45^\circ$  to the isolation linear polarizer. Therefore, each component will be attenuated by  $1/2$  by the linear polarizer and cancelled with its partner when the Stokes parameter is determined.

Before proceeding with the details of how the polarization optics isolate a particular Stokes component of interest, Mueller Calculus will be reviewed, which will enable us to track how each polarization optic effects the polarization of all of the Stokes components.

### 2.6.1 Review of Mueller Calculus

Mueller calculus can be used to analyze the effects that a specific polarization optic will have on a specific polarization of light. In this method, the polarization properties of light are represented by the Stokes vector  $S_0$  (Equation 2.1) and the polarization properties of the polarization optic are represented by a matrix. In general, the Muller matrix for a waveplate with a retardance of  $\delta$  and the angle of the fast axis relative to the horizontal, in degrees, of  $\phi$  is given by:

$$M = \begin{vmatrix} 1 & 0 & 0 & 0 \\ 0 & C^2 + S^2 \cos \delta & SC(1 - \cos \delta) & -S \sin \delta \\ 0 & SC(1 - \cos \delta) & S^2 + C^2 \cos \delta & C \sin \delta \\ 0 & S \sin \delta & -C \sin \delta & \cos \delta \end{vmatrix} \quad (2.3)$$

where:

$$C = \cos(2\phi) \quad (2.4)$$

and

$$S = \sin(2\phi). \quad (2.5)$$

The polarization state of the output light can then be calculated by:

$$S_1 = M S_0, \quad (2.6)$$

where  $S_1$  is the Stokes vector out the output light,  $M$  is the Mueller matrix of the optic under consideration and  $S_0$  is the Stokes vector of the input light.

For example, horizontal linearly polarized light can be represented by the Stokes vector:

$$S_0 = \begin{pmatrix} 1 \\ 1 \\ 0 \\ 0 \end{pmatrix}. \quad (2.7)$$

The Mueller matrix for a  $\frac{1}{4}$ -wave plate, whose fast axis is rotated  $45^\circ$  from the horizontal, is:

$$M = \begin{pmatrix} 1 & 0 & 0 & 0 \\ 0 & 0 & 0 & -1 \\ 0 & 0 & 1 & 0 \\ 0 & 1 & 0 & 0 \end{pmatrix}. \quad (2.8)$$

Multiplying the input Stokes vector by the Muller matrix of the polarization optic yields:

$$S_1 = \begin{pmatrix} 1 \\ 0 \\ 0 \\ 1 \end{pmatrix} \quad (2.9)$$

which is the Stokes vector that represents right-hand circular polarized light, as one would expect.

If it is desired to determine the effect that a series of polarization optics will have on an input polarization, the Muller matrix of each successive optic is multiplied in series by:

$$S_1 = M_n M_{n-1} \dots M_1 M_2 S_0. \quad (2.10)$$

The Muller matrices for several common retarders, at several ideal angles of rotation, and the Stokes vectors for several ideal polarizations of light, are given in Appendix A.

### 2.6.2 Principles of Retarders

Retarders (or wave plates) are optical devices that are used to control and/or analyze the polarization of light. The optic is made of a birefringent material having two indices of refraction – the ordinary index  $n_o$  and the extraordinary index  $n_e$  – whose axes are perpendicular to each other. By definition,  $n_e > n_o$ . The ordinary axis is referred to as the fast axis and the extraordinary axis is referred to as the slow axis.

Light traveling through any medium has a velocity that is dependent on the effective index of refraction of the optical material. The velocity is given by:

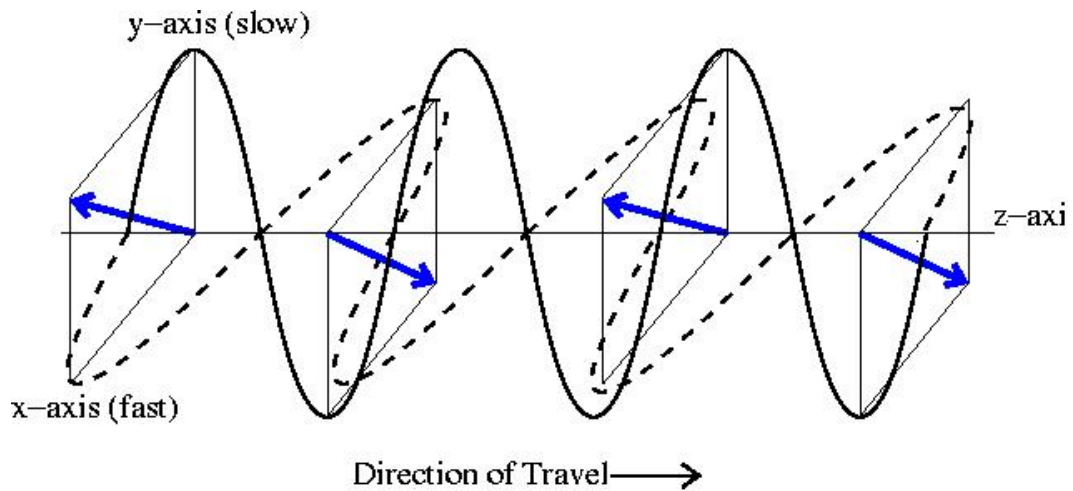
$$v = c / n, \quad (2.11)$$

where  $c$  is the speed of light in a vacuum and  $n$  is the effective refractive index.

Retarders operate by effectively vectorially decomposing the incident light into two orthogonal linearly polarized components, one parallel to the fast axis and the other parallel to the slow axis. Light traveling parallel to the slow axis experiences a higher index of refraction and, therefore, travels with a slower velocity. This light is thus delayed (or retarded) when compared to the light that is traveling parallel to the fast axis. This phase shift between the two orthogonal components produces a change in the output polarization.

An example of how retarders operate is shown in Figures 2.8 & 2.9. Linearly polarized light is input into a retarder at an angle of  $45^\circ$  to the fast axis (x-axis). The input

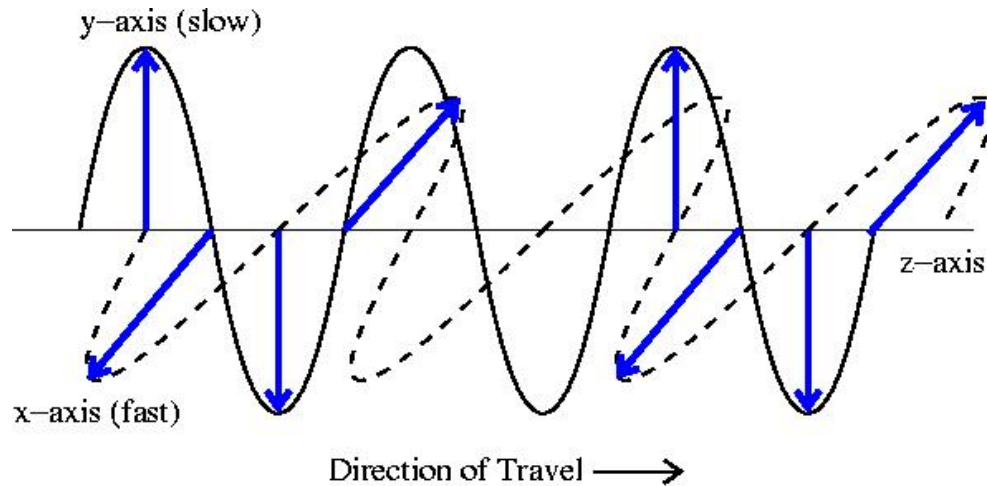
light is decomposed into two orthogonal components (dark solid wave and dashed wave), one parallel to the fast axes (x-axis) and the other parallel to the slow axes (y-axis) of the optic. If one traces the path of the head of the vector-sum of the two orthogonal components (blue vector) as the light wave moves along the z-axis from left to right, one will see that the vector oscillates from upper-left to lower-right, indicating light linearly polarized  $45^\circ$  to the fast-axis (Figure 2.8).



**Figure 2.8** Orthogonal decomposition of linearly polarized light.

In this example, the retarder induces a phase shift of  $90^\circ$  to the component that is parallel to the slow axis (the dark solid wave) as shown in Figure 2.9. If one now traces the path of the head of the vector summation of the two components (blue vector), as viewed from the direction in which the light is traveling, one will see that the vector is rotating counter-clockwise, indicating circularly polarized light.





**Figure 2.9** Orthogonal decomposition of circularly polarized light.

The retardance of an optic, in waves, is given by:

$$\delta = \beta t \lambda, \quad (2.12)$$

where  $\beta = (n_e - n_o)$  is the birefringence of the optical material and  $\lambda$  and  $t$  are, respectively, the wavelength of light and the thickness of the birefringent material in similar units. In the above example, the light that was parallel to the slow axis was delayed by  $90^\circ$  or  $1/4$ -wave. Thus the optic would be referred to as a  $1/4$ -wave plate.

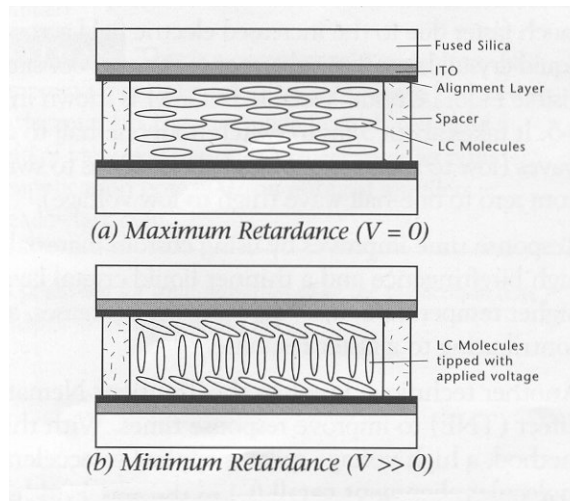
### 2.6.3 Nematic Liquid Crystal Variable Retarders

The Nematic Liquid Crystal Variable Retarders (LCVR) used for the DVMG were purchased from Meadowlark Optics in Frederick, CO. These variable retarders are continuously tunable wave plates, whose retardance is a function of an applied voltage. The units that are used for the DVMG were specifically designed to operate in the visible portion of the spectrum (400 – 700 nm) and have a transmission, at 610 nm (the operating wavelength of the DVMG), of approximately 96%. The entire unit is contained in an

aluminum housing that is 7.62 cm (3 inches) in diameter, 2.54 cm (1 inch) thick and has a clear aperture of 4.32 cm (1.7 inches) (labeled D in Appendix B).

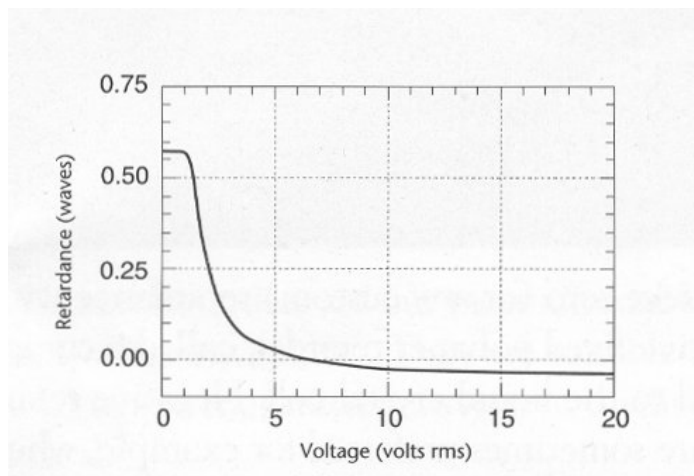
The operating temperature range of the LCVR is from 10° C (50° F) to 50° C (120° F). The retardance of the LCVR, at a given applied voltage, is a function of temperature. From an environmental temperature point of view, the telescope and much of the accompanying instrumentation, including the DVMG, are exposed to outside temperatures as discussed in Section 2.2. These temperatures can typically range from 35° C (95° F) in the summer to -12° C (10° F) in the winter. Therefore, the LCVR must be contained in a temperature controlled housing. This housing maintains a constant temperature, within the operating range of the LCVR, so that the retardance is only a function of applied voltage. The details of the temperature controller are discussed in Section 2.6.7.

The operating principle of the LCVR is the following. Two optically flat fused silica windows are spaced a few microns apart, forming a cavity. The windows are coated with a thin layer of transparent conductive indium-tin-oxide (ITO) forming two parallel electrodes. The ITO coating is specifically designed for maximum transmission in the visible and near-infra-red portion of the spectrum. The cavity is filled with a birefringent nematic liquid crystal material. A characteristic of the nematic liquid crystal material is that, on average, the molecules are aligned with their long axes parallel to each other but with their centers randomly distributed. With no voltage applied, the long axes of the molecules are parallel to the optical windows. In this state, the optic produces maximum retardance (Figure 2.10A, courtesy [45]).



**Figure 2.10** Schematic & operation of the nematic liquid crystal variable retarders.

When a voltage is applied, the molecules begin to turn away from being parallel to the optical windows, reducing the retardance of the optic. When the long axes of the molecules are perpendicular to the windows the minimum retardance is achieved (Figure 2.10B). As indicated in the figure, the molecules at the surface of the windows are unable to rotate freely. This causes a residual non-zero retardance even at maximum voltage (20 volts). However, zero retardance is achieved with the introduction of an additional layer of birefringent material, with a fixed negative retardance, onto the optical window during the manufacturing process. Thus, all values of retardance, between zero and  $\frac{1}{2}\lambda$  of light can be achieved by setting the applied voltage to the appropriate value (Figure 2.11, courtesy [45]).

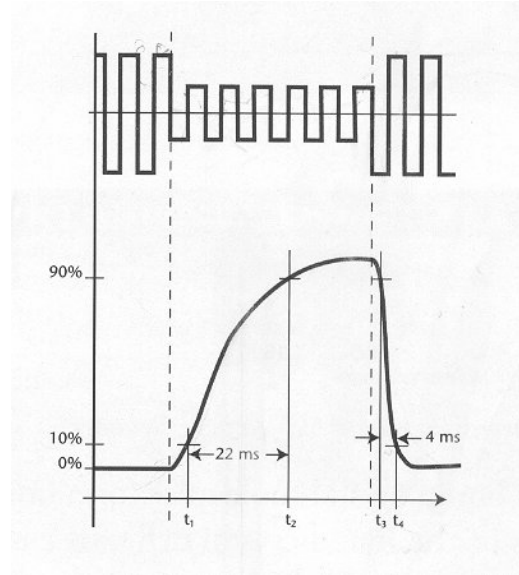


**Figure 2.11** Example of retardance vs. input voltage for the LCVR.

The retardance of the LCVR is set via an input electrical control signal. This control signal must be a 2 kHz square wave, of adjustable amplitude. This is most easily achieved using Meadowlark's model D2040 Liquid Crystal Digital Interface (labeled J in Appendix B). This unit receives a value, between 0 and 20000, via the parallel port of the instrument control computer, and creates a 2 kHz square wave whose amplitude, in millivolts, is determined by the input value. Therefore, the instrument control software can easily and quickly change the retardance of the LCVR to the required value.

The response time of the LCVR (the time from when the applied voltage is changed to the time the desired retardance is actually achieved) is a function of several parameters. Thickness of the birefringent material, viscosity and temperature all effect the response time. In addition to these parameters, the response time is also a function of the direction of the change in the retardance. If the retardance is increasing (the birefringent molecules are rotating towards their relaxed position as in Figure 2.10A) the response time is determined by the mechanical relaxation time of the molecules. If the retardance is decreasing (the birefringent molecules are rotating away from their relaxed

position, as in Figure 2.10B), the response time is determined by the response of the molecules to the applied electric field. Figure 2.12 (courtesy [45]) shows typical response times of the LCVR for both increasing and decreasing retardance. As can be seen, time required to change from low retardance to high retardance is much greater than the time required to change from high retardance to low retardance.



**Figure 2.12** Typical response time of a LCVR.

#### 2.6.4 Ferroelectric Variable Retarders

The Ferroelectric Liquid Crystal (FLC) adjustable waveplate used for the DVMG was purchased from Displaytech in Boulder, CO. This adjustable retarder has a fast axis (see Section 2.6.2) can be set to one of two angles of rotation separated by  $45^\circ$  by an applied voltage. The unit that is used for the DVMG was specifically designed to operate as a  $\frac{1}{2}$ - $\lambda$  plate at 610 nm (the operating wavelength of the DVMG) and has a transmission of approximately 80%. The entire unit is contained in an aluminum housing that is 3.81 cm (1.5 inches) in diameter, 1.27 cm ( $\frac{1}{2}$  inch) thick and has a clear aperture of 2.54 cm (1 inch).

Briefly, the operating principle of the FLC is the following. The FLC unit contains a thin layer of FLC material, which is composed of long rod-shaped molecules, sandwiched between two parallel optical windows. The windows are coated with a thin coating of transparent material forming electrodes. The long axes of the FLC molecules tend to orient themselves parallel to each other, defining the fast birefringent axis of the optic. The applied electric field produces a torque causing the molecules to reorient themselves to one of the two angles of rotation, thus defining the two angles of the fast axis of the  $\frac{1}{2}\lambda$  plate.

The signal which determines which of the two angles of rotation the FLC will be driven to is provided by the Displaytech DR95 driver unit. This driver unit is controlled by a simple TTL signal where a logical 0 input, from the instrument control computer, indicates an angle of rotation of  $0^\circ$  while a logical 1 input indicates an angle of rotation of  $45^\circ$ . In addition to the simplicity of controlling the FLC via the Displaytech driver, there is the added advantage of safety. The signal provided to the FLC by the driver is simply  $\pm 5$  volts DC, depending on which state the FLC is to be driven to, while the KDP crystal, which was replaced by the FLC crystal upon its failure in 1996, required a 5 kV drive signal.

The response time of the FLC is much faster than that of the LCVR. The typical time required to switch from one state to the other is on the order of 100  $\mu$ Sec. Since the typical exposure time of a single image is 120 mS and the response time of the LCVR is on the order of a few tens of mS this is considered to be instantaneous when considering the operation of the DVMG.

The FLC is designed to operate at 21° C (70° F). Since the telescope and its accompanying instrumentation are exposed to the outside environmental temperature (as discussed in detail in Section 2.2) the FLC unit must also be contained in a temperature controlled housing.

### **2.6.5 Three Crystal Optical Layout**

The rotation and retardance values for the two LCVRs and the FLC that will select the Stokes components (I,  $Q_H$ ,  $Q_V$ ,  $U_A$ ,  $U_B$ ,  $V_R$  &  $V_L$ ) can be found in Tables 2.1 & 2.2, respectively. Note that the calibration of the retardances and the rotation angles of the two Liquid Crystal Variable Retarders (LCVR<sub>1</sub> & LCVR<sub>2</sub> in Figure 2.1) and the rotation angle of the Ferroelectric Liquid Crystal (FLC in Figure 2.1) will be discussed in Section in 2.6.6.1.

Also note that the I image is simply a 610.3 nm intensitygram and is not involved in the determination of the solar magnetic field. The intensitygram is used as the corresponding “white-light” image to the magnetograms that are generated using the Stokes-U, Q and V images and is presented here for completeness.

**Table 2.1** Polarization Crystal Rotation Angles

Stokes Component	LCVR <sub>1</sub> *	LCVR <sub>2</sub> *	FLC
I	0°	45°	0°
Q <sub>H</sub> Q <sub>V</sub>	0°	45°	0° 45°
U <sub>A</sub> U <sub>B</sub>	0°	45°	0° 45°
V <sub>R</sub> V <sub>L</sub>	0°	45°	0° 45°

\* - Note that the LCVR are variable retarders and do not change rotation.



**Table 2.2** Polarization Crystal Retardance Values

Stokes Element	LCVR <sub>1</sub>	LCVR <sub>2</sub>	FLC <sup>ψ</sup>
I	0-λ	0-λ	½-λ
Q	¼-λ	¼-λ	½-λ
U	0-λ	0-λ	½-λ
V	0-λ	¼-λ	½-λ

ψ - Note that the FLC is a fixed ½-λ plate that has two rotation values.

As an example, exactly how the polarization optics isolate the  $V_R$  component using Mueller matrices, will be reviewed. Similar examples can be performed for the other five polarization components of the Stokes vector ( $Q_H$ ,  $Q_V$ ,  $U_A$ ,  $U_B$ , &  $V_L$ ).

As was discussed in Section 2.8.1, the Mueller matrix for the light output from any series of retarders is:

$$S_1 = M_n M_{n-1} \dots M_1 M_2 S_0, \quad (2.13)$$

where  $S_1$  represents the output light,  $S_0$  represents the input light and  $M_x$  represents the Mueller matrices of each optic, in order. In the case of the DVMG:

$$S_1 = M_3 M_2 M_1 S_0 \quad (2.14)$$

where  $M_1$  and  $M_2$  represent the Mueller matrices of LCVR<sub>1</sub> & LCVR<sub>2</sub>, respectively and  $M_3$  represents the Mueller matrix of the FLC.

In all cases,  $S_0$ , which represents the input light ( $Q_{H0}$ ,  $Q_{V0}$ ,  $U_{A0}$ ,  $U_{B0}$ ,  $V_{R0}$  &  $V_{L0}$ ), is:

$$Q_{H0} = \begin{vmatrix} 1 \\ 1 \\ 0 \\ 0 \end{vmatrix}, \quad Q_{V0} = \begin{vmatrix} 1 \\ -1 \\ 0 \\ 0 \end{vmatrix}, \quad (2.15, 2.16)$$

$$U_{A0} = \begin{vmatrix} 1 \\ 0 \\ 1 \\ 0 \end{vmatrix}, \quad U_{B0} = \begin{vmatrix} 1 \\ 0 \\ -1 \\ 0 \end{vmatrix}, \quad (2.17, 2.18)$$

$$V_{R0} = \begin{vmatrix} 1 \\ 0 \\ 0 \\ 1 \end{vmatrix}, \quad V_{L0} = \begin{vmatrix} 1 \\ 0 \\ 0 \\ -1 \end{vmatrix}. \quad (2.19, 2.20)$$

When isolating the  $V_R$  component:

$$M_1 = \begin{vmatrix} 1 & 0 & 0 & 0 \\ 0 & 1 & 0 & 0 \\ 0 & 0 & 1 & 0 \\ 0 & 0 & 0 & 1 \end{vmatrix}, \quad M_2 = \begin{vmatrix} 1 & 0 & 0 & 0 \\ 0 & 0 & 0 & -1 \\ 0 & 0 & 1 & 0 \\ 0 & 1 & 0 & 0 \end{vmatrix}. \quad (2.21, 2.22)$$

$$\& M_3 = \begin{vmatrix} 1 & 0 & 0 & 0 \\ 0 & 1 & 0 & 0 \\ 0 & 0 & -1 & 0 \\ 0 & 0 & 0 & -1 \end{vmatrix}. \quad (2.23)$$

Solving Equation 2.14, where  $S_1$  represents the six output Stokes components ( $Q_{H0}$ ,  $Q_{V0}$ ,  $U_{A0}$ ,  $U_{B0}$ ,  $V_{R0}$  &  $V_{L0}$ ):

$$Q_{H1} = \begin{vmatrix} 1 \\ 0 \\ 0 \\ 1 \end{vmatrix}, \quad Q_{V1} = \begin{vmatrix} 1 \\ 0 \\ 0 \\ -1 \end{vmatrix}, \quad (2.24, 2.25)$$

$$U_{A1} = \begin{vmatrix} 1 \\ 0 \\ -1 \\ 0 \end{vmatrix}, \quad U_{B1} = \begin{vmatrix} 1 \\ 0 \\ 1 \\ 0 \end{vmatrix}, \quad (2.26, 2.27)$$

$$V_{R1} = \begin{vmatrix} 1 \\ -1 \\ 0 \\ 0 \end{vmatrix} \quad \& \quad V_{L1} = \begin{vmatrix} 1 \\ 1 \\ 0 \\ 0 \end{vmatrix}. \quad (2.28, 2.29)$$

Note that  $V_{R1}$  is the Mueller matrix for linearly polarized light in the vertical direction (parallel with the isolation linear polarizer) and will thus pass through the isolation linear polarizer while  $V_{L1}$  has been completely blocked. The other four components are attenuated by  $\frac{1}{2}$ . Thus, the image taken with the CCD camera in this example is of the  $V_R$  component of the Stokes vector. The accompanying components of the Stokes vector ( $Q_H$ ,  $Q_V$ ,  $U_A$ ,  $U_B$ , &  $V_L$ ) are subsequently acquired. The details of the actual creation of magnetograms from the Stokes components is presented in Chapter 3.

### 2.6.6 LCVR and FLC Calibration

The rotation angle of the two nematic liquid crystal variable retarders (LCVR) (the Stokes parameter selectors) and the single ferroelectric crystal (FLC) (the component selector) must be calibrated to the optical axis of the instrument. These three optics are attached to the optical bench of the instrument on mounts, which can be adjusted in rotation angle. The optical axis of the instrument, while ultimately arbitrary, is defined by the input linear polarizer of the birefringent filter, which is also used to isolate the particular Stokes parameter that is to be imaged, as discussed at the beginning of Chapter 2. The angle of this linear polarizer is rotated  $22^\circ$  CCW from the vertical (when looking up the optical axis from the CCD camera). Also, the voltages that determine the retardance values for each LCVR must be set. Calibrating both the rotation angle of the optics and the voltages for the retardances must be done for each optic independently and

by experiment. With practice and a cloudless sky, the entire process can be accomplished by two people, one operating the instrument control computer and the other at the telescope adjusting the rotation of the crystals, in a few hours. The order in which the three polarization optics are calibrated is ultimately irrelevant. Therefore, the calibration procedure will be discussed in the order that the optics are mounted in the light path.

The voltages for each LCVR must be easy to set and change during the calibration procedure. To accomplish this task, a program, provided by the manufacturer, which allows the user to manually set the LCVR voltages is used. This program communicates with the Liquid Crystal Digital Interface via the parallel port. The user can simply input the desired voltage, in milli-volts, and the digital interface produces the required 20 kHz square wave with the desired amplitude.

As discussed in Section 2.6.5, the fast axis of LCVR<sub>1</sub> must be calibrated to 0° and the fast axis of LCVR<sub>2</sub> must be calibrated to 45°. Also, one state of the fast axis of the FLC must be calibrated to 0°. Since the rotation angle of the two states of the FLC are, by design, separated by 45°, only the angle of one of the two states need be calibrated. The voltages which set each LCVR to both 0-λ and ¼-λ must also be determined.

**2.6.6.1 Calibration of LCVR<sub>1</sub> and LCVR<sub>2</sub>.**      Goal - Calibrate the rotation angle of LCVR<sub>1</sub> to 0° and determine the voltages that will produce 0-λ and ¼-λ of retardance.

Step 1) Remove all of the polarization optics from the optical bench of the DVMG (except the input linear polarizer of the birefringent filter, the angle of which defines the optical axis of the instrument) (Figure 2.13).

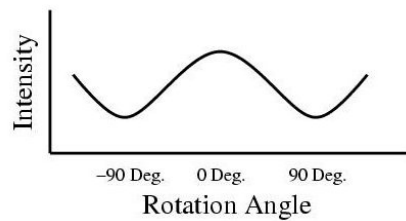


**Figure 2.13** Optical diagram of Step1 of calibrating LCVR<sub>1</sub>

Step 2) Align a linear polarizer, mounted at the front of the instrument (LP<sub>1</sub> in Figure 2.14), to be parallel with LP<sub>2</sub> (Figure 2.14). This is accomplished by slowly rotating LP<sub>1</sub> while monitoring the brightness of the image with the CCD camera mounted on the instrument. LP<sub>1</sub> is rotated until the brightness of the image is at a maximum (Figure 2.15). The fast axis of LP<sub>1</sub> is now oriented to 0°.

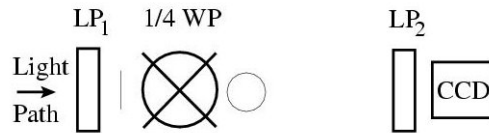


**Figure 2.14** Optical diagram of Step 2 of calibrating LCVR<sub>1</sub>.



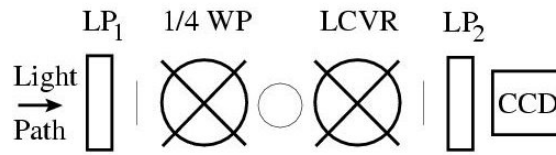
**Figure 2.15** Light intensity at the CCD vs. rotation angle of LP<sub>1</sub> for Step 2.

Step 3) Mount a fixed  $\frac{1}{4}\lambda$  plate (QWP in Figure 2.16) immediately after  $LP_1$  and calibrate its rotation angle to  $45^\circ$ . This is accomplished by slowly rotating the fixed  $\frac{1}{4}\lambda$  plate, while again monitoring the brightness of the image with the CCD camera, until the brightness of the image is at a minimum. When the rotation angle of the QWP is at  $45^\circ$  the QWP will convert the input linear polarization into circular polarization which will be attenuated by  $\frac{1}{2}$  by  $LP_1$ . It will become clear as the calibration procedure continues as to why a linear polarizer  $\frac{1}{4}\lambda$  plate combination need be used to produce circular polarization instead of an individual circular polarizer. The linear polarizer and the  $\frac{1}{4}\lambda$  plate are used only to calibrate the rotation angle of the two LCVRs and the FLC and the retardances of the two LCVRs. After the calibration procedure is complete they are removed from the instrument.

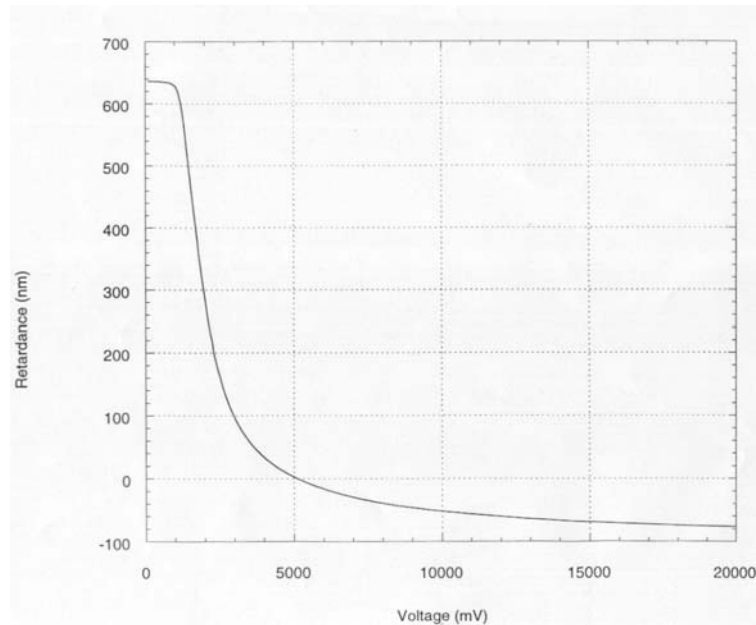


**Figure 2.16** Optical diagram of Step 3 of calibrating  $LCVR_1$ .

Step 4)  $LCVR_1$  is mounted in the light path between the  $LP_1$  / QWP set and  $LP_2$ . Using the retardance vs. voltage plot for that particular LCVR, which was supplied by the manufacturer shown in Figure 2.18, the retardance of  $LCVR_1$  is set to approximately  $\frac{1}{4}\lambda$  by the instrument control computer.



**Figure 2.17** Optical diagram of Step 4 of calibrating LCVR<sub>1</sub>.

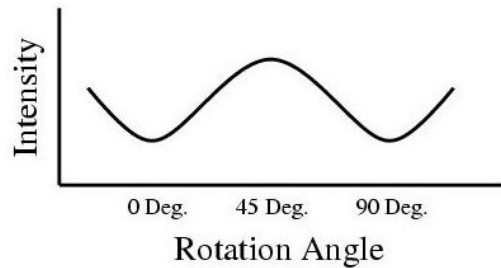


**Figure 2.18** Typical retardance vs. voltage plot for a LCVR.

Step 5) LCVR<sub>1</sub> is slowly rotated while the brightness of the image is monitored by the CCD camera. A  $\frac{1}{4}\lambda$  plate will convert circular polarization into linear polarization that is oriented  $45^\circ$  to its fast axis. Therefore, LCVR<sub>1</sub> is rotated until the brightness of the

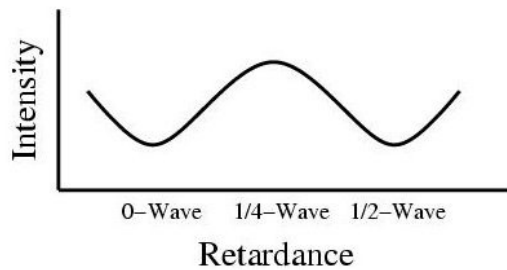


image reaches a maximum. The rotation angle of the fast axis of LCVR<sub>1</sub> is approximately 45° (Figure 2.19).



**Figure 2.19** Light intensity at the CCD vs. rotation angle of LCVR<sub>1</sub> for Step 5.

Step 6) The retardance of LCVR<sub>1</sub> is manually adjusted, via the instrument control computer, until the brightness of the image is again at a maximum (Figure 2.20).



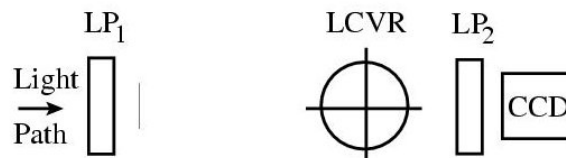
**Figure 2.20** Light intensity at the CCD vs. retardance of LCVR<sub>1</sub> for Step 6.

Step 7) Repeat steps 3 and 4 until there is no change in both the rotation angle and retardance settings. This typically takes an additional two iterations.

Step 8) Remove the  $\frac{1}{4}\lambda$  plate.

Step 9) Adjust the retardance of LCVR<sub>1</sub> until the brightness of the image is at the maximum. When the retardance of LCVR<sub>1</sub> is set to  $0-\lambda$ , the input vertical linear polarization will pass through LCVR<sub>1</sub> unchanged will be unattenuated by LP<sub>2</sub>. When the retardance deviates from  $0-\lambda$  the input vertical linear polarization will be converted to elliptical polarization which will be at least partly attenuated by LP<sub>2</sub>.

Step 10) Rotate LCVR<sub>1</sub> 45°.



**Figure 2.21** Optical diagram of Steps 9 & 10 of calibrating LCVR<sub>1</sub>.

The rotation angle of LCVR<sub>1</sub> is now calibrated to  $0^\circ$  and the voltages which will set the retardances to  $0-\lambda$  and  $\frac{1}{4}-\lambda$  have been determined.

The procedure for calibrating the rotation angle of the fast axis and the retardance voltages for LCVR<sub>2</sub> is the same as for LCVR<sub>1</sub> except step 10 is omitted. The rotation angle of LCVR<sub>2</sub> would then be calibrated to  $45^\circ$ .

It is required that each individual iteration, in calibrating either the rotation angle of a particular optic or the voltage for a particular retardance, be accomplished as fast as possible. The Sun is continuously either rising or setting. As it does so, the amount of air that the Sunlight is passing through, on its way to the telescope, is either continuously increasing (when the Sun is setting) or decreasing (when the Sun is rising). This causes the total extinction of the atmosphere to continuously change and, thus, the total apparent

brightness of the Sun. This effect can easily be seen by the CCD camera of the instrument in just a few minutes. A way to minimize this effect is to perform the calibration centered on local noon when the altitude of the Sun changes most slowly.

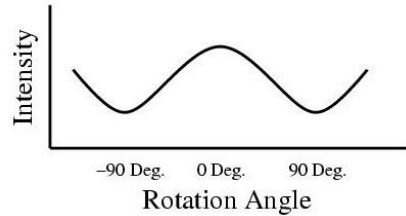
**2.6.6.2 Calibration of FLC.**            Goal - Calibrate the rotation angle of the FLC to  $0^\circ$  and  $45^\circ$ .

The FLC is much easier to calibrate than are the LCVRs. The FLC is a fixed  $\frac{1}{2} - \lambda$  plate whose fast axis can be rotated to either of two rotation angles which are separated by  $45^\circ$ . Since the two states are, by design, separated by  $45^\circ$  only the rotation angle of one of the states need be calibrated. And, since the retardance of the FLC is fixed at  $\frac{1}{2} - \lambda$  there are no retardance voltages to calibrate.

Step 1) Remove all of the polarization optics and align a linear polarizer ( $LP_1$  in Figure 2.14) to be parallel with the entrance linear polarizer of the birefringent filter ( $LP_2$  in Figure 2.14, as in Steps 1 & 2 of the previous section).

Step 2) Rotate  $LP_1$   $90^\circ$ , so it is crossed with  $LP_2$ .

Step 3) Mount the FLC between the crossed linear polarizers and set the FLC so it is at its  $45^\circ$  rotation. When the fast axis of a  $\frac{1}{2} - \lambda$  plate is oriented  $45^\circ$  to the axis of linear polarized light, the linear polarization will be rotated by  $90^\circ$ . Rotate the FLC until the brightness of the image is at a maximum. The FLC is now aligned  $0^\circ$  and  $45^\circ$  to the optical axis of the instrument.



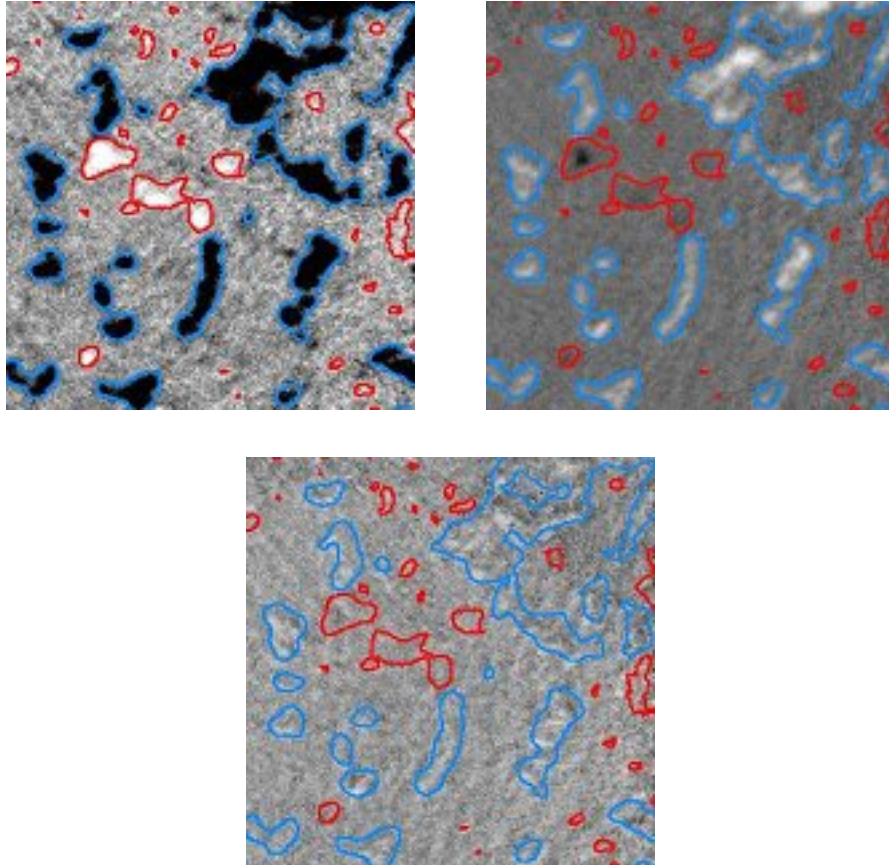
**Figure 2.22** Light intensity at the CCD vs. rotation angle of the FLC for Step 3.

### 2.6.6.3 Check Cross-talk and Vectors of a Round sunspot Near the Center of the Solar Disk.

After all three polarization optics have been calibrated, they are installed on the optical bench of the 25 cm vacuum-refractor. There are two additional steps in the calibration of the polarization optics. First, actual Stokes parameter images are acquired and visually inspected for cross-talk. Second, the instrument is tested on a simple round sunspot that is located near the center of the solar disk, when such a feature is available on the Sun. Both of these checks of the data room the instrument will test whether the polarization optics have been calibrated properly and operating as expected.

Cross-talk will be discussed, in detail, in Section 3.3.5. Briefly, cross-talk is specifically defined by the contamination of the Stokes-Q and/or U parameters by features that should only appear in the Stokes-V parameter. That is, longitudinal magnetic fields that appear in the transverse measurements. An example of cross-talk is shown in Figure 2.23. The upper-left image is a Stokes-V parameter (longitudinal magnetogram), of an area of quiet-Sun (where only weak magnetic fields are present) near the center of the solar disk, the upper-right image is a Stokes-Q parameter (one of the components of the transverse magnetic field measurement), for example, that is contaminated with cross-talk and the bottom image a Stokes-Q parameter where the cross-talk has been corrected (correction of cross-talk will be discussed in Section 3.3.5.2). A Stokes-U parameter with

cross-talk would look similar. The contours levels have been set to  $\pm 20$  Gauss. The contours in the center and right images are the same as those that have been drawn in the left image to help identify the cross-talk features. The field of view is  $150 \times 150$  arc-sec.



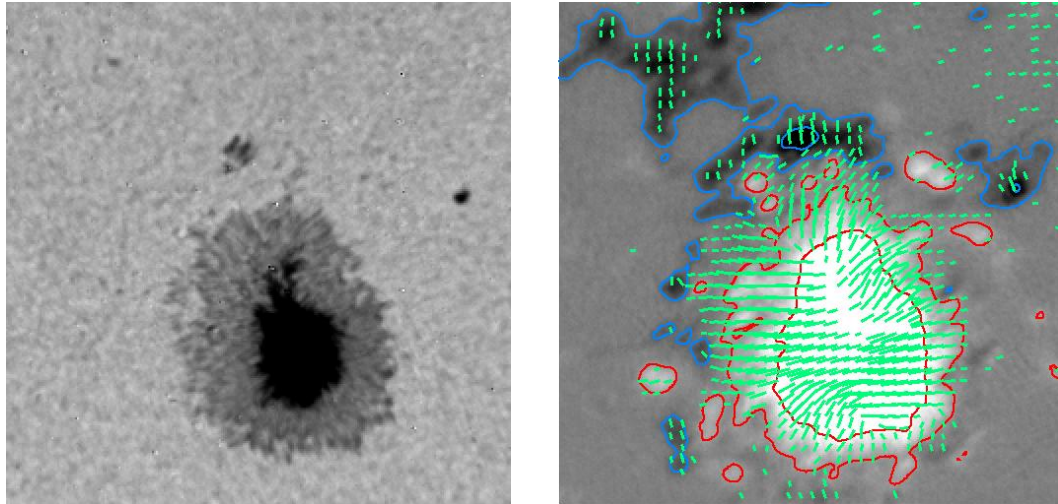
**Figure 2.23** Example of cross talk in a Stokes-Q image.

Ideally, the Stokes-Q & U parameters should be basically featureless when imaging regions of quiet-Sun near the center of the solar disk (this will be explained in greater detail in Section 3.3.5). One can see in the upper-right image in Figure 2.23 that there are many features in the uncorrected Stokes-Q parameter that are correlated with features in the Stokes-V parameter. If cross-talk features are present after the polarization

optics have been calibrated, the rotation angle and/or retardance voltages can be adjusted slightly until the cross-talk is minimized. It should be noted that the cross-talk in Figure 2.23 was intentionally exaggerated so the cross-talk features might be more easily seen in the Stokes-Q parameter.

The second, and final, way to check if the rotation angle and the retardance values of the polarization optics have been properly calibrated is to generate vector magnetograms of a simple round sunspot which is located near the center of the solar disk (the details of how to generate vector magnetograms from the Stokes-Q, U & V parameters will be discussed in detail in Chapter 3).

Theory and experience tells us that the transverse magnetic field of a simple round sunspot, when viewed near the center of the solar disk (to avoid projection effects) should be radial. Therefore, acquiring data in this ideal case provides an excellent method to test whether the instrument is working properly. A vector magnetogram of a simple round sunspot is shown in Figure 2.24. The left image is a 610.3 nm intensitygram of NOAA 10306 on 03Mar12, while the right image is the corresponding vector magnetogram. The field of view is 150 x 150 arc-sec. One can see that the direction of the transverse magnetic field (as represented by the green arrows) of the primary sunspot is generally radial, indicating that the instrument is functioning properly. Testing the magnetograph on a simple round sunspot will again be address in Section 3.8.1.



**Figure 2.24** Sample vector magnetogram of a simple round sunspot.

### **2.6.7 LCVR Temperature Control and LCVR Mounting**

As stated in Section 2.6.3, the retardance of the nematic Liquid Crystal Variable Retarders is both a function of temperature and applied voltage. To accurately adjust the retardance of the LCVRs by controlling only the voltage, the temperature must be stabilized. The operating temperature range of the LCVR is from 10° C (50° F) and 50° C (120° F). As long as the LCVR is held within these limits, it ultimately does not matter at which temperature the unit operated.

Since it is quite common for the ambient temperature of the telescope to be below 10° C (Section 2.2), the LCVRs must be heated to avoid damage. Also, since it is quite rare that the ambient temperature of the telescope is ever above 32° C (90° F), the temperature of the LCVRs can be stabilized at this value, as this is well within the operating temperature range. This makes the temperature control problem relatively simple since the controller will only have to heat the unit and never cool it.

The controller selected to maintain a constant temperature of the LCVRs is the CN76000 Microprocessor-Based Temperature/Process Controller (labeled A in Appendix B) from Omega Engineering, Inc. Briefly, the CN76000 is an auto-tune PID single-input / single-output controller (see Appendix C for additional information on the specifications of the CN76000). The unit was mounted in a plastic housing, attached to the telescope near the LCVRs, which contains the required circuit logistics (switches, fuses, etc.) (labeled B in Appendix B).

The temperature sensor used is a precision  $100\Omega$  Pt RTD-850 probe from Omega (C in Appendix B). This temperature probe was chosen for the following two reasons. First, it will provide  $0.1^\circ\text{C}$  resolution when used with the CN76000 controller. Second, the probe is built into a  $\frac{1}{4}$ " stainless-steel hex-head housing with #8-32 threads (resembling a small screw). This conveniently threads into the #8-32 tapped hole in the aluminum housing of the LCVR (D in Appendix B), thus, with the addition of some thermal compound, assures a good mechanical and thermal coupling between the housing and the temperature sensor (see Appendix D for additional information on the  $100\Omega$  Pt RTD-850 temperature probe).

To apply heat to the aluminum housing a flexible silicon rubber fiberglass insulated heater from Omega is used (E in Appendix B). These heaters are available in various sizes. The heater chosen ( $1'' \times 10''$ ) fits around the circumference of the aluminum housing, thus providing uniform heating. With a maximum of 25 Watts of heat dissipation, this heater is more than adequate to keep the LCVR at the desired temperature (the heating duty cycle is typically on the order of 10% even on the coldest



days). (See Appendix E for additional information on the flexible silicon rubber fiberglass insulated heater.)

The aluminum housing of the LCVR is enclosed in an insulating plastic container (F & G in Appendix B) that was machined to fit the LCVR housing and heater combination. This plastic container attaches on to a rotator which mounts on to the optical bench of the 25 cm vacuum-refractor, thus allowing the rotation of the LCVRs to be calibrated to their specific requirements (Section 2.6.6). The apertures of the insulating plastic container are covered with optical windows, which allows light to pass through the LCVR while maintaining a thermal barrier between the LCVR and the ambient air.

## 2.7 The Birefringent Filter

The details of the construction of a birefringent filter, in general, can be found in [46] & [47]. Briefly, the operation of a birefringent filter depends on the transmission of light through a birefringent material, such as Calcite or Quartz, which is sandwiched between parallel linear polarizers. This set of three optics represents an element of the filter. In such an element, the transmission of light will be a function of wavelength, temperature and the birefringent index, which is a characteristic of the birefringent material, and the thickness of the birefringent material. The transmission through a birefringent element is then:

$$\tau = \text{COS}^2 ( ( \mu (\lambda, T) d \pi ) / \lambda ) \quad (2.30)$$

where  $\tau$  is the transmission,  $\mu$  is the birefringent index,  $\lambda$  is the wavelength of light,  $T$  is the temperature and  $d$  is the thickness of the birefringent material. In an actual

birefringent element, the birefringent material with the desired birefringent index is chosen and the birefringent optic is polished to the appropriate thickness. The temperature of the element is carefully held at the design temperature by a temperature controller. The transmission of an actual birefringent element is a function of wavelength only. The transmission of a birefringent element can be visualized by a sine-wave where the x-axis is wavelength, the y-axis is the percent transmission and the frequency of the plotted curve is a function of the thickness of the birefringent element (a thicker birefringent element will produce an output sine-wave of higher frequency).

Typically, a birefringent filter consists of a series of elements, where the thickness of the birefringent optic in each subsequent element is twice that of the previous element. Thus, the output of a birefringent filter is the superposition of the outputs from each element and can be determined by:

$$\tau = \text{COS}^2 \left( \left( \mu d_1 \pi \right) / \lambda \right) \text{COS}^2 \left( \left( \mu d_2 \pi \right) / \lambda \right) \dots \text{COS}^2 \left( \left( \mu d_N \pi \right) / \lambda \right) \quad (2.31)$$

where  $d_1$  is the thickness of the first element,  $d_2$  is the thickness of the second element and  $d_N$  is the thickness of the N-th element. The output of the filter can be represented by a set of narrow peaks (on the order of 0.025 nm) in transmission separated by a wide range of wavelengths (on the order of 5 nm) where the transmission is essentially zero, thus producing the so-called “picket-fence” output of the filter. The full-width-half-maximum (FWHM) of a birefringent filter (the band-width of each individual peak) is determined by the thickness of the thickest element and the free-spectral-range (FSR) (the wavelength difference between adjacent peaks) is determined by the thickness of the thinnest element. The specific characteristics of each element are designed such that one

of the output peaks falls at, or very near, the operating wavelength of the filter and the side-lobes are attenuated by the pre-filter, as discussed previously.

The birefringent filter used in the DVMG, constructed by Zeiss in Germany, was originally designed to work as an H $\alpha$  filter (656.3 nm) and has a band-width of 0.025 nm. It was converted to work as a Ca I filter at 610.3 nm by rotating the internal Calcite elements, while monitoring the light output on a spectrograph, until the primary band-pass was near the Ca I absorption line.

The wavelength of the pass-band can be adjusted, over a range of approximately 1.6 nm, by rotating the input polarizer by an external thumb-wheel (one knob unit equals  $3.7 \times 10^{-4}$  nm). It is important to be able to calibrate the wavelength of the pass band on the birefringent filter for two primary reasons. First, to compensate for shifts in the wavelength of the filter due to slight temperature changes. Second, to compensate for the Doppler shift in light due to the rotation of the Sun.

It is undesirable to heat the entire instrument, even though the entire instrument is nominally insulated from the environment by a protective cover. Any heat generated on, or near, the telescope will ultimately leak into the air surrounding the telescope, especially through the aluminum optical benches of the telescope structure, and possibly cause thermal air currents that will disturb the seeing. Thus, the filter is somewhat subject to the changing temperatures of the ambient air. Although the filter does have a thermostat and a temperature control system this system does not control the temperature of the filter perfectly, especially when there are large variations in the day to day temperature (see Section 2.2). Fortunately, the diurnal temperature variations of the ambient air are insufficient to noticeably effect the temperature of the filter. Thus, the

central wavelength of the birefringent filter tends to be stable over the course of a single observing session and, indeed, over the course of several weeks. Typically, the calibration of the birefringent filter need only be checked on the order of once a month, unless the day to day ambient air temperature changes by a value which is much greater than typical.

The central wavelength of the birefringent filter must also be calibrated to compensate for the Doppler effect due to the rotation of the Sun . The Sun rotates at approximately 2 km/sec at the equator. The Doppler shift can be calculated from:

$$v / \delta v = \lambda / \delta \lambda, \quad (2.32)$$

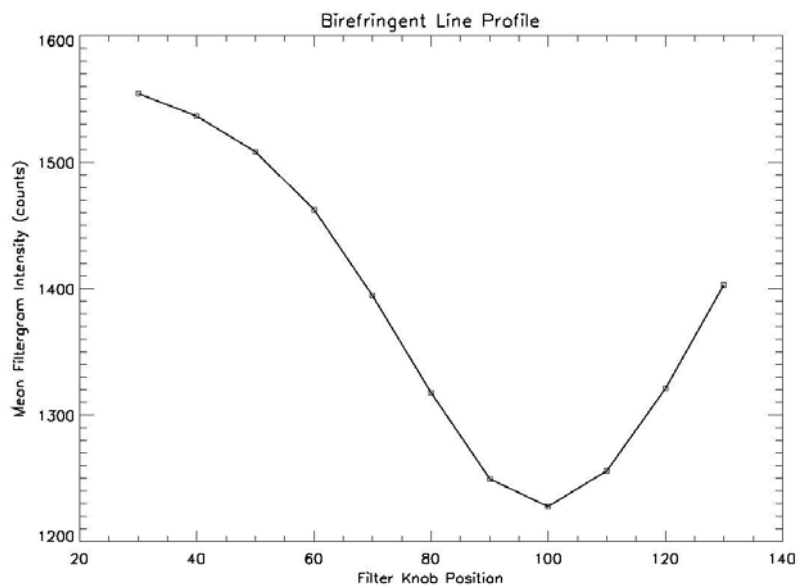
where  $v$  is the velocity and  $\lambda$  is the wavelength of light. Using  $3 \times 10^5$  km/sec as the velocity of light, 2 km/sec as the velocity of the Sun relative to the Earth at the solar equator at the solar limb and 610 nm as the wavelength of light translates to a Doppler shift of 0.004 nm (0.004 nm towards the blue end of the spectrum at the east limb where the solar rotation vector is towards the Earth and 0.004 nm toward the red end of the spectrum at the west limb where the solar rotation vector is away from the Earth). Since this Doppler shift is a significant fraction of the width of the Ca I absorption line (0.015 nm) it must be compensated for by tuning the central wavelength of the birefringent filter by the appropriate amount.

In theory, one must also compensate for the Doppler shift due to the rotation of the Earth (the light is shifted towards the blue end of the spectrum in the morning where the velocity vector is toward the Sun and the light is shifted toward the red end of the spectrum in the evening where the velocity vector is away from the Sun). At the equator,

the Earth rotates at approximately 0.5 km/sec which translates into a Doppler shift of 0.001 nm (the Doppler shift is proportionately less as the observing site approaches the poles). In practice, however, this need not be done. The Doppler shift imparted by the Sun's rotation dominates that imparted by the Earth's. Also, and more importantly, the band-pass of the birefringent filter (0.025 nm) is much greater than the width of the absorption line (0.015 nm). The amount of contamination of the magnetic signal does not noticeably change due to the changing Doppler shift of the absorption line during the course of the day so this effect can be, and is, ignored. However, if an instrument were to use a Fabry-Perot' filter to isolate the magnetically sensitive absorption line, which typically have a band-pass that is much more narrow than a birefringent filter, this effect may very well have to be compensated for.

From time to time, the birefringent filter must be calibrated to insure that it is tuned to the wing of the Ca I absorption line at 610.3 nm. Fortunately, calibrating the birefringent filter is quite simple and only takes a few minutes. The procedure is as follows. The telescope is pointed at or near the center of the solar disk where the line of sight velocity vector from solar rotation is essentially zero. The birefringent filter is tuned to the continuum just to the blue side of the Ca I absorption line using the external thumb-wheel. A single intensitygram is taken, noting both the position of the tuning thumb-wheel and the average intensity of the image which is displayed as the image is acquired, and saved to disk. The birefringent filter is tuned 0.004 nm (10 knob units) to the red end of the spectrum and another intensitygram is taken. This process is continued until the filter is tuned through the center of the absorption line (typically ~130 knob units). A simple program, written in Interactive Data Language (IDL), is run which plots

the filter knob units as the x-axis and the average intensity of the intensitygram images as the y-axis (Figure 2.25). The filter is then retuned to the knob unit corresponding to the center of the blue wing of the absorption line (typically 30 knob units or 0.012 nm). If magnetograms are to be taken near the solar limb the birefringent filter is then retuned towards the blue or red end of the spectrum, depending on which limb of the Sun is being imaged.

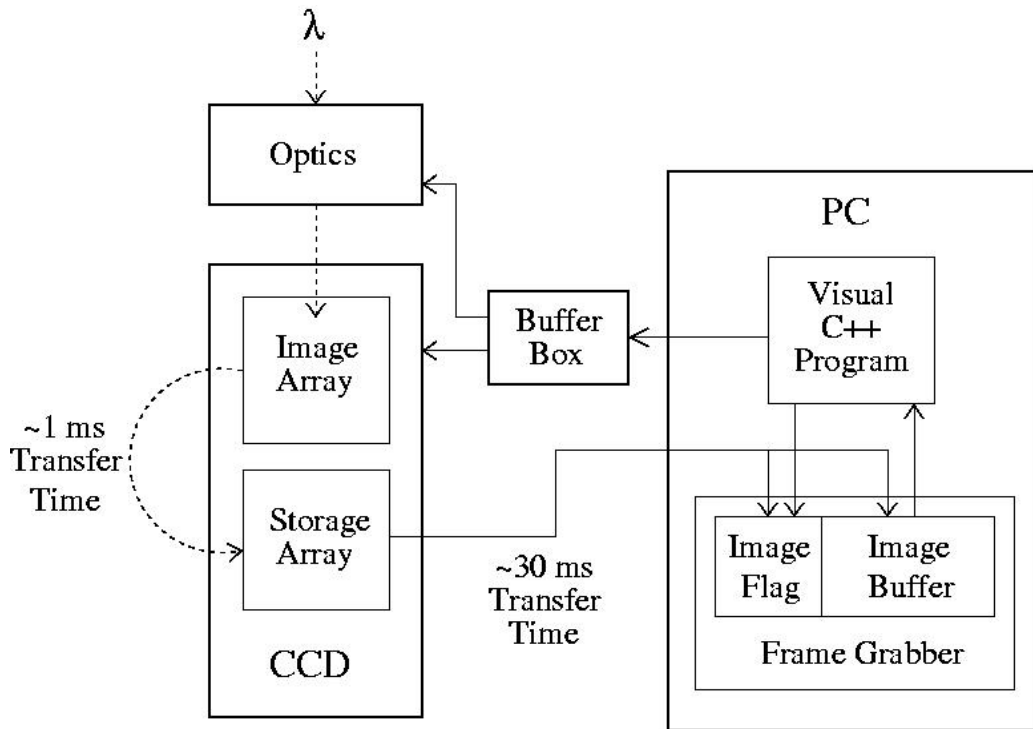


**Figure 2.25** Ca I line profile.

## 2.8 The CCD Camera, Image Capture Board & Instrument Control Program

A block diagram of how the CCD camera, image capture board and instrument control program interact is shown in Figure 2.26. The detector used for the DVMG is a Silicon Mountain Design (SMD) 1M15 frame transfer un-cooled CCD camera with a 1024 x 1024 pixel array, 12-bit digitization and a digital shutter. The camera was designed for high speed industrial machine vision applications (product inspection, crystallography,

etc...). The pixel size is  $14\mu \times 14\mu$  with a filling factor of 70%. The spectral response of the camera at 610 nm (the wavelength of the spectral line used by the DVMG) is 15%. The camera is capable of taking images at 15 frames-per-second at full 1024 x 1024 resolution or 30 frames-per-second when used in 2x2 binning. The images are transferred to the camera control computer via an RS422 data line to the image capture board controlled by the camera control program written in Visual C++.



**Figure 2.26** Block diagram of how the CCD camera, frame grabber board and instrument control program interact.

The SMD 1M15 CCD camera was designed to take images at a maximum rate of 30 Hz. To enable this high frame rate, the camera was equipped with a frame transfer CCD detector. Light is blocked, by an opaque coating, from a portion of each pixel, which is used to temporarily store the image while a subsequent image is being

integrated in the light sensitive portion of the pixels. In the case of the SMD 1M15 camera, the total opaque area is 30% of each pixel. At the end of each exposure, the image is transferred from the light sensitive portion of the pixels to the image storage portion of the pixels in ~1 ms. The image that is stored in the frame transfer portion of the array is then transferred to the frame grabber board at the same time that the next image is being integrated, thus allowing simultaneous image transfer and integration. Of course, blocking light from a portion of each pixel reduces the sensitivity of the camera. However, this reduction in sensitivity is a necessary tradeoff to achieve the fast frame rate of the camera.

In the case of the DVMG, the integration time is 120 ms (to allow enough time for the pixel wells to approximately fill when imaging near the center of the solar disk to take full advantage of the 12-bit capability of the camera) and the time to transfer an image from the camera to the image capture board is ~30 ms. When an image is successfully transferred from the camera to the image capture board, a “new image” flag is set which is continually polled by the Visual C++ instrument control program, after which the image is copied into the RAM of the instrument control computer. If the current image stored in the image capture board is not copied by the instrument control program before the next image is transferred from the camera, the current image in the image capture board will be overwritten.

#### CCD Camera - Binning

The camera can be either used in the full 1024 x 1024 pixel mode or a 2 x 2 binning mode. The binning mode electronically sums neighboring pixels on the chip to provide a net 512 x 512 pixel array, with four times the sensitivity of the non-binned chip, but with



$\frac{1}{2}$  the resolution. Due to the poor light throughput of the instrument, as discussed in Section 2.5, the DVMG is always used in the 2 x 2 binning mode. The optics of the telescope were designed to provide an image scale of 0.6 arc-sec / pixel which is a good compromise between telescope resolution, instrument light level and the size of a typical active region on the Sun.

### CCD Camera - Exposure Triggering Mode

The camera may be run in either free running or externally triggered modes. In the free running mode, the camera will simply take images at the rate it was programmed to via the RS232 serial line and upload the images to the image capture board. However, when part of the DVMG, the camera exposures must be synchronized with the states of the polarization crystals. Therefore, the camera must be used in the externally triggered mode. In this case, the camera is programmed, via the RS232 serial line, to accept a TTL pulse (provided by the DVMG control computer via trigger buffer box, Figures 2.2 & 2.26) which triggers the beginning of the exposure whose length was also programmed via the RS232 serial line when the instrument was initialized.

## **2.9 The Weak-Field Approximation**

### **2.9.1 Introduction**

The DVMG, which is a filter based magnetograph (Section 1.4.3), uses the weak field approximation to measure to solar magnetic field. The primary advantage of using the weak field approximation is that magnetograms can be obtained quickly and easily with a minimum of observational time.

Since the narrow-band filter naturally provides a two-dimensional monochromatic image in the wing of the magnetically sensitive absorption line being used, the instrument simply needs to integrate enough images in each of the two particular Stokes components required to generate the desired Stokes element to produce the desired signal-to-noise ratio and display the difference of the two images divided by their sum (the details of this process will be described in detail in Chapter 3). This data can be acquired very quickly since the instrument does not need to acquire the profile of the absorption line.

Of course, using the weak field approximation has some disadvantages. The first disadvantage is some loss in sensitivity, as compared to measurements made with a spectrograph, arises from the fact that a typical narrow band filter has a finite band-pass that is close to the width of the absorption line. In the case of the DVMG, the FWHM of the Ca I 610.3 nm line is approximately 0.015 nm, while the FWHM of the band-pass of the Lyot filter used on the DVMG is 0.025 nm. Therefore, when the Lyot filter is tuned to the center of the wing of the absorption line some portion of the line that is not in the linear range contaminates the observation, which reduces the sensitivity.

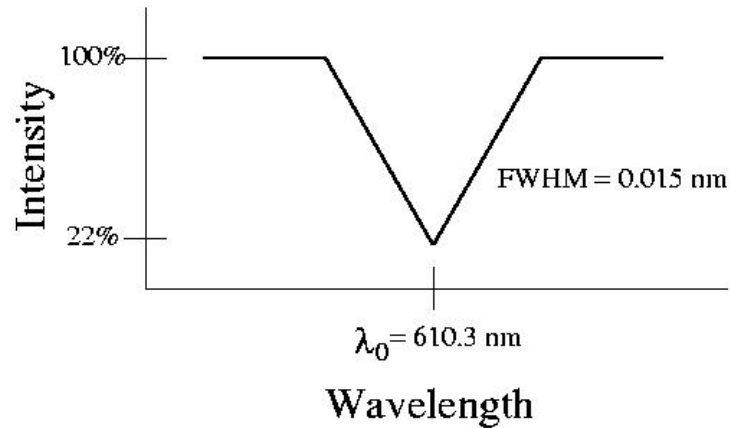
There is also the problem of Zeeman saturation. As will become clear in Figure 2.23 below, the weak field approximation is only valid when measuring magnetic fields below a certain threshold value. For the Ca I absorption line at 610.3 nm used by the DVMG, this value is on the order of ~3000 Gauss. However, this limitation can be tolerated since magnetic fields of this strength are only found in the umbras of sunspots (Figure 1.6). As discussed in Section 1.2, the intensity of the umbras of sunspots are on the order of ~10% of the photosphere. This low signal level results in “holes” in the

magnetograms at the center of large sunspots (as can be seen in Figure 3.30 in Section 3.7.3).

The other primary disadvantage to using the weak field approximation is that the line profile information of the absorption line is not available. From this information, one can not only determine the strength of the magnetic field but can also determine the properties of the solar atmosphere where the absorption line was created such as temperature, pressure, etc (as discussed in Section 5.3.5). For this information, other magnetograms, which acquire the line profile information, must be relied upon. Since the primary objective of the DVMG is to obtain vector magnetograms at a high cadence (~1 min), the tradeoffs made to use the weak field approximation can easily be tolerated. The brief overview of the weak field approximation, as follows, is from [47], [48], [49] & [50].

### **2.9.2 Brief Overview of the Weak Field Approximation**

Recall that the Ca I absorption line used by the DVMG approximates a Gaussian curve (as seen in Figure 2.6 above). In the simplification provided by the weak field approximation, each wing of the absorption line is replaced by a straight line, whose slope equals the slope of the actual absorption line in the center of the line wing (replacing the Gaussian absorption line by an approximately equivalent triangle) (Figure 2.22).

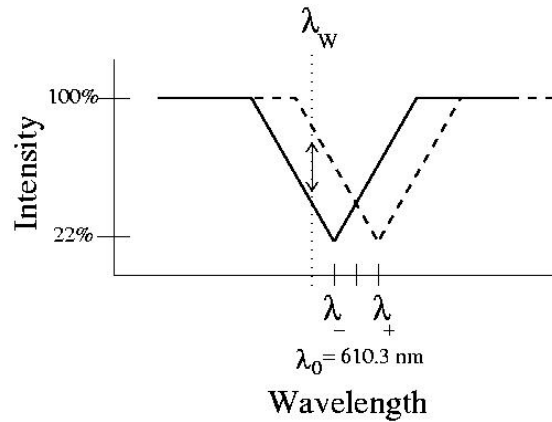


**Figure 2.27** Straight-line approximation of the Ca I 610.3 nm absorption line.

If there is a longitudinal magnetic field present, the single absorption line will split into two overlapping lines (with different circular polarization) (Figure 2.24).  $\Delta\lambda$  is a function of the strength of the local magnetic field by:

$$\Delta\lambda = 4.67 \times 10^{-12} \lambda^2 B g \quad (2.33)$$

where  $\lambda$  is the wavelength in nm, B is the strength of the magnetic field in Gauss and g is the Lande factor of the particular absorption line being used (2.0 in the case of the Ca I line at 610.3 nm). Note that for the visible portion of the solar spectrum,  $\Delta\lambda$  is always very small when compared to the overall width of the absorption line. For example, a magnetic field of 1000 Gauss will produce a wavelength shift of only 0.0035 nm as compared to the FWHM width of the 610 nm absorption line of 0.0150 nm. Therefore, it would not be possible to distinguish the two components of the absorption line as shown in Figure 2.24 if they were not oppositely circularly polarized.



**Figure 2.28** Example of the Zeeman splitting in the straight line approximation of the Ca I absorption line.

The magnitude of the longitudinal magnetic field, in Gauss, can then be calculated from:

$$B_L = K_L V, \quad (2.34)$$

and the magnitude and direction of the transverse magnetic field, in Gauss and radians, respectively, can be calculated from:

$$B_T = K_T * (Q_3^2 + U_3^2)^{1/4}, \quad (2.35)$$

$$\alpha = (\pi/180) * (90^\circ + 22^\circ) - \frac{1}{2} \text{arc-tan}(U_3/Q_3), \quad (2.36)$$

where  $K_L$  is the longitudinal calibration constant of the instrument,  $V$  is the percentage of circularly polarized light,  $K_T$  is the transverse calibration constant of the instrument, and  $Q$  &  $U$  are the percentages of linearly polarized light in the coordinate systems orientated at  $0^\circ/90^\circ$  and  $\pm 45^\circ$ , respectively. Where

$$V = (V_R - V_L) / (V_R + V_L), \quad (2.37)$$

$$Q = (Q_H - Q_V) / (Q_H + Q_V), \quad (2.38)$$

$$U = (U_A - U_B) / (U_A + U_B), \quad (2.39)$$

where  $V_R$ ,  $V_L$ ,  $Q_H$ ,  $Q_V$ ,  $U_A$  &  $U_B$  are the individual Stokes components. The values of  $K_L$  &  $K_T$  were previously determined by [48] to be:

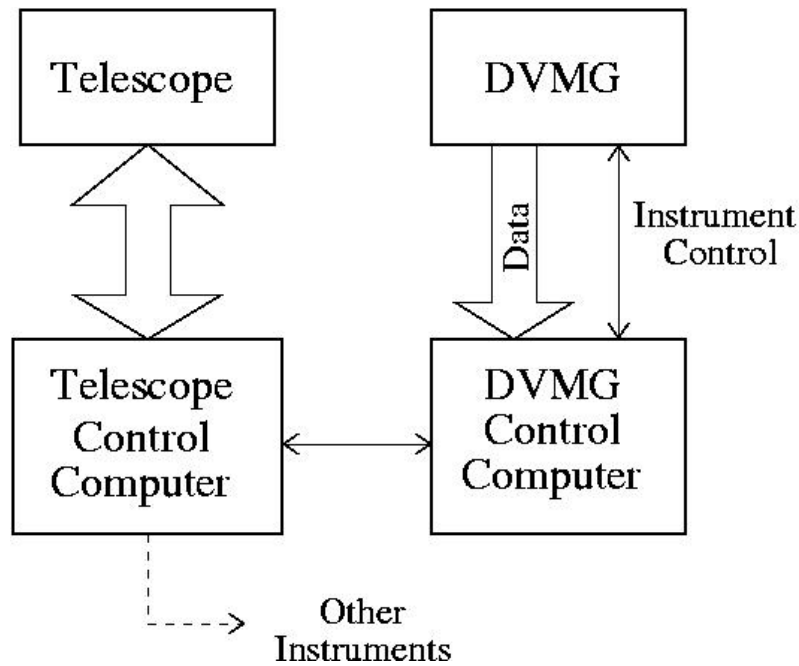
$$K_L \sim 16000 \quad (2.40)$$

$$K_T \sim 4600. \quad (2.41)$$

The acquisition of the Stokes components and the calculation of the magnetic field will be addressed, in detail, in Section 3.

## **2.10 DVMG & Telescope Control Computers and Overall System Schematic**

An overall system schematic is shown in Figure 2.25. Both the DVMG and Telescope Control computers are tower PCs. The operating system for the DVMG is Windows-95 (with a Visual C++ program running the instrument, Section 2.8.3) while the operating system for the Telescope Control Computer is Linux.



**Figure 2.29** General control schematic.

The DVMG and Telescope Control Computers (TCC) communicate via their respective serial ports. When Sunlight is available at the center optical bench on the 25 cm vacuum-refractor, on which the DVMG is located, the TCC signals the DVMG to begin obtaining a set of data (the exact details of which are determined by the observer depending on the goals of the observations for that particular day, Section 3.2). The TCC also passes the right ascension and declination of the center of the field-of-view. This information is stored in the FITS header of each image saved by the DVMG. The instrument control computer informs the TCC when the DVMG is finished taking the current data set so the light can be redirected to the other instruments mounted on the 25 cm vacuum-refractor.

Next, Chapter 3 will basically follow a typical day of observing describing the set-up and use of the instrument. Also, the procedure for reducing the data and creating vector magnetograms will be discussed, in detail.



## **CHAPTER 3**

### **OBSERVATIONS AND DATA REDUCTION**

Chapter 3 will deal with the details of the process of collecting data with the Digital Vector Magnetograph (DVMG) throughout a typical observing day. In Appendix F, the background information, including the details of setting up the instrument to acquire the particular type of data desired, is provided. In this chapter, it is assumed that these details are already in hand, and begin with the acquisition of the flat field images and dark frames, which are used to correct non-uniformities in the data arising from the instrumentation and telescope optics. Next, the thought process that goes into choosing the particular region on the Sun that is to be observed and how the instrument is to be configured and operated for achieving the goals of any particular observation will be discussed. After the data are acquired, the flat field and dark frame images must be applied, the data must be archived for future use and a web page is automatically generated, which provides a synopsis of the observations that were taken each day and are available on the BBSO public archive FTP site. The purpose of this web page is to enable those interested in the magnetogram data to quickly and easily determine what regions on the Sun were observed each day. Finally, the quality of the data will be evaluated and sample longitudinal magnetograms and vector magnetograms of simple and complex active regions will be shown.

### 3.1 Acquisition of Dark and Flat Field Frames

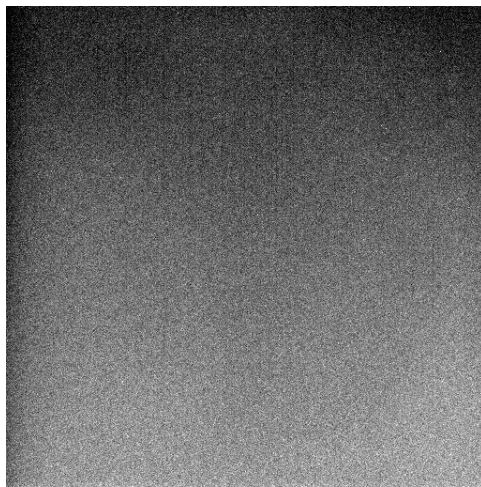
So-called “dark images” from the optical system are an essential step in data calibration. A dark current image is an image taken with an instrument under the exact same conditions that the data are to be taken except that the light is blocked from traversing the system. There are two components to the dark image – the thermal image and the read-out noise. The thermal image is produced by electrons which have enough energy to jump across the energy well of the detector under the impetus of their own thermal motion and is a function of the exposure time and temperature. The read-out noise is a characteristic of the camera electronics (quantum transfer efficiency, A/D conversion, etc.) and tends to be very stable with time and temperature.

The intensity of the thermal signal can be reduced by decreasing the exposure time and/or cooling the detector. Because the exposure time used for the DVMG is relatively short (120 ms) and the thermal signal that is created under typical ambient conditions (0° C to 30° C) during a typical exposure is low, the total dark signal for the DVMG is a small, but still significant, component of the data and, therefore, must be dealt with.

To acquire a dark image, the light is blocked from traversing the instrument and many individual images are acquired in rapid succession. For the DVMG, typically 1000 individual images are used. These individual dark images are automatically averaged to produce a single dark frame image that is normalized to a single exposure and will be used to correct the thermal signal and read-out noise in the data images taken during that observing day. Because the ambient temperature tends to not radically change during the

course of an observing day, only a single dark image is required to correct the thermal and read-out noise from the data collected in any one observing day.

A sample dark image is shown in Figure 3.1. In this example, the minimum value in the dark image is 94 counts, the maximum value is 1365 counts and the mean value is 128 counts. Note that the full-well value is 4095 counts. The image shown in Figure 3.1 is displayed with extreme contrast to accentuate the features of the image which are actually very subtle.



**Figure 3.1** Sample dark image.

The gradient in the dark image is caused by the way pixels of the CCD chip are read out. In this case, the pixels in the top row are read out first. Then, all subsequent rows are shifted up and the next row is read out. This process is continued until all of the rows are sampled. Therefore, the voltages that are initially collected by the bottom row of pixels are stored on the chip longer than those that are initially collected by the top row of pixels. Since the level of the dark signal is a function of time, those pixels that are stored on the CCD chip longest have the largest dark signal.

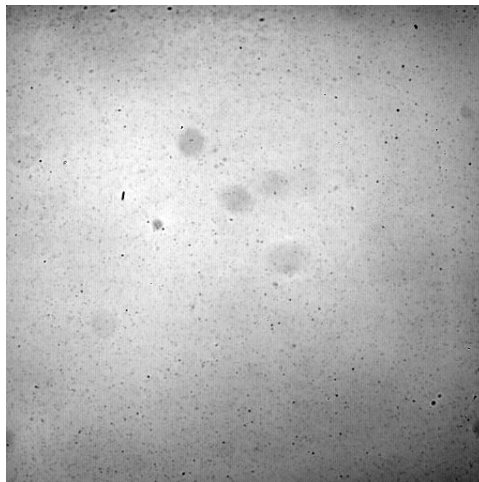
The images produced by any real optical system are plagued by non-uniformities that are not a part of the real target of the system. Dust on the optics, spatial non-uniformities in the transmission of the filters and spatial non-uniform sensitivity of the detectors all contribute to this problem. Dealing with dust on the optics is especially important when working with a telescope system that is essentially in an outside environment (see Section 2.2). The purpose of using flat fields is to remove these non-uniformities.

Ideally, a flat field can be obtained by taking an image of a perfectly uniform target. Any non-uniformities in the image would thus be the result of real non-uniformities in the optical transmission of the instrument and/or in the sensitivity of the detector. Non-uniformities in the data can then be corrected by dividing the data by the flat field image.

Flat field images are obtained for night-time telescopes by either imaging a uniformly illuminated flat white screen or imaging the twilight sky. Both of these targets closely approximate the perfectly uniform illuminated target that is required to obtain a flat field. Unfortunately, the acquisition of flat field images for an instrument that is designed to observe the Sun is not that simple. For a uniform white screen or the twilight sky to be used as the target for the acquisition of a flat field image, the brightness of the flat field target must be on the order of the brightness of the data target. Since the brightness of the sky is nowhere near that of the Sun, and it is impractical to construct an artificial light source that is of similar intensity to that of the Sun, another way must be found to generate flat field images for solar instrumentation.

One method for generating flat field images for solar instrumentation is to take many single frame images, in rapid succession, of a relatively featureless area of the Sun while the telescope is moving. When these individual images are averaged, the relatively subtle features on the Sun, imaged at slightly different locations on the detector in each successive image because of the motion of the telescope, are averaged out leaving the stationary non-uniformities.

The flat field frames for the 610.3 nm intensitygram data (Stokes-I) produced by the DVMG are acquired in this manner. Typically, 1000 images are used to create the flat field frames for the Stokes-I images. A sample flat field image for the Stokes-I image is shown in Figure 3.2 As with the dark image, the flat field for Stokes-I images is displayed with extreme contrast to accentuate the non-uniformities in the raw images. A sample application of the flat field for the Stokes-I images will be presented in Section 3.4. Note the non-uniformity in the transmission of the Lyot filter (the “porthole” effect) and the specs of dirt on various optical surfaces.



**Figure 3.2** Sample flat field image.

Unfortunately, this method, while very easy in application, is not suited to the magnetogram data produced by the DVMG (Stokes-V, Q & U-images). First, the creation of a magnetogram requires the acquisition of many individual frames, as opposed to an intensitygram which requires only a single frame. As will be discussed in Section 3.6.1, a magnetogram can typically require dozens to hundreds of frames to develop an acceptable signal-to-noise ratio in the data. Therefore, the time required to generate a single magnetogram is typically much much greater than the time required to acquire an intensitygram. When multiplied by the number of individual magnetograms that would be required to generate a flat-field frame using this method that time would simply be unacceptably long. Also, as noted previously, to use this averaging method to generate a flat field frame the solar features must be relatively subtle. The features in a magnetogram, which will be shown in Sections 3.7 and 3.8, even when imaging relatively weak magnetic fields, are not subtle. For these two reasons, the time required to generate enough magnetograms and the fact that the magnetic features are not subtle, this averaging method will not work for producing flat field frames for magnetogram data. Therefore, another method must be found.

To that end, many solar instruments use the Kuhn-Lin method for making flat field images [51]. Briefly, a single image is taken at some position that is free from sunspots so as to determine the response of the optical system to a “bland” source. Then, two sets of four images are taken at slightly different positions relative to the first image. The first set includes four images that are displaced by some small amount (5 arc-sec), relative to the field of view of the instrument, north, south, east and west. The second set includes four images that are displaced by some moderate amount (50 arc-sec) in the

same directions. These nine images are then fed into the Kuhn-Lin algorithm which calculates the final flat field image that will be used to correct the non-uniformities in the DVMG data. For a detailed discussion of the Kuhn-Lin method please see [51].

Each individual component of the magnetograms produced by the DVMG requires its own corresponding flat field image. Therefore, a total of seven flat field images are required to completely correct for the non-uniformities in the DVMG data. One flat field is required to correct for the I-images and two flat field images are required for each of the magnetogram components (Stokes-V, Q & U images). It typically takes approximately 20 minutes to collect the necessary data to create the seven flat field images for the DVMG.

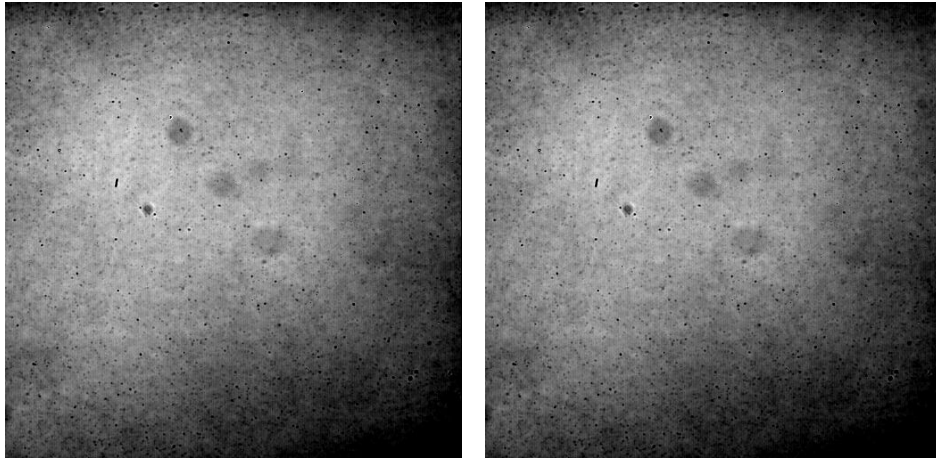
While the non-uniformity in the quantum efficiency of detectors and the non-uniformity in the transmission of the filters is stable with time, the amount and location of the dust on the optics is continually changing with time. (This is not necessarily the case with oil-filled filters, especially those filters that are mounted on the moving parts of the telescope. As the telescope moves throughout the day to track the Sun, the oil in the filters may slowly flow in response to the changing gravity vector, which may produce slight spatial changes in the transmission of the filter. Also, oil-filled filters may slowly leak their contents, thus requiring re-filling occasionally, which can also produce slight spatial changes in the transmission of the filter. Both problems, however, are unavoidable when using oil-filled filters. Thus, possible temporal changes in the spatial transmission of the oil-filled filters must be accepted. Fortunately, these changes in the spatial transmission of the oil-filled filters tend to be slight and, thus, tolerable.) Small amounts of dust are continually collecting on exposed optics. In addition, as the telescope moves

throughout the day to track the Sun, slight flexure in the telescope and instrument mounting change the position of the dust relative to the detector. If the position of the dust changes relative to the detector the flat field correction will not only fail to remove the dust images but will also add additional spurious features. Therefore, the quality of the correction of the non-uniformities in the data, provided by any individual flat field image, deteriorates with time. Thus, new flat field images must be acquired from time to time.

However, experience has taught us that any individual flat field image will adequately correct the instrumentally induced non-uniformities in typical data for at least several hours. Therefore, only one set of flat field images are typically required per day. Of course, if better correction is required by the specifications of the observations for any particular day, any desired number of flat field images may be acquired, with the corresponding penalty of reduced observing time.

Typical flat field images for the individual Stokes-V components are shown in Figure 3.3. Flat field images for the individual Stokes-Q and U components look similar. The image on the left is the flat field image used to correct the non-uniformities in the left-hand circularly polarized channel while the image on the right is that which is used to correct the non-uniformities in the right-hand circularly polarized channel. While these two images look identical to the eye they are actually different. This difference can be seen by subtracting one image from the other. The actual application of the flat field and dark images will be discussed, and the results presented, in Section 3.4.





**Figure 3.3** Typical flat field images for the individual Stokes components.

### 3.2 Target Choice

As discussed in Section 2.2, the DVMG is a high resolution instrument. The field of view of the DVMG is  $\sim 300$  arc-sec on a side (note that the Sun is  $\sim 2000$  arc-sec in diameter). Thus, only a small portion ( $\sim 3\%$ ) of the solar surface can be imaged at any one time. Therefore, a decision must be made as to which area on the Sun is to be imaged with the DVMG.

The primary factor which determines which area of the Sun is to be imaged with the DVMG, or with any solar instrument, is the goal of the observations that are being carried out at that particular time. Because the primary responsibility of BBSO is the monitoring and study of dynamic solar activity, the observations tend to focus on the region on the Sun with the most complex magnetic field at that time, which is the source of all solar activity (see Section 3.9.2 for an example of an active region with a complex magnetic field). However, if visiting scientists has other specific goals to their observations, or if there is a special joint observing campaign with other ground-based

and/or satellite solar observatories, any other area of interest on the Sun can be targeted at any time.

A powerful tool that is used to help determine which area on the Sun that will be observed at any particular time is the web-page based Active Region Monitor (ARM), a sample of which can be seen in Figure 3.4. This web page automatically collects various types of full-disk solar images from different solar observatories around the world ( $H\alpha$  from the BBSO  $H\alpha$  network, longitudinal magnetogram and continuum images from the Michelson Doppler Imager (MDI) on board the Solar and Heliospheric Observatory spacecraft (SOHO), etc.) and presents a synopsis of these images in a convenient format along with a numerical listing of the NOAA active regions that are current on the solar disk. It also lists all recent solar flares (in the “events” column in the lower-right of Figure 3.4) along with other pertinent information about solar activity.

Using the general information provided by ARM combined with the near real-time high resolution vector magnetograms from the DVMG, the observer can quickly evaluate all of the active regions on the Sun and determine which is most likely to produce activity.

<20040907 <Week <Rotation Active Region Monitor Rotation >Week > 20040909>

NOAA Regions

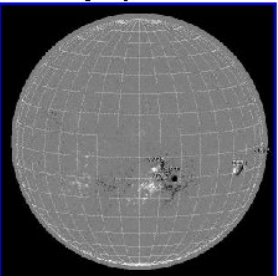
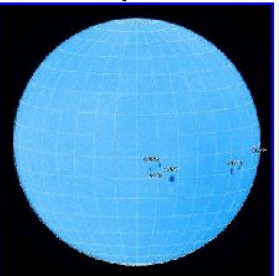
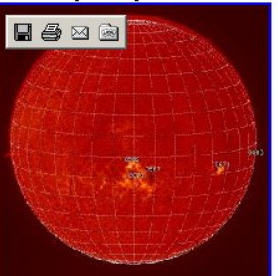
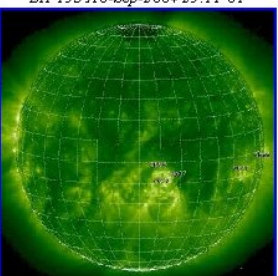
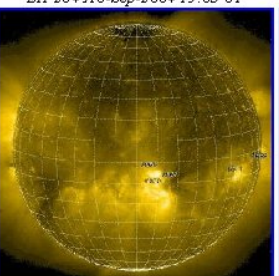
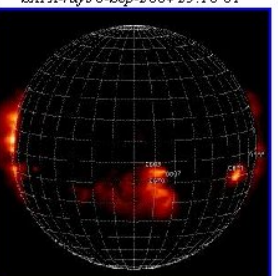
[0667](#)

[0668](#)

[0669](#)

[0670](#)

[0671](#)

[ARM Home](#)

[GOES X-rays](#)

[Protons](#)

[Electrons](#)

[SEC Events](#)

[SSW Events](#)

[RHESSEI Times](#)

[Search Archive](#)

Welcome to the Active Region Monitor (ARM) at NASA Goddard Space Flight Center's Solar Data Analysis Center (SDAC), and now at the Korean Astronomy Observatory's mirror site. These pages contain the most recent solar images from the Global H-alpha Network, together with continuum images and magnetograms from the Michelson Doppler Imager (MDI) and EUV images from the Extreme-ultraviolet Imaging Telescope (EIT) onboard the ESA/NASA Solar and Heliospheric Observatory (SOHO). Solar event movies and flare identifications are linked from the Lockheed Martin Last Events page. Full-disk GONG+ magnetograms and magnetic gradient maps are supplied courtesy of the US National Solar Observatory, while soft X-ray images are provided by the NOAA Solar X-ray Imager (SXI).

A developmental version of the automated Flare Prediction System (FPS) is also available on these pages. The FPS algorithm calculates the probability of each region producing C-, M-, and X-class events based on almost eight years of data from the NOAA Space Environment Center. Check out our news pages for up-to-date changes to ARM.

ARM is an integral component of the [Max Millennium Program of Solar Flare Research](#).

GONG+ Magnetogram
MDI Magnetogram
MDI Continuum
GHN H-alpha
EIT 304 Å
EIT 171 Å
EIT 195 Å
EIT 284 Å
SXI X-rays
Full-disk Slideshow

Today's NOAA Active Regions						
Number	Location	Hale	McIntosh	Area	NSpots	Events
0667	S11W18 (290°, -293°)	$\alpha/\beta$	Hkz/Dao	0290/0240	04/10	-
0668	S09W91 (940°, -145°)	$\alpha/\alpha$	Axx/Hsx	0010/0050	01/01	<a href="#">C1.1(07:06)</a>
0669	S06W08 (132°, -218°)	$\beta/\beta$	Dai/Dso	0090/0050	15/12	<a href="#">C1.0(19:57)</a>
0670	S14W10 (161°, -345°)	$\beta/\alpha$	Bxo/Axx	0010/0010	14/04	-
0671	S11W56 (777°, -246°)	$\beta/\beta$	Dso/Dsi	0080/0040	11/05	-

Events not associated with currently named NOAA regions: C1.5(00:59) / C2.8(13:40)

Note: The tabulated data are based on the most recent NOAA/USAF Active Region Summary issued on 08-SEP-2004 00:30 UT, the values to the right of the forward slashes representing yesterdays values or events. The region positions are valid on 8-Sep-2004 23:30 UT.

Figure 3.4 Example of the Active Region Monitor (ARM) web page.

### 3.3 Sample Reduction of Data

After the raw data are collected, several steps are required to process the data into useable images. These steps are listed as follows:

Step 1) – Acquire the raw Stokes components ( $I_1$ ,  $V_{R1}$ ,  $V_{L1}$ ,  $Q_{H1}$ ,  $Q_{V1}$ ,  $U_{A1}$ , &  $U_{B1}$ ).

Step 2) – Correct images for flat field non-uniformities and dark signal.

Step 3) – Calculate the Stokes parameters (Stokes-V, Q & U)

Step 4) – Create the longitudinal magnetograms.

At this point, the longitudinal image is complete (Stokes-V). However, the transverse images (Stokes-Q & U) require additional steps for the creation of vector magnetograms:

Step 5) – Correct the Stokes-Q & U images for cross-talk (if applicable).

Step 6) – Calculate the vector magnetic field in polar coordinates.

Step 7) – Convert the vector magnetic field into Cartesian coordinates.

Step 8) – Plot the vector magnetic field.

These steps will each be discussed, in detail, in the following sections.

#### 3.3.1 Step 1 - Acquisition of Raw Data

Appendix F will deal with setting up the instrument to take data. All images are initially stored as uncorrected (no post processing such as flat field correction, etc.) One file each for the Stokes-I, U, Q & V components. The images are automatically corrected for instrument non-uniformity (flat field) and thermal signal (dark frame) at the end of each day by the archive computer (Section 3.5).

The Stokes-I file is a single 610.3 nm intensitygram image ( $I_1$ ) while the Stokes-V, Q & U files each contain the two components required to generate their respective Stokes parameter ( $V_{R1}$  &  $V_{L1}$  to generate the Stokes-V parameter,  $Q_{H1}$  &  $Q_{V1}$  to generate the Stokes-Q parameter and  $U_{A1}$  &  $U_{B1}$  to generate the Stokes-U parameter). A description of each Stokes component follows:

$I_1$  – 610.3 nm intensitygram

$V_{R1}$  – Right circular polarization component of the Stokes-V parameter.

$V_{L1}$  – Left circular polarization component of the Stokes-V parameter.

$Q_{H1}$  – Horizontal linear polarization component of the Stokes-Q parameter.

$Q_{V1}$  – Vertical linear polarization component of the Stokes-Q parameter.

$U_{A1}$  – “Positive-slope” linear polarization component of the Stokes-U parameter.

$U_{B1}$  – “Negative-slope” linear polarization component of the Stokes-U parameter.

### 3.3.2 Step 2 - Application of the Flat Field and Dark Frame Images

Now that the initial data have been acquired, all that remains is to calculate the vector magnetograms using a few simple steps (see the above list). First, the raw data must be calibrated for instrument non-uniformity (flat field) and thermal signal (dark frame). Each Stokes component ( $I_1$ ,  $V_{R1}$ ,  $V_{L1}$ ,  $Q_{H1}$ ,  $Q_{V1}$ ,  $U_{A1}$ , &  $U_{B1}$ ) has a unique flat field frame (Section 3.2).

The raw data are calibrated by:

$$I_2 = (I_1 - D) / F_I \quad (3.1)$$

$$V_{R2} = (V_{R1} - N_{VR} * D) / F_{VR} \quad (3.2)$$

$$V_{L2} = ( V_{L1} - N_{VL} * D ) / F_{VL} \quad (3.3)$$

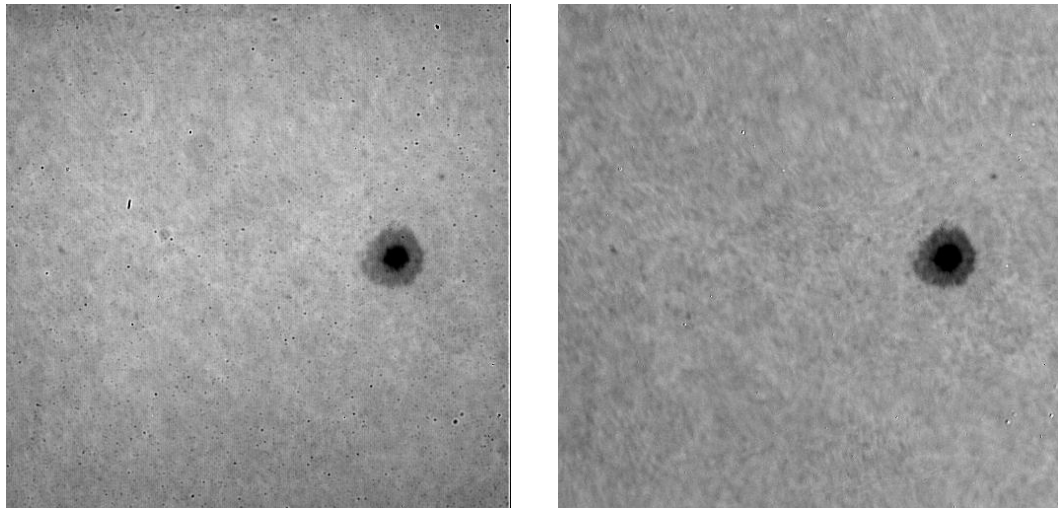
$$Q_{H2} = ( Q_{H1} - N_{QH} * D ) / F_{QH} \quad (3.4)$$

$$Q_{V2} = ( Q_{V1} - N_{QV} * D ) / F_{QV} \quad (3.5)$$

$$U_{A2} = ( U_{A1} - N_{UA} * D ) / F_{UA} \quad (3.6)$$

$$U_{B2} = ( U_{B1} - N_{UB} * D ) / F_{UB} \quad (3.7)$$

Where  $I_1$  and  $I_2$  are the raw and corrected 610.3 nm intensitygrams, respectively,  $D$  is the dark frame (thermal image) normalized to a single integration,  $F_I$  is the flat field frame for the  $I_1$  image, the images with the subscript “2” are the corrected files, the images with the subscript “1” are the raw files (see Section 3.4.1 above),  $N$  is the number of integrations in the raw file corresponding to its subscript ( $N_{VR}$  is the number of integrations in  $V_R$ , etc.), and the  $F$  images are the flat field frame for each corresponding raw image ( $F_{VR}$  is the flat field frame for  $V_R$ , etc.).



**Figure 3.5** Example of the results of the application of the dark and flat field images to the raw data.

Figure 3.5 shows an example of the results of correcting a raw image for instrument non-uniformity and thermal signal. The image on the left is the raw 610.3 nm intensitygram while the image on the right is the 610.3 nm intensitygram after correction. All of the other Stokes components show similar improvements.

### 3.3.3 Step 3 - Calculation of the Stokes Parameters

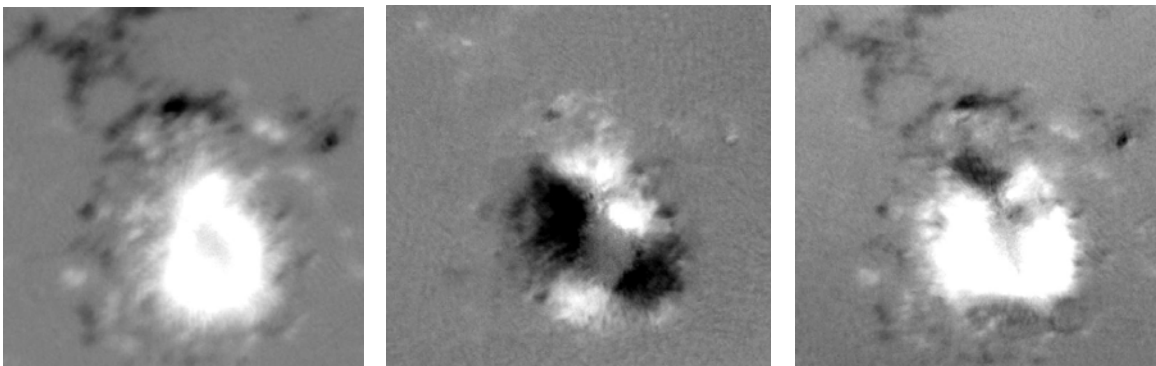
After the raw data have been corrected for instrument non-uniformity and thermal signal, the individual Stokes parameters can be easily calculated by:

$$V = (V_{R2} - V_{L2}) / (V_{R2} + V_{L2}) \quad (3.8)$$

$$Q = (Q_{H2} - Q_{V2}) / (Q_{H2} + Q_{V2}) \quad (3.9)$$

$$U = (U_{A2} - U_{B2}) / (U_{A2} + U_{B2}). \quad (3.10)$$

The sample of the resulting Stokes-V, Q & U images that are displayed from left to right in Figure 3.6, are of NOAA Active Region 10123 on 03Jul12. The field-of-view shown is 150 x 150 arc-sec.



**Figure 3.6** Sample of Stokes-V, Q & U images.

### 3.3.4 Step 4 - Longitudinal Magnetogram

The strength of the longitudinal magnetic field can be easily determined from the Stokes-V parameter by simply multiplying V by the longitudinal calibration constant of the instrument (see [48] for a review of the determination of the calibration constants of the instrument),

$$B_L = K_L * V, \quad (3.11)$$

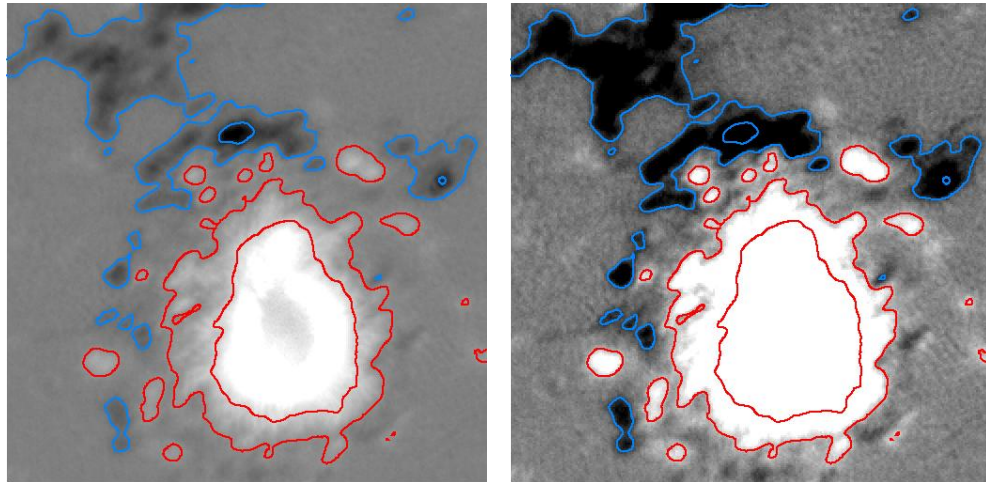
where  $B_L$  is the strength of the longitudinal magnetic field in Gauss and  $K_L$  is the longitudinal calibration constant of the instrument in Gauss per percent polarization. In the case of the DVMG, the longitudinal calibration constant is  $1.6 \times 10^4$ . The individual pixel values in  $B_L$  are now the strength of the magnetic field in Gauss in the line-of-sight direction. As discussed in Section 2.1, all of the locations in the image where the magnetic field is directed toward the observer will be positive, while all of the locations in the image where the magnetic field is directed away from the instrument will be negative.

The longitudinal magnetogram can then be conveniently displayed where all of the positive values are plotted as shades of white, all of the negative values are plotted as shades of black and the areas where no magnetic field is present is plotted as a uniform gray as can be seen in Figure 3.7. The positive and negative saturation values, for each respective plot, are chosen whether the user is interested in the details of the overall morphology of the strong magnetic fields of the region (left image) or in the details of the small-scale weak fields (right image). In the case of the magnetogram shown in Figure



3.7, the image on the left is presented with a saturation value of  $\pm 200$  G while the image on the right is presented with a saturation value of  $\pm 800$  G.

If desired, contours representing the strength and direction of the magnetic fields can also be overlaid on the longitudinal magnetograms. This is especially helpful in the regions of the magnetograms that are stronger than the saturation values of the plot. In the case of the magnetograms, the contours are set to  $\pm 100$  G and  $\pm 500$  G.

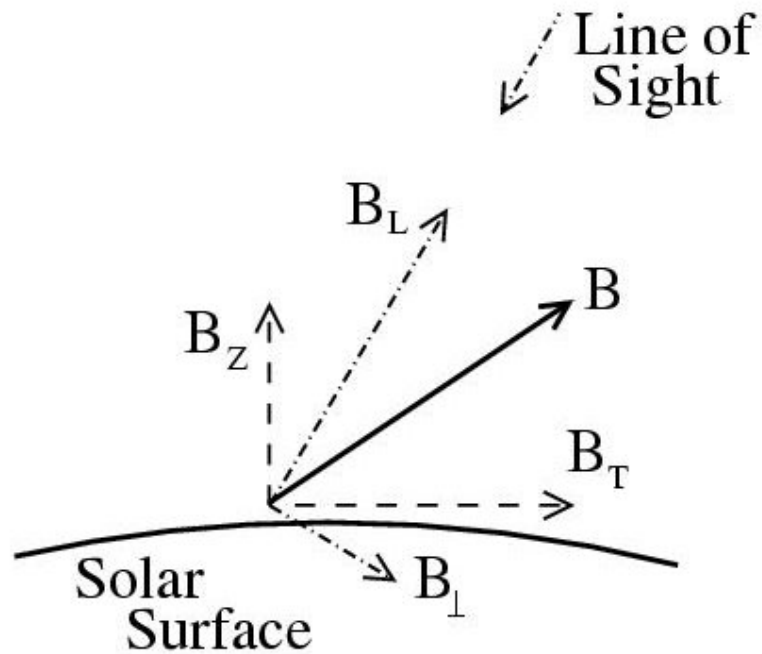


**Figure 3.7** Longitudinal Magnetogram.

### 3.3.5 Step 5 - Cross Talk

When evaluating data obtained by a solar magnetograph, more than how well the flat field and dark images correct for the non-uniformities produced by the instrumentation must be considered. It must also be determined whether the individual components of the magnetograph are working as intended. Primarily, it must be insured as to whether the main filter is tuned to the proper wavelength (this is discussed in Section 2.7.1) and whether the polarizers are properly adjusted to produce reliable Stokes-U, Q and V components (as discussed in Section 2.6.6). Changes in the characteristics of these components can be subtle and the performance of each must be carefully checked.

**3.3.5.1 Review of Magnetic Field Components.** First, let us review some terms dealing with the orientation of magnetic fields on the Sun. Some terms describing the orientation of the magnetic fields on the Sun are relative to the local solar surface while other terms are relative to the line-of-sight. The terms that describe the orientation of the magnetic fields that are relative to the solar surface are the vertical and tangential components, while the terms that describe the orientation relative to the line-of-sight are the longitudinal and transverse components. The longitudinal magnetic fields are those whose vectors point along the line-of-sight while the transverse magnetic fields are those whose vector



**Figure 3.8** Schematic of the components of the magnetic field.

Figure 3.8 shows a schematic of the components of the magnetic field where  $B$  is the actual magnetic field vector,  $B_z$  is the vertical and  $B_t$  is the tangential components (relative to the solar surface) and  $B_L$  is the longitudinal and  $B_{\perp}$  is the transverse components (relative to the line-of-sight). These terms must be kept clear because their description of the magnetic field on the surface of the Sun changes with the location of the area that is observed relative to the center of the solar disk. For example, near the center of the solar disk, the vertical field is approximately equal to the longitudinal field. However, the vertical field is approximately equal to the transverse field when viewed near the solar limb.

**3.3.5.2 Correct for Cross Talk.** In the case of solar magnetographs, cross-talk is specifically defined by the contamination of the Stokes-Q and/or U images by features that should only appear in the Stokes-V images. That is, longitudinal magnetic fields that appear in the transverse measurements. Cross-talk can be caused by spurious polarization imparted to the light by the instrumentation or polarization elements that are not precisely tuned to their optimum values (in retardance and/or rotation angle). Since the DVMG is mounted on the center optical bench of the 25 cm vacuum-refractor, where no reflections are needed, instrumental polarization is minimized. Therefore, the most likely cause of cross-talk in the DVMG is polarization optics that are not correctly tuned, in retardance and/or rotation angle (Sections 2.6.6 & 2.6.6.3).

Solar magnetographs tend not to suffer from contamination of the longitudinal measurements by the transverse measurements for the following reasons. It is a property of the magnetic fields on the Sun that the vertical magnetic fields tend to be much stronger than the tangential fields (except in the cases of strong active regions in which

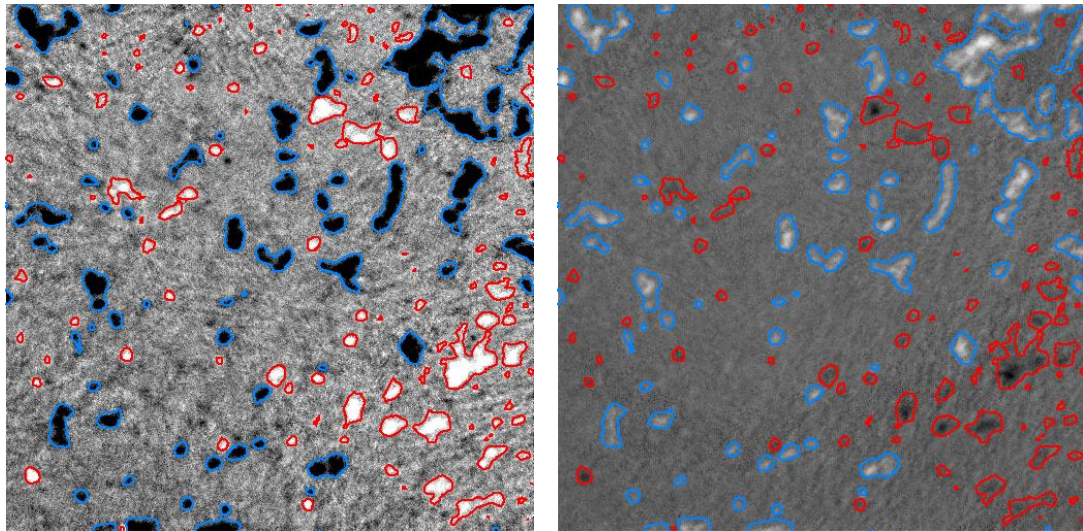
the magnetic fields are highly twisted). Solar magnetographs tend to observe regions on the Sun that are as close as possible to the center of the solar disk to eliminate the foreshortening effect of objects when viewed near the solar limb. Since most of the fields on the solar surface are approximately vertical, the longitudinal component of the field tends to dominate when viewed near the center of the solar disk. Compounding this fact is, everything else being equal, the polarization signal produced by a given longitudinal magnetic field is much stronger than the corresponding polarization signal produced by a transverse field of equal strength.

In actual practice, it is difficult to determine exactly which features, if any, in a particular Stokes-Q or U image are actually cross-talk. To determine the cross talk, the correlation of features between the Stokes-V & Q and Stokes-V & U images is evaluated, and it is assumed that those features are contamination from the Stokes-V image into the Stokes-Q and/or U images. However, it is not necessarily the case that all of the features that are correlated between the Stokes-V & Q and/or Stokes-V & U images are actually cross-talk. Therefore, care must be taken when evaluating the cross-talk of a magnetogram.

When evaluating the cross-talk of a magnetogram, it is important to ensure that the majority of the features in the Stokes-V, Q and U images consist of longitudinal magnetic field. In that case, the Stokes-Q and U images should be basically featureless (except for any instrumental non-uniformities as discussed in Section 3.1 which should have been corrected with the flat field frames as discussed above). The location on the Sun where this is most likely to be the case is a region of quiet Sun (where no active region is present) at or near the center of the solar disk. Since the magnetic fields found in

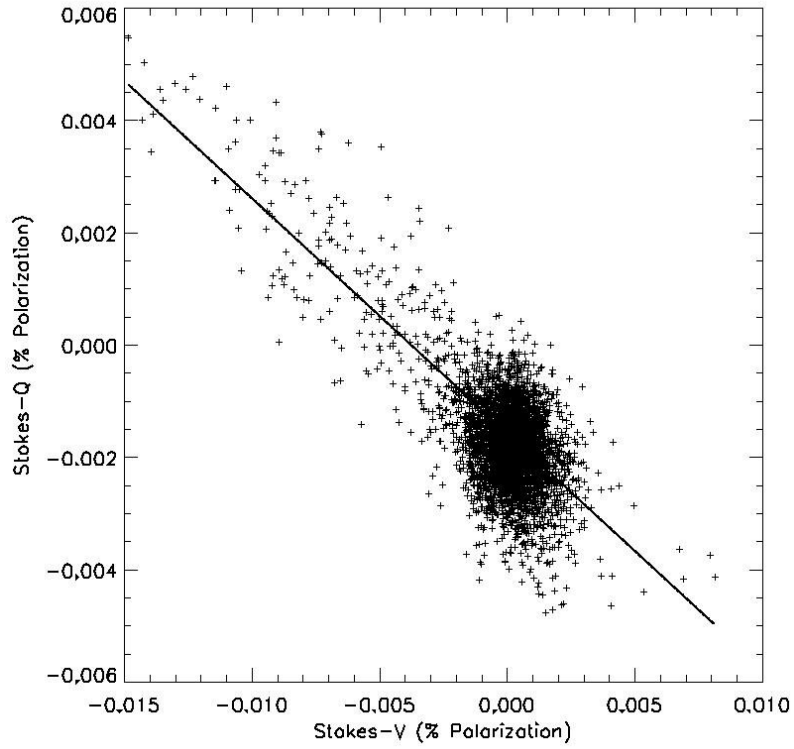
the quiet Sun tend to be mostly vertical (as discussed above), they consist entirely of the longitudinal component when located at the center of the solar disk. Therefore, the cross talk of the instrument can be determined by evaluating images of the quiet Sun taken at or near the center of the solar disk. The procedure for determining and correcting the cross-talk follows.

**3.3.5.3 Determining and Correcting for Cross Talk.** The first step in determining the cross talk in the DVMG data is to take a series of Stokes-V, Q and U images of the quiet Sun near the center of the solar disk (Section 3.7.2.2 above). An example of this data set is shown in Figure 3.9 In this example, the left image is the Stokes-V (longitudinal magnetogram) parameter while the right image is the Stokes-Q parameter. The white features in the Stokes-V image represent the longitudinal magnetic fields that are directed towards the observer while the black features represent the longitudinal magnetic fields that are directed away from the observer. The contours mark the location of the 20 Gauss level in the Stokes-V image. The same contours are plotted in the Stokes-Q image to help identify the cross-talk features that are present in that image. Note that the amount of cross-talk which appears in this example is intentionally much worse than is typical to enable the longitudinal features to be easily identified in the Stokes-Q images.



**Figure 3.9** Example of cross-talk.

Next, scatter-plots of the Stokes-Q vs. V and the Stokes-U vs. V images are created by plotting  $V_{(n,m)}$  as the x-axis and  $Q_{(n,m)}$  as the y-axis (for the Stokes-V/Q set),  $V_{(n,m)}$  as the x-axis and  $U_{(n,m)}$  as the y-axis (for the Stokes-V/U set), where (n, m) are the individual pixels in the 512 x 512 pixel images. Next, the best linear fit to the scatter-plots is found, where the slope of the best fit represents the percentage of cross-talk of the Stokes-V image into the Stokes-Q & U images. The scatter plot and the best fit for this example can be seen in Figure 3.10. Note that while all of the Stokes-V & Q data are plotted, only those data points where the absolute value of the Stokes-V parameter (the x-axis) were greater than 0.003% were used to calculate the best straight-line fit to avoid the regions in the images that are dominated by noise.



**Figure 3.10** Example of a cross talk scatter plot.

In this example, the V/Q cross-talk is 42%. Again, this value is much worse than typical. In general, the cross-talk tends to be on the order of 5%. The cross-talk can then be corrected by:

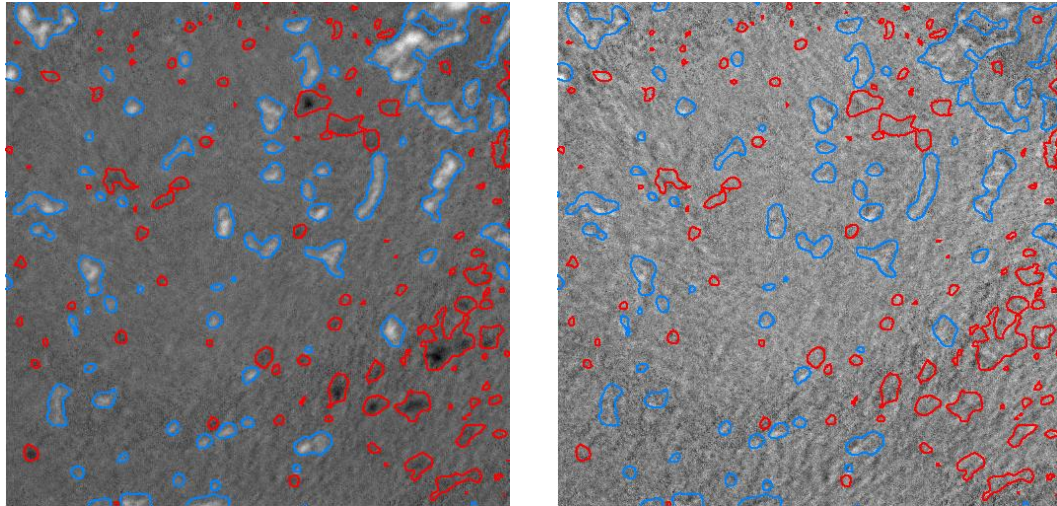
$$Q_3 = Q_2 - C_Q * V_2 \quad (3.12)$$

$$U_3 = U_2 - C_U * V_2 \quad (3.13)$$

where  $V_2$ ,  $Q_2$  &  $U_2$  are the original Stokes-V, Q & U images (which have already been flat field and dark image corrected),  $Q_3$  &  $U_3$  are the Stokes-Q & U images that have been corrected for cross-talk contamination and  $C_Q$  &  $C_U$  are the cross-talk. The resulting  $Q_3$  image can be seen in Figure 3.11 (note that there is are similar improvements in the case of the Stokes-U parameter). The left image in Figure 3.11 is the Stokes-Q parameter



before correcting for the cross talk (the same image that appears on the right side of Figure 3.9, above) while the right image is the Stokes-Q parameter after cross-talk correction. It can be seen that the majority of the features that appear in the original Stokes-Q image have been removed.



**Figure 3.11** Example of correction for cross-talk.

Note that correcting for the cross-talk will tend not to remove all of the features in the Stokes-Q & U images that are correlated with the features that appear in the Stokes-V image. First, there may be a small transverse component in the solar magnetic field that is real, even in quiet-Sun magnetic fields. Also, the linear fit is a compromise value for the average cross-talk across the entire image. In actual practice, there might be slight variations in the cross-talk as a function of image position so the average cross-talk value might not completely correct for the cross-talk across the entire image.



### 3.3.6 Step 6 - Vector Magnetograms

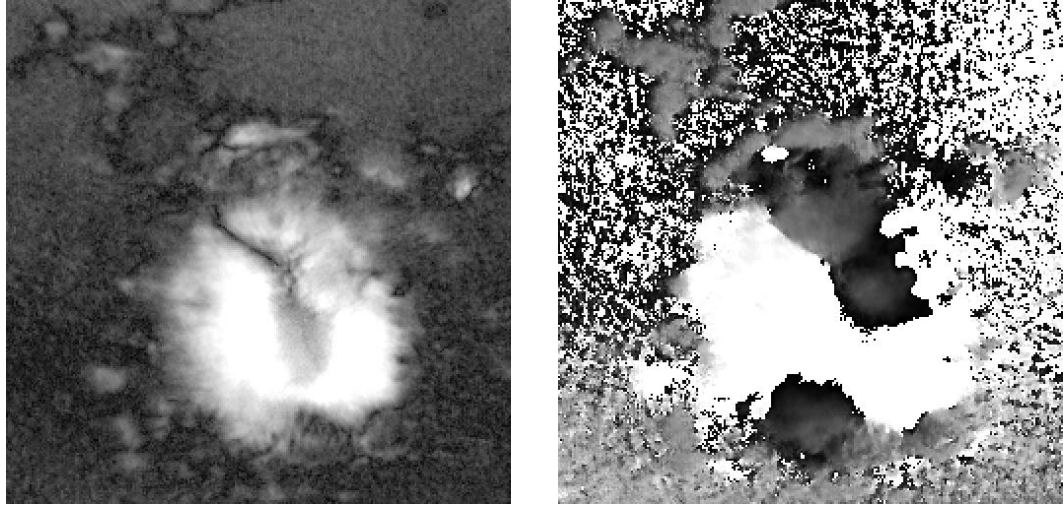
Note that the nature of the longitudinal magnetic field is self-evident from a visual inspection of the V image (left) as displayed in Figure 3.6 in Section 3.3.3. However, the nature of the transverse magnetic field is not at all obvious from a visual inspection of the Q and U images associated with the V image. Therefore, additional work must be done on the Q and U images to determine the transverse magnetic field.

The magnitude and direction of the transverse magnetic field, in polar coordinates, at every point in the image can be calculated by:

$$B_T = K_T * (Q_3^2 + U_3^2)^{1/4} \quad (3.14)$$

$$\alpha = (\pi/180) * (90^\circ + 22^\circ) - \frac{1}{2} \text{arc-tan}(U_3/Q_3), \quad (3.15)$$

where  $B_T$  is the magnitude in Gauss,  $\alpha$  is the azimuth angle (measured in radians) of the transverse magnetic at every point in the image and  $K_T$  is the transverse calibration constant of the instrument. In the case of the DVMG, the longitudinal calibration constant is  $4.6 \times 10^3$ . The purpose of the  $22^\circ$  correction in the calculation of  $\alpha$  is to account for the fact that the optical axis of the instrument (as defined by the input linear polarized of the birefringent filter) is rotated  $22^\circ$  CCW from the vertical (when looking up the optical axis from the CCD camera). The resulting  $B_T$  and  $\alpha$  are shown in Figure 3.12.



**Figure 3.12**  $B_T$  (left) and  $\alpha$  (right) images.

The left image displayed in Figure 3.12 shows the magnitude of the transverse magnetic field  $B_T$ . In an image of this type (where the displayed value is all of the same sign), pure black represents transverse magnetic fields with a magnitude of zero while pure white represents the magnetic field with the largest magnitude in the image (267 Gauss in this particular example). The right image displayed in Figure 3.12 is the azimuth angle  $\alpha$ , in radians, of the transverse magnetic field at every point in the image. Here, pure black represents a transverse magnetic field with an azimuth angle of zero radians while pure white represents a transverse magnetic field with an azimuth angle of  $\pi$  radians.

As can be seen from Figure 3.12, the actual characteristics of the transverse magnetic field, when using the  $B_T$  and  $\alpha$  images, is still not self evident, as it is when using the Stokes-V parameter to view the longitudinal magnetic field (left image in Figure 3.6 in Section 3.3.3 above). Therefore, it is advantageous to plot the transverse magnetic field in a way that is more visually self evident.

### 3.3.7 Step 7 - Converting Vector Magnetic Field into Cartesian Coordinates

To that end, the magnetogram data, which is in polar coordinates ( $B_T$  and  $\alpha$ ) is converted into Cartesian coordinates and the magnitude and direction of the magnetic field are plotted as vectors superimposed on either the 601.3 nm intensitygram (Figure 3.13, left image) or the longitudinal magnetic field (Figure 3.13, right image).

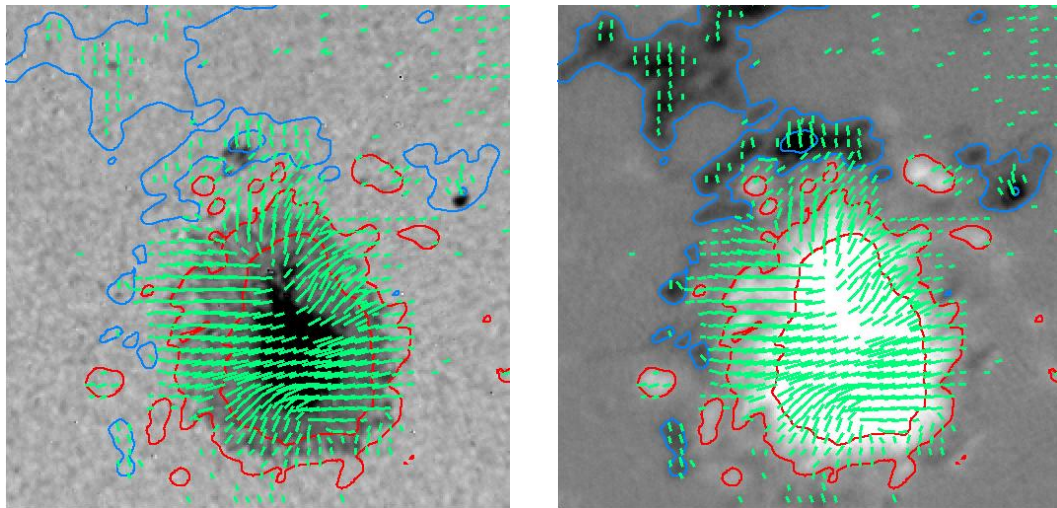
The magnitude of the transverse magnetic field in the x and y-dimensions are thus simply given by:

$$B_X = B_T * \cos (\alpha) \quad (3.16)$$

$$B_Y = B_T * \sin (\alpha). \quad (3.17)$$

### 3.3.8 Step 8 – Plot the Vector Magnetograms

The results are shown in Figure 3.13. The left image shows the vectors of the transverse field overlaid on the 610.3 nm intensitygram and the right image shows the vectors overlaid on the longitudinal magnetogram.



**Figure 3.13** Vector magnetogram.

### 3.3.9 180° Ambiguity in Vectors

When closely studying the details of the transverse solar magnetic field, one must take care to resolve the 180° ambiguity in the azimuth of the observed transverse magnetic fields ( $\alpha$  in Section 3.4.4 above). Note that this particular subject is being presented for the sake of completeness and will not be discussed in detail since it is mostly extraneous to the primary presentation. For a detailed discussion of the problem, and a presentation of one possible solution, please see [55].

The Stokes-Q & U parameters provide us with the magnitude and orientation of the transverse magnetic field but they do not show the direction in which the transverse field is pointed. This ambiguity arises from the fact that for a given real transverse magnetic field the Stokes-Q & U parameters are identical to those from a magnetic field of the same magnitude, pointed in the opposite direction (unlike the longitudinal field where the Stokes-V parameter changes sign when the direction of the actual magnetic field changes sign). In actual practice, however, it is often not difficult to determine the actual direction of the magnetic field associated with active regions by visual inspection.

For example, it is known that, for a relatively simple round sunspot (as shown in Figure 3.13, above), the magnetic field should be nearly radial from the center of the spot (an example of this will also be shown in Section 3.7.4 below). The polarity of the spot is known from the longitudinal magnetogram. Therefore, if the spot has a positive polarity (white in the longitudinal magnetogram) the magnetic fields will be directed radially outward from the center while if the spot has a negative polarity (black in the longitudinal magnetogram) the magnetic fields will be directed nearly radially in towards the center. Typically, confusion only arises when the magnetic fields of strong active region become

highly twisted (when the transverse field is oriented approximately parallel to the boundary between the positive and negative longitudinal field). In that case, more care must be taken to properly calculate the actual direction of the magnetic field at points in the magnetogram where confusion might arise. This is especially important in strong active regions since the locations of the  $180^\circ$  ambiguity most often are associated with the occurrence of strong solar flares. For discussions on the various methods used to solve the  $180^\circ$  ambiguity in the azimuth of the observed transverse magnetic fields see [52], [53] & [54] as well as the paper mentioned above.

Also note that the vectors presented throughout this work, and on the Real-Time Magnetograms Web Page, are represented as lines and not arrows. Making sure that all of the vectors are displayed with the correct direction is a complicated process beyond the scope of this work. Also, as can be seen from the papers referenced in Section 3.4.5, there is not a single method that is accepted as standard to resolve this  $180^\circ$  ambiguity. Therefore, for the sake of simplicity, the transverse magnetic field is plotted as lines, instead of arrows which are normally associated with the representation of vectors, for the sake of simplicity.

### **3.3.10 Magnetograms on the Web**

Since the primary responsibility of BBSO is the monitoring and study of dynamic solar activity and the timely presentation of this information to the solar community, it is advantageous to make the most up-to-date vector magnetograms available as soon as possible. To accomplish this task, the observer can execute a simple software tool that will grab the most recent data from the DVMG. The data will be calibrated using the most recent flat field and dark frame images that are available and posted to the BBSO

“Latest Images” web page. The observer can input the exact region in the image that is to be presented in addition to the saturation and contour levels of the longitudinal magnetogram and the lower limit of the transverse magnetic field data that will be presented. From this information, the software tool generates 610.3 nm intensitygram (Stokes-I parameter) and longitudinal magnetic field images (Stokes-V parameter) that are presented alone and with longitudinal contours and transverse vectors overlaid on each.

**BBSO**  
Big Bear Solar Observatory

- General Information
- Staff
- Data
- Publications
- Meetings
- Projects
- Images
  - Live H-alpha
  - Latest
  - Gallery
  - Webcam
- Movies
- Local
- Links

Big Bear Solar Observatory  
40386 North Shore Lane  
Big Bear City, CA 92314  
Phone: (909) 866 5791  
FAX: (909) 866 4240

### High Resolution Observations

**BBSO high resolution 'white-light' image:** The direct image was observed with the digital vector magnetograph system in the line wing of the Cal line at 6103 Å at the 25 cm vacuum refractor. The image was recorded at 20:17:28 (UT) on August 25, 2004. (44 kBytes)

**BBSO high resolution digital magnetogram:** This longitude magnetograph image was observed with the digital vector magnetograph system at the 25 cm vacuum refractor. The image was recorded at 20:17:28 (UT) on August 25, 2004. (28 kBytes)

**BBSO high resolution digital vector magnetogram:** This vector magnetograph image was observed with the digital vector magnetograph system at the 25 cm vacuum refractor. The image is an overlay of the longitudinal and transverse fields. Red contour is positive and blue is negative polarity. Green is transverse fields. The image was recorded at 20:17:28 (UT) on August 25, 2004. The contours levels are set to +/- 100 and +/- 300 Gauss. (60 kBytes)

**BBSO high resolution digital magnetogram:** This vector magnetograph image was observed with the digital vector magnetograph system at the 25 cm vacuum refractor. The image is an overlay of the direct image, longitudinal and transverse fields. The image was recorded at 20:17:28 (UT) on August 25, 2004. The contours levels are set to +/- 100 and +/- 300 Gauss. (72 kBytes)

The high resolution images are not p-angle corrected. BBSO's high resolution images are available on our [FTP Archive](#).

**Figure 3.14** Sample of DVMG data on the BBSO Latest Images web page.

Figure 3.14 shows a sample of the vector magnetogram data on the BBSO latest images web page. The portion of the web page that is shown is from the high resolution section. From top to bottom the images are: 610.3 nm intensitygram, longitudinal

magnetogram, vector magnetogram w/ the longitudinal magnetogram as the background and vector magnetogram w/ the 610.3 nm intensitygram as the background. These images on the web page can be updated within seconds if desired by the observer by simply executing the simple software tool mentioned above.

### **3.4 Archiving the Data**

A major challenge with the logistics of operating a solar observatory is the storage of data. The main solar telescope at BBSO can have as many as seven cameras collecting data, at various wavelengths and image resolutions, simultaneously. The exact number of cameras, and the configurations in which they are operated, depends on the goals of the observations that day. These various cameras can consistently collect from five to seven gigabytes of data per day. Storing these data in a way that is relatively automatic and economical while, at the same time, will allow quick and convenient access to the data is of paramount importance.

To solve this problem, a central archiving computer has the task of collecting all of the data taken each day and storing those data on Digital Linear Tapes (DLT) which are capable of storing 40 gigabytes of data each. The data from each individual camera is initially stored on the computer which controls that camera. At the end of each observing day, the observer executes a script on the main archiving computer which collects all of the data taken that day from each individual instrument control computer. These data are then calibrated using the flat field and dark frames for each instrument that were obtained and calculated that day (see Section 3.1.1). Both the raw and calibrated data are stored on the DLT. Finally, a CD ROM is made which contains samples of each type of data

collected that day along with a log file which indexes the data so it can be easily located and restored when needed.

### **3.5 Automatic Web Page for Reviewing the Data**

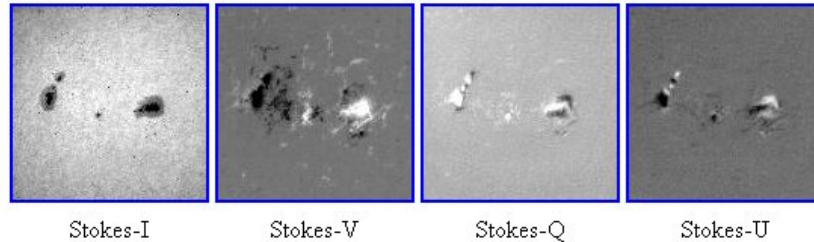
To enable people who are interested in using past magnetogram data to quickly, and easily see which active region, or regions, were observed on any particular day, the main archiving computer executes an automatic script at the end of each observing day. This script generates a web page which displays a sample data set of each unique active region that was observed that day. Written in Interactive Data Language (IDL), this script automatically reads the coordinates and active region number from the FITS header of each set of images (Stokes-I, V, Q and U) observed that day. Thumbnail images of each Stokes component are created so interested parties can see which active regions were observed each day and whether full stokes vectors or only longitudinal data were obtained. This web page also provides convenient web links to the observing logs and Active Region Monitor web page (ARM, see Section 3.2, above) for that day. The daily magnetogram summary web page can be found by accessing the daily archive for each day via the BBSO home page.

A sample of the DVMG Data Summary page for 04Jun16 is shown in Figure 3.15. Any interested party can quickly see that two active regions were observed that day (NOAA 10634 and NOAA 10635) and that a full Stokes data set (Stokes-I, V, Q & U) was obtained for each active region. Additional information about the details of the observations performed that day can be seen in the observing logs.



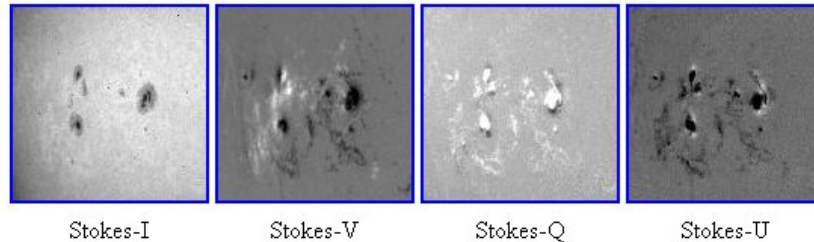
---

NOAA 10634. For additional info please see the [observing log](#).



---

NOAA 10635. For additional info please see the [observing log](#).



---

This page was automatically generated at 19:05 on 2004JUN16.

**Figure 3.15** A sample of the DVMG Data Summary page for 04Jun16.

Note that vector magnetograms are not generated for the DVMG Data Summary page for the following reasons. First, vector magnetograms tend to require user input to specifically set the area of each field-of-view for which a vector magnetogram will be generated and also input parameters such as the longitudinal magnetogram saturation level, the longitudinal contour levels, etc. These parameters are unique for each active region and are best left to the user who is working with specific vector magnetogram data of a specific active region. Secondly, since the purpose of the DVMG Data Summary

page is to simply provide a list of which active regions were observed on any particular day and whether vector magnetograms or longitudinal magnetograms were obtained it is not necessary to generate vector magnetograms for each data set.

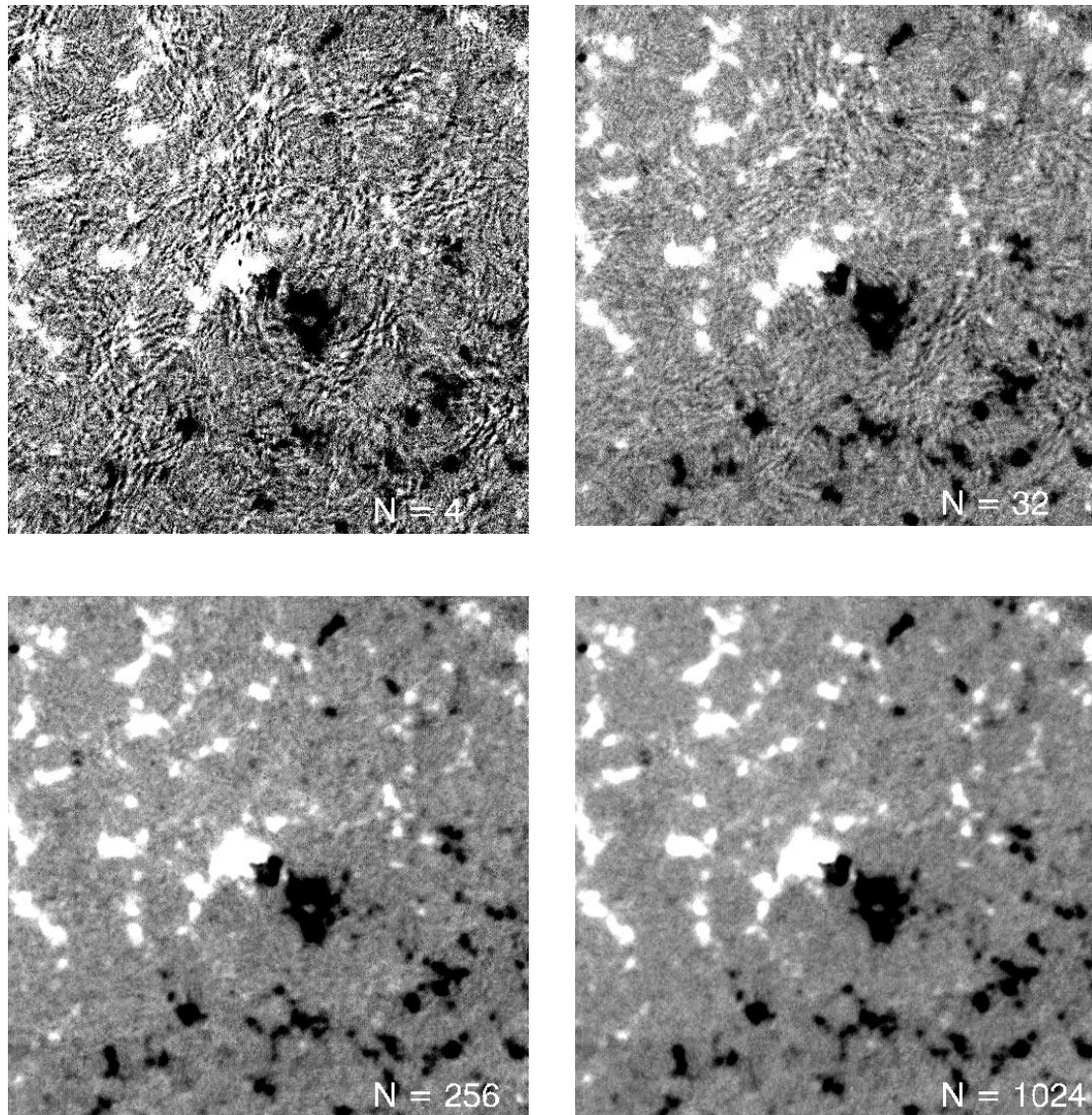
### **3.6 Evaluation of Data**

#### **3.6.1 Image Sensitivity vs. Number of Integrations**

The polarization signal, produced by the Zeeman effect, is only a small portion of the total light emitted from any individual location on the solar surface even when the magnetic field is relatively strong (the polarization signal from a 1000 Gauss field is ~6%, for example). Recall that a longitudinal magnetogram is produced by dividing the difference between the right and left-hand circularly polarized Stokes components by their sum:

$$V = (V_R - V_L) / (V_R + V_L), \quad (3.18)$$

where  $V_R$  is the integration of a number of right-hand circularly polarized images and  $V_L$  is the integration of a number of left-hand circularly polarized images. In general, the sensitivity of any individual magnetogram is a function of the number of integrations. This can clearly be seen in the longitudinal magnetograms shown in Figure 3.16.



**Figure 3.16** Four quiet-Sun longitudinal magnetograms obtained on 04Jan29.

Figure 3.16 shows four quiet-Sun longitudinal magnetograms obtained on 04Jan29. All magnetograms are presented with a saturation level of  $\pm 50$  G. The upper-left magnetogram was produced with four total integrations (0.48 sec total integration time), the upper-right magnetogram was produced with 32 total integrations (3.84 sec total integration time), the lower-left magnetogram was produced with 256 integrations

(30.72 sec total integration time) and the lower-right magnetogram was produced with 1024 integrations (122.88 sec total integration time).

One can easily see by simple visual inspection that the upper two magnetograms, which were produced with relatively few total integrations are relatively noisy when compared to those magnetograms that were produced with a greater number of integrations. It should be kept in mind, however, that the saturation level was intentionally set relatively low ( $\pm 50$  G) to accentuate the noise in these images.

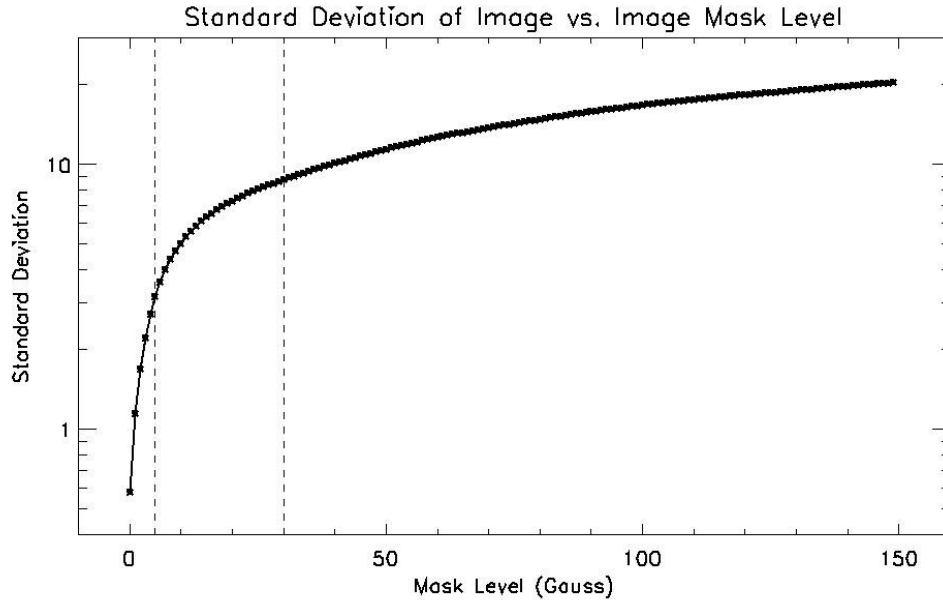
To quantify how the noise in longitudinal magnetograms is a function of the total number of integrations, one can plot the standard deviation of the data in areas where there are no real magnetic features vs. the total number of integrations of a series of magnetograms, each with a successively greater number of integrations (the total number of integrations in the images used for this test are  $2^N$ , where  $N = 2, 4, \dots, 10$ ). This procedure requires two steps. The first step is to separate the locations in the images that are dominated by noise from those that are dominated by real magnetic features by creating a mask which will identify the locations of the noise. The second step is then to determine the level of the noise in each successive image. The details of these two steps are discussed below.

#### Step 1) Determine Threshold of Noise Mask

The question now becomes how to select which areas in the magnetograms that should be used to determine the noise in each image. One method is to manually select regions where there are no real magnetic features by visual inspection. However, this method has the disadvantages of being prone to errors, since it is not necessarily reliable to visually distinguish very subtle features from noise, and of being tedious since a large number of

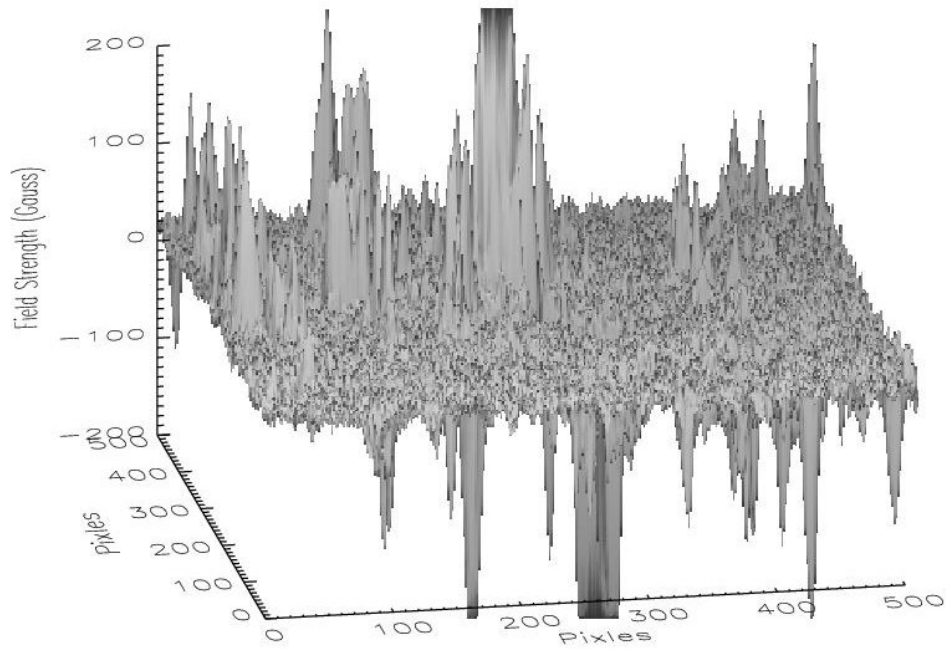
test areas are desired to accurately sample the entire image. Another method is to determine the standard deviation of the locations in the images whose signal level is below a certain threshold. This threshold value should be set so the portions of the image that are to be tested are dominated by noise. The question then becomes how to determine the threshold value at which the images should be tested.

To accomplish this task, a noise mask is generated which identifies all portions of the image created from 1024 total integrations (because the image with the greatest number of integrations in the test set presumably has the lowest noise) whose magnitude is below some selected threshold (150 Gauss to begin, in this case). Then, the standard deviation (in Gauss) of the portion of the image selected by that noise mask is determined. The threshold of the noise mask is then continually decreased (in 1 Gauss increments) and the standard deviation of the portion of the image that is selected by each new noise mask is determined, in turn. The standard deviation of the portion of the image selected by each unique noise mask is plotted vs. the threshold of each noise mask. The result is shown in Figure 3.17.



**Figure 3.17** The standard-deviation of the portion of the longitudinal magnetogram produced with 1024 total integrations (as shown in Figure 3.16) that was selected by the noise mask vs. the threshold of each noise mask.

A few points of discussion from the result seen in Figure 3.17. First, note that the standard deviation decreases as the threshold, used to create the noise mask, decreases. This is expected since the locations in the images with strong magnetic fields will be excluded as the threshold is lowered. This is demonstrated visually in Figure 3.18, which is a 2D surface plot of the lower-right magnetogram (the magnetogram with the most integrations) in Figure 3.16, above. It can be seen that, as the threshold value decreases, the strong features (here represented as the large peaks in Figure 3.18) are excluded from consideration and the standard deviation of the remaining portions of the image, taken as a whole, will thus decrease.

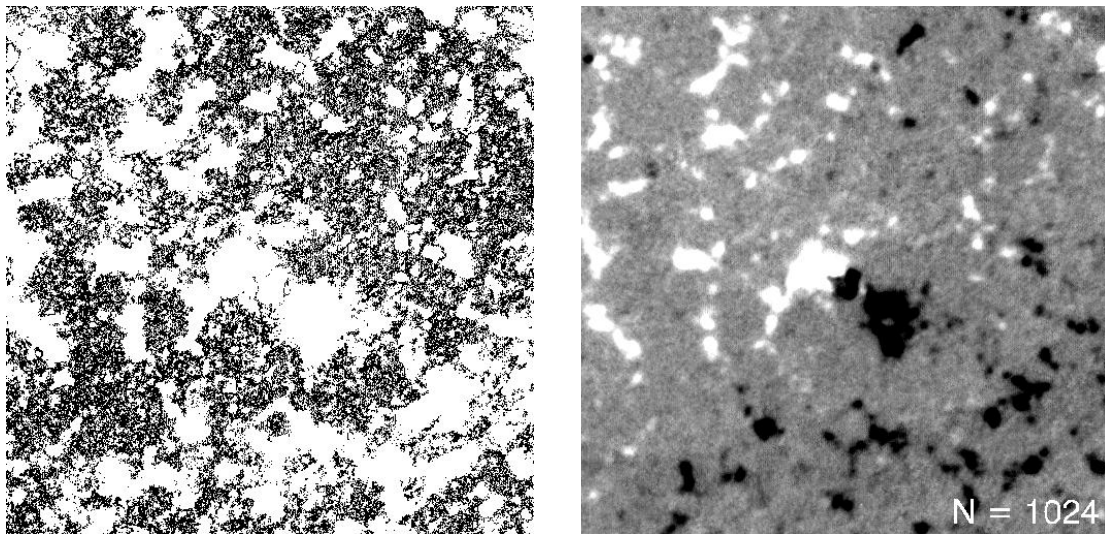


**Figure 3.18** 2D surface plot of the lower-right magnetogram in Figure 3.16.

Another point to note in Figure 3.17 is that the plot can be divided into three regions. The first region, from the highest magnetic field value to  $\sim 30$  G, the second region from  $\sim 30$  G to  $\sim 5$  G and the third region below  $\sim 5$  G. These three regions are indicated by the vertical dashed lines in Figure 3.17. The plot is approximately linear, when plotted in a linear-log scale, in the first and third regions. The reason for this is the following. When the threshold of the noise mask is greater than  $\sim 30$  G the standard deviation of the image is dominated by the strong, and therefore real, features in the image. When the threshold of the noise mask is less than  $\sim 5$  G the standard deviation of the image is dominated by the noise, since the vast majority of the real features have been excluded. The region in the plot between  $\sim 30$  G and  $\sim 5$  G is a transition region when the primary influence on the standard deviation calculation shifts from the real features to the

noise. Since the current goal is to determine the magnetic field strength below which the image is primarily dominated by noise, the threshold of the noise mask, from Figure 3.17, is selected to be 5 G (which is where the influence of the “real” features ends). This threshold value should exclude the vast majority of real magnetic features and include only the locations in the image which are dominated by noise.

The noise-mask that was used to determine the dependence of the sensitivity of the magnetograms on the total number of integrations is shown on the left in Figure 3.19, below, along with the magnetogram that was created from 1024 total integrations on the right (repeated from Figure 3.16, above). The black areas in the mask indicate the locations in the magnetogram where the strength of the magnetic field is less than 5 G.



**Figure 3.19** The noise mask (left) and the lower right longitudinal magnetogram from Figure 3.16.

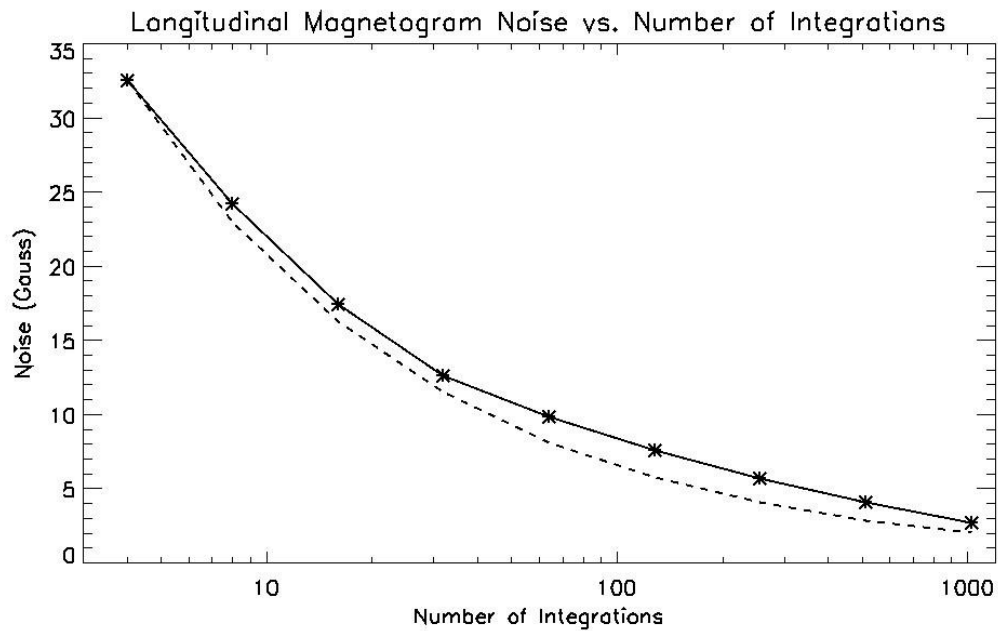


Step 2) – Determine the Noise Level of the Images as a Function of the Number of Integrations

Using the above mask, the standard deviation of the nine magnetograms, that were created each from an increasing number of total integrations (4, 8, 16, 32, 64, 128, 256, 512 & 1024), is calculated. The result is shown in Figure 3.20 The solid line is a plot of the standard deviation in each magnetogram using the above mask vs. the total number of integrations. The dashed line is a plot of:

$$\frac{1}{\sqrt{N}}, \quad (3.19)$$

(which is how one would expect the noise to decrease under ideal conditions) using the noise value from the magnetogram with four total integrations as a reference, where N is the total number of integrations.



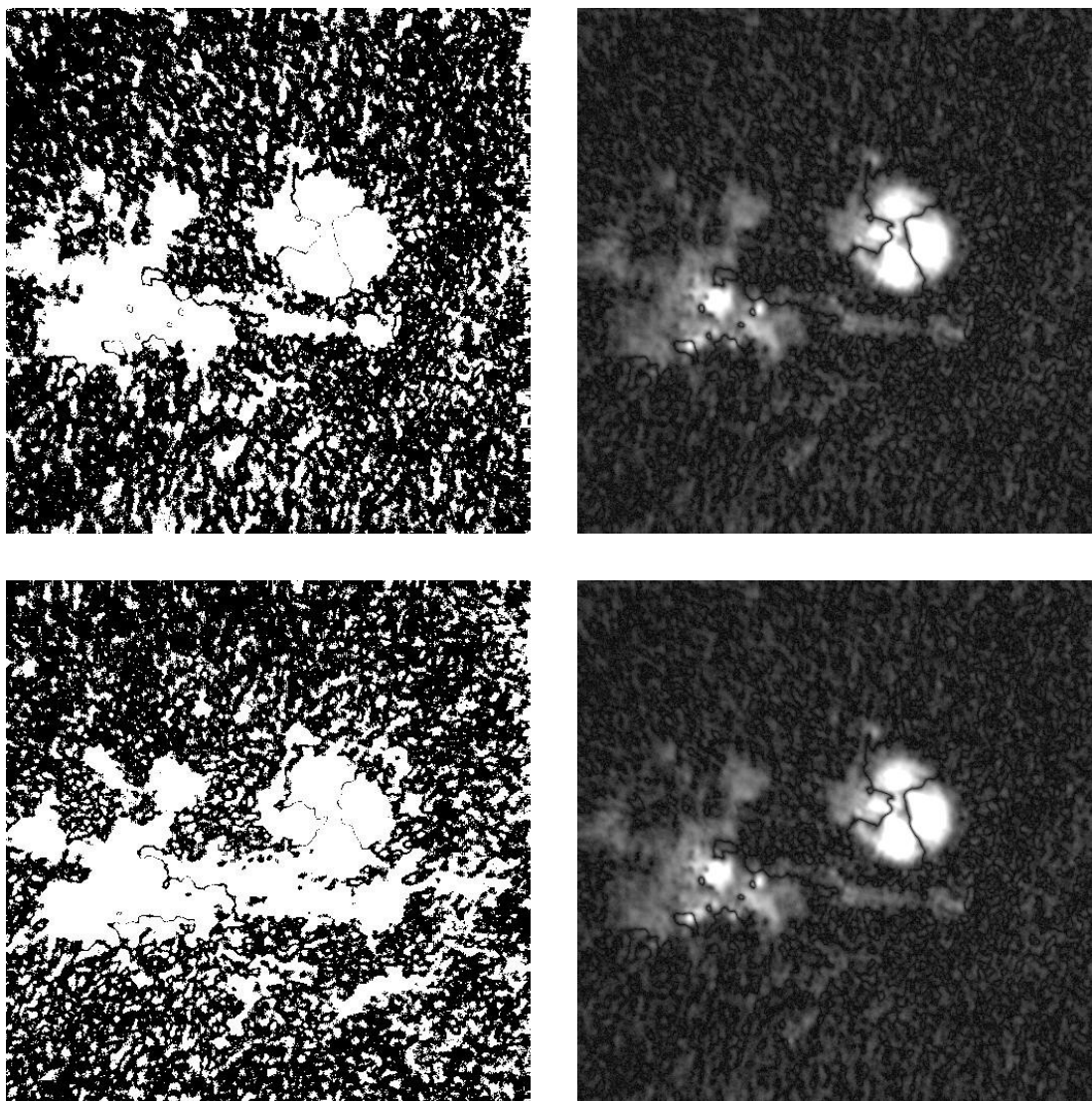
**Figure 3.20** The standard deviation of a set of longitudinal magnetograms vs. the number of integrations in each image.

One can see that the noise does decrease as the total number of integrations increases. However, the noise does not decrease quite as fast as one might expect from the ideal case. At a certain point, integrating longer does not detect weaker magnetic fields because of the blurring effect of the atmosphere of the Earth and the fact that the weakest features on the Sun are stable only for a few minutes (recall that it takes ~123 seconds to integrate 1024 images). This plot indicates that the practical lower limit for detecting longitudinal magnetic fields on the Sun is ~4 G (when 1024 integrations are used to create the magnetogram), with the typical scale of 0.6 arc-sec per pixel (which is the standard scale of the DVMG). If one wishes to detect weaker magnetic fields, the scale of the images would have to be decreased (thus concentrating more light on each pixel) with the accompanying loss in resolution or the instrument must be modified to provide greater light throughput.

A similar test can be performed on the Stokes-Q and U images. The left images in Figure 3.21 show noise maps for Stokes-Q & U images while the right images show the corresponding Stokes-Q & U images. The images used for this test are transverse magnetic field images based on:

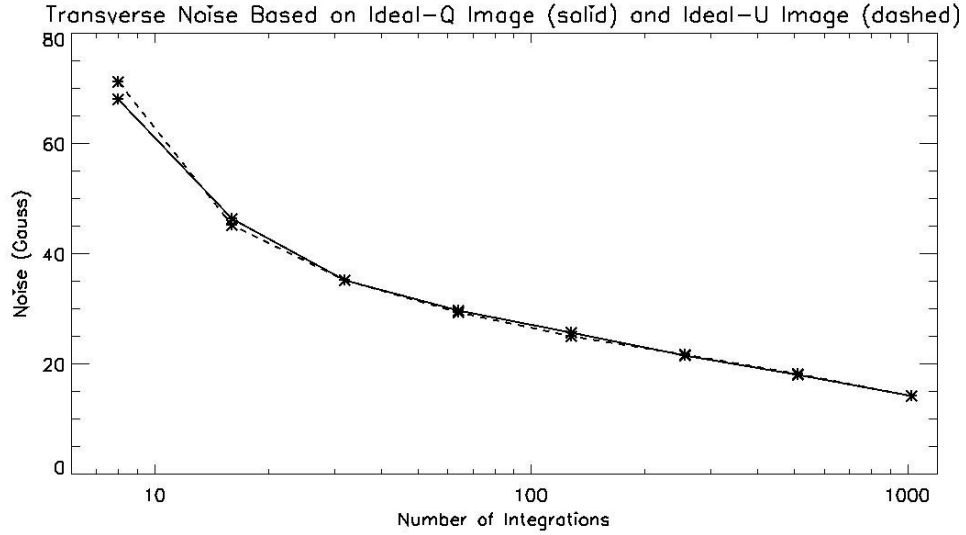
$$B_T = K_T * (Q^2 + U^2)^{1/4} \quad (3.20)$$

(as in Section 3.4.4, above) where the U parameter of the magnetic field is assumed to be zero for the determination of the noise in the Q image and the Q parameter of the magnetic field is assumed to be zero for the determination of the noise in the U image. (This idealization is to keep the noise test for the Stokes-Q and U parameters in context with that for the Stokes-V parameter).



**Figure 3.21** BT (left images) and  $\alpha$  (right images) images for the Stokes-Q (upper set) and Stokes-U (lower set) images.

A plot of the noise (in Gauss) vs. the number of integrations is shown in Figure 3.22. The solid line indicates the noise of the ideal Stokes-Q parameter while the dashed line indicates the noise of the ideal Stokes-Q parameter. Note that, from Figure 3.20, the practical lower limit for detecting longitudinal magnetic fields on the Sun is  $\sim 15$  G (when 1024 integrations are used to create the magnetogram).



**Figure 3.22** A plot of the noise (in Gauss) vs. the number of integrations for the idealized Stokes-Q (solid) and idealized Stokes-U (dashed) images.

Note that, the measurements of the transverse magnetic fields tend to be less accurate than the measurements of the longitudinal magnetic field. For a given magnetic field strength, the polarization signal for a transverse magnetic field is  $\frac{1}{2}$  the strength as that of the same longitudinal magnetic field, thus requiring a longer integration which allows more time for seeing to degrade the image. Then, to create the transverse magnetic field image, two long integrations (Stokes-Q and U), which were not obtained simultaneously, must be combined. Also, a filter-based magnetograph which uses the weak-field approximation (line profile method) to measure the magnetic field via the Zeeman effect is not optimized to measure the Stokes-Q and U components. Thus decreasing the sensitivity of the instrument to transverse magnetic fields. Cross-talk, which is contamination of the Stokes-Q and U components by the longitudinal magnetic field as discussed in Section 3.7.2, slight non-uniformities in the operation of the liquid crystals and slight changes in the optimal flat field images over time must also be

considered. In actual practice, the lower limit for reliable measurements of transverse magnetic field on the Sun tends to be on the order of 100 Gauss.

### **3.6.2 Image Post Processing (Alignment and Selection)**

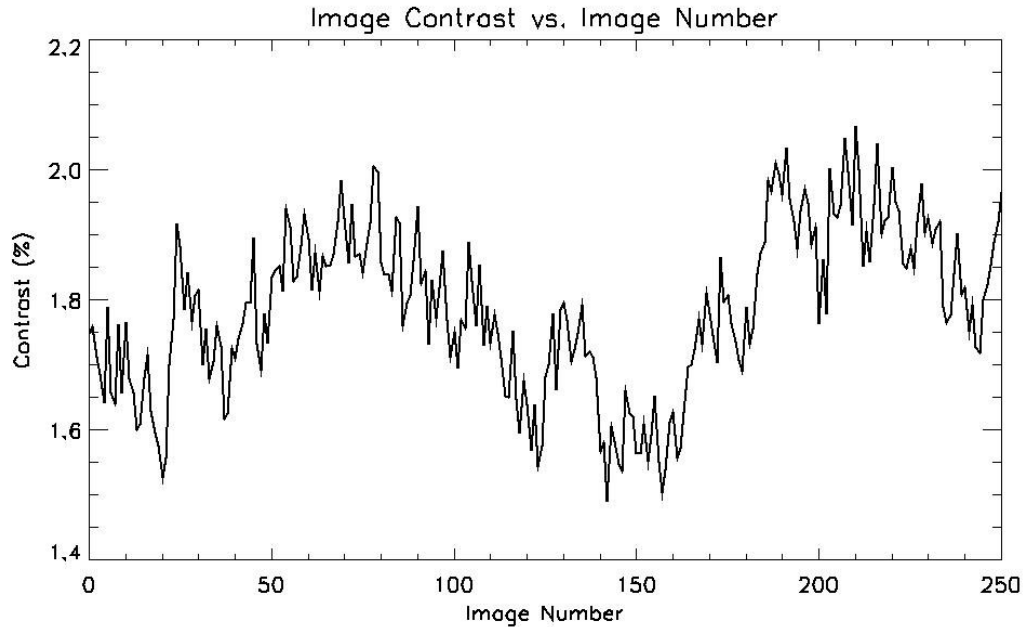
As stated several times previously, images that are produced by ground-based telescopes suffer from seeing, the continual shimmering caused by the atmosphere of the Earth. The net result of seeing is that ground-based observations can not reach the theoretical resolution that is determined by the aperture of the primary objective (a mirror in the case of a reflecting telescope or a lens in the case of a refracting telescope). While the effects of seeing are unavoidable, they can be minimized. When determining where to install a ground-based telescope, the climate at the site (in the number of clear days per year) and the seeing are both studied very carefully. Only sites that have many clear days per year and also have relatively good seeing are selected. Then, once the location of the telescope is determined, great care is taken when constructing the telescope and the building that will contain the telescope so that the good seeing at the site is preserved. The building is constructed in such a way as to maintain proper air flow around the telescope, sources of heat are kept far away from the telescope, etc.

However, even when a site with relatively good seeing is selected and care is taken to preserve that good seeing, the images produced by any telescope always suffer degradation from the blurring effects of the atmosphere. This is especially the case with images that require long integrations (many seconds) such as magnetograms (see Section 3.7.1, above).

In general, to obtain a longitudinal magnetogram (for example), many integrations are simply averaged. During the integration, the quality of each consecutive image is

continually changing and the images are continuously being translated (in right ascension and declination) slightly as the quality of the seeing changes in real time. These two effects degrade the quality of the final magnetogram. To illustrate the continuous variation in the quality and translation of the images produced by a ground-based telescope, a series of 256 magnetograms was obtained as rapidly as possible. Each magnetogram contained a total of 4 integrations (for a total of 0.48 sec of integration time each). The time between each consecutive magnetogram is  $\sim 3 \frac{1}{2}$  seconds.

To evaluate the quality of the magnetograms, the contrast of the magnetograms was plotted vs. the image number, as was discussed previously in Section 3.1.3.1. This can be seen in Figure 3.23. One can see that there can be a significant change in the contrast of an individual magnetogram in just a few seconds. (Note that there can be significant changes in image quality on the time scale of several tens of milli-seconds, as can be seen in Figure F.1 in Appendix F.3.1.)



**Figure 3.23** Plot of the contrast of a set of magnetograms vs. the image number.

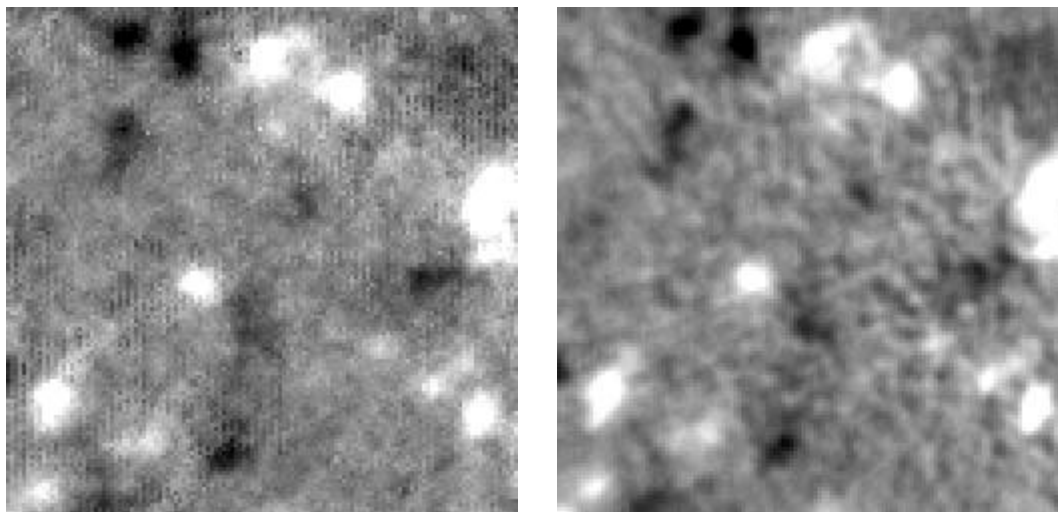
Figure 3.24, plots of image translation in arc-sec vs. image number, referenced to the first image in the series. The solid line represents the translation in right ascension, while the dashed line represents the translation in declination. One can see that, for this particular series of magnetograms, the translation can be as much as  $\sim 3$  arc-sec ( $\sim 5$  pixels). The result of this real-time change in translation is that the magnetogram will be blurred during the integration by imaging an individual feature on several pixels, thus lowering the effective resolution of the magnetogram.



**Figure 3.24** Plot of image translation of a set of magnetograms in arc-sec vs. image number.

One method to mediate this degradation of magnetograms caused by seeing is to produce many magnetograms, each with few integrations, and save each magnetogram as a separate file (as was done in the example above). The individual magnetograms can then be tested for quality, selecting only the best magnetograms in the set, and aligned before integrating the magnetograms into the final magnetogram. The results of image selection and alignment can be seen in Figure 3.25.



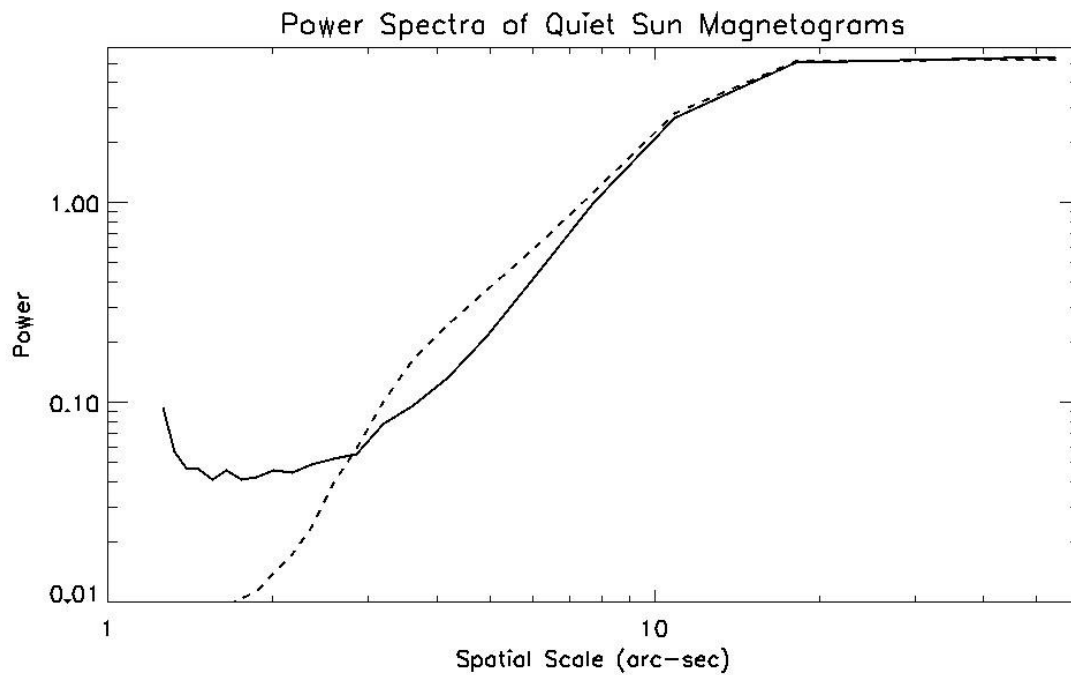


**Figure 3.25** Longitudinal magnetograms not using (left) and using image selection & alignment.

The images in Figure 3.25 show a fraction of the total field-of-view of the DVMG. In this case, the images are 75 x 75 arc-sec (as opposed to the full field-of-view of 300 x 300 arc-sec). The left image is the integration of the first consecutive 128 magnetograms without performing any image selection or alignment. The right image is the integration of the 128 magnetograms, which had the best contrast (from Figure 3.23) after the magnetograms had been aligned. One can clearly see that the magnetic features in the right image (with selection and alignment) are more clearly defined than the same features in the left image (without selection and alignment).

The improvement made by selecting the images with the best contrast and then aligning the magnetograms can be estimated from Figure 3.26. The solid line is a power spectra obtained from the left magnetogram in Figure 3.25 while the dashed line is a plot of the power spectra of the right magnetogram in Figure 3.25. The x-axis of the figure is in arc-sec. One can see that for features that are from 3 to 7 arc-sec in size (for this example) there is an obvious improvement in the power spectra, thus proving that

selecting the best images and then aligning them did indeed yield an improvement to the small scale features in these images. Of course, the primary tradeoff to gain this improvement in small details in the magnetograms is the additional post-processing required. However, if one is interested in studying the details of the small-scale magnetic features on the Sun, especially during less than ideal seeing conditions, this method can definitely improve the resolution of the magnetograms.



**Figure 3.26** Power spectra of left (solid) and right (dashed) magnetograms in Figure 3.25.

### 3.7 Sample Longitudinal Magnetograms

A few sample longitudinal magnetograms (Stokes-V), both of the quiet-Sun and of an active region, along with their corresponding 610.3 nm intensitygrams will now be presented and some important characteristics of each will be discussed.

As previously discussed, longitudinal magnetograms are easily visualized immediately from their Stokes-V parameter. The magnitude and direction of the magnetic field are represented by the intensity levels of a B&W image. All positive magnetic fields whose magnitude is greater than a set saturation level are plotted as pure white while all negative magnetic fields whose magnitude is greater than the set saturation level are plotted as pure black. Any magnetic field whose magnitude is less than the set saturation level are plotted as a gray level whose intensity corresponds to the magnitude and direction of the magnetic field at that point.

The saturation point can be set to optimize the image so the details of the strong magnetic fields may be emphasized (with a high saturation point) or the fine structure of the weak magnetic fields may be studied (with a low saturation point). The value of the saturation level will typically depend on the location on the Sun which is being imaged. When studying the quiet-Sun one tends to use a lower saturation value since the quiet-Sun does not contain strong magnetic fields while a higher saturation level is typically used to view active regions to gain an overall idea of the complexity of the magnetic field as a whole. Of course, this saturation level is only used to control the display setting of the image and does not effect the actual data contained in each image.

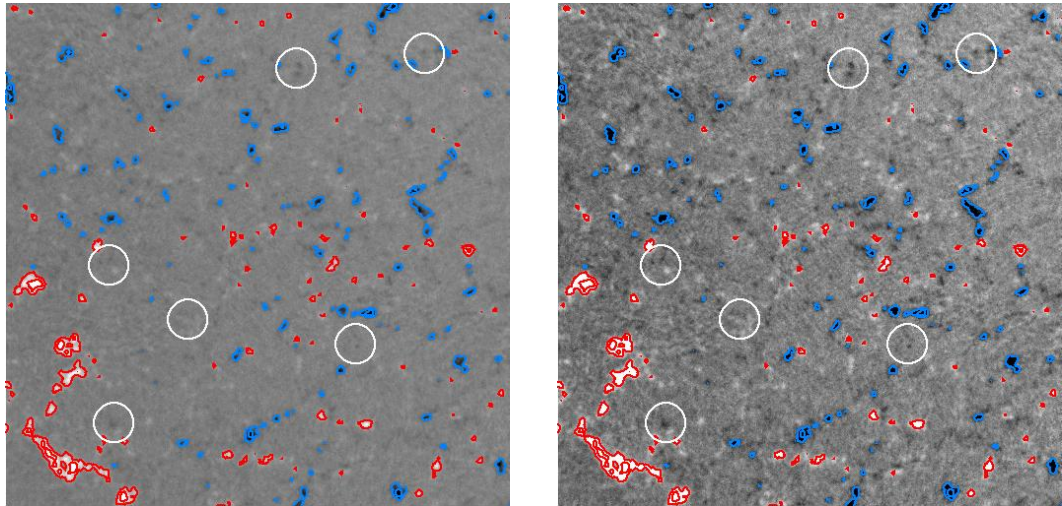
### **3.7.1 Sample Quiet-Sun Longitudinal Magnetogram**

Figure 3.27 shows a typical quiet-Sun magnetogram obtained at 15:57 UT on September 13, 2004 displayed using two different saturation levels. The left image is displayed using a saturation level of  $\pm 200$  G while the right image is displayed using a saturation level of  $\pm 75$  G. The contours are set to  $\pm 200$  G and  $\pm 50$  G. Red contours are typically used to indicate the positive longitudinal fields and blue contours are typically used to indicate

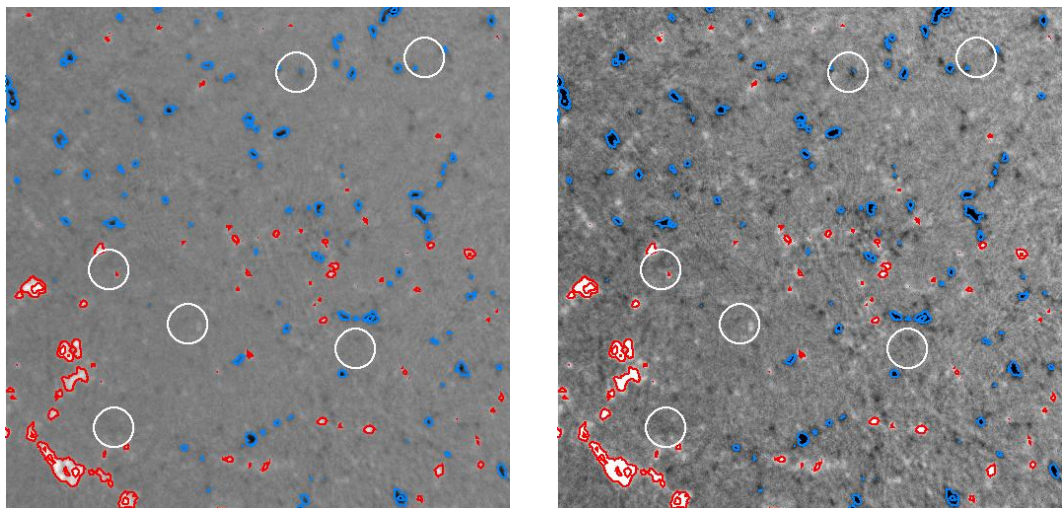
the negative fields. The magnetogram is the average of 128 pairs of the Stokes-V parameter (34 sec total integration time). The field of view is 300 arc-sec x 300 arc-sec.

The strongest positive magnetic field in this particular image is 415 G while the strongest negative magnetic field is -346 G. The smallest features visible are ~10 G (some of which are marked by the white circles). One can see that the left image emphasizes the overall structure of the relatively weak quiet Sun magnetic fields, which make up the network field, while the right image emphasizes the very small scale structures (on the order of 1 arc-sec or 725 km) and the weakest magnetic elements on the Sun while the details of the stronger fields are saturated.

Figure 3.28 shows a magnetogram obtained under comparable seeing (to the magnetogram shown in to Figure 3.27) at 16:32 UT, 35 minutes after those displayed in Figure 3.27, obtained (the contrast of the  $V_R$  component used to create the magnetogram shown in Figure 3.27 is 1.98% while the contrast of the  $V_R$  component used to create the magnetogram shown in Figure 3.28 is 1.90%). A careful study of the fine details of these images will reveal changes in the small scale structure of the magnetic field, even over this short time. The white circles in both figures mark the locations of a few examples where changes can be seen.

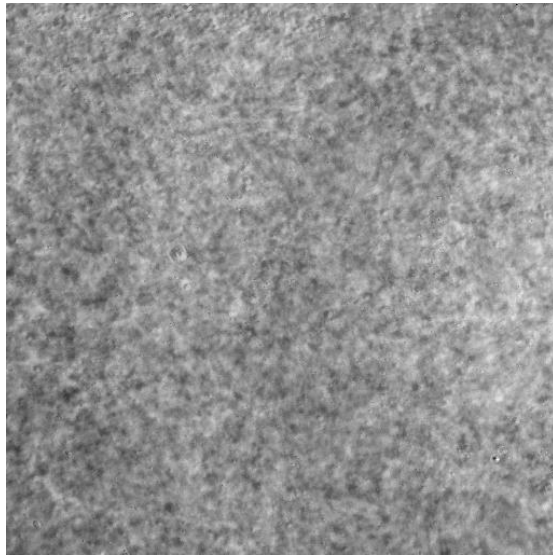


**Figure 3.27** Quiet Sun longitudinal magnetogram acquired at 15:57 UT on September 13, 2004.



**Figure 3.28** Quiet Sun longitudinal magnetogram acquired at 15:57 UT on September 13, 2004.

Figure 3.29 is of the 610.3 nm intensitygram (shown for completeness) which corresponds to the magnetogram in Figure 3.27. Note that there are no sunspots in this image because the magnetic fields found in the quiet-Sun are not strong enough to suppress the convective heat transfer from beneath the photosphere (Section 1.2).

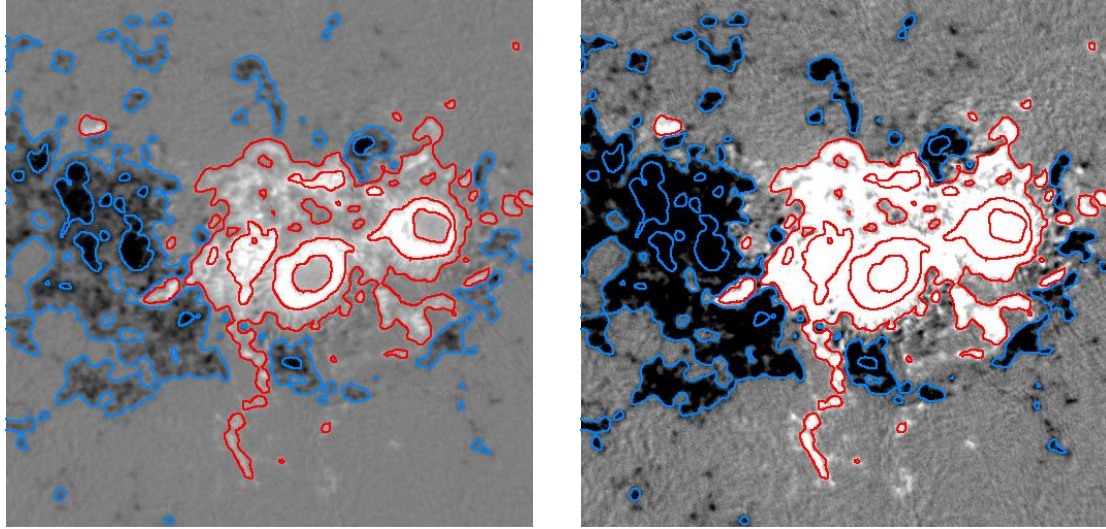


**Figure 3.29** 610.3 nm intensitygram obtained at 15:57 UT.

As discussed previously, longitudinal magnetograms (Stokes-V) alone are sufficient to accurately represent the magnetic field of the quiet-Sun, especially when viewed at or near the center of the solar disk, because the magnetic fields of the quiet-Sun are mostly vertical to the solar surface and the transverse components (Stokes-Q & U) are basically zero.

### **3.7.2 Sample Active Region Longitudinal Magnetogram**

Figure 3.30 shows longitudinal magnetograms of active region NOAA 10652 on July 23, 2004. The left image is displayed with a saturation level of  $\pm 750$  G while the right image is displayed with a saturation level of  $\pm 200$  G. The contour levels are set to  $\pm 500$  G and  $\pm 200$  G. The field-of-view in both cases is  $150 \times 150$  arc-sec. Again, one can see that the image with the higher saturation level emphasizes the overall morphology of the active region while the image with the lower saturation level allows one to study the details of the weaker magnetic fields.



**Figure 3.30** Longitudinal magnetogram of active region NOAA 10652 obtained July 23, 2004.

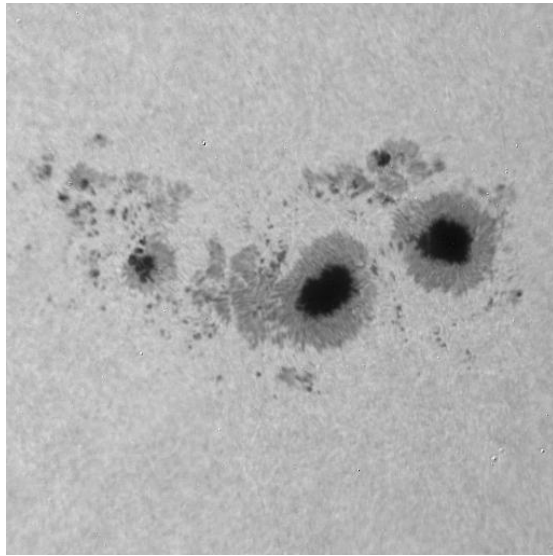
A few remarks regarding the magnetogram of NOAA active region 10652 in Figure 3.30 above. First, the magnetic field at the center of the sunspots (corresponding to the umbras of the sunspots) appears to be weaker than those fields found further from the center of the sunspots. This can easily be seen in the left image of Figure 3.30 as the “holes” in the positive (white) magnetic field. This is an example of Zeeman saturation (Section 2.9.1). For a brief review, recall that the splitting of the absorption line used to measure the magnetic field is a function of the strength of the magnetic field. Using the weak field approximation, the DVMG infers the strength of the magnetic field on the Sun by measuring the difference in intensity of the right and left-hand polarized (in the case of the longitudinal magnetic field) light from the Sun in the wing of the Ca II 610.3 nm absorption line. However, if the splitting becomes too great, this approximation no longer holds true and the strength of the magnetic field is no longer a function of the

difference in intensity between the two polarizations. Hence, the name weak field approximation (see Section 2.9.1 for a more detailed explanation of Zeeman saturation).

Also note that while the active region is generally bipolar – the leading (western) part is positive (white) and the following (eastern) part is negative (black) – also note that there is some negative magnetic field mixed in with the positive and some positive magnetic field mixed in with the negative (this is more clearly seen in the right image in Figure 3.30). This effect is known as “magnetic mixing”. Areas of an active region where magnetic mixing is present tend to be the most interesting because these areas typically have large gradients in the magnetic field and also the magnetic fields tend to be highly twisted. Thus, the areas of magnetic mixing tend to be the locations where large amounts of energy are stored and the likelihood of a solar flare in areas of magnetic mixing tends to be high. While the gradients in the magnetic field can be determined from the longitudinal magnetic field (Stokes-V) by plotting the contours (as in Figure 3.30) the direction of the transverse magnetic field needs to be plotted to see the twist. Displaying the full vector magnetic field will be addressed in Section 3.8.

Figure 3.31 shows a 610.3 nm intensitygram which corresponds to the longitudinal magnetogram shown in Figure 3.30. The total integration time is 120 ms. The image has been corrected for dark signal and flat field non-uniformities and has been edited using an unsharp-masking technique to allow details in both the quiet-Sun and the penumbras of the sunspots to be viewed simultaneously. North is to the top and east is to the left. Note that the umbras of the sunspots correspond to the strongest magnetic fields while the penumbras of the sunspots correspond to somewhat weaker magnetic fields (Section 1.2).





**Figure 3.31** 610.3 nm intensitygram corresponding to the magnetogram shown in Figure 3.30.

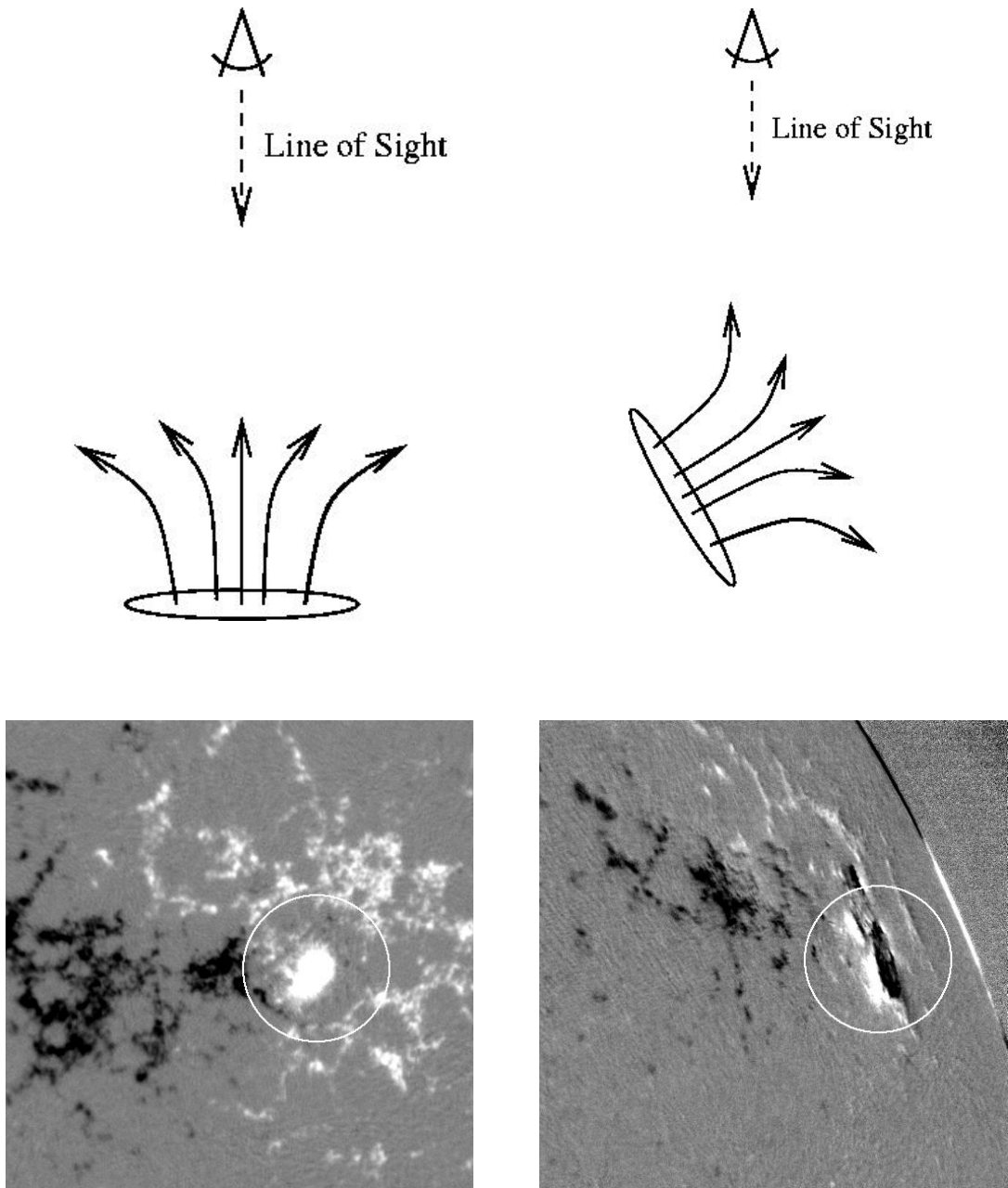
### **3.7.3 The Limb (Canopy) Effect**

At the beginning of Section 3.8, it was stated that the magnitude and direction of the longitudinal magnetic field is represented visually by the gray scale value of the longitudinal magnetogram. In the actual data, the magnitude is represented by the scalar value in each pixel and the direction is represented by the corresponding sign. This remains true. However, it must be kept in mind that the review of magnetic field components as discussed in Section 3.7.2.1 above.

Recall that the coordinate reference for the longitudinal magnetic field is the line-of-sight. If, for example, the magnetic field is pointing towards the Earth, it is perceived as positive (white). It must also be noted that the line-of-sight is continually changing due to the rotation of the Sun (recall that the Sun at the equator completes one rotation in ~28 days). For example, when a positive (white) mono-polar area of an active region is carried near the solar limb by the rotation of the Sun, the limbward portion of the field

will begin to point away from us. Note that this is not a change in the actual direction of the magnetic field, relative to the solar surface, but simply a projection effect due to the changing line-of-sight due to the rotation of the Sun. Thus, the longitudinal magnetic field in that area will now appear negative (black).

Figure 3.32 shows an example of the limb effect, including a schematic of the fan-like structure of the magnetic field. The image on the left shows a longitudinal magnetogram of NOAA active region 10663 on August 25, 2004 when it was near the center of the solar disk with a corresponding schematic of the solar magnetic field while the image on the right depicts the same active region several days later on August 30, 2004 later when it was near the solar limb. Note that the leading (westward, on the right identified with the circle) portion of the active region is a positive (white) sunspot. Note that the limb-ward portion of the main sunspot has reversed polarity from positive (white) to negative (black). From the schematics in Figure 3.32, it can be seen that the orientation of the magnetic field relative to the solar surface has not changed. The polarity of the limb-ward portion of the magnetic field has reversed because the rotation of the Sun has changed the line-of-sight and the limb-ward portion of the magnetic field is directed away from us along the line-of-sight. (Also note that the black and white stripe effect, which appears on the solar limb, is caused by the apparent motion of the solar limb during the integration due to seeing and not a real magnetic effect.)



**Figure 3.32** Example of the Limb Effect.

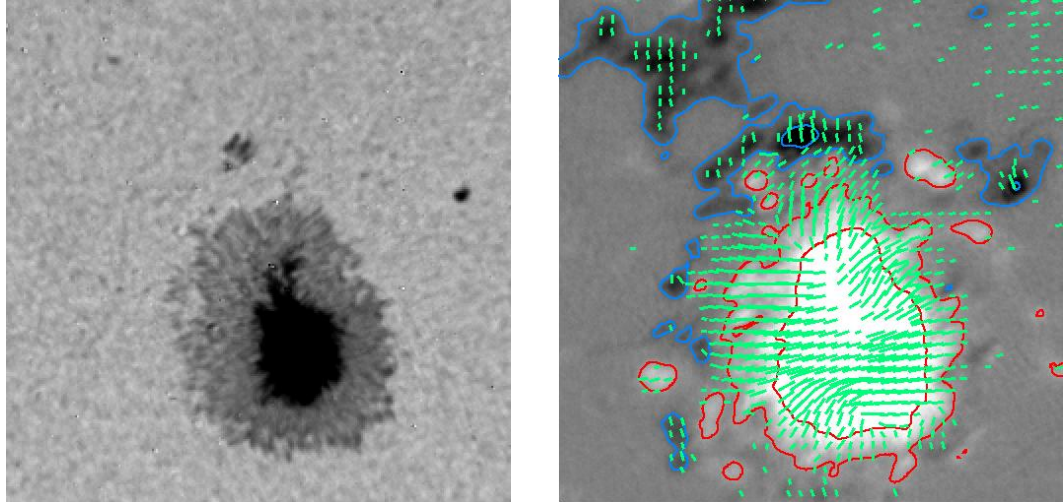
### **3.8 Sample Vector Magnetograms**

To conclude Chapter 3, sample vector magnetograms will be presented and discussed. The procedure for creating the vector magnetograms was discussed in Section 3.4.4, above. A set of magnetograms from before and after a solar flare will be presented which will note the dynamics of solar phenomena, which will be discussed in detail, in Chapters 4 and 5.

#### **3.8.1 Test Instrument on a Simple Round Sunspot**

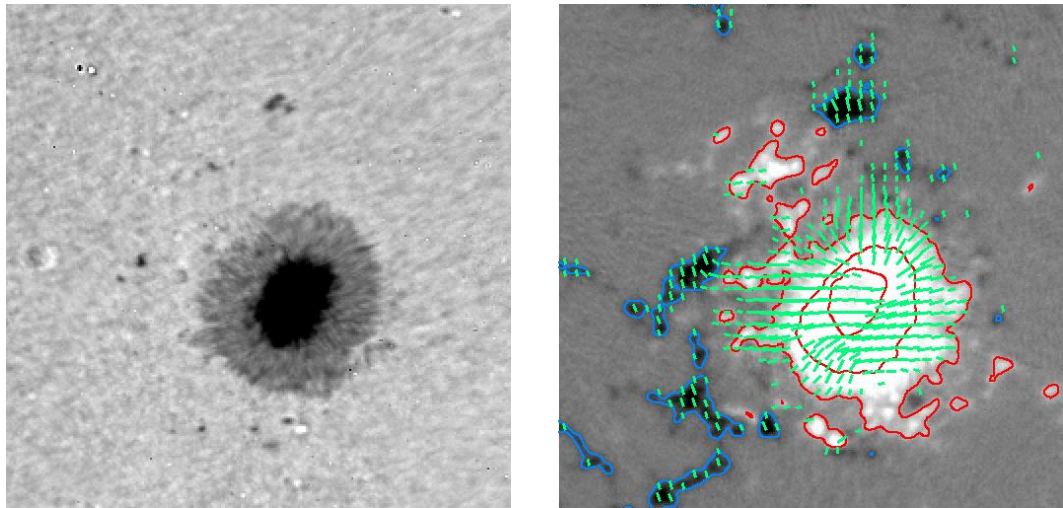
Figures 3.33 and 3.34 show two examples of vector magnetograms of NOAA active regions 10306 on March 12, 2003 and 10330 on April 8, 2003, respectively. Both active regions are dominated by simple round sunspots. The field-of-view in both figures is 150 x 150 arc-sec. The left images in both figures are 610.3 nm intensitygrams while the right images are the corresponding vector magnetograms.

The background images of the vector magnetograms are the longitudinal magnetograms as discussed in Section 3.8.2 above. In Figure 3.33 the saturation level has been set to  $\pm 500$  G while in Figure 3.34 the saturation level has been set to  $\pm 300$  G. The contours (red and blue lines) have been set to  $\pm 500$  G and  $\pm 100$  G in both cases.



**Figure 3.33** 610.3 nm intensitygram (left) and vector magnetogram (right) of active region NOAA 10306 on 03Mar12.

The length and direction of the green lines in the magnetogram image represent the strength and direction of the transverse magnetic field, respectively. It should be noted that the vectors near the center of the sunspots, especially those in Figure 3.34, tend not to be reliable due to Zeeman saturation, which was discussed previously (Section 2.9.1).

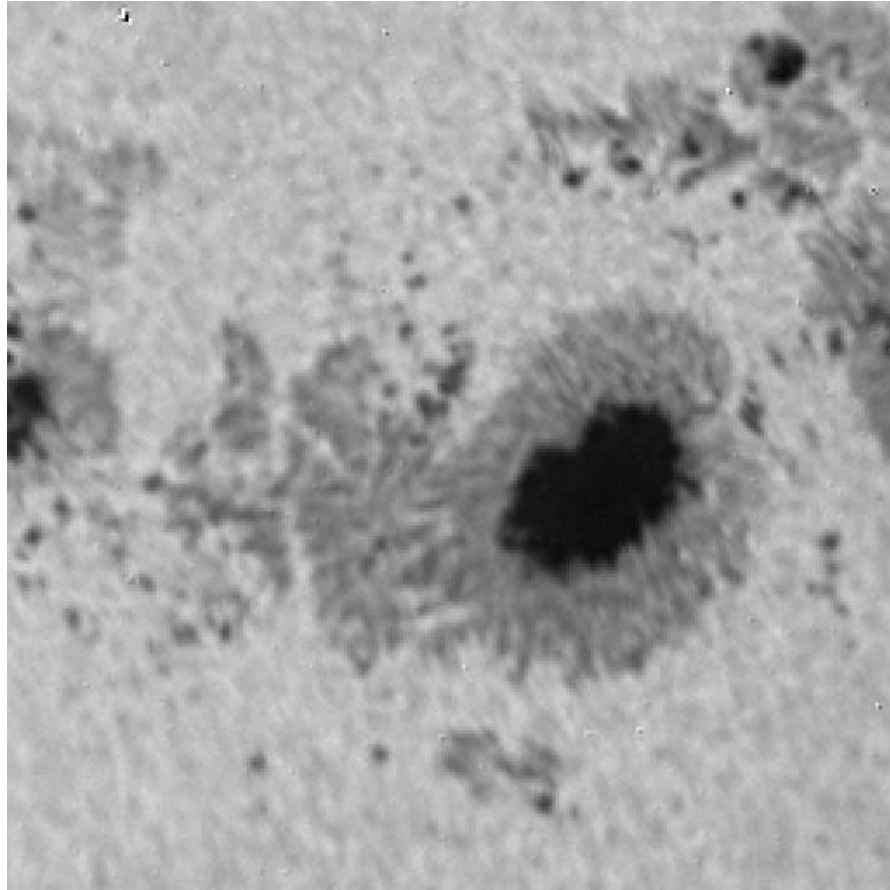


**Figure 3.34** 610.3 nm intensitygram (left) and vector magnetogram (right) of active region NOAA 10330 on 03Apr08.

The reason that it is important to acquire vector magnetograms of simple round sunspots is that it is known, from theory and experience, that the transverse magnetic fields of such a sunspot should appear to be generally radial when viewed near the center of the solar disk, where the projection effects are at a minimum, as can be seen in Figures 3.33 and 3.34. A simple round sunspot provides us with a nearly ideal case to test whether the instrument and the code that reduces the data is working properly, especially when the instrument is in the final stages of development and all of the individual components are being integrated on the telescope. Therefore, it is always a good idea to acquire vector magnetogram data when a simple round sunspot is near the center of the solar disk to ensure the instrument is working properly. When there is confidence in the vector magnetograms produced from a simple round sunspot and are sure that the instrument is working properly then there will be confidence in the vector magnetograms produced from a more complex active region (Section 3.9.2).

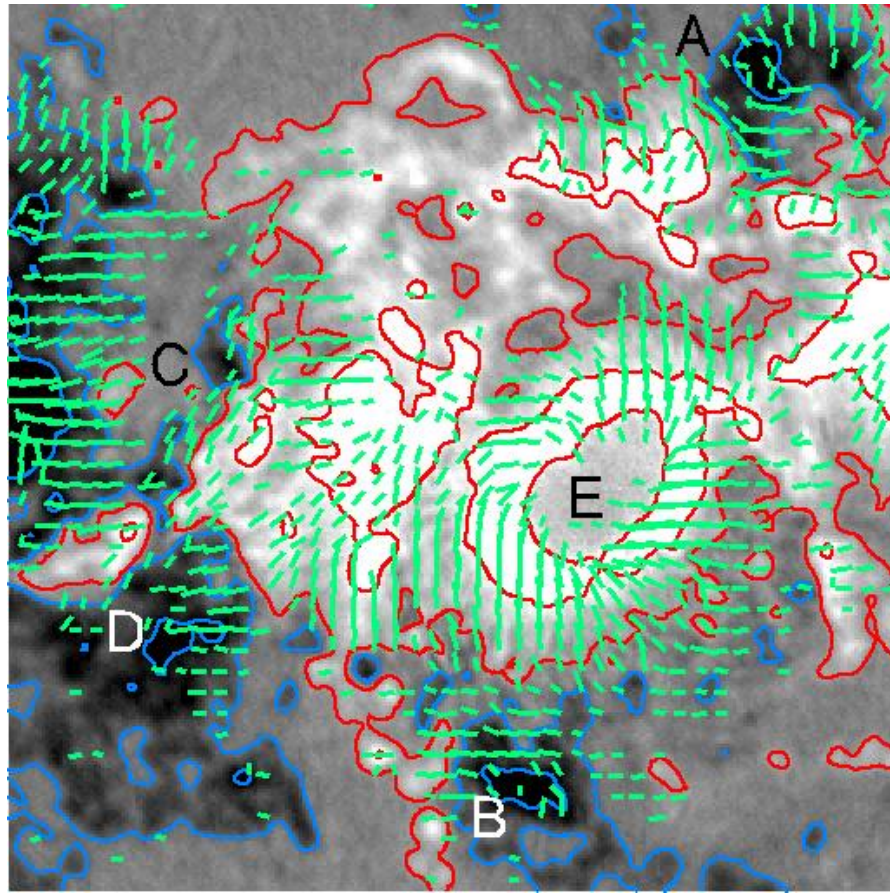
### **3.8.2 Active Region With a Complicated Magnetic Field**

Figures 3.35 And 3.36 show an example of complex NOAA active region 10652 on July 24, 2004. Figure 3.35 shows the 610.3 nm intensitygram while Figure 3.36 shows the vector magnetogram. The saturation level for the longitudinal magnetogram has been set to  $\pm 500$  G and the contour levels have been set to  $\pm 500$  G and  $\pm 100$  G. The field of view is 150 x 150 arc-sec. One can see that, unlike the two active regions presented in the previous section, NOAA active region 10652 is a complicated active region. Actually, NOAA active region 10652 is much larger than the field-of-view shown here but only  $\frac{1}{4}$  of the total field-of-view is presented so the finer details of this active region can be properly displayed



**Figure 3.35** 610.3 nm intensitygram of active region  
NOAA 10652 on 04Jul24.





**Figure 3.36** Vector magnetogram of active region NOAA 10652 on 04Jul24.

A few points of discussion about this active region. The magnetic field in NOAA active region 10652 is relatively complex. Note that this active region contains areas where there is are large magnetic gradients (the area to the lower-right of A and the area to the upper-left of B), areas where there is strong magnetic shear (when the angle of the transverse magnetic field, indicated by the green lines, deviates from normal to the contour lines) (the area to the lower-right of A and the area to the right of C) and areas of magnetic mixing (the area to the upper-left of D). Also note the twist in the radial magnetic field in the main sunspot in the image (the area around E). All of these



characteristics of the magnetic field (strong gradients, shear, magnetic mixing and twist) indicate that the magnetic field is storing magnetic energy and will likely produce large solar flares. Also note the area of Zeeman saturation (the “hole” in the magnetic field at E) in the center of the largest sunspot.

## CHAPTER 4

### RAPID CHANGES IN THE SOLAR MAGNETIC FIELD

As was discussed in Chapter 1, the Sun is a dynamic object. Activity on the surface of the Sun ( $T \sim 6000\text{K}$ ) comes in the form of groups of sunspots known as active regions. These active regions are areas on the Sun where very strong magnetic fields (up to  $\sim 5000$  Gauss) have emerged from beneath the surface. These magnetic fields suppress the convective heat transfer near the top of the convection zone allowing the photosphere under the influence of the magnetic fields to cool ( $T \sim 5000\text{K}$ ) and appear darker than the nominal solar surface.

Wound up by the turbulent motions of the solar material at the top of the convection zone, the solar magnetic field can accumulate enormous amounts of potential energy. Strong solar magnetic fields can reorient themselves on time scales of less than one hour. (In actuality, the changes most likely occur in just a few minutes. However, the energy released by large flares heats the photosphere enough to change the profile of the absorption line used to measure the field making the measurements at the exact location of the flare inaccurate. Unfortunately, this is a limitation of magnetographs which use the weak-field approximation to measure the solar magnetic field. This effect can last from a few minutes to a few hours depending on the size of the flare.) These rapid changes in the configuration of the magnetic fields release the potential energy stored in the form of solar flares and Coronal Mass Ejections (CME) ejecting high energy particles into interplanetary space which can affect the earth (Section 1.2.2). To accurately study the true dynamics of the solar magnetic field, observations with both a high time cadence and

high spatial resolution of both the longitudinal and transverse components of the solar magnetic field are required. Therefore, many observations, with a high time cadence, from before and after the flare to have sufficient data to be confident of the trends.

In addition to a high time cadence, the observations must also be of sufficient spatial resolution to detect the small details ( $\sim 1$  arc-sec) in the solar magnetic field. On the scale of a typical active region the changes in the solar magnetic field, even after a large flare, tend to be subtle. To study the general morphology of the longitudinal magnetic field is insufficient to glean any but the very obvious changes from before and after a flare. Not to mention, the transverse component would be missing, and, therefore, the true magnitude and direction of the magnetic field. Only recently have instruments become available that can measure both the longitudinal and transverse components of the solar magnetic field, of an entire active region, with sufficient time cadence ( $\sim 1$  minute) and sufficient spatial resolution ( $\sim 1$  arc-sec) to study the changes in the solar magnetic field that occur during a solar flare.

In the following sections of this chapter, three cases will be presented in which the changes in the solar magnetic field during solar flares were studied.

## **4.1 Rapid Changes of Magnetic Fields Associated with Six X-Class Flares**

### **4.1.1 Introduction**

The evolution of photospheric magnetic fields before, during and after solar flares is extremely important but not well understood. Even though many authors have studied the problem for nearly four decades, the results, thus far, have not been conclusive. While some authors reported a decrease in the strength of the magnetic field after, and

presumably associated with, solar flares ([56], [57], [58] & [59]) some others argue that the changes are consistent with a general trend in the evolution of the magnetic fields of active regions [60].

It has been established, from the early studies of the relationship of solar flares to the morphology of the magnetic field of an active region, that strong flares most often occur near the neutral lines of the vertical component of the magnetic field of an active region where there is a strong gradient in the magnetic field and where the horizontal component is strongly sheared. This shear in the horizontal component experience substantial flare related changes. Wang et al. [61] determined that the magnetic shear of an active region may increase after the occurrence of an X-class flare. This result initially appears to be counterintuitive because the magnetic shear is expected to decrease as the total magnetic energy of the active region decreases. Chen et al. [62] studied more than 20 M-class flares and determined that there was essentially no apparent changes in the magnetic fields associated with the flares. The results from studies conducted at the Marshall Space Flight Center [63] & [64] showed inconclusive results. The morphology of the magnetic field of an active region may or may not change as the result of a solar flare and the magnetic shear in the active region may decrease, increase or remain the same.

Two very recent papers provide some key understanding of this subject. Kosovichev & Zharkova [65] studies high resolution Michelson Doppler Imager (MDI) magnetogram data for the 2000 July 14 “Bastille Day Flare” and found both a permanent decrease in the magnetic flux and a short term magnetic transient. The first phenomenon was explained by the release of magnetic energy and the second by high energy electrons

bombarding the solar surface. Spirock et al. [66] (Section 4.2) studied the X20 flare on 2001 April 02, at the time the largest solar flare in the last few decades, and found that, after the flare, the magnetic flux of the leading polarity increased by approximately  $6 \times 10^{20}$  Mx, while there was no obvious change in the magnetic flux in the following polarity. Two explanations were offered: the observed changes were the result of new flux emergence and/or a change of the direction of the field from more vertical to more horizontal.

Motivated by the recent advances in the topic, the remaining inconsistencies in the results and the recent upgrade of the vector magnetograph system at the Big Bear Solar Observatory (BBSO), in addition to the aforementioned X20 flare, four recent X-class flares were studied and re-examined the X9 flare of 1991 March 22, which was previously studied by [68]. In this section, six events were summarized and it was found that unbalanced, rapid and permanent flux increase might be a common property of major solar flares. Because these flares were associated with fast halo coronal mass ejections (CME), the observations may also provide clues to the understanding of the mechanisms that trigger CMEs.

#### **4.1.2 Observations and Data Reduction**

The data that is presented include magnetograms, optical intensitygrams and X-ray emission flux curves to show the location, magnetic morphology and temporal evolution of the flares under study. The five different data sets used in this study will now be discussed.

1) For four of the six events, BBSO Digital Vector Magnetograph (DVMG) data is used, which typically covers an area of approximately 300 arc-sec x 200 arc-sec. This

new system has a much improved sensitivity and resolution compared to that of the old BBSO Video Magnetograph system. The hardware has been described in detail by [66] (and the subject of this thesis). It consists of a 0.025 nm band-pass filter, an SMD 1024 x 1024 pixel 12-bit CCD camera and three liquid crystals used as polarization analyzers. Each data set consists of four images: 610.3 nm intensitygram (Stokes-I), line-of-sight magnetogram (Stokes-V) and the transverse magnetogram (Stokes-U and Q). The camera is re-binned to 512 x 512 mode to increase the sensitivity of the magnetograms. After re-binning, the pixel resolution is approximately 0.6 arc-sec / pixel. The line-of-sight sensitivity is approximately 2 Gauss while the transverse sensitivity is approximately 20 Gauss. The cadence for a complete set of Stokes images is typically one minute.

In this section, a comparison study of the line-of-sight magnetograms, for all of the events, is made. For the three events for which vector magnetograms are available, only the results of which there is confidence will be presented. For each vector magnetogram, the cross talk is corrected by scatter plots of the Stokes-V verses the Stokes-Q and the Stokes-V verses the Stokes-U. Because the current DVMG system at BBSOI does not use any mirrors, the instrument polarization is negligible. The 180° ambiguity in the direction of the vectors is resolved by comparing the vector magnetograms with the extrapolated potential fields using the line-of-sight field as the boundary condition. Although the resulting vector maps look reasonable, the potential field method is not sufficient for more quantitative studies such as analyses of electric currents and the three-dimensional structure of magnetic fields. A more detailed study of these data sets will be published in a sequence of follow-up papers.

2) For one of the events (2001 April 06) BBSO data was not available. Therefore, high resolution, high cadence line-of-sight magnetograms from the MDI on board the Solar and Heliospheric Observatory (SOHO) was used. MDI mainly obtains full-disk Dopplergrams for the investigation of solar oscillations. In addition, MDI provides full-disk longitudinal magnetograms with a cadence of one minute and an image scale of 2 arc-sec [67].

3) To show the spatial structure and temporal evolution of the flares, both high resolution and full disk  $H\alpha$  images from BBSO and hard X-ray time profiles from the Yohkoh Hard X-ray Telescope (HXT) as well as from its Wide Band Spectrometer (WBS) was used.

4) For the 2001 August 25 event, high resolution and high cadence white light data from the Transition Region and Coronal Explorer (TRACE) to study the sunspot evolution was used. This data was used to compare with the white light data from BBSO observations to ensure that the two data sets agree. TRACE 17.1 nm images were used to determine the location of the flare ribbon on the 2001 April 06 event.

5) C2 and C3 coronagraph data from the Large Angle Spectrometric Coronagraph (LASCO) on board SOHO were used to check the nature of the CMEs, if there were any, associated with each particular flare under study. LASCO data were available only for the five events in 2001. No coronagraph data was available for the 1991 March 22 event.

### **4.1.3 Results**

For each event, the process of analysis was begun with the line-of-sight magnetograms. To determine the location of any obvious changes in the magnetic field of the active region, movies of the line-of-sight magnetic field, from well before to well after each

particular event, were created. Then, two regions of study for each event were chosen. The first region encompasses the flare. Then, to ensure that any changes seen were not the result of external or instrumental effects, such as varying seeing, problems with the liquid crystals or filter, etc., a control region, that was away from the location of the flare and did not display any temporal changes in the magnetic field as a result of the flare was used. Then, both the positive and negative flux in the flaring region, normalized by the reference region, was plotted. As shall be shown, the rapid changes are localized for some cases but are spread over the entire sunspot region for other cases.

**Table 4.1** Overview of Flares

Date	Starting Time (UT)	Peak Time (UT)	AR Number	Size	Location (deg)	$\Delta T$ (minutes)	$\Delta P$ (Mx)	$\Delta F$ (Mx)
1991 Mar 22 .....	2230	2247	6555	X9.0	S23, E20	50	$1 \times 10^{20}$	0
2001 Apr 2 .....	2132	2151	9393	X20	N19, W65	100	$6 \times 10^{20}$	$-1.5 \times 10^{20}$
2001 Apr 6 .....	1910	1921	9415	X5.6	S20, E31	40	$4 \times 10^{20}$	$-4 \times 10^{20}$
2001 Aug 25 .....	1623	1645	9591	X5.3	S17, E34	10	$1.8 \times 10^{20}$	$-0.8 \times 10^{20}$
2001 Oct 19 .....	1613	1630	9661	X1.6	N15, W29	60	$3 \times 10^{20}$	$-0.4 \times 10^{20}$
2001 Oct 22 .....	1744	1759	9672	X1.2	S18, E16	60	$11 \times 10^{20}$	$-2 \times 10^{20}$

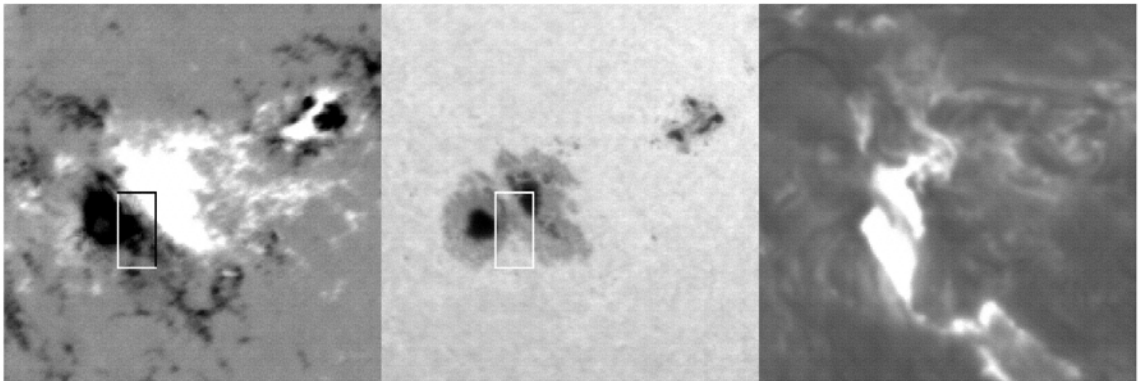
Table 4.1 provides an overview of these six events. It includes the times of the flares, NOAA active region number, the GOES X-ray classification, the location on the disk of the event, the timescale and the amount the magnetic flux changed. Please note that the first (1991 march 22) and second (2001 April 02) events have been discussed in detail in two previous papers [68] and [66], respectively). From the table, a common property, shared by all of the events, can be noted: there is an impulsive and permanent increase of the magnetic flux in the leading polarity only. In all cases, the flux of the following polarity tends to decrease to some extent. In Table 4.1, the “Starting Time” is the flare starting time as determined from Solar Geophysical Data, the “Peak Time” is the



time of the flare peak, the “Location” is the heliospheric coordinates, in degrees, of the active region, “ $\Delta T$ ” is the time it took for the flux to change from the preflare level to the post-flare level (changeover time), “ $\Delta P$ ” is the amount of flux change for the following (trailing) polarity.

The six events will now be discussed in detail. First, the four events that may be due to the emergence of inclined flux ropes will be discussed and then the two events that may be due to the expansion of P-spots after the flare.

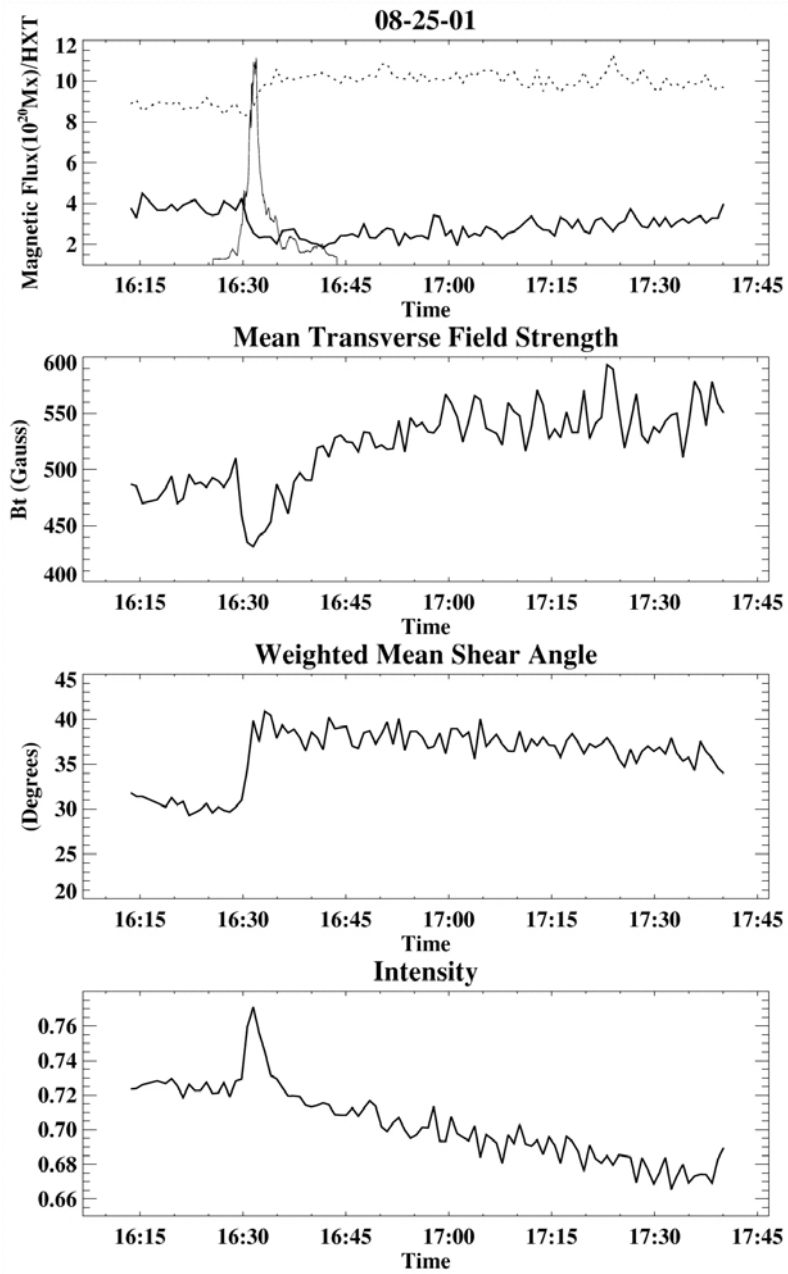
#### 4.1.3.1 2001 August 25 X5.3 Flare.



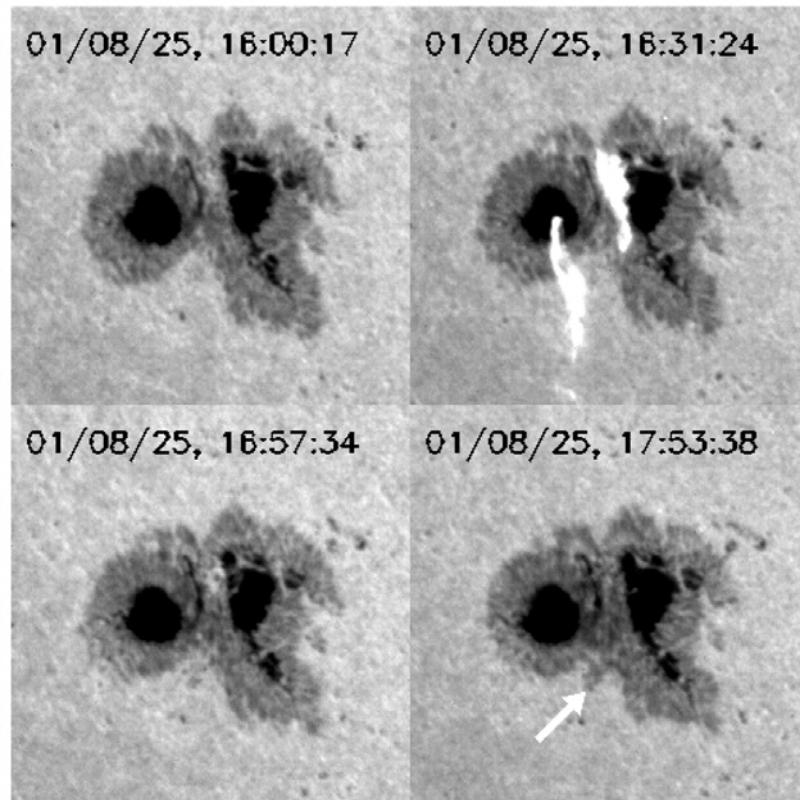
**Figure 4.1** Line-of-sight magnetogram (left), white-light (center) and  $H\alpha$  images of the 2001 August 25 flare that occurred in AR 9591. The field of view is 190 arc-sec x 190 arc-sec. The box marks the flux calculation area. The  $H\alpha$  image shows the morphology of the flare.

This flare exhibited the most impulsive changes among the six flares considered in this section. The flux “changeover” was completed within ten minutes. For this event, the area of the new flux appearance can be easily pinpointed. It is the area along the neutral line as marked by the white box in Figure 4.1. As shown in Figure 4.2, the leading (negative) flux in this box increased by approximately  $1.8 \times 10^{20}$  Mx while the following (positive) flux decreased by approximately  $0.8 \times 10^{20}$  Mx. The transverse field strength in

this region also experienced a rapid increase on the order of 70 Gauss. The weighted mean magnetic shear angle rapidly increased by  $10^\circ$ . This shear angle is defined as the angular difference between the potential and measured transverse fields, weighted by the measured transverse field strength. Note that, as shown in the bottom panel of Figure 4.2, the mean intensity of the box decreased gradually, beginning immediately after the flare, indicating the formation of new sunspot area. The mean intensity of 1.0 indicates the mean photospheric intensity outside of the sunspots. Both BBSO and TRACE white light movies show the formation of new sunspot area clearly. Figure 4.3 shows four TRACE white light images. The arrow denotes the formation of new sunspot area, which is predominantly in the form of penumbra.



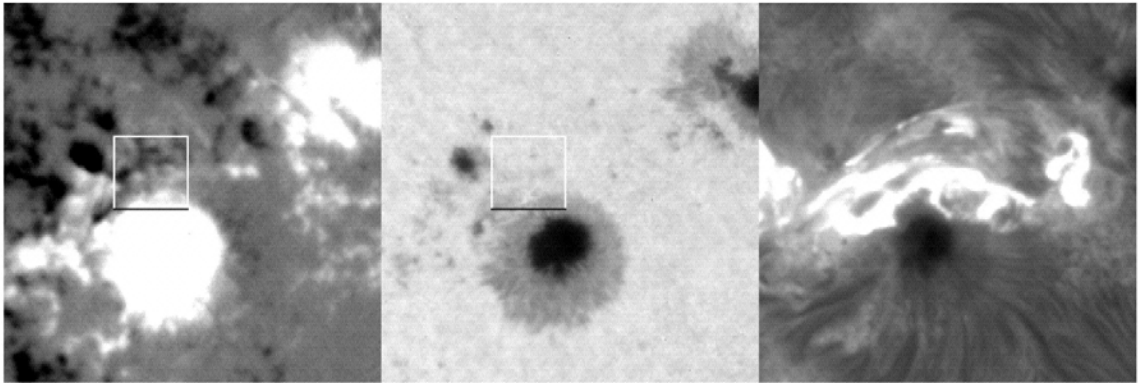
**Figure 4.2** (First panel) Evolution of magnetic flux in AR 9591 on 2001 August 25. The solid line represents the following (positive) flux, while the dashed line represents the leading flux (negative). The thin solid line is the Yohkoh hard X-ray curve in the high-energy channel of HXT. (Second panel) Evolution of transverse field strength. (Third panel) Weighted mean shear angle. (Bottom panel) Mean intensity in the box.



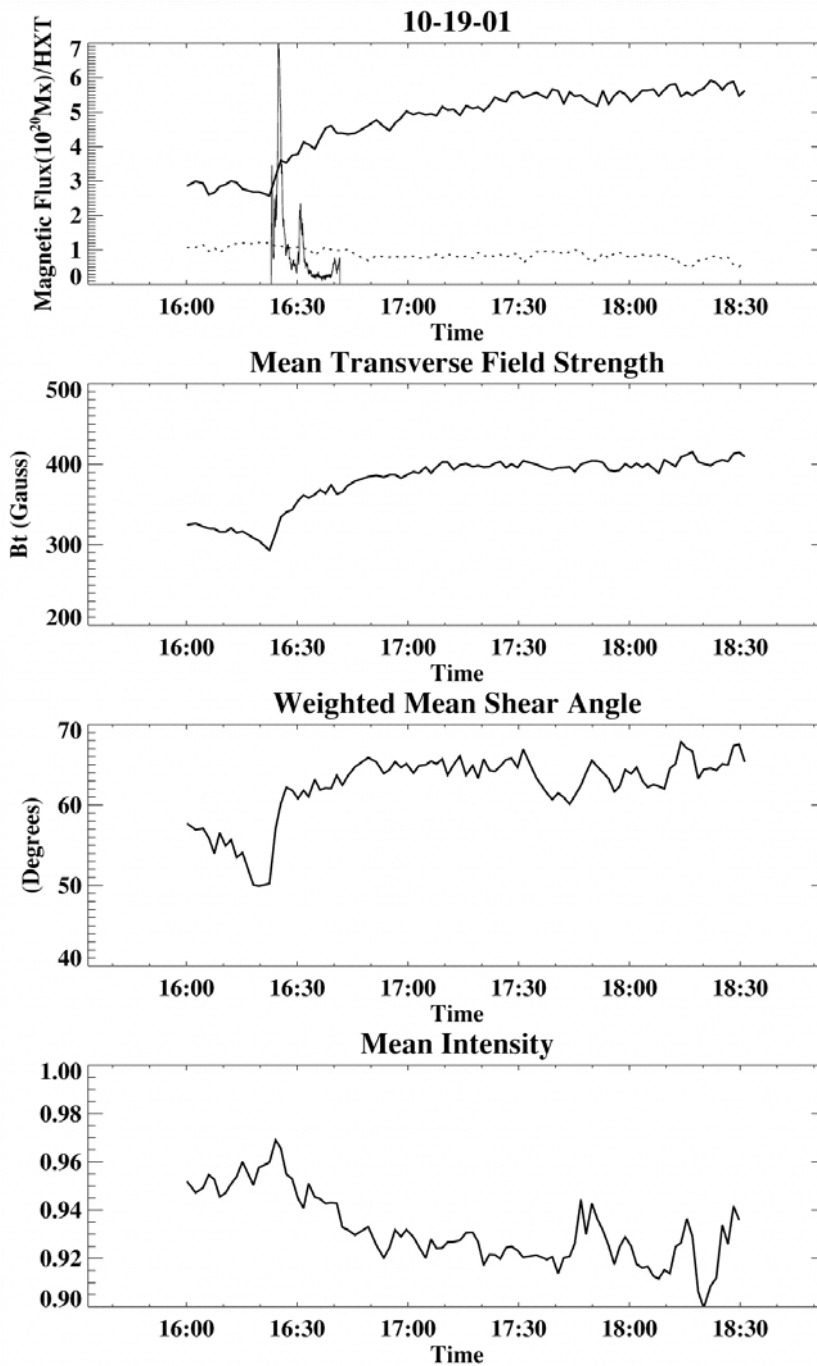
**Figure 4.3** Sequence of TRACE images showing the 2001 August 25 flare. The new penumbral area is indicated by the arrow. The time of the flare maximum is approximately 16:32 UT.

#### 4.1.3.2 2001 October 19 X1.6 Flare.

Figure 4.4 shows the magnetic configuration and flare morphology of the 2001 October 19 event. Again, in Figure 4.5, the magnetic field changes in the area marked by the box in Figure 4.4 are plotted. The trend of the changes for this flare is very similar to that of the 2001 August 25 flare. However, the changeover is rather gradual. The amount of flux increase in the leading (positive) polarity was  $3.0 \times 10^{20}$  Mx while the following (negative) flux decreased by  $0.4 \times 10^{20}$  Mx, over the timescale of 60 minutes. The decrease of the following flux is primarily due to the cancellation of the newly formed positive flux by the previously existing negative flux around the leading spot.



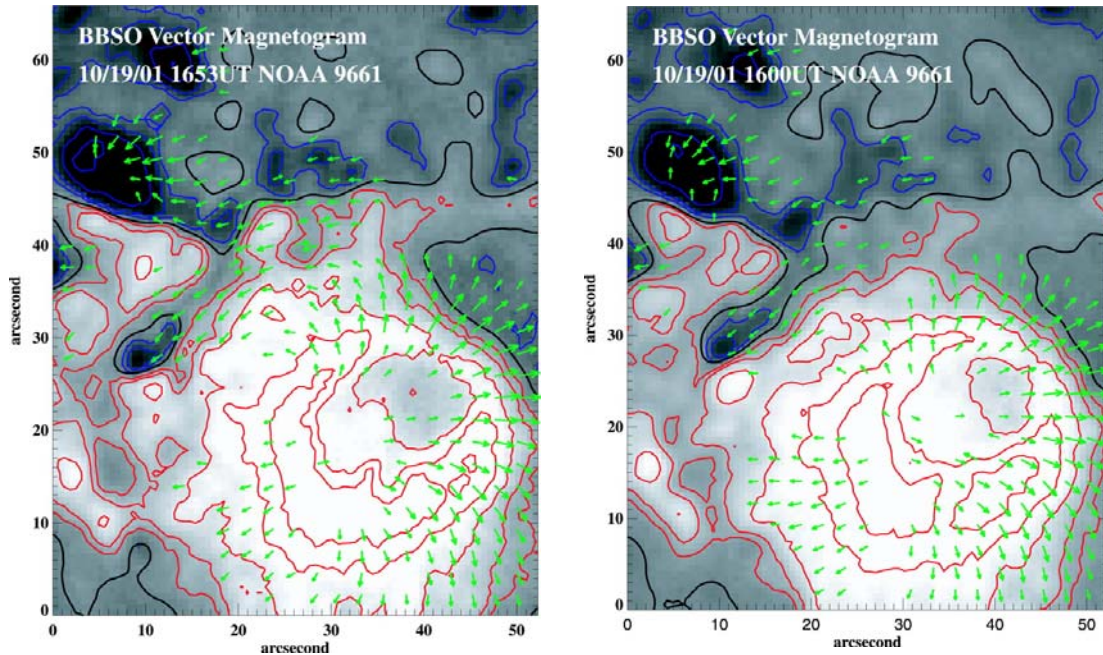
**Figure 4.4** Line-of-sight magnetogram (left), white-light (center) and  $H\alpha$  images for the flare of 2001 October 19 that occurred in AR 9661. The field-of-view is 120 arc-sec x 120 arc-sec. The box marks the flux calculation area. The  $H\alpha$  image shows the morphology of the flare.



**Figure 4.5** (Top) Evolution of magnetic flux on 2001 October 19. The solid line represents the leading (positive) flux, while the dashed line represents the following (negative) flux. The thin solid line is the Yohkoh hard X-ray curve in the high-energy channel of HXT. The remaining panels are as in Figure 4.2.

For this event, the increase in the transverse field has the same trend as that of the line-of-sight field. The mean value of the transverse field in the calculation box increased by 90 Gauss. The weighted mean shear angle increased by almost  $10^\circ$ . The increase in the shear angle occurred during a period of 15 minutes, which was much more rapid than that of the change in the line-of-sight and transverse field strength. In the bottom panel of Figure 4.5, the mean intensity of the box is plotted. The mean photospheric value is defined as 1.0. Therefore, the decreasing intensity indicates the appearance of new sunspot area. As is the case with the 2001 August 25 event, the new sunspot area is in the form of penumbra.

In Figure 4.6, vector magnetograms from before and after this flare are compared. The thick black lines are the magnetic neutral lines. The neutral line that runs approximately horizontal across the image at approximately  $y = 45$  arc-sec is the primary location of the increase in the magnetic field strength and shear angle.



**Figure 4.6** Vector magnetograms of 2001 October 19 of AR 9661. (Left) Magnetic fields before the flare. (Right) Magnetic fields after the flare. Grey scale represents the line-of-sight magnetic field strength, which is also plotted as contours (red as positive, blue as negative). The green arrows indicate the transverse fields. The dark black lines are the magnetic neutral lines where the line-of-sight field is zero.

This is another clear example of new flux appearance immediately following a flare. As will be discussed later, the explanation for the observed changes in the magnetic flux of each active region requires that the new flux be very inclined to allow the appearance of only one polarity.

**4.1.3.3 2001 April 02 X20 Flare.** This flare was studied extensively [66] (Section 4.2) using both BBSO and MDI data. This was the only one of the six events that was very close to the limb ( $65^\circ$  West). The leading (limb-ward, positive) flux increased by  $6.0 \times 10^{20}$  Mx while the following (disk-ward, negative) flux basically remained unchanged, or, perhaps decreased slightly ( $1.5 \times 10^{20}$  Mx which is approximately the level of the noise of the measurement). The authors suggested two possible theories to explain this event: the



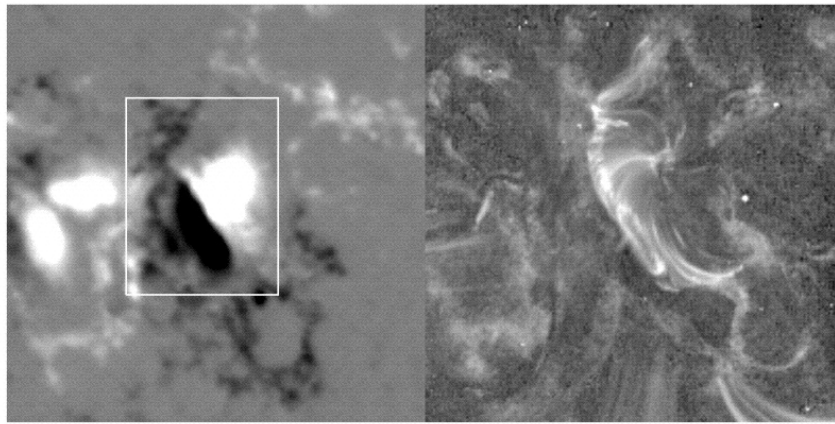
emergence of a very inclined flux loop and/or a change in the direction of the magnetic field from more vertical to a more inclined orientation.

There are some limitations to these explanations (please refer to the discussion in Section 4.4). Because the region was close to the limb and there were no transverse magnetic field observations, the slight decrease of the following flux was difficult to explain. Using the experience gained from the study of the other events discussed in this section, all of which are located near the disk center, it is postulated that the decrease of the magnetic flux of the following polarity could be due to flux cancellation by some of the newly emerged leading flux with the opposite polarity that previously existed.

**4.1.3.4 Re-evaluation of the 1991 March 22 X9 Flare.** Wang & Tang [68] discussed this flare in detail and found that there was an increase in the leading (positive) flux by  $1.0 \times 10^{20}$  Mx. They were unable to detect any change in the following (negative) flux. The negative flux was mostly encompassed within the major sunspot. The BBSO Magnetograph systems are not able to measure large sunspot umbral fields accurately because of Zeeman saturation (Section 2.2) and the reduced light level of the umbra of the sunspot. Because of these limitations, any change in the strength of the negative component of the magnetic field remains undetermined.

As noted when the results of this event are compared with the result of the other events, the lack of change of the flux in the following polarity may be true and not due to observational and/or instrumental effects. For this event, the authors claimed that abrupt flux emergence was the likely cause of the flux increase. The appearance of new sunspot area, coinciding with the flux increase, supports this argument. In addition, the magnetic shear along the neutral line of the active region increased impulsively.

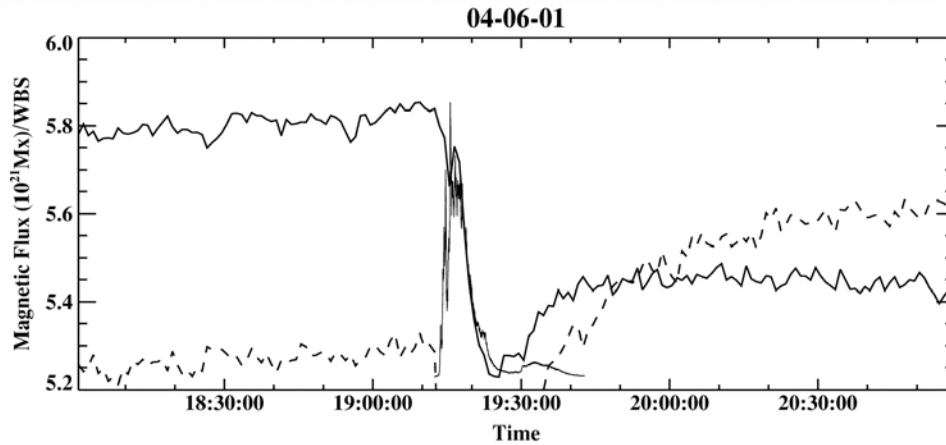
**4.1.3.5 2001 April 06 X5.6 Flare.** For this event there were no BBSO magnetograms available. Therefore, MDI magnetograms are used to calculate the changes in the magnetic flux. Figure 4.7 shows a magnetogram ½ hour before the flare (left panel) as well as the flare morphology as seen in the TRACE 17.1 nm observation (right panel). The box in the magnetogram marks the region of the flux calculation.



**Figure 4.7** (Left) Line-of-sight magnetogram of 2001 April 6 of AR 9415. The box marks the flux calculation area. (Right) TRACE 171A image during the flare. The field-of-view is 200 arc-sec x 200 arc-sec.

Figure 4.8 shows the evolution of the positive and negative magnetic flux. The Yohkoh WBS hard X-ray plot is superimposed on the magnetic flux plots to indicate the timing of the flare. The following (positive) flux decreased by  $4 \times 10^{20}$  Mx while the leading (negative) flux increased by  $4 \times 10^{20}$  Mx. This is the only event in this study where a substantial decrease in the flux of the following polarity was found. It appears that this flux change is over the entire sunspot area. The flux reduction of both polarities, during the flare, is likely due to line weakening, although [65] explained that it is caused by the bombardment of the solar surface by high energy electrons. However, the study of

the evolution of flux during the impulsive phases of a flare is not an essential topic of this section.

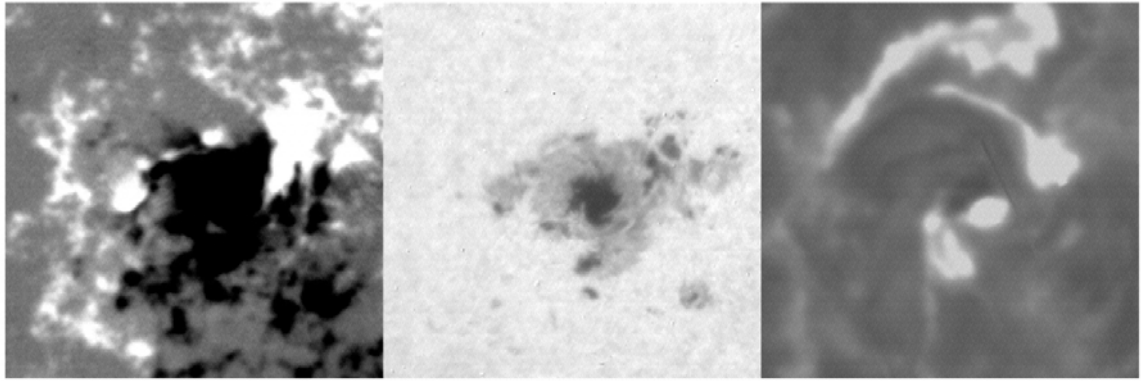


**Figure 4.8** Evolution of negative (leading polarity, dashed line) and positive (following polarity, thick solid line) magnetic flux in AR 9415 on 2001 April 6. The thin solid line is the Yohkoh/WBS hard X-ray curve.

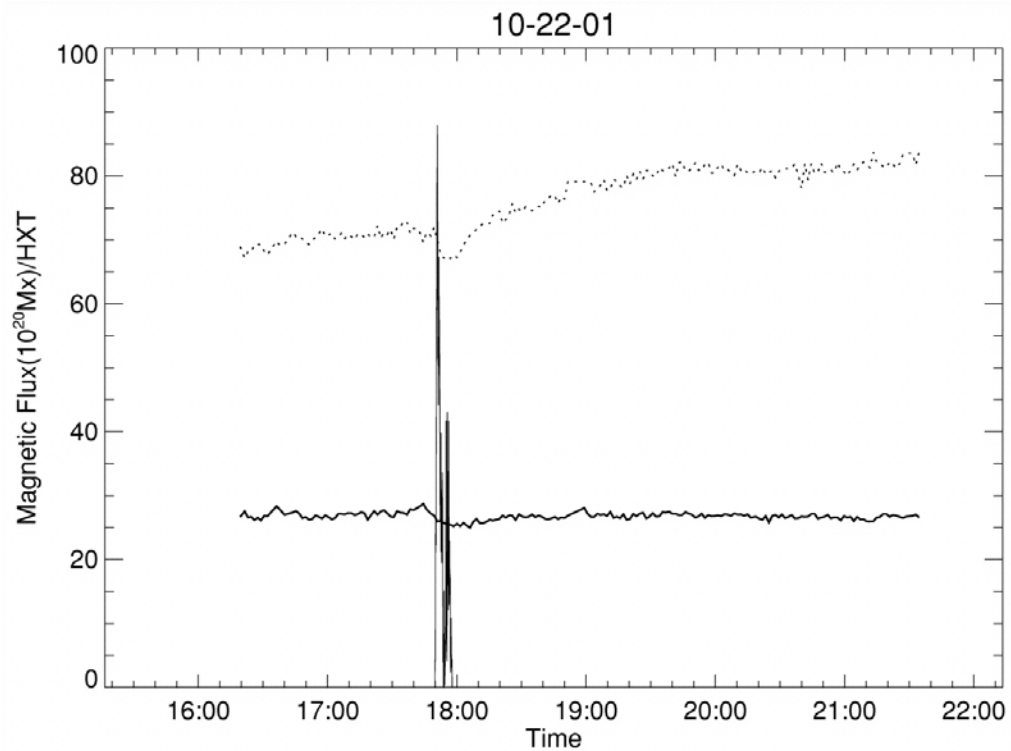
#### 4.1.3.6 2001 October 22 X1.6 Flare.

For this event, the exact location of the flux

change after the flare could not exactly be determined. It appears that the entire leading spot grew in size and added leading (negative) flux in the amount of  $12 \times 10^{20}$  Mx, while the following (positive) flux dropped by  $2 \times 10^{20}$  Mx. Figure 4.9 shows the magnetogram (left panel), white light (center panel) and H $\alpha$  (right panel) images for this event. The flux calculation was based on the entire  $120 \times 120$  arc-sec window. Figure 4.10 shown the evolution of the flux, along with the Yohkoh HXT curve to indicate the time of the flare. There were no obvious impulsive changes of the transverse magnetic field, mean intensity or shear angles. Therefore, these parameters were not included.



**Figure 4.9** Line-of-sight magnetogram (left), white-light (center) and H $\alpha$  images (right) of the 2001 October 22 flare that occurred in AR 9672. The field-of-view is 120 arc-sec x 120 arc-sec. The H $\alpha$  image shows the morphology of the flare.



**Figure 4.10** Evolution of the line-of-sight magnetic flux in AR 9672 on 2001 October 22. The solid line represents the following (positive) flux, while the dashed line represents the leading (negative) flux. The thin solid line is the Yohkoh hard X-ray curve in the high energy channel of HXT.

#### 4.1.4 Summary and Discussion

There are two common properties to these six X-class flares: 1) There was an impulsive and permanent change in the magnetic flux associated with each flare. 2) The leading flux always increased while the following flux tended to decrease, although by a much smaller amount.

For four of the events the exact area where the flux changed can be determined with precision. This area is always at the core of the flaring neutral line. For the two additional events the change appears to have been more uniform over the entire sunspot area.

A difficult problem immediately presents itself. If a region is close to the disk center, Maxwell's law requires that the flux emergence should be balanced. The positive and negative flux should increase by the same amounts, unless the new flux is extremely inclined. It does not seem possible for one polarity to increase and the other to decrease.

In the paper by [66] (Section 4.2 below), the unbalanced flux increase for the 2001 April 02 event was explained by two possible mechanisms:

1) With the emergence of a very inclined flux tube, only the limb-ward polarity would show a flux increase. This scenario can explain some signatures of flux emergence, such as the appearance of the new umbral area associated with the 1991 March 22, the 2001 August 25 and the 2001 October 19 flares. However, this suggestions could not explain the decrease of flux in the following polarity. It has since been determined that the decrease in the following flux could be due to flux cancellation between newly emerged leading flux and previously existing following flux. The 2001 August 25 and October 19 events both showed the best proof of this.

The new flux emergence could be the result of a relaxation of magnetic energy in the upper atmosphere, which would enable the subsurface flux to emerge more easily. The increase of magnetic shear signifies that the newly emerged flux is also sheared. It should also be noted that the shear increase was predicted by [69] as a result of the relocation of DC currents to the lower atmosphere from higher up in the corona after the flare.

2) The unbalanced flux increase could also be the result of a change in the orientation of the magnetic field. For the limb event of 2001 April 02 the field would become more inclined in the leading polarity after the flare. However, for all other events discussed in this section, the flares were closer to disk center. Therefore, the increase in the line-of-sight flux of the leading polarity requires the field in that location to become more vertical after the flare, while the decrease of the line-of-sight component of the following flux would require the field, in that location, to become more inclined. The vector magnetograph observations for 2001 August 25 and October 19 do not support this explanation.

There is also a third possible explanation:

3) After the relaxation of the magnetic field in an active region, the preceding sunspot may expand slightly. The other way to look at this is that the electric current of the sunspot decrease after a flare, causing pinch force to decrease and therefore the spot to expand. The actual flux will not increase because of this effect. However, some flux may move out of the umbral area that had more Zeeman saturation before the flare. The results of the 2001 April 06 and October 22 events seem to support this view. Even

though this may be due to an observational effect, the sudden expansion of P-spots after a major flare deserves theoretical explanation.

**Table 4.2** Explanation of Findings

Date	Magnetic Shear	CME	New Spot	Explanation(s)
1991 Mar 22 .....	Increase	Unknown	Yes	1
2001 Apr 2 .....	No vector data	Partial halo	No	1 and 2
2001 Apr 6 .....	No vector data	Halo	No	3
2001 Aug 25 .....	Increase	Halo	Yes	1
2001 Oct 19 .....	Increase	Halo	Yes	1
2001 Oct 22 .....	No change	Halo	No	3

Table 4.2 summarizes the change of the magnetic shear and possible explanation(s) for all six events. In addition, there is no existing theory to explain why the leading flux area should preferentially experience flux increase. At the current time, there is no unified theory to explain the current observations, even though each event can be explained by one or two theories. There is confidence that the observational results are substantially above any systematic errors.

For all of the five events in 2001, C2 and C3 coronagraph data from LASCO was available. All of these events were associated with halo CMEs. Therefore, understanding the findings here would help the understanding of the mechanism responsible for triggering CMEs. As an example, the erupting flux rope model should be noted in, [71] & [72]. This model predicts an increase of tangential magnetic flux associated with a CME.

However, the details of the parameters of the model (timescale and amount of flux emergence) need to be carefully compared with the observations.

## **4.2 Rapid Changes in the Longitudinal Magnetic Field Related to the 2001 April 2 X20 Flare**

### **4.2.1 Introduction**

It is known that a solar flare is a sudden release of energy previously stored in the magnetic field of the Sun. Understanding how the magnetic energy is stored and released is a fundamental problem for solar physics. Are foot-point motions responsible for the accumulation of energy in the corona, or does the emergence of twisted magnetic fields from below the photosphere being the excess energy, which is then released? For many decades, solar physicists have been looking for flare related changes in the photosphere magnetic field, which would provide some information as to how an active region stores and releases its energy.

Rapid flare related changes in the magnetic field have been reported in many studies (see for example [73], [74] & [75]). The magnetic shear angle [76], the transverse field strength and the length of the neutral line are found to be associated with the probability of solar flares [77]. However, there is no strong correlation between the shear angle and the occurrence of flares. After a flare, the shear can decrease, remain the same [78] & [79] or increase [80].

Cameron & Sammis [81] reported changes in the longitudinal magnetic field after the X9.3 flare on 1994 May 24, which occurred near the western solar limb. The authors claim that the field became stronger on the limb-ward side of the neutral line and weaker on the side closer to the center of the solar disk. The observed changes were interpreted



as a rearrangement of the transverse component of the magnetic field. However, a quantitative analysis was not developed.

In this study, observations of the longitudinal magnetic field made with the BBSO DVMG, the Michelson Doppler Imager on board the Solar and Heliospheric Observatory (SOHO/MDI) [82] and the Global Oscillation Network Group (GONG) full-disk magnetograms of a two ribbon flare which occurred on 2001 April 2 in NOAA Active Region 9393, located at N20°, W65° are presented. The data show rapid and significant changes in the longitudinal magnetic field close to the neutral line of the active region.

#### **4.2.2 Data and Instrumentation**

The Big Bear Solar Observatory observed NOAA AR 9393 each day as it crossed the solar disk from 2001 March 24 to 2001 April 2 with its standard complement of instruments on both the 65 cm vacuum reflector and the 25 cm vacuum refractor. The 65 cm vacuum reflector was configured with its scanning Zeiss filter to take a set of H $\alpha$  center-line and  $\pm$  0.06 nm images every 90 seconds with a 512 x 512 pixel CCD camera yielding 0.4 arc-sec/pix sampling. The three benches on the 25 cm vacuum refractor were configured with a Ca II K Lyot filter, an  $\alpha$  Lyot filter tuned to center line and a 0.025 nm Zeiss H $\alpha$  filter retuned to the magnetically sensitive Ca I line at 610.3 nm, which is used for the DVMG. Each instrument on the 25 cm vacuum refractor uses a 512 x 512 pixel CCD camera, which yields 0.6 arc-sec/pixel sampling. This setup was configured to provide intensitygrams at Ca II K, H $\alpha$  and Ca I and a longitudinal magnetograms with 100 integrations every 30 sec.

During the past several years, BBSO has been involved in an aggressive program to upgrade its instrumentation. At the forefront of this effort has been the development of

the DVMG, which has replaced the old Video magnetograph system on the 25 cm vacuum refractor [83]). The BBSO DVMG is a filter-based magnetograph that uses the weak-field approximation to measure the magnetic field.

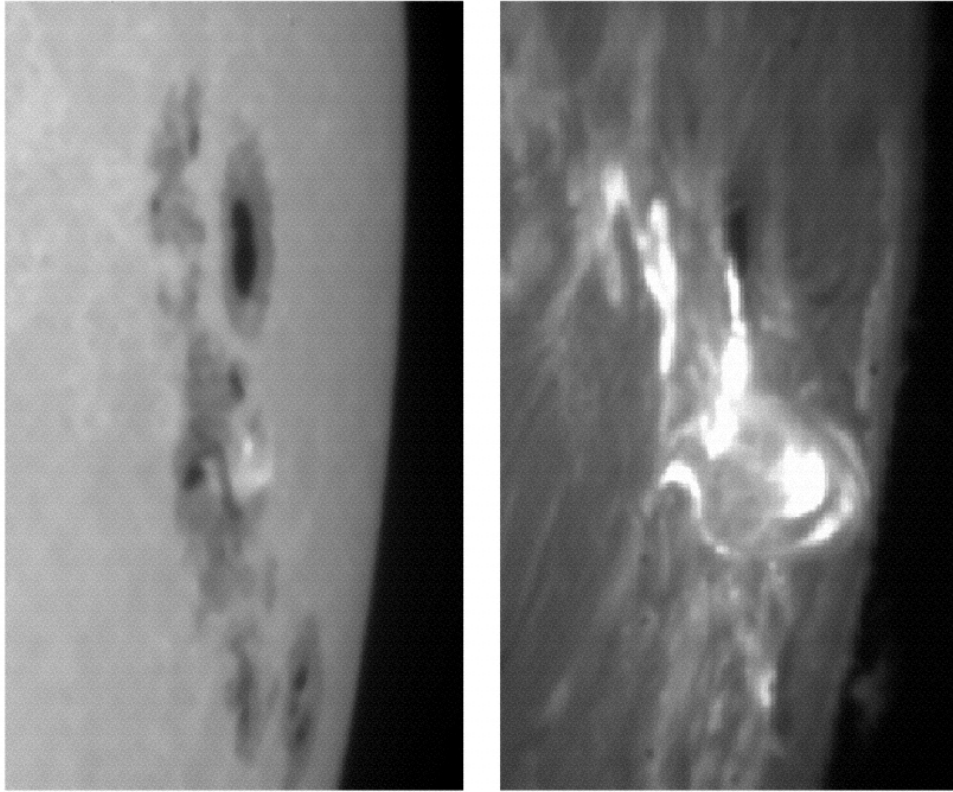
The DVMG uses two nematic liquid crystal variable retarders, whose retardance can be controlled with an applied voltage, to select a particular polarization state (610.3 nm intensitygram, Stokes-V, Q or U) by converting the desired input polarization set into an orthogonal set of linear polarizations [84]. A single ferroelectric liquid crystal, which is a fixed  $\frac{1}{2}\lambda$  retarder whose rotation angle can be selected to be either  $0^\circ$  or  $45^\circ$ , acts as the fast modulator of the system. This ferroelectric crystal, working with a fixed linear polarizer, is used to select one of the orthogonal linear polarization components. Light is then fed through a 0.025 nm birefringent filter, tuned to the wing of the magnetically sensitive Ca I line at 610.3 nm, and finally imaged onto a 512 x 512 pixel CCD camera. Due to the fact that, at the time of the flare, the active region was near the western limb, the 0.025 nm birefringent filter was tuner approximately 0.0035 nm to the red end of the spectrum to compensate for the Doppler shift induced by solar rotation (Section 2.2). The exposure time is typically 30 ms (currently, the exposure time is 120 ms) and the images are taken at a rate of 12 frames per second (currently, the frame rate is 7 frames per second).

Two images, one taken at each state of the ferroelectric crystal, constitutes a magnetogram pair. The difference between a magnetoigram pair, referred to as a Stokes-V, Q or U images, depending on the state of the nematic liquid crystals, divided by their sum, is a magnetogram. The signal level of the magnetogram represents the percent polarization of the light and is directly proportional to the strength of the magnetic field

up to the magnetic field strength level where the weak-field approximation no longer holds true.

Because of the weak strength of the polarization signal in a single image pair, many image pairs are summed to increase the signal-to-noise ratio. Typically, to measure the longitudinal magnetic field in an active region, 128 image pairs are summed, which requires an integration time of approximately 10 seconds. The images provided by the DVMG were then corrected for dark-current and flat-field non-uniformity. The corrected 610.3 nm intensitygram and Stokes-V images are the final data products analyzed in Section 4.2.

### 4.2.3 Results



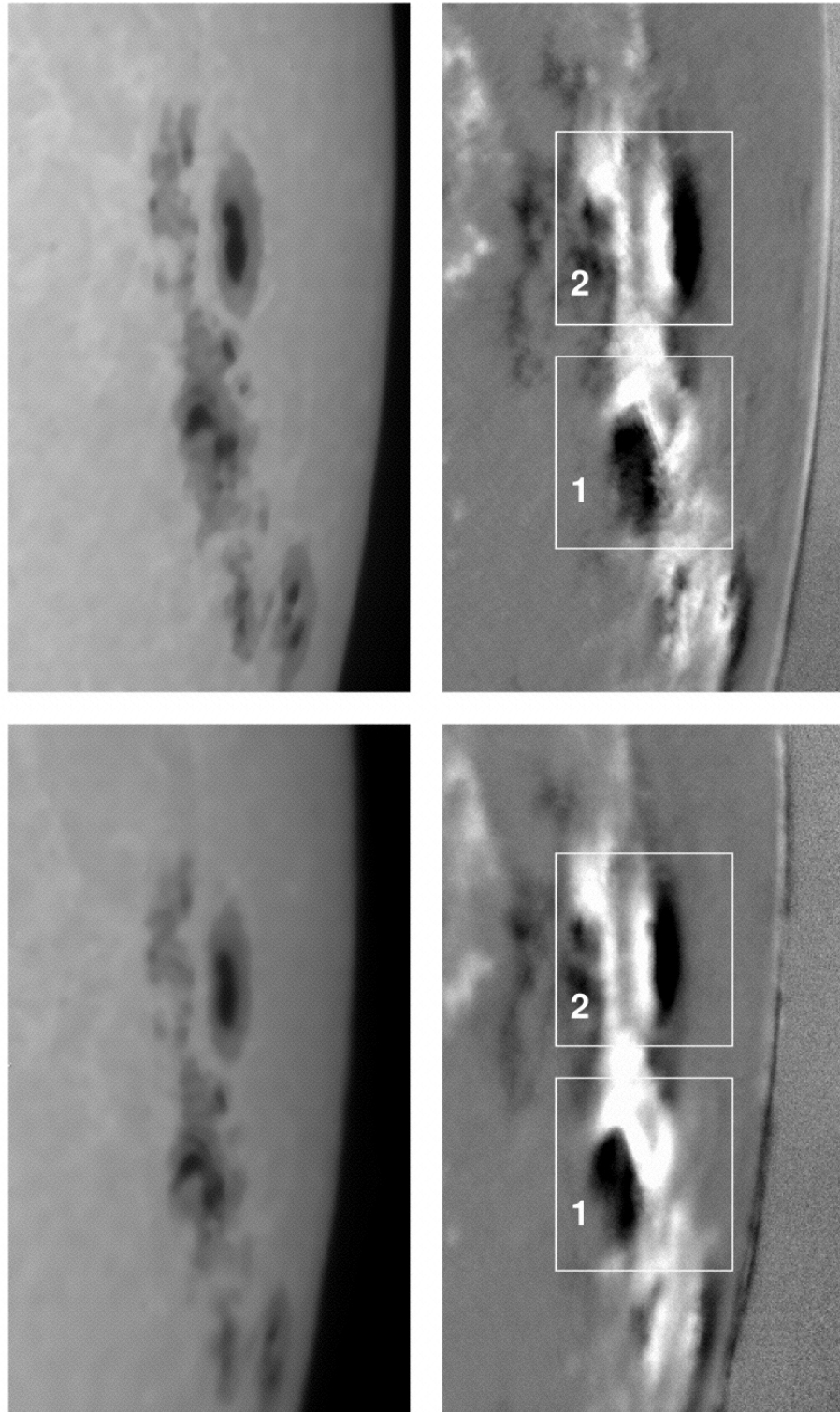
**Figure 4.11** Ca I (left) and H $\alpha$  center-line (right) intensitygram taken during the flare.

Figure 4.11 shows Ca I (left panel) and H $\alpha$  center-line (right panel) intensitygrams taken during the flare. The location of the flare can be seen as the bright region near the center of the Ca I intensitygram image. Figure 4.2 shows two sets of Ca I intensitygram and Stokes-V images from before (top panel) and after (bottom panel) the flare, which occurred at approximately 21:50 UT. From a movie made of the longitudinal magnetogram images from well before until well after the flare, it appeared that there was a stable positive (white) flux increase along the neutral line (an imaginary line dividing the positive and negative flux regions), while the negative (black) flux remained the same. This can be seen in Box 1 in the top and bottom panels of Figure 4.2.

To test whether this indeed was the case, the total flux in the area near the flare, indicated by Box 1 in Figure 4.12, was calculated with respect to time. Care was taken to ensure that the images were properly aligned so that the summing boxes encompassed the same area on the Sun throughout the test sequence. As can be seen in Figure 4.3, the BBSO DVMG data show that, in the region of the flare, indicated by the solid curves in the top panel, the total positive flux (white) increased by approximately 25% while the total negative flux decreased by approximately 5%. It is believed that this 25% increase is far above the noise level.

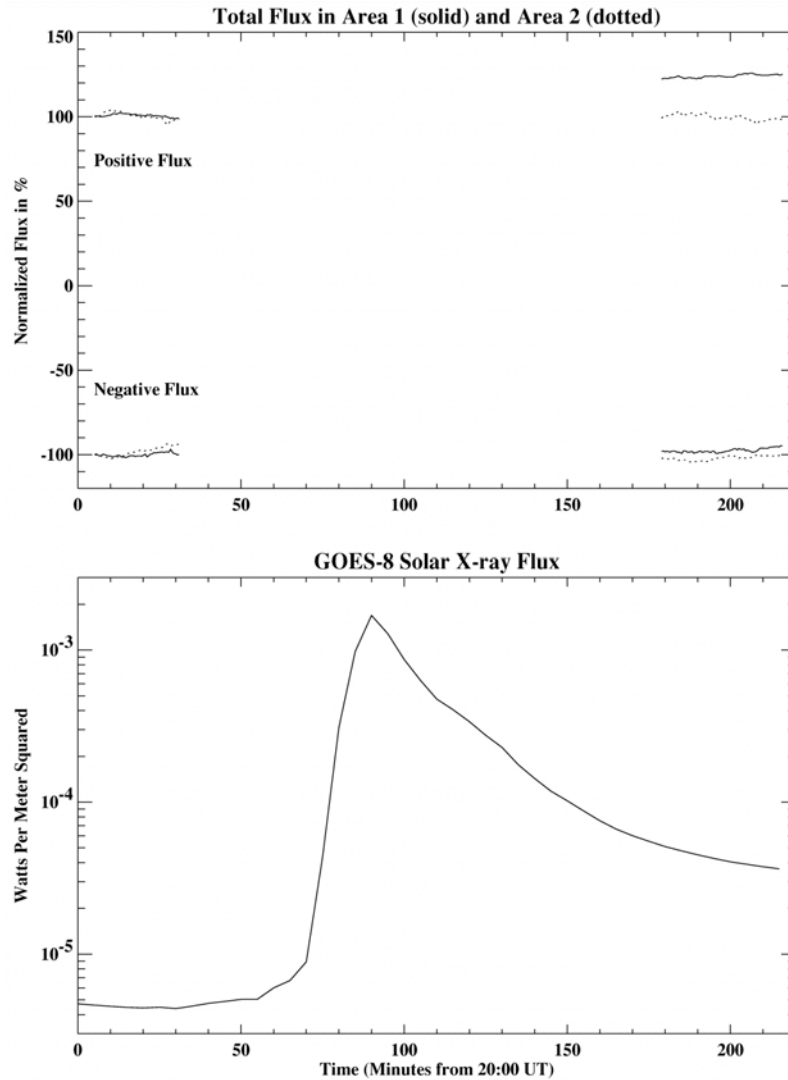
**Table 4.3** Magnetic Flux Values Before the Flare at 20:00 UT.

Flux	Box 1	Box 2
Positive flux (Mx).....	$2.22 \times 10^{21}$	$2.43 \times 10^{21}$
Negative flux (Mx) .....	$1.72 \times 10^{21}$	$1.20 \times 10^{21}$



**Figure 4.12** Two sets of Ca I intensitygrams and Stokes V images from before (top) and after (bottom) the flare.

To ensure that any changes seen were not the result of external or instrumental effects, such as poor seeing, changing light levels caused by the setting Sun, problems with the filter or liquid crystals, etc., the total flux with respect to time was also measured in a control region indicated by Box 2 in Figure 4.12. In the selection of the control region, two factors were taken into account. Because of the fact that the location of the flare was near the limb, it is advantageous to use a control region that was at or near the same longitude of the flare to rule out any projection effect differences between the flare and control regions. Also, the control region should ideally contain both positive and negative flux that are approximately of the same magnitude as the positive and negative flux in the flare region so that the calibration constant of the instrument will be the same in both cases.



**Figure 4.13** Evolution of the magnitude of the positive and negative normalized flux in the region of the flare (solid line) and the control region (dotted line). The bottom panel shows the GOES-8 X-ray flux during the flare.

The results of this test can also be seen in Figure 4.13. Both the total positive and negative flux remained constant in the control region, denoted by the dotted curves, indicating that the changes seen in Box 1 are real and not the result of external or instrumental effects. Table 4.11 lists the total magnetic flux in Boxes 1 and 2 at the beginning of the test sequence.



The gap in the data from ~30 to ~180 minutes is due to the fact that, during the flare, the measurements of the magnetic field are not reliable because of line weakening caused by chromospheric heating. Because the interpretation of the dynamic of the magnetic field during the flare is not within the scope of this particular discussion, and the magnetic field in the region of the flare can not be reliably measured by the type of magnetograph used at BBSO, the data between 30 and 180 minutes will not be used in the discussion and conclusion of this section.

In addition to the BBSO DVMG data, SOHO MDI and GONG full-disk magnetogram data for the same period was also analyzed and is presented in Figure 4.3. The same calculations, using identical flux summing boxes, was performed on the SOHO MDI and GONG data as was performed on the BBSO data. In general, the SOHO MDI and GONG magnetogram data agree with the BBSO data. Therefore, there is confidence that the BBSO DVMG has provided reliable results for this event.

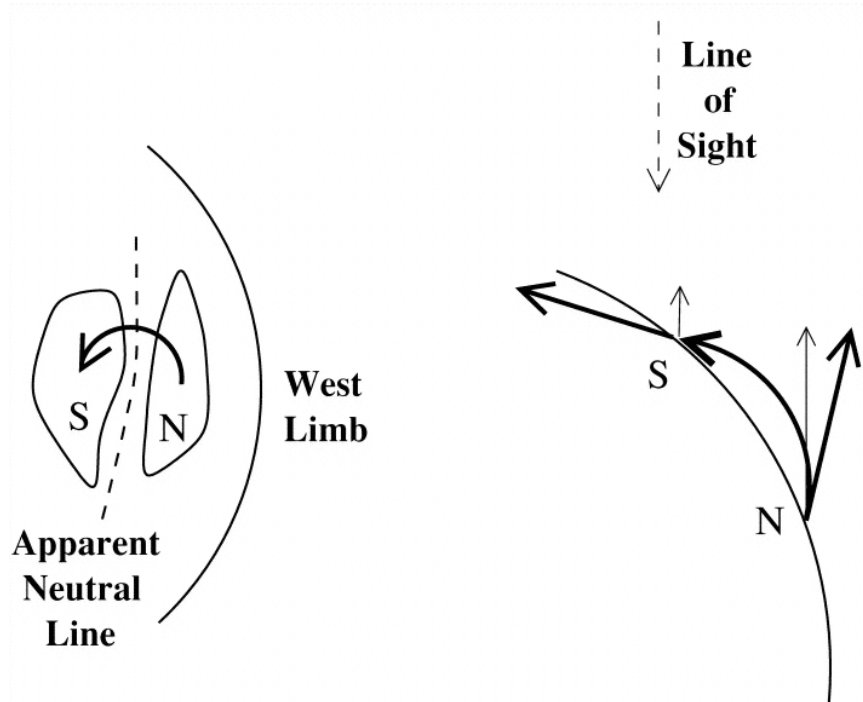
The primary result that should be stressed is that the negative flux in the flare region, and both the positive and negative flux in the control region, remained approximately constant after the flare, as compared to before the flare, while there was a dramatic increase in the positive flux in the region of the flare, as can be seen in Figure 4.13.

#### **4.2.4 Discussion and Conclusions**

Cameron & Sammis [81] observed variations in the longitudinal magnetic field near the west limb after a strong X9.3 flare. Their interpretation is that the field changes are induced by the rearrangement of the tangential components of the magnetic field associated with the inverse polarity magnetic configuration present above the neutral line

(see [85]). However, they did not present any quantitative analysis of the data, and the stated field changes were only inferred from visual inspection of the magnetogram images.

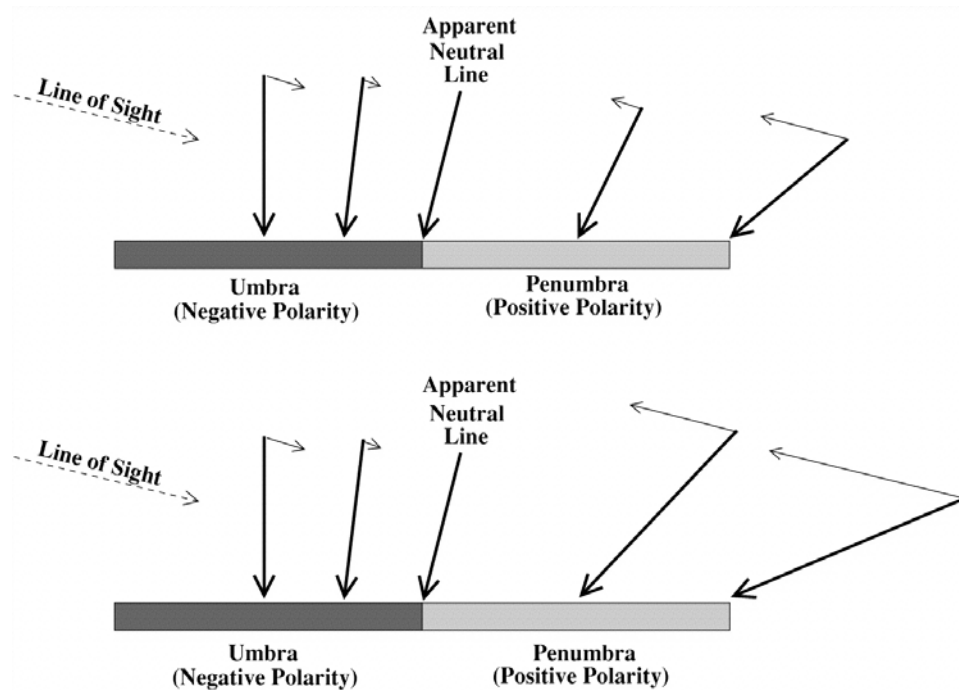
Earlier magnetic field observations suggest other possible scenarios, which can produce the observed changes. Emergence of new magnetic flux inside the sunspot penumbra can account for the observed changes in the magnetic field. Asai et al. [86] observed recurrent  $H\alpha$  surges from the light bridge in a sunspot umbra, which is considered to be evidence of emerging flux in a sunspot, as proposed by [87]. Wang & Tang [68] and [80] have observed that a pair of new umbrae may emerge on either side of the neutral line, immediately after major X-class flares, coinciding with an increase in the shear angle.



**Figure 4.14** Schematic of how the emergence of the magnetic flux inside the limbward penumbra of a negative polarity sunspot can be seen, at the western solar limb, as an increase in the positive polarity field.

Figure 4.14 shows that, because of the effect of projection, the emergence of magnetic flux inside the penumbra of a negative polarity sunspot can be seen at the western solar limb as an increase in the positive polarity field and a slight decrease in the negative polarity field. As a result of the emergence, the magnetic field in the penumbra would become stronger and more horizontal.

A cross-sectional view of the sunspot, which demonstrates a possible magnetic field configuration that could account for the observed changes reported in this work, is shown in Figure 4.15. The top panel demonstrates the magnetic configuration before the flare, while the bottom panel demonstrates the magnetic configuration after the flare. The actual magnetic field is represented by the dark arrows, while the longitudinal component, in the direction of the line of sight, is represented by the light arrows. The penumbra of the negative polarity spot that is closer to the solar limb appears positive because of the limb projection effect. Note that, as shown in the bottom panel, any increase in the strength of the magnetic field and/or inclination in the limb-ward penumbra would lead to an increase in the positive longitudinal magnetic field.



**Figure 4.15** Cross-sectional view of the sunspot, which demonstrates a possible magnetic field configuration that could account for the observed changes. The top panel displays the configuration before the flare, while the bottom panel displays the configuration after. The thick vectors represent the actual magnetic field, while the thin vectors show the line-of-sight component.

Magnetic reconnection during a two-ribbon flare produces a post-flare loop system. The foot-points of the system coincide with the observed changes in the magnetic field. It is known that the rapid evolution of a post-flare loop system lasts for several hours after the onset of the flare. The evolution of the system would then result in changes of the magnitude and/or tilt of the photospheric magnetic field in the penumbra (Figure 4.5) which can be observed as strengthening of the longitudinal field.

### 4.3 Magnetic Field, H-Alpha and RHESSI Observations of the 2002 July 23 Gamma-Ray Flare

#### 4.3.1 Introduction

Filament eruptions, coronal mass ejections (CMEs) and associated photospheric activity, such as solar flares, indicate an ongoing relaxation of large-scale, highly stressed solar magnetic fields. Release of magnetic energy during such processes is expected to be accompanied by some variations in the magnetic field. Earlier studies report both the localized changes associated with the major polarity inversion line [88], [89], [90], [91], [92], [68], [93], [81], [66] & [94] and global changes, when the entire photospheric and coronal fields in an active region are involved in a flare [95], [96], [97], [98].

Wang et al. [94] summarized the results of a study for six X-class flares and found that there were rapid and permanent changes in the magnetic flux related to the impulsive phase of the flares. Moreover, these events exhibited a puzzling signature in that the changes of the magnetic flux of the two polarities were not balanced. The leading flux always increased while the following flux tended to decrease, although by a much smaller amount. Spirock et al. [66] suggested two possible mechanisms to explain the unbalanced flux variations for the 2002 April 2 flare: The emergence of a very inclined flux tube and/or a change in the orientation of the magnetic field. Later, [94] offered third explanation. The expansion of the preceding sunspot, as a result of the relaxation magnetic field, after a flare.

Very often large flares are accompanied by powerful coronal mass ejections, which can cause severe geomagnetic storms when expelled toward the earth. There are several competing approaches to explain magnetic eruptions and extensive multi-

wavelength data sets, including magnetic field measurements, can be used to provide a discriminator between different models and/or mechanisms.

One approach has been developed by many authors over the years [99], [100], [101], [102], [103] & [104]. It advocates the idea that the energy for eruptions is stored in a flux rope, which is formed long before the eruption occurs. The tether-cutting model [105], on the other hand, suggests that an impulsive major energy release begins deep in a highly sheared core field via reconnection which forms a flux rope. The released magnetic fields then erupt into interplanetary space. All of these models predict that no remote EUV and/or H $\alpha$  emission in a quiet Sun area outside the site of a flare should precede the eruption.

The break out model [106] & [107], instead, assumes that a sheared core field pushes through an overlaying restraining field and a slow reconnection begins at a neutral point high in the corona. At this stage, EUV crinkles and/or remote H $\alpha$  brightenings are expected to occur at the foot-points of the overlaying field lines involved in the reconnection [108]. After the restraining force of the overlaying field is significantly weakened due to the reconnection, the sheared core field then explosively erupts into interplanetary space. As the erupted field leaves the lower atmosphere, it stretches the remaining overlaying field lines, which immediately reconnect beneath the escaping magnetic field while releasing magnetic energy and forming post flare loops at the site of eruption. There are observations that strongly support this prediction. Sterling & Moore [108] and [109] interpreted the EIT crinkles, which occurred before an eruption as evidence for the breakout model.

H $\alpha$ , magnetograph, EUV and X-ray data for the 2002 July 23 flare observed at the east solar limb was analyzed. This gamma-ray flare occurred in Active Region NOAA 0039 and was a long duration event that peaked around 00:28UT. The focus in the current sections is on the evolution of magnetic fields associated with the flare.

### **4.3.2 Observations**

The data set that is used in this study includes vector magnetograms and H $\alpha$  images from the Big Bear Solar Observatory (BBSO), full disk longitudinal magnetograms from the Michelson Doppler Imager (MDI) and EUV images from the Extreme Ultraviolet Imaging Telescope on board the Solar and Heliosphere Observatory (SOHO) and X-ray data from the Ramaty High Energy Solar Spectroscopic Imager (RHESSI).

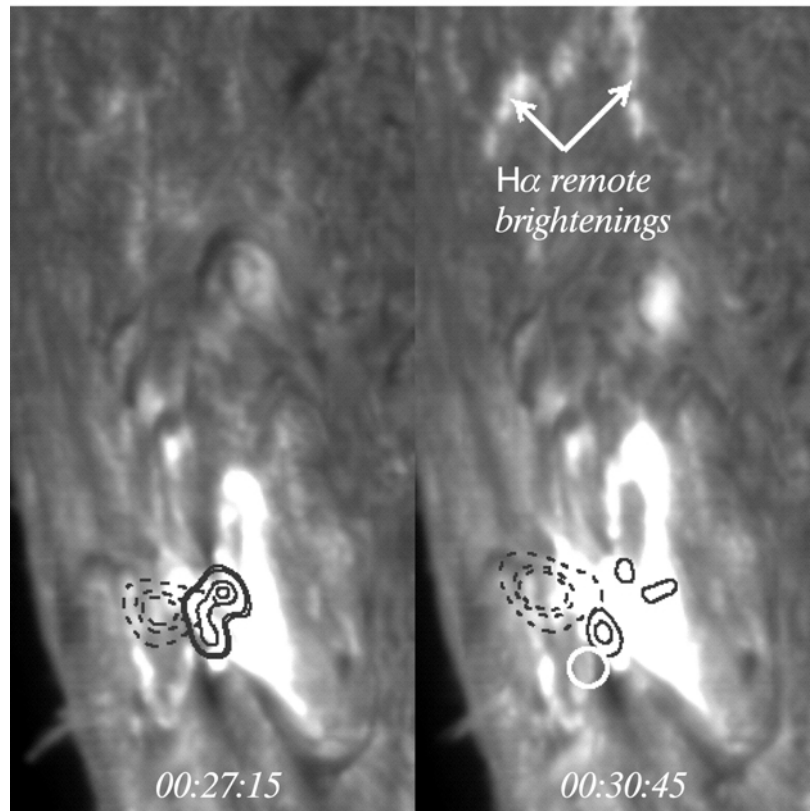
The Digital Vector Magnetograph (DVMG) system at BBSO has a much improved sensitivity and resolution compared to that of the old BBSO Video magnetograph system. The hardware has been described in detail by [84]. It consists of a 0.025 nm band-pass filter, an SMD 1024 x 1024 12-bit CCD camera and three liquid crystals used as polarization analyzers. Each data set consists of four images taken in the blue wing of the 610.3 nm spectral line: a intensitygram (Stokes-I), a line-of-sight magnetogram (Stokes-V) and a transverse magnetogram (Stokes-U and Stokes-Q). The camera is typically re-binned to 512 x 512 pixels to increase the sensitivity of the magnetograms. After re-binning, the pixel resolution is approximately 0.6 arc-sec. The line-of-sight magnetic sensitivity is approximately 2G, while the transverse sensitivity is approximately 20G. The cadence for a complete set of Stokes images is typically one minute.

BBSO magnetograms, used to study this flare, cover two time ranges: 1) from 20:00 UT to 22:45 UT on July 22 and 2) from 00:37 UT to 01:54UT on July 23. In order to cover a longer time period, and to also have independent confirmation of the BBSO observations, one minute cadence full-disk MDI magnetograms were also used.

Much of the energy released during a flare is used to accelerate, to very high energies, electrons (emitting primarily X-rays) and protons and other ions (emitting primarily gamma rays). The goal of the RHESSI mission is to combine, for the first time, high-resolution imaging in hard X-rays and gamma rays with high-resolution spectroscopy, so that a detailed energy spectrum can be obtained at each point in the image [110]. RHESSI has complete coverage of this flare. In this study, RHESSI data at several energy bands, which is necessary to understand the relationship between the structure of the magnetic field and energy release sites, was used.



### 4.3.3 The Gamma-Ray Flare as seen in Multi-Wavelength Data

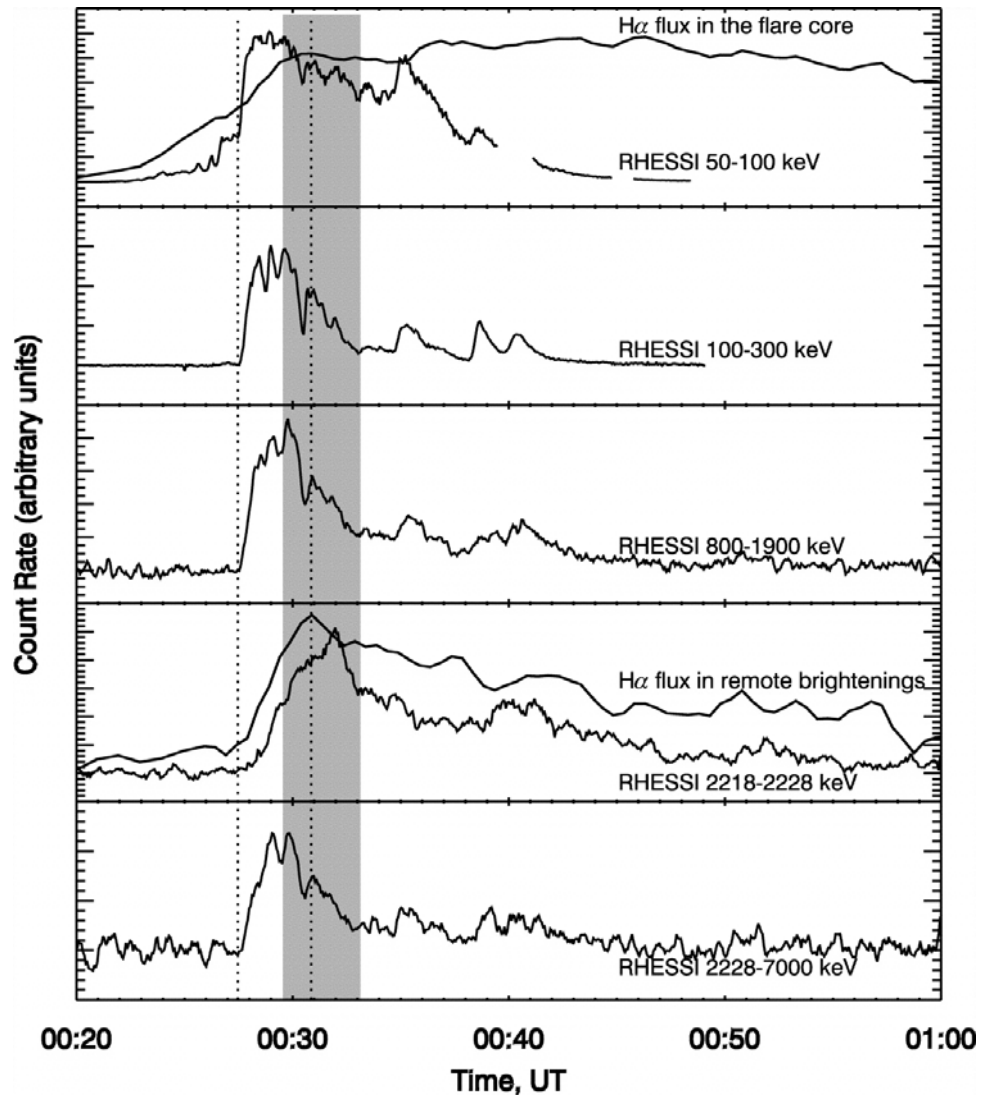


**Figure 4.16** BBSO  $H\alpha$  images of the X4.8 two-ribbon flare on 2002 July 23. The field-of-view is 118 arc-sec x 280 arc-sec. The dashed contours are the corresponding RHESSI X-ray emissions in the energy range of 12 to 20 keV, while the solid contours are for the 100 to 150 keV energy band. The white circle in the right panel shows the position of the 2.223 MeV centroid. North is up and west is to the right.

Figure 4.16 shows the X4.8 two-ribbon flare on July 23 2002, which was the sole gamma-ray flare observed by RHESSI thus far. The background images are BBSO  $H\alpha$  intensitygrams at two different times near the peak of the flare. The corresponding RHESSI hard X-ray emission in the 12 to 20 keV energy band is shown with dashed contours, while the solid contours indicate the hard X-ray emission between 100 to 150 keV. According to [111], the HXR emission, which were dominant above 30 keV was

related to the photospheric foot-points, while the lower energy emission was associated with a gradual coronal X-ray source.

In Figure 4.17, the time history of the  $H\alpha$ , HXR and gamma-ray emission are plotted. The thick line in the top panel of Figure 4.17 shows  $H\alpha$  flux determined at the flare core, where the HXR sources and flare ribbon were observed. The  $H\alpha$  flare started at 00:20 UT, approximately seven minutes before the onset of the impulsive HXR emission. The 50 to 100 keV HXR emission abruptly rises at 00:27:30 UT and peaks at approximately 00:28:30 UT. Other energy bands (100 to 300 keV, 800 to 1900 keV and 2218 to 7000 keV) show very similar time profiles. However, the 2218 to 2228 keV source behaves quite differently. The white circle in Figure 4.16 shows the position of the 2218 to 2228 keV emission centroid, which was significantly displaced from the other HXR sources. There is no sudden rise of the 2218 to 2228 keV emission at the beginning of the flare (see 4th panel in Figure 4.17). Instead, it increases slowly, reaching maximum at about 00:31:38 UT, four minutes after the peak in the HXR emission (the gray vertical bar in Figure 4.17 shows FWHM for this gamma-ray source). A weak  $H\alpha$  flare emission and a surge were observed south-east of the gamma-ray centroid.



**Figure 4.17** (Thin lines) Light curves for 50 – 100, 100 – 300, 800 – 1900, 2218 – 2228 and 2228 – 7000 keV energy bands. (Thick lines) H $\alpha$  light curves for the flare core (top panel) and the for remote brightening (fourth panel).

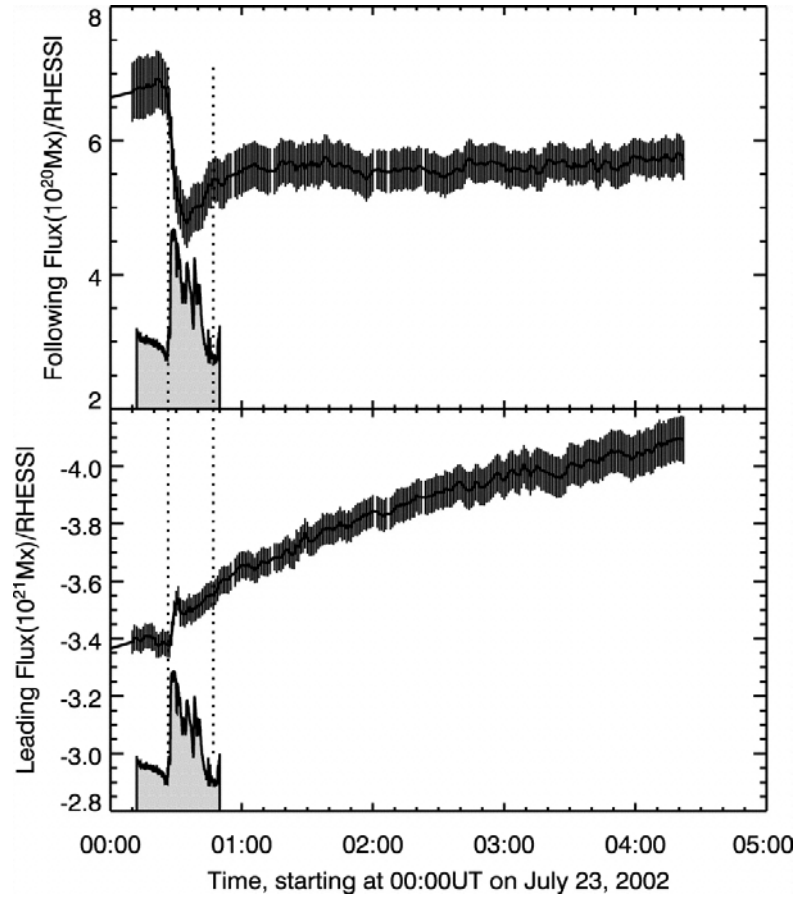
It should be emphasized that the weak and irregular H $\alpha$  emission seen at 00:30:45 UT outside the active region (indicated by the arrows in Figure 4.16). This remote emission was observed as a chain of H $\alpha$  brightenings in a remote quiet Sun area approximately 160 arc-sec north of the active region (Tang and Moore 1982). The thick line in the 4th panel of Figure 4.17 shows the average light curve of those remote

brightenings. The remote H $\alpha$  emission began to gradually rise only at the onset of the impulsive HXR flare and reached a maximum at approximately 00:31:00 UT, which was approximately one minute earlier than the peak of the 2218 to 2228 keV source. The comparison between the time profiles for the remote brightenings and the gamma-ray source shows that those two light curves are very similar within the 00:20 UT to 00:33 UT time interval. However, the 2218 to 2228 keV source lags relative to the H $\alpha$  source by approximately 60 sec. It should also be noted that the peak of the remote H $\alpha$  brightenings coincides with the well pronounced secondary peak in the RHESSI X-ray flux at 00:31UT (right dotted line in Figure 4.17).

#### **4.3.4 Rapid Changes of the Longitudinal Magnetic Field Associated with the Flare**

**4.3.4.1 Magnetic Flux Changes from the Observed Data.** The Mill data, that which has been utilized here, have longer, more complete coverage, and better stability, so only the MDI flux time profiles are presented here. Figure 4.18 shows the time profiles of magnetic flux and the RHESSI hard X-ray flux (in arbitrary units) in the 100 to 150 keV energy range as a function of time. The total MDI flux was determined by separately summing positive and negative flux densities inside a box which enclosed the entire area of the active region shown in Figure 4.19. The error bars in Figure 4.18 indicate the standard deviation determined individually for each magnetogram by calculating the total flux for nine different positions of the box. The flux time profiles are plotted for the leading (negative) and the following (positive) polarity by the thin solid lines. The magnetic field measurements between 00:26 UT and 00:47 UT, when strong HXR emission occurred, were, most probably, affected by the flare and are not reliable (see

Figure 4.20 for the position of the HXR emission relative to the longitudinal magnetic field).



**Figure 4.18** MDI positive (top) and negative (bottom) magnetic flux and the RHESSI XRT flux (shaded area in arbitrary units) in the 100 – 150 keV energy range shown as a function of time.

There was a very rapid and substantial change in both the leading and the following magnetic flux. Immediately after the flare (at 00:47:UT, the right vertical dashed line in Figure 4.18), the total leading (negative) flux increased by approximately 6%, while the total following (positive) flux decreased by approximately 14%. These changes were permanent and the flux did not return to the pre-flare level after the flare ended. Since the total positive and negative flux measured before and after the flare are

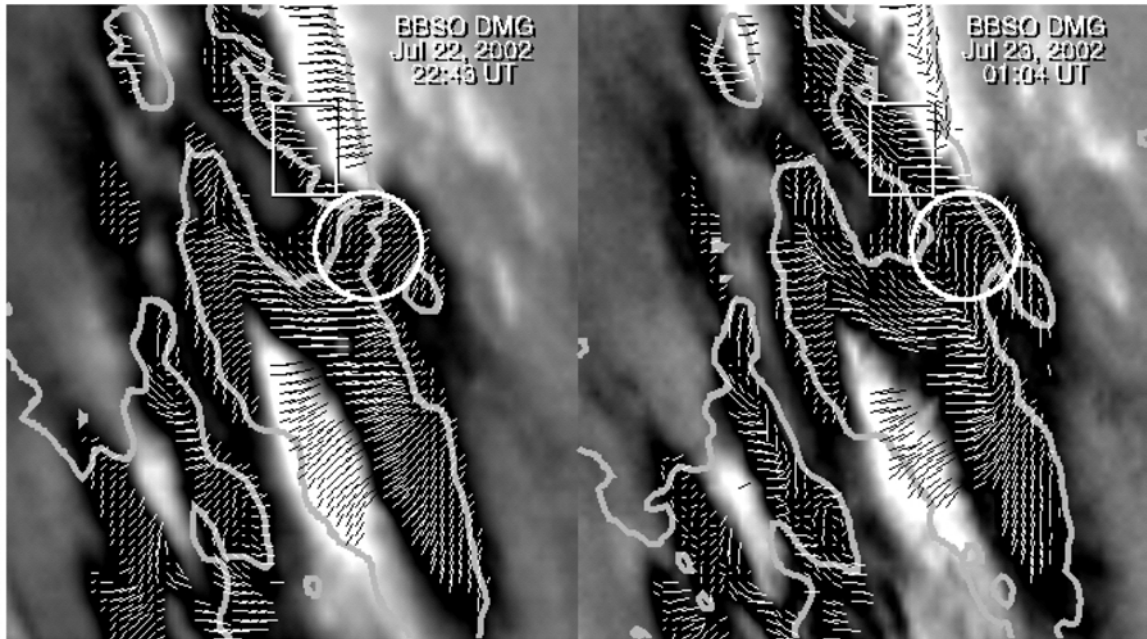
compared, a change of the line profile during the flare is not of a serious concern. Please note that the negative flux (Figure 4.18, lower panel) was continuously increasing during the observing period. It is believed that this gradual growth started before the flare onset and was temporarily interrupted by the rapid fluctuations of the magnetic flux during the impulsive phase of the flare.

The apparent changes of the longitudinal magnetic field at the solar limb (Figure 4.20) are artificial and purely due to the fact that variations in seeing change the position of the solar limb in the field of view between the acquisition of two consecutive circularly polarized images. When a longitudinal magnetogram is produced by subtracting one image from another one obtains an artificial signal, which usually changes rapidly from one magnetogram to another. The noise signal at the solar limb can be distinguished from the persistent changes in an active region which can be traced from one magnetogram to another.

It should also be noted that while the radiation measured close to the solar limb in the 610.3 nm photospheric spectral line is emitted from higher, and thus cooler, layers of the solar atmosphere, this radiation is still mainly formed in the photosphere. Thus, a contribution function for the blue wing of the Ca I 610.3 nm spectral line, determined close to the solar limb [112] shows that this part of the spectral line forms within 400 km from the  $\tau = 5000$  level, i.e. below the transition region between the photosphere and the chromosphere. Therefore, the field measurements made in the blue wing of the Ca I 610.3 nm spectral line refer to the photosphere.

Figure 4.19 shows two BBSO DMG vector magnetograms before (July 22 at 22:43 UT) and after (July 23 at 01:04 UT) the flare. Due to the close proximity of the

active region to the east solar limb (longitude of  $-70^\circ$ ) the 180 degree ambiguity could not be removed. Therefore, the line segments in Figure 4.19 only show the orientation of transverse magnetic fields.



**Figure 4.19** Two BBSO DVMG vector magnetograms acquired before (July 22 at 22:43 UT, left) and after (July 23 at 01:04 UT, right) the 2002 July 23 gamma-ray flare. The backgrounds are longitudinal magnetograms (white/black correspond to  $\pm 350$  Gauss). The leading polarity is negative (black). The gray thick contours outline the photospheric-penumbral boundary of the sunspots. The black and white line segments display the transverse magnetic field, while the box and circle mark the areas where the magnetic flux changes were studied in detail. North is up and west is to the right.

The total positive and negative flux were calculated, from the BBSO magnetograms, over the same area of the active region as it was done in the case of the Mill data, i.e., over the entire longitudinal magnetograms shown in Figure 4.19. According to the BBSO data, the leading (negative) flux increased by about 5% while the following (positive) flux decreased by about 13%. These relative changes are in very good agreement with the MDI flux variations, although the absolute values of the MDI

and BBSO magnetic flux are somewhat different (compare columns 2 and 3 in Table 4.16). This discrepancy in the absolute flux can be due to differences in the spatial resolution and sensitivity of the instruments.

**Table 4.4** Magnetic Flux Values Before and After the Flare as Measured from MDI and BBSO.

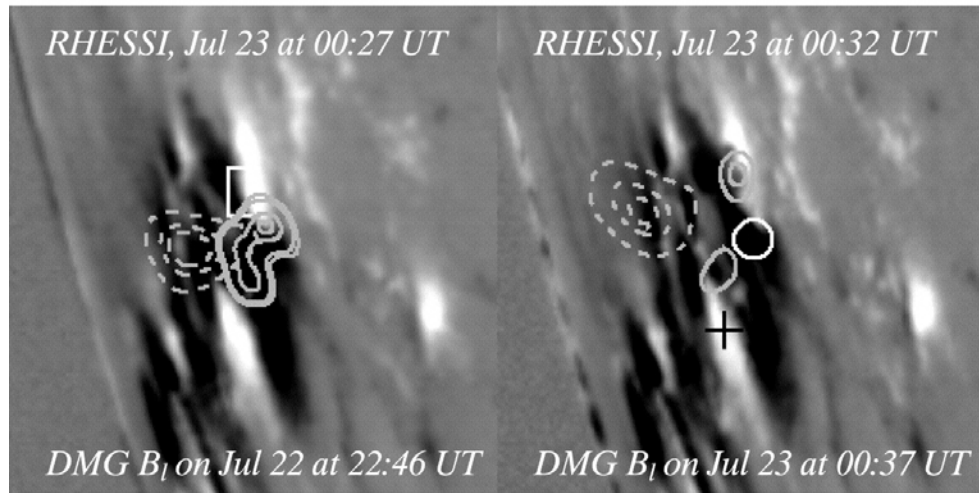
TIME	$F^+ / F^-$ ( $\times 10^{21}$ Mx)		$F^-$ (CIRCLE) ( $\times 10^{20}$ Mx)	$F^-$ (BOX) ( $\times 10^{19}$ Mx)
	MDI	BBSO		
Before.....	+0.7/-3.4	+0.8/-4.2	-1.0	-1.9
After.....	+0.6/-3.6	+0.7/-4.4	-1.3	-5.9
Change (%).....	-14/+6	-13/+5	+30	+210

The BBSO magnetograms in Figure 4.19 illustrate the changes in the longitudinal magnetic field, which were detected by calculating the total flux over the active region. The most dramatic and obvious changes occurred in two regions, marked by the circle and the box in Figures 4.19 and 4.20.

The region marked by the circle is where the northern HXR foot-point source was located at the beginning of the flare (solid contours in Figure 4.20 at 22:46 UT). The magnetograms show that both the line of sight component and the transfer field were affected by the flare at this area: 1) the peak intensity of the longitudinal magnetic field, inside the circle, increased from -800 G to -1100G, 2) the total negative flux increased by ~30% from  $-1.0 \times 10^{20}$  Mx to  $-1.3 \times 10^{20}$  Mx (see also 4th column in Table 4.16), 3) the penumbral bridge, which connected the two major sunspots became wider (compare the gray contours inside the circles), 4) before the flare, the transverse field was largely oriented along a southeast-northwest line, while after the flare the transverse field was



already mainly oriented along the north-south line. All of the facts above, especially the increase of the penumbral bridge, allow speculation that the emergence of new magnetic flux, inside the circle, was associated with the flare. This suggestion is supported by high resolution BBSO H $\alpha$  center-line and off-band (-0.07 nm) images taken two hours before the flare peak (Figure 4.21). In the center of the off-band image (right panel) one can see an elongated cold surge, indicated by the arrow, which existed for several hours before the flare. The foot-point of this surge was located inside the circle (see also Figures 4.19 and 4.20). Also, the negative polarity (leading flux) was gradually increasing during the observed period, which may be interpreted as a signature of emerging flux. According to [113] the surge may indicate ongoing flux emergence in the area. Since the circled area and the position of the earlier HXR foot-point source coincide, it can further be assumed that the new flux may have triggered the gamma-ray flare by alternating the topology of the magnetic field and/or adding twist to the system [110] & [114].

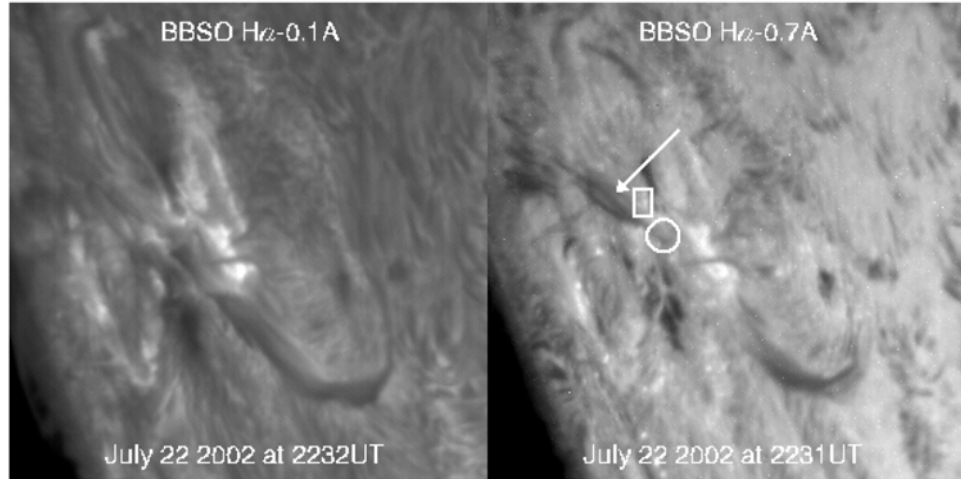


**Figure 4.20** RHESSI data (the same as in Figure 4.16) plotted over two BBSO longitudinal magnetograms (while/black correspond to  $\pm 450$  Gauss) acquired before and after the flare. The box and the circle are the same as in Figure 4.19. The cross marks the position of the 2.223 MeV source centroid. North is up and west is to the right.

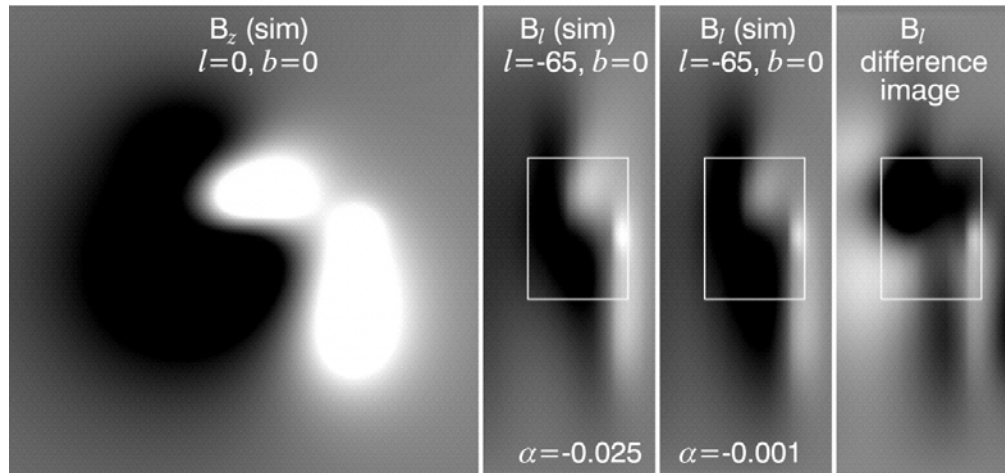
Another area of a great interest is marked by the box in Figure 4.19. A comparison of the two magnetograms shows that the negative magnetic polarity inside the box had increased threefold (from  $-1.9 \times 10^{19}$  Mx to  $-5.9 \times 10^{19}$  Mx, see also 5th column in Table 4.16) largely due to devouring the positive polarity (the position of the neutral line had shifted). The orientations of the line segments inside the box indicate that before the flare the transverse field was largely oriented along an east-west line, while after the flare it was mainly oriented along a southwest-northeast line. Distinctive from the previous case (the circled area), the increase of the penumbral area inside and near the box was not significant and could not account for the threefold increase in the negative flux. The above variations qualitatively correspond to what would be expected if the magnetic field changes its inclination by veering from the observer toward the solar limb. When the veer of the magnetic field vector becomes large enough that the angle between the line-of-sight and the vector of the magnetic field exceeds  $90^\circ$ , then the longitudinal

magnetic field can change its sign and the neutral line will shift. It seems to be the case in the studied event. The box marks the position where the western foot-points of a fast evolving post-flare loop (PFL) system and the northern HXR foot-point source were located in the late and gradual phase of the flare (see Figure 4.20 at 00:37 UT in this section and Figure 1F in [111]). It is known that a PFL system is a new topological link in active region and it is expected that the magnetic field changes its orientation and/or inclination as the PFL system forms.

**4.3.4.2 Magnetic Flux Variations Inferred from Simulated Data.** In order to find out whether the re-orientation of the magnetic field is indeed capable of producing noticeable changes in the total magnetic flux, a series of simple simulations of a linear force-free field (LFFF) were conducted. First, a  $B_z$  magnetogram was constructed with an "S"-shaped neutral line, which is to be used as a boundary condition (see Figure 4.22, left panel). The reason to do so was because there was no observational data for this event suitable for the modeling. Indeed, the longitudinal magnetogram, observed at a longitude of  $-70^\circ$ , in fact represents a component almost tangential to the solar surface and, as such, it can not be used as a boundary condition in this model.



**Figure 4.21** BBSO H $\alpha$  center (left) and H $\alpha$  -0.07 nm (right) images obtained  $\sim$ 2 hr before the flare. One of the foot-points of a cold surge, indicated by the arrow, is located at the position of the earlier XRT foot-point and is probably associated with flux emergence. The box and the circle are the same as in Figure 4.19 (see also Figures 4.16 & 4.20).



**Figure 4.22** Simulated magnetograms: vertical component,  $B_z$ , shown at the center of the solar disk (left) and the longitudinal component of an LFFF calculated with parameter  $\alpha = 0.025 \text{ arc-sec}^{-1}$  and  $\alpha = 0.001 \text{ arc-sec}^{-1}$  (middle two panels), as seen at the eastern limb. White/black is a magnetic field intensity exceeding  $\pm 500$  Gauss. The right panel shows the difference image between the two longitudinal components (black represents areas where the longitudinal component decreased).

It should be emphasized that this numerical exercise is not meant to reconstruct the coronal magnetic field above the observed active region. This was done to only make an estimate whether a change in the inclination of a magnetic field is capable of producing significant variations in the total magnetic flux.

In order to model a magnetic field above the simulated active region, a method to calculate a LFFF described in [115] was used. This method leads to the modeling of a field not only by varying the force-free field parameter  $\alpha$ , which defines the amount of twist in an active region, but also by selecting non-photospheric boundary conditions. The upper bound of  $\alpha$  is limited by the number of nodal points in a 3D grid which is used to calculate a force-free field. The finer the grid the smaller  $\alpha$  can be used in the model. In this case, a LFFF was calculated everywhere inside a 240 x 240 x 160 arc-sec volume with a spatial resolution of 3 x 3 x 2 arc-sec.

Two sets of a LFFF were simulated: one with a large amount of twist ( $\alpha = -0.025$  arc-sec<sup>-1</sup>) and the other had nearly potential field configuration ( $\alpha = -0.001$  arc-sec<sup>-1</sup>). The final step in the simulations was to project modeled vector magnetograms at the eastern solar limb (longitude = -65°) and to calculate the corresponding line-of-sight components, which are shown in Figure 4.22 (two middle panels). The difference image between these two projected magnetograms (right panel) reveals that there is a significant difference between them.

The white box in Figure 4.22 marks the area that was used to calculate the total positive and negative magnetic flux. The calculations indicate that in the nearly potential configuration the leading (negative) simulated flux increased by 24%, while the following (positive) polarity decreased by about 59% as compared to the twisted

configuration. Since the photospheric boundary was the same in both simulations (no new flux emergence), the flux variations in the simulated line-of-sight magnetograms are purely due to changes in the orientation of the magnetic field. Therefore, it has been concluded that the reorientation of the magnetic field is capable of producing significant variations in the observed line-of-sight magnetic flux.

#### **4.3.5 Discussion**

At the beginning of the discussion, the observations presented in the previous sections will be summarized. According to GOES measurements, the X4.8/2B gamma-ray flare started at 00:18 UT on 2003 July 23. A noticeable gradual increase of H $\alpha$  emission began at 00:20 UT at the site of the flare and no associated EUV crinkles or remote H $\alpha$  emission were detected at this time. About seven minutes later the major energy release event started, which was determined by the impulsive rise of HXR emission at 00:27 UT (Figure 4.17). Only after the HXR emission peaked, several remote H $\alpha$  brightenings appeared in a quiet Sun region at a location about 160 arc-sec north of the active region and their intensity reached a maximum at about 00:31 UT, when the secondary peak in the HXR emission occurred. A 2218 to 2228 keV gamma-ray source was observed almost simultaneously with the remote H $\alpha$  brightenings. However, this gamma-ray emission was located inside the active region and was displaced from the main HXR sources. The light curves of the gamma-ray source and the remote H $\alpha$  brightenings are very similar during the period of their gradual increase, though, the gamma-ray light curve lags by approximately 60 seconds relative to the light curve of the remote brightenings. The high time cadence MDI line-of-sight magnetograms showed that after the flare the following (positive) polarity of the active region decreased by about 14%,

while the leading polarity (negative) did not show significant rapid flare-associated change. The leading polarity was gradually increasing for the entire observed period. Furthermore, BBSO high resolution vector magnetograms showed a significant increase of the penumbra area located between the H $\alpha$  flare ribbons as well as changes in the direction of the transverse magnetic field.

The multi-wavelength data for the flare show that, in this event, significant flare-related emission occurred in the core of the flare, prior to the occurrence of the remote H $\alpha$  brightenings. The timing of this particular event does not agree with what would be expected from the breakout model, which predicts that EUV crinkles and/or remote H $\alpha$  brightenings should occur prior to the major energy release event. On the other hand, the models which advocate an eruption of a pre-existing flux tube [99], [100], [101], [102], [103] & [104] or those which require reconnection to form an unstable flux tube [105] are more successful in interpreting this event because they predict that an earliest energy release event should occur in the core field at the site of a flare.

One possible sequence of events during the July 23rd flare will be discussed in the framework on the flux tube and tether cutting models. It is suggested that new emerging flux, discussed in the previous section, disrupted the stability of the pre-existing magnetic configuration (it may also have brought additional twist to the system) and thus triggered a large scale eruption of the magnetic field. The erupted field stretched field lines, which later reconnected beneath the escaping fields and formed a system of post flare loops. The foot-points of these new loops are normally seen in the chromosphere as H $\alpha$  ribbons, early parts of which spatially coincide with hard X-ray sources. As the eruption proceeds,

the reconnection point moves upward causing the hard X-ray sources and H $\alpha$  ribbons to move apart.

Analysis of the motion of the HXR source during the flare (see Figure 3 [111]) showed that the coronal (Figures 4.20 and 4.16, dashed contours) and the northern foot-point source (solid contours) were moving with a comparable speed and in a similar direction, while the southern foot-point source did not display similar motions. It is believed that the different motion patterns of the hard X-ray sources is a manifestation of the upward motion of the reconnection point and was caused by different intensities of the magnetic fields at the foot-points of the PFL system. Generally speaking, during a flare equal amounts of positive and negative magnetic flux should reconnect. In the case of high-density flux (as in a sunspot umbra) the foot-points of the reconnecting field lines occupy a smaller area than the low density foot-points (as in sunspot penumbra). Since HXR emission is a result of the precipitation of high energy electrons at the foot-points of the reconnecting magnetic field lines, then a source associated with the low-density flux will display a wider variety of displacement, while the high-density source would remain nearly stationary. Indeed, Figure 4.20 seems to support this explanation by showing two BBSO longitudinal magnetograms overlapped by the same RHESSI contours as shown in Figure 4.16. The stationary southern HXR foot point was located in a strong field ( $\sim 1000$  Gauss) at the umbra-penumbra border of the negative polarity sunspot, while the moving northern foot-point was associated with the much smaller positive polarity sunspot which moved along the outer edge of the sunspot penumbra, where the magnetic flux density was noticeably lower ( $\sim 600$  Gauss).



It is further suggested that the remote  $H\alpha$  brightenings and the 2218-2228 keV gamma-ray source were quite possibly caused by an interaction between the erupted field and an general large scale magnetic field spanning the active region. After the erupted field pushed high into the corona (according to the data it was about 3 min after the eruption began) it may have reconnected with an overlaying field. Strictly speaking, one would expect to observe  $H\alpha$  and X-ray signatures of this secondary reconnection both remotely and in the core region. If so, the peaks in the HXR emission detected at 0031 UT in the core of the flare and the remote  $H\alpha$  brightening may be signatures of this second reconnection. Note, that there was no significant HXR emission detected at the remote  $H\alpha$  source. The X-ray counterpart of the remote  $H\alpha$  source was, if it existed at all, at least 25 times weaker than the main HXR sources. The increase in the  $H\alpha$  emission at the core site, however, could not be detected mainly due to the high  $H\alpha$  intensity of the core. The similarity between the light curve of the remote  $H\alpha$  brightenings and that of the 2218-2228 keV gamma-ray source is suggestive that those two sources are related and a common process accelerated both electrons and ions. However, (which was against all expectations) the gamma-ray source was offset from the HXR source and only weak  $H\alpha$  activity was seen in its vicinity.

Hurford et al. [116] proposed that the offset may be a result of the acceleration which may occur far from the site of the flare. The accelerated ions traveled over a long distance before encountering the chromosphere. This explanation agrees with the suggestion of a second reconnection event high in the corona. Although the remote  $H\alpha$  brightenings and the gamma-ray source light curves are similar, the gamma-ray source lags the HXR. emission and the remote  $H\alpha$  sources by about 60 s. Hurford et al. [116]

pointed out that the 2223 ke V emission from deuterium is delayed by  $\sim 100$  s due to preceding thermalization and capturing of fast neutrons in the photosphere. The estimated and observed time delays are close which can be interpreted as further evidence that the remote H $\alpha$  source and the gamma-ray source were produced by a common acceleration process.

Finally, a question as to how and when the erupted flux tube was formed still remains open. Was an erupted flux tube formed immediately prior to the eruption as suggested by the tether-cutting model or was it embedded in the magnetic field long before the flare? The available data are not sufficient to make a solid conclusion. However, the observed changes in the photospheric magnetic field detected at the foot-points of the PFL system can be interpreted to be in favor of the tether-cutting model. Indeed, in the case of an eruption of a pre-existing flux tube, a nearly potential overlaying field stretches and re-closes underneath the erupted field thus reforming to another near potential configuration. It is, therefore, not expected to see significant variations in the orientation of the field lines. However, when two (or more) sheared and independent magnetic fluxes reconnect during a flare, the sheared core field changes, so a more potential topology reinstates and this process should give rise to changes in the inclination and/ or the orientation of the magnetic field lines, which is observed in this particular case. A two-dimensional representation of this magnetic topology is depicted in Figure 3 of [117].

In conclusion, the tether-cutting model can successfully explain the observed occurrence of all events discussed in the present study. It is also suggested that a two-step reconnection process is required to explain the occurrence and the location of the offset

gamma-ray source observed in the 2002 July 23 flare. The first reconnection occurs deep in the core field and it is major energy release event. The second reconnection occurs between the erupted field and a general overlying coronal field which produces the secondary peak in hard X-ray emission and a displaced gamma-ray source.

## CHAPTER 5

### SOME CURRENT AREAS OF STUDY

In the current chapter, some recent results will be presented (Chapters 5.1 and 5.2) which will further illustrate the strengths of the Digital Vector Magnetograph (DVMG) with observations that push the limits of currently available instrumentation.

#### 5.1 High Cadence Observations of an Impulsive Flare

##### 5.1.1 Introduction

High cadence X-ray and microwave observations exhibit a sub-second temporal fine structure in solar flares, called elementary flare bursts (see [118] for a review). They are attributed to the fine structure in coronal magnetic fields and are related to the aggregation of photospheric magnetic fields into small scale magnetic elements. From a sample of nearly 3000 HXR solar flares as observed with the HXR burst spectrometer on the Solar Maximum Mission (SMM), [119] found that a portion of the events had a sub-second temporal structure. More recent HXR observations from BATSE on board the Compton Gamma-Ray Observatory (CGRO) provide a much improved sensitivity and energy resolution and a temporal resolution down to 64 ms. Aschwanden et al. [120] used the sub-second temporal structure to study the scales of magnetic loops in flares by applying the time-of-flight method. However, the above observations are only moderately resolved in time and they lack spatial resolution and information about the corresponding magnetic structure.

Impulsive hard X-ray emission in the early phase of a flare is generally regarded as a result of collisional degradation of non-thermal electrons in the dense chromosphere ("thick target") by non-thermal bremsstrahlung [121] & [122]. The heating and ionization of the chromosphere by non-thermal electrons can produce optical ( $H\alpha$  for example) emission nearly simultaneously with hard X-ray bursts [123], [124], [125], [126] & [127]. Specifically, the emission in the wing of the  $H\alpha$  line may be produced via Stark broadening by electrons moving down to the deep chromosphere [128]. In more detail, the emission is due to non-thermal ionization by fast electrons down to the deep chromosphere. The ionization could increase the electron number density in the deep chromosphere by an order of magnitude and the micro-electric field thus produced can produce the Stark effect - the splitting of atomic energy levels. Several authors have actually calculated the electron number density and line profiles [123] & [129].

Spatially resolved observations in the line wings of  $H\alpha$  can be used to track down the precipitating sites of the non-thermal electrons which also produce HXR emission [125], [130] & [131]. There have been some efforts to observe temporal fine structures during the impulsive phase with moderate spatial resolution. High cadence  $H\alpha$  observations were carried out with a system developed by [132] with a time cadence of 0.5 seconds. Kaempfer & Magun [133] studied the evolution of  $H\alpha$  flares with a 1.4 second cadence. These studies could identify some flare foot-points as sites of precipitation, from which the optical emissions exhibited no, or very short, delay (1 to 2 seconds) with respect to the HXR bursts and microwave emission. However, the temporal resolution of these observations is still not sufficient to monitor the often reported sub-

second variations of "elementary bursts" and the moderate spatial resolution is not sufficient to reveal the intrinsic details of the emission sources.

A new fast frame rate (30 fps) CCD camera installed at BBSO enables the study solar flares with an order of magnitude better temporal resolution. Magnetograms of moderate temporal resolution (1 minute) and spatial resolution (approximately 1 arc-sec) provide important context data. Observing under the excellent seeing conditions at BBSO [134] one would expect to obtain more information on temporal and spatial fine structures of impulsive flares. In the near future, it is expected that BBSO observations will be combined with the High Energy Solar Spectroscopic Imager (HESSI) mission [135] for even more detailed investigations on fine structures of solar flares.

### **5.1.2 Observations and Data Reduction**

The GOES C5.7 flare occurred at 18:09 UT on 1999 August 23 in active region NOAA 8673. It was also observed by BATSE on board CGRO. Unfortunately, because of the low flux of this flare, BATSE did not trigger its high-cadence mode. The cadence of the available continuum data is 1.024 seconds.

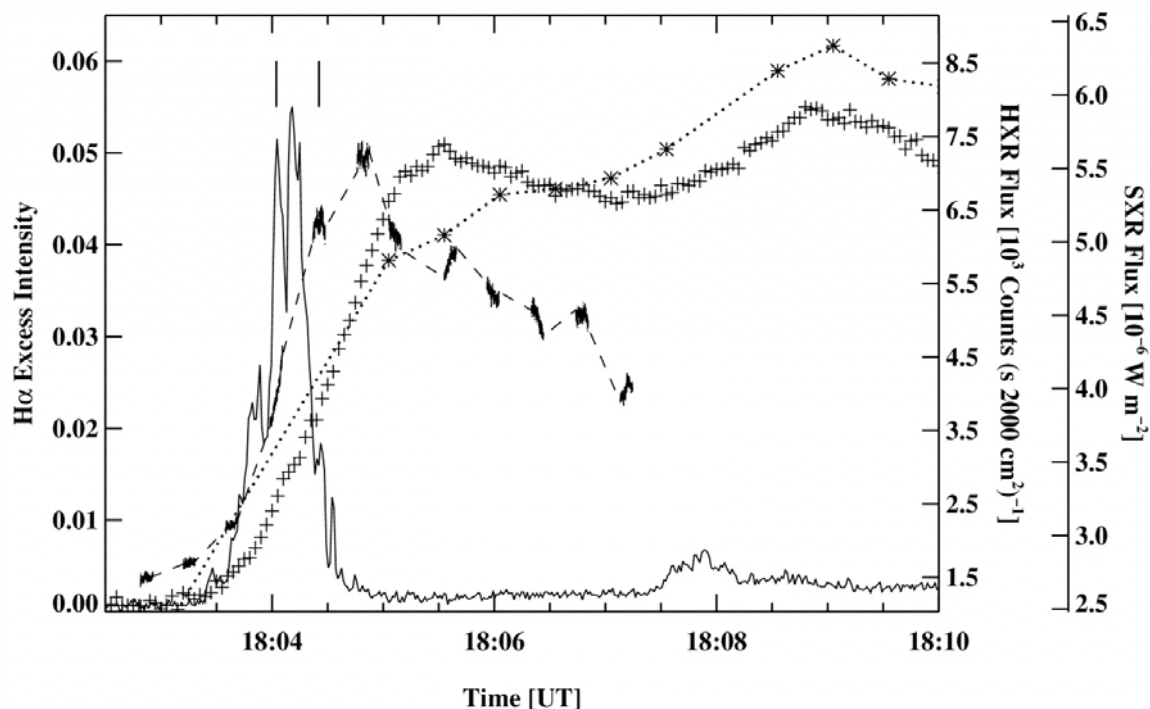
The observations at BBSO completely cover this flare. High cadence  $H\alpha$  observations in the far blue wing are the key data set for this study. A 1024 x 1024 pixel, 12-bit frame transfer CCD camera manufactured by Silicon Mountain Design (SMD) was used to gather the DVMG data. The SMD 1M15 camera is binned to 512 x 512 pixels to increase the signal-to-noise ratio and the frame rate from 15 fps to 30 fps. Such a high frame rate is achieved at the cost of continuous coverage which results in an interruption of 15 seconds for every 200 frames or 7 seconds of data. The exposure time of each individual frame is 8 ms. The image scale is approximately 0.39 arc-sec / pixel. The

observing wavelength is selected by using a Zeiss filter with a bandpass of 0.025 nm. The filter is tuned to 0.13 nm in the blue wing of H $\alpha$  line to study the impulsive behavior of flares, since the center line contains thermal contamination and the red wing contains the component of chromospheric condensation [125].

Supplementary full-disk H $\alpha$  center-line observations are obtained routinely every day with a cadence of 30 seconds to 1 minute and a spatial resolution of approximately 2 arc-sec [136]. Magnetic fields in the active region are observed with the videomagnetograph system [137]. The image scale is 0.5 arc-sec, and the cadence is 1 minute. Only line-of-sight magnetic fields were measured on that day. All the data sets are carefully aligned with standard methods developed by the BBSO group. The accuracy of alignment is usually better than 1 arc-sec.

### 5.1.3 Results

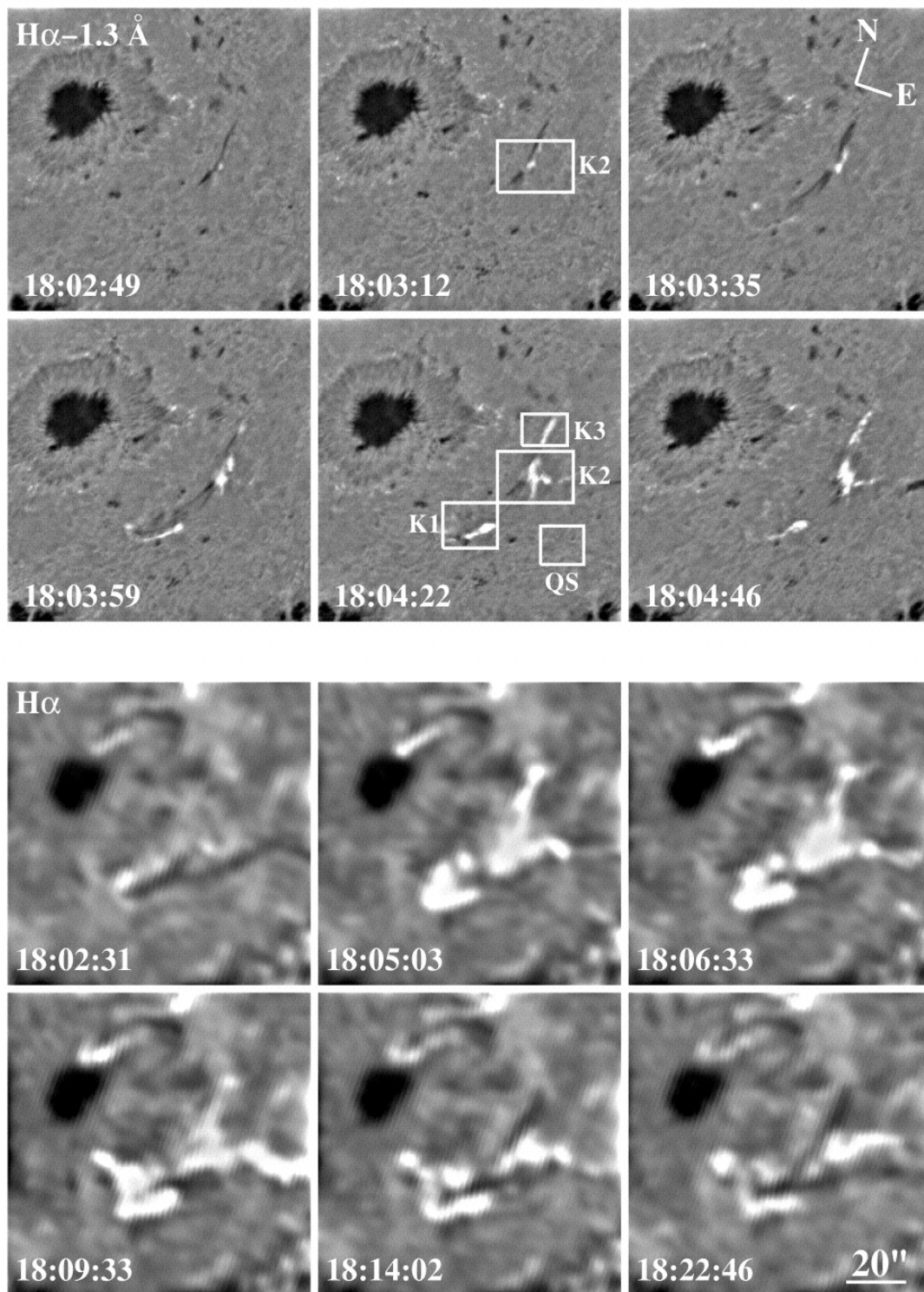
**5.1.3.1 General View of the Flare.** In Figure 5.1, the integrated light curves at different wavelengths are presented. The flare exhibits a typical impulsive phase defined by the impulsive HXR emission showing both fast rise and fast decay. The 25 to 50 keV HXR flux is detected by the most sunward detector of BA TSE. The HXR emission lasts for about 1 minute and consists of several spikes each on the order of less than 10 seconds. It is believed that these HXR temporal structures are due to the continuous acceleration of non-thermal electrons. The main phase is defined by the gradual SXR 0.1 to 0.8 nm (plus signs) and H $\alpha$  line center (dotted curve) emission which peaks a few minutes after the HXR emission. The rise and decay rates of the H $\alpha$  – 0.13 nm emission (dashed line) are between the rates for HXR and SXR as anticipated from the calculation by [125].



**Figure 5.1** Time profiles of GOES soft X-ray (+), BASTE hard X-ray (solid line), H $\alpha$  line center (dotted line) and H $\alpha$ -0.13 nm (dashed line) emissions of the 1999 August 23 flare. The H $\alpha$  light curves indicate the excess emission, i.e., the flare intensity with the quiet region intensity subtracted and then normalized to the quiet region intensity. The two vertical bars in the plot indicate the two intervals of the H $\alpha$ -0.13 nm emission analyzed in the paper and plotted in Figures 5.5 & 5.6.

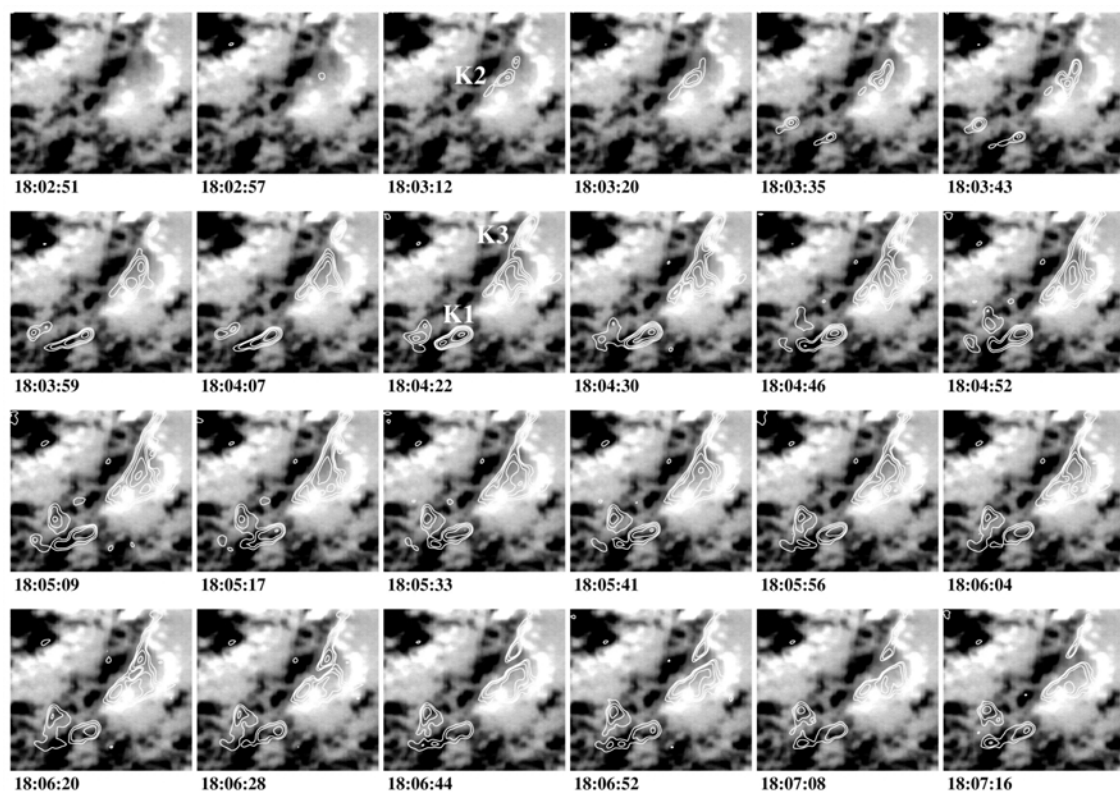


Figure 5.2 demonstrates the morphology of the flare. The top six panels show the sequence of  $H\alpha - 0.13$  nm images during the impulsive phase and the bottom six panels show  $H\alpha$  line center images throughout the flare evolution. The line center images were from full-disk observations, so the resolution appears to be lower. The flare starts close to a filament and at 18:02:49 UT a section of the dark filament appears in the blue band image, indicating a partial eruption of the filament. In the  $H\alpha$  blue wing, an early brightening (K2) appears at this location in less than 1 minute. Two other bright kernels (K1 and K3) appear at approximately 18:03:59 UT, 1 minute after the brightening of the center patch. From the center-line images in the later period, the flare brightening is visible in a much more extended area and evolves into a more complicated sites.



**Figure 5.2** Time sequence of H $\alpha$ -0.13 nm (top six panels) and H $\alpha$  line center (bottom six panels) images showing the evolution of the flare. The white boxes in the figures indicate the regions from which H $\alpha$ -0.13 nm light curves were obtained at the three flare kernels and the quiet-Sun region.

It is important to understand the magnetic structure of the flare. Figure 5.3 shows the evolution of the flare superimposed on the magnetogram. The intensity of the flare at  $H\alpha - 0.13 \text{ nm}$  is presented in contour maps, covering the period 18:02:51 UT to 18:07:16 UT. All of the images are background subtracted (subtracted by the image taken at 18:02:00 UT). The magnetogram, obtained at 18:02 UT, is presented as a gray-scale which serves as the background in all of the panels. The initial brightening K2 at 18:03 UT is not on any magnetic element. Instead, it appears between two magnetic elements of opposite polarity. This is somehow surprising, since the  $H\alpha$  far wing should show sites of particle precipitation, which are usually located at the foot-points of the magnetic loops. K1 and K3, on the other hand, are co-spatial with magnetic elements. This may be due to magnetic reconnection between two loops,  $K1^- - K2^+$  and  $K2^- - K3^+$ , as illustrated by the sketch in Figure 5.9. The loop  $K1^- - K2^+$  connects the negative polarity at K1 and the positive polarity at K2 and the loop  $K2^- - K3^+$  connects the negative polarity at K2 and the positive polarity at K3. After reconnection, the newly formed low-lying loop,  $K2^+ - K2^-$  was very close to the chromosphere and appears as the initial brightening of the flare. Since the two foot-points  $K2^+$  and  $K2^-$  were very close, the emission at K2 cannot be spatially resolved.

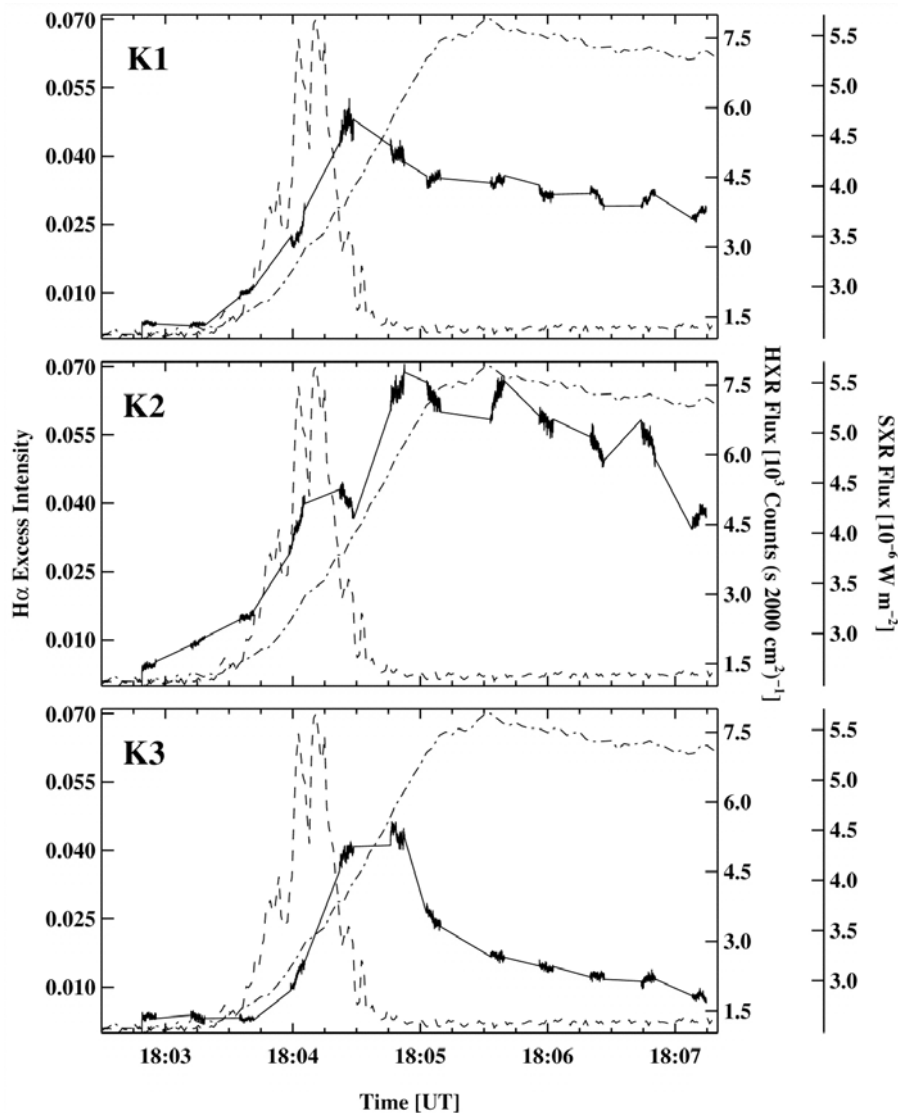


**Figure 5.3** Time sequence of H $\alpha$ -0.13 nm flare emission as shown by contours; the contour levels are 0.05, 0.1, 0.2, 0.4 and 0.8 of the maximum of the emission. The background is the magnetogram obtained right before the flare.

In the following sections, it is not distinguished as to whether the H $\alpha$  – 0.13 nm emission was from the foot-point or from the loop top, but refer to the bright patches as "flare kernels."

**5.1.3.2 Evolution of Flare Kernels.** To further analyze the evolution of the spatially resolved flare emission, light curves of the individual flare kernels were obtained. Three regions covering the three flare kernels are defined, as indicated by the white boxes in Figure 5.2. For each box, the mean of the flare intensity was computed by subtracting the quiet-Sun region intensity and then normalizing to the quiet-Sun region

intensity. These light curves indicate the temporal evolution of the excess flare emission in the  $H\alpha$  line.



**Figure 5.4** Time profiles of the flare emission in  $H\alpha$ -0.13 nm at three flare kernels (solid line) compared with BASTE hard X-ray emission (dashed line) and GOES soft X-ray 0.1 to 0.8 nm emission (dot-dashed line).

Figure 5.4 shows the light curves at the three flare kernels. The three kernels apparently exhibit different temporal profiles. The emissions in K1 and K3 both

demonstrate a fast rise and the decay phase consists of two episodes. A fast decay followed by a slow decay, which is similar to the findings of [133].

It is interesting that K2 also shows two distinct episodes in its evolution. Up until 18:04:30 UT, the light curve shows more similarity to the HXR bursts, though the H $\alpha$  data at the HXR maximum are missing, and there is enhanced emission even before the HXR starts to rise. After the impulsive phase, the H $\alpha$  emission displays a gradual behavior, and the temporal evolution shows more similarity to the SXR emission. The temporal behavior of the spatially resolved flare kernels confirms the scenario suggested above, that K2 is the site where two magnetic loops reconnect. The initial energy release occurs at K2 and soon the accelerated electrons precipitate along the reconnecting loops to produce the HXR emission and the impulsive H $\alpha$  blue wing emission.

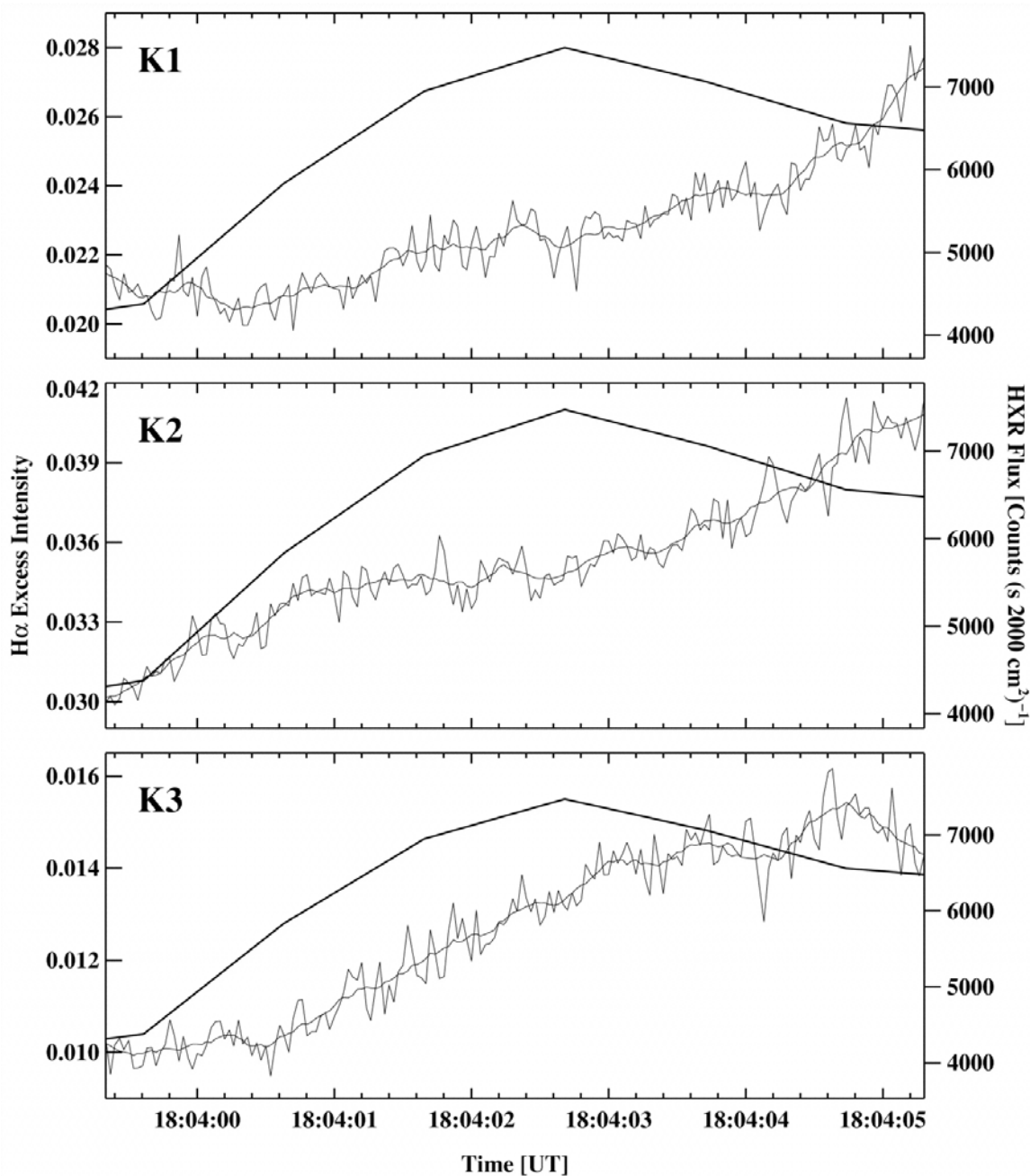
### 5.1.3.3 Temporal Correlation with HXR.

The unprecedented high-cadence observations offer a unique opportunity to investigate the possible correlation between the HXR bursts and deep chromospheric emission on a fine timescale. Specifically, three of the H $\alpha$  – 0.13 nm data sets are obtained during the impulsive phase when there is significant HXR emission.

1. Time interval 18:03:35 to 18:03:41 UT - During this period, the HXR emission rises monotonically as do the emissions at K1 and K2. This suggests that the chromosphere at these two sites, probably as conjugate foot-points of loop K1<sup>-</sup> - K2<sup>+</sup>, begins to be heated by non-thermal electrons. But the HXR photon counts during this period are still too low for any detailed investigation.

2. Time interval 18:03:59 to 18:04:06 UT - Figure 5.5 shows the temporal evolution of the H $\alpha$  – 0.13 nm intensities for the three kernels and a corresponding 10-

point smoothed curves as well as the HXR flux (thick line) from the most sunward detector of BATSE. During this period, the HXR emission shows a peak, while all three H $\alpha$  kernels exhibit a monotonic rise. Because of the data gap at the H $\alpha$  – 0.13 nm, the exact time lag between the HXR maximum and H $\alpha$  – 0.13 nm maximum can not be determined, but the delay is at least 2 to 3 seconds. The temporal correlation between any of the two kernels is strong (greater than 80%), suggesting simultaneous chromospheric heating at all three sites.



**Figure 5.5** Comparison of H $\alpha$ -1.3A intensity (thin lines) and hard X-ray flux (thick lines) for three flare kernels during the time interval 18:03:59 to 18:04:06 UT. For the H $\alpha$  emission, both the raw data and a 10 point smoothed curve are plotted.

3. Time interval 18:04:22 to 18:04:29 UT - In this period, HXR shows two spikes, which are covered by the H $\alpha$  blue wing observations. This time interval gives the best opportunity to investigate the temporal correlation between HXR and H $\alpha$  - 0.13 nm



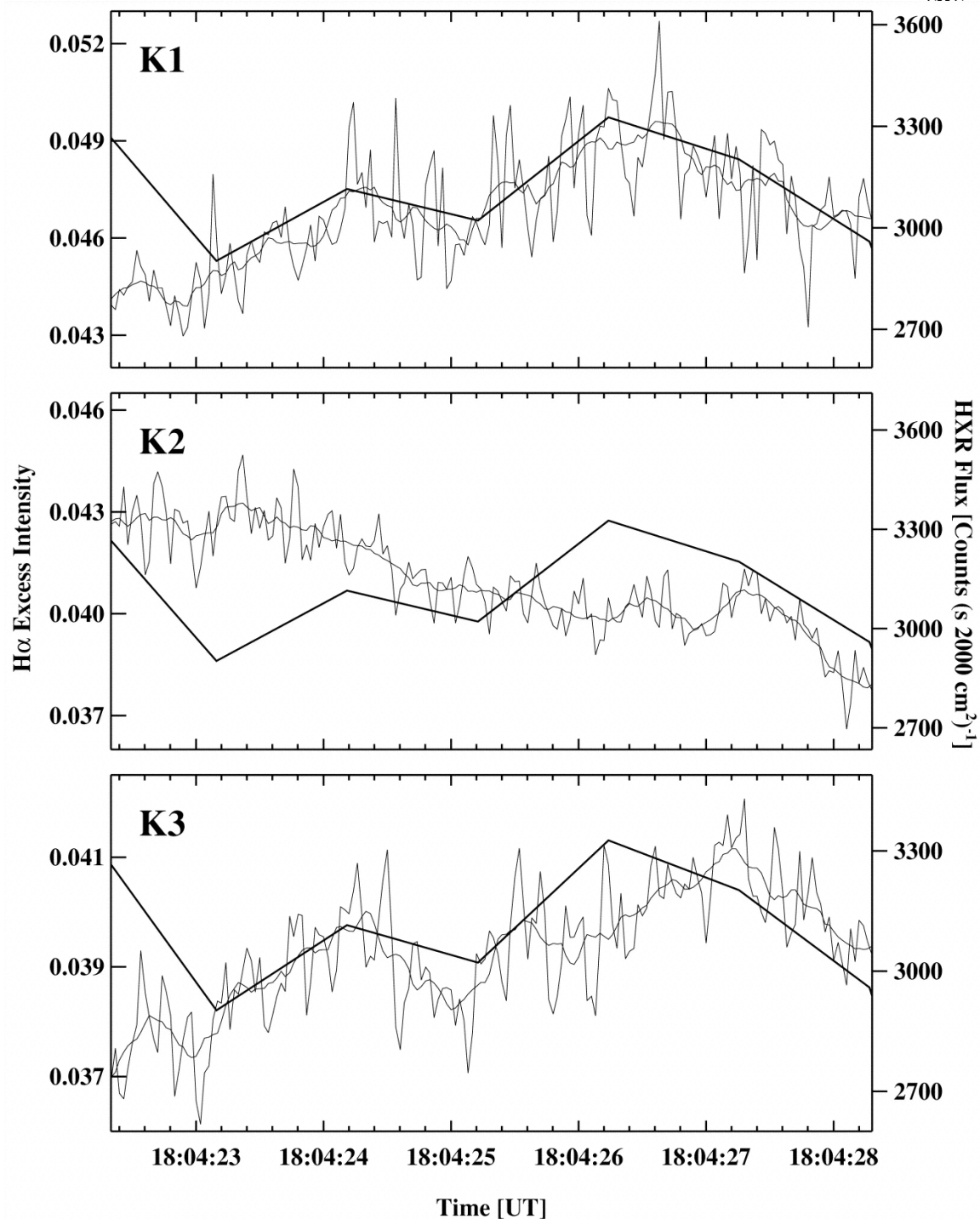
emission. Figure 5.6 illustrates the  $H\alpha - 0.13$  nm intensities at the three kernels and the hard X-ray flux in this time interval. It is obvious that in K2, there is no correlation between X-ray and  $H\alpha$  emission. K3 shows some degree of linear correlation (54%) between HXR and  $H\alpha$  emission, while K1 has the best correlation (92%) within the HXR time resolution. It is evident that continuous electron acceleration is present during this period, and the HXR source could be located at K1 with some contribution from K3. This also suggests that in this event, during the late impulsive phase, continuous electron precipitation occurs at the conjugate foot-points of the newly formed  $K1^- - K3^+$  loop.

The difference in the time profiles of the  $H\alpha$  kernels at different time intervals will be discussed in Chapter 5.1.4.

**5.1.3.4 High-Frequency Fluctuation in the Flare Kernels.** During the C5.7 flare event, the BATSE HXR detector was working at a rather low cadence. However, the  $H\alpha$  blue wing emission, especially during the times of strong temporal correlation with HXR bursts, can be used as a proxy for electron beam heating to examine high-frequency fluctuations. First, the fluctuations due to seeing and the temporal variations of the sky brightness are examined. The seeing induced fluctuations are determined from the contrast variations of a quiet-Sun region. They are on the order of only 0.05%. The variations in the sky brightness are determined from the light curve of the quiet-Sun region, and they are about 0.06%. Therefore, the fluctuations due to both seeing variations and the change of the sky brightness are negligible in the following analysis.

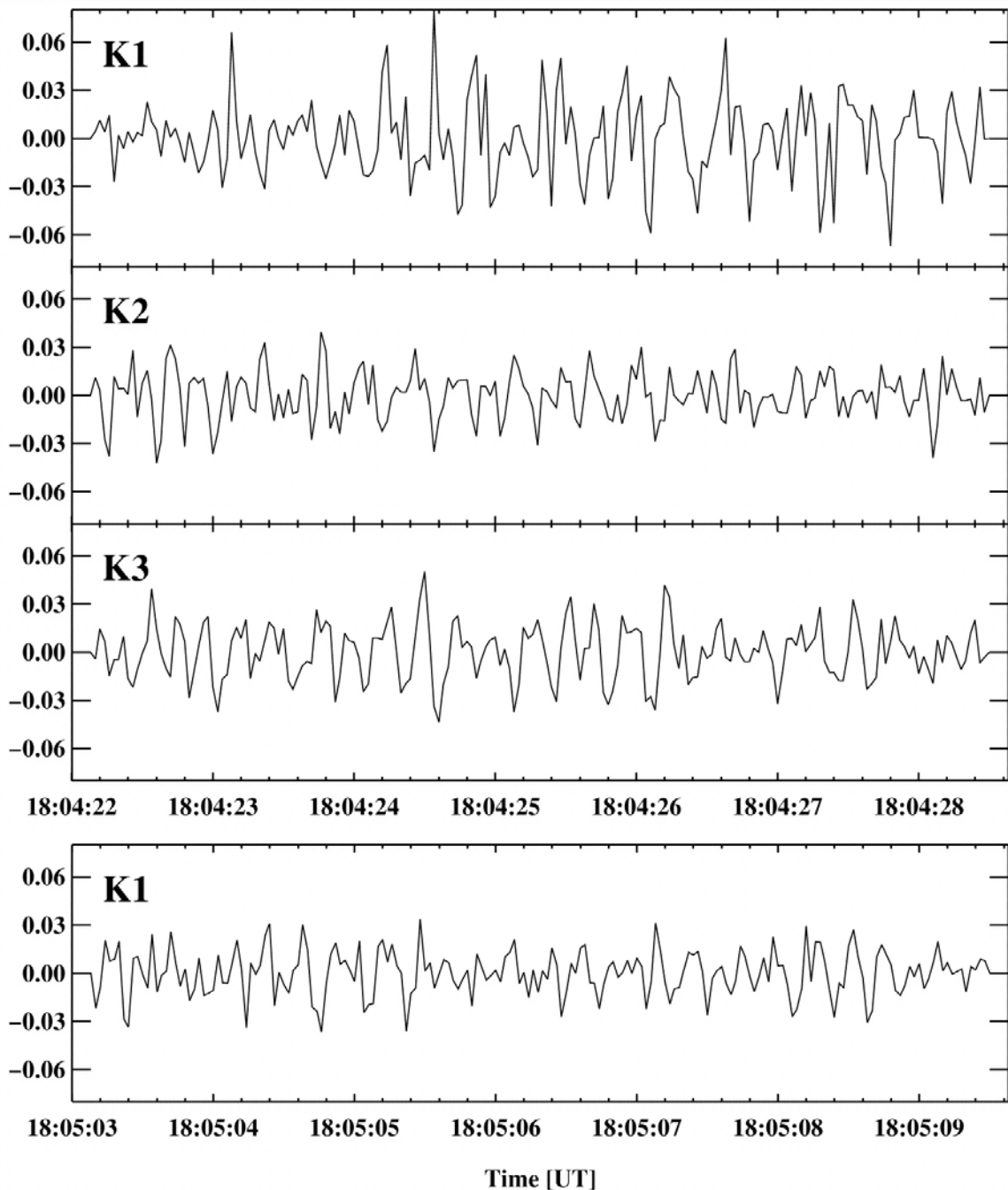
In Figure 5.6, it is noted that some larger fluctuations at K1 than at K2 and K3. In the top three panels of Figure 5.7, the same light curves are shown as those displayed in Figure 5.6 but with the low-frequency component subtracted. The amplitude of the

fluctuations at K1 is greater than at K2 and K3, and the standard deviation of the high-frequency components at K1 is about twice of that at K2 and K3.

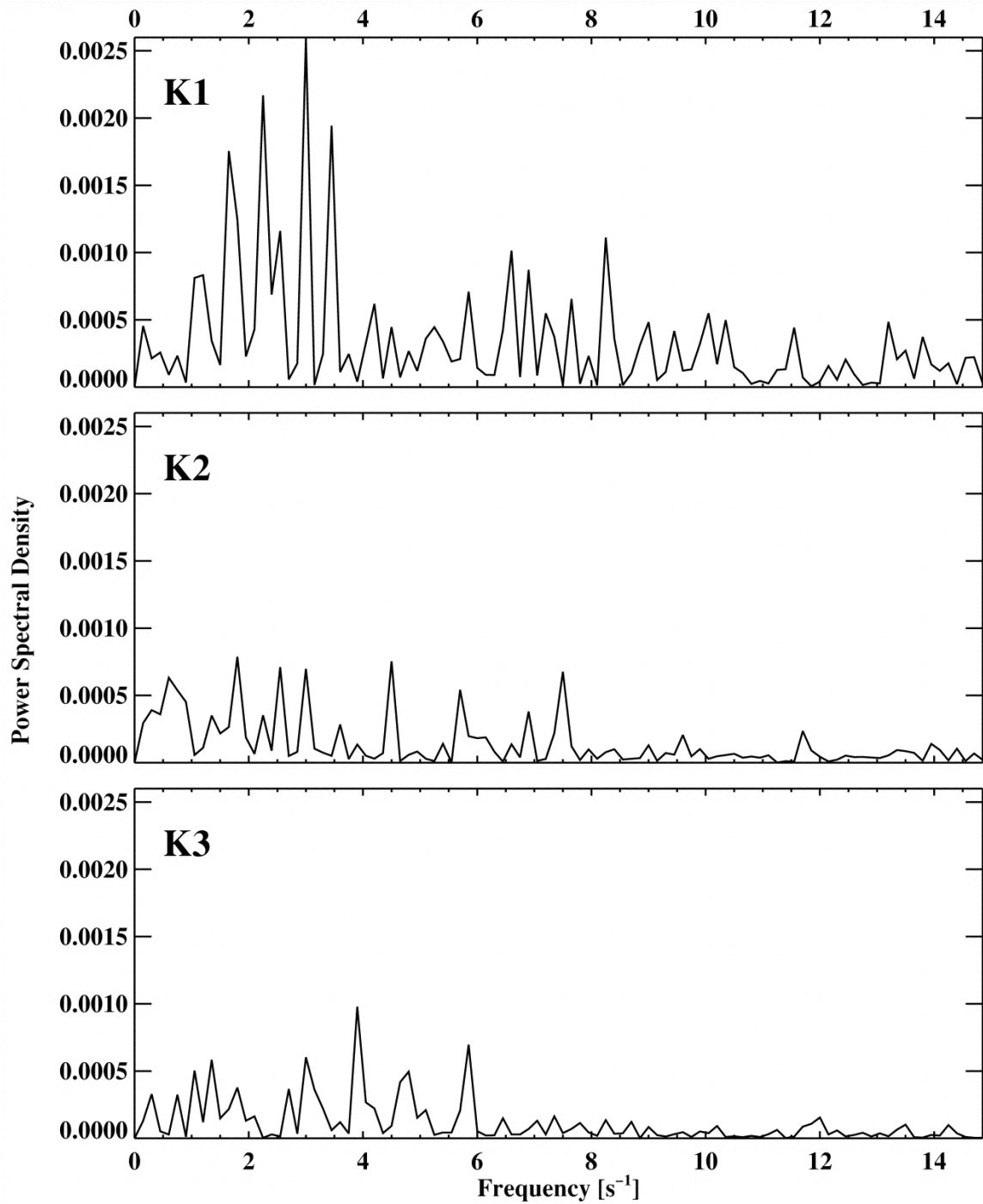


**Figure 5.6** Comparison of H $\alpha$ -0.13 nm intensity (thin lines) and hard X-ray flux (thick lines) for three flare kernels during the time interval from 18:04:22 to 18:04:29 UT. For the H $\alpha$  emission, both the raw data and a ten point smoothed curve are plotted.

To estimate the frequency of the fast variations, the temporal power spectrum of the H $\alpha$  light curves were computed. A Hanning high-pass filter, with a cutoff of 1 second to remove slow variations, was used. Figure 5.8 illustrates the power spectra of the H $\alpha$  – 0.13 nm residual intensity at K1, K2, and K3. It evidently exhibits fast variations at K1 with a dominant frequency range between 1.5 to 3.3 Hz, indicating the fast-varying temporal structures at a timescale of 0.3 to 0.7 seconds. This is the same timescale previously reported in the observations of HXR fast variations [119], [138], [132] & [139].



**Figure 5.7** Time profiles of H $\alpha$ -0.13 nm flare emission. The ten point smoothed background is subtracted from all of the curves. The top three panels show fluctuations at three flare kernels in the time interval shown in Figure 5.1. The bottom panel shows the variations at K1 in a time interval 40 sec later.



**Figure 5.8** Power spectra of the fast variations of the H $\alpha$ -0.13 nm emission at the three flare kernels 18:04:22 to 18:04:29 UT.

Note that such high-frequency fluctuations only exist in this time interval when the best temporal correlation between  $H\alpha - 0.13$  nm and HXR emission is present. In the bottom panel of Figure 5.7, a similar curve for K1 is plotted at a different time interval 40 seconds later, when there is no HXR emission. The amplitude of the fluctuation in this panel is comparable to that in the second panel. Such a comparison indicates that the high-frequency fluctuations observed at K1 during the 18:40 UT time interval were related to the so-called "elementary HXR burst."

From the original images, K1 is carefully examined. The fluctuations reflect intensity changes in the same patches at a spatial scale of less than 1 arc-sec, but not appearances and/or disappearances of different small patches. With even higher spatial resolution, the fast fluctuations may be fully spatially resolved.

It should be noted that the origin of the rapid fluctuations in kernel K1 is still unclear when there is no high-cadence hard X-ray data to compare with. The possibility that the fluctuation in K1 is due to seeing can not be ruled out. However, it is believed that everything that could have been tested for this specific case was attempted and found no evidence that the larger fluctuation is due to the seeing. Also, different boxes covering the kernels, when the various fluxes were calculated, were used and no difference in the time profiles were found. So selection of the box is not a problem. Images were de-stretched so the differential seeing is very small. The absolute confidence will only come out of the comparison with hard X-ray time profile. Until HESSI is operational, this point will remain unclear.

**5.1.3.5 Summary of Results.** High-cadence observations of a C5.7 flare on 1999 August 23 were obtained yielding the following results:

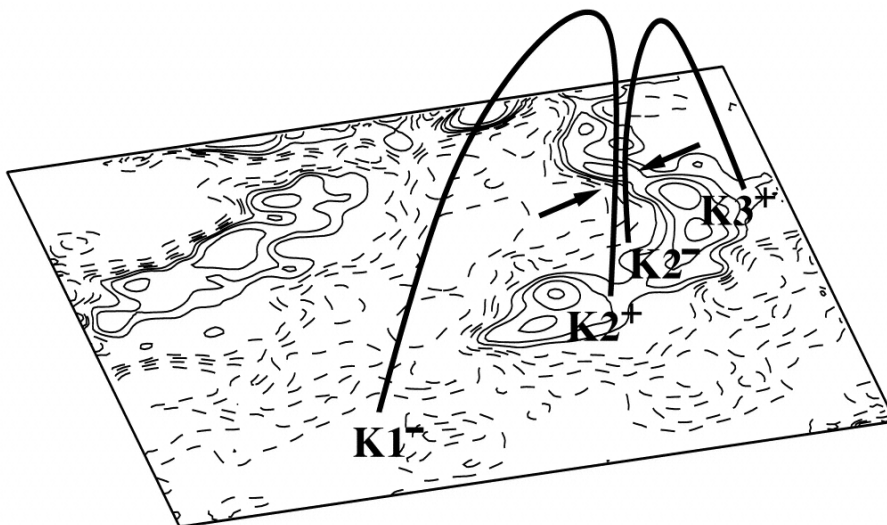
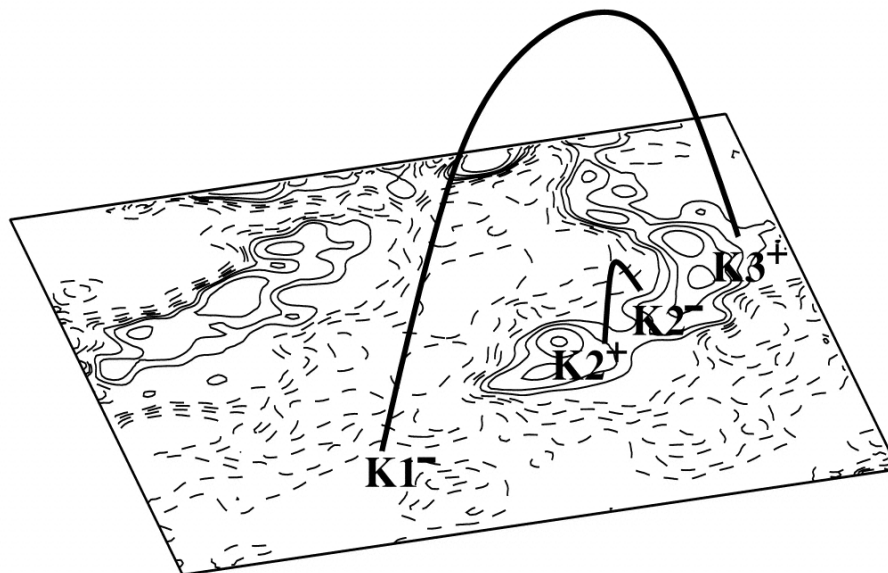
1. Three flare kernels were observed in  $H\alpha - 0.13$  nm during the impulsive phase of the flare. The flare starts in a non-magnetic area at the magnetic neutral line. A scenario on how the top of a dense low-lying loop is the initial energy release site was developed.

2. The temporal behavior of these three kernels was analyzed with respect to the HXR emission. It was found that, during a 7 second period, the brightening at one of the three flare kernels (K1), possibly the foot-point of a flare loop, follows the variation of the HXR flux very closely. Therefore, it has been concluded that it is the source of HXR emission.

3. The flare kernel K1 illustrates the best correlation with HXR. The  $H\alpha$  emission at this kernel shows fast fluctuations on a timescale of 0.3 to 0.7 seconds. They are the real signature of the temporal fine structure of the flare, and they indicate high-frequency electron acceleration and precipitation at the foot-point of the flare loop, which also gives rise to the HXR " elementary bursts " as reported by [132].

The three observed flare kernels at  $H\alpha - 0.13$  nm are located at the top of a compact loop, and two foot-points of a long, overlying loop. The low-lying compact loop is the product of magnetic reconnection (see Figure 5.9), while the HXR-correlated foot-point brightenings demonstrate high-frequency variations which are an important impulsive phase behavior of solar flares.



**(a) Before reconnection****(b) After reconnection**

**Figure 5.9** Sketch of the magnetic configuration of the flare before and after the reconnection. The background contours show the line-of-sight magnetogram taken before the flare as in Figure 5.3. The solid (dashed) lines indicate the positive (negative) magnetic polarities, and the contour levels are  $\pm 20, 50, 100$  &  $200$  Gauss.

#### 5.1.4 Discussion

The high-cadence observations are designed to investigate the "elementary bursts" previously reported in HXR and radio microwave observations. From the above analysis, positive evidence that the variations in the HXR burst and  $H\alpha - 0.13$  nm emission are strongly correlated have been obtained, and the existence of a high-frequency variation from the  $H\alpha$  observations has been confirmed. The observations demonstrate that the dominant fast variations in the impulsive phase of the flare are on a timescale of 0.3 to 0.7 seconds, which can be unambiguously detected with a temporal resolution of better than 0.066 seconds. The sub-second HXR bursts are supposed to represent "quantized" injections of accelerated electrons [140], possibly the result of many small-scale reconnections. The fact that changes of the locations of the impulsive  $H\alpha - 0.13$  nm emission sources have not been observed suggests that the filamentary structures are confined to a scale of less than a few hundred kilometers at the level of photosphere.

The chromospheric observations were made in the  $H\alpha$  blue wing based on the assumption that the  $H\alpha$  blue wing emission should come from a "thick-target" via Stark broadening by non-thermal electrons penetrating into the deep chromosphere. Out of the three flare kernels studied, two can be identified as deep chromospheric foot-point sources, but a possible loop top source, that is apparently not located at a magnetic element but is at the magnetic neutral line, has been observed. It raises an interesting question: what kind of chromospheric heating mechanism can produce  $H\alpha - 0.13$  nm emission at the top of a loop? Since the most important condition to produce  $H\alpha$  far wing emission is the electron density, this loop must be very low and dense. If the magnetic reconnection occurs at a low altitude in this loop, it is also likely that after the impulsive

phase when HXR emission ends, heating of the chromosphere via thermal conduction in the flare loop could be very efficient and  $H\alpha - 0.13$  nm is probably still not far enough from the line center to avoid thermal impact.

It is also puzzling that the HXR emission peaks at least 2 to 3 seconds before the  $H\alpha - 0.13$  nm emission in the very early stage of the impulsive phase. This non-negligible delay of chromospheric off-band emission with respect to the HXR emission may be due to the ionization timescale of the chromosphere. According to [125], the chromospheric ionization timescale is determined by the intensity of the non-thermal flux deposited to the chromosphere. For the non-thermal flux of  $1 \times 10^{11}$  ergs  $\text{cm}^{-2} \text{s}^{-1}$ , this timescale is estimated to be 0.3 to 0.4 seconds, while for less strong flux, the ionization timescale can amount to a few seconds. Hence, the delay of  $H\alpha$  emission can be as large as a few seconds. Since the flare is only a C5.7 event, the HXR flux is at least one order of magnitude weaker than  $1 \times 10^{11}$  ergs  $\text{cm}^{-2} \text{s}^{-1}$ . It is proposed that the observed time delay in the early impulsive phase is due to ionization of the cool chromosphere. While 30 seconds later, a good temporal correlation between hard X-ray bursts and  $H\alpha$  emission because has been observed, by then, the chromosphere is sufficiently ionized and can respond promptly to the further input of electron beams which also produces HXR bursts in the late impulsive phase. It is unlikely that the time delay in the early stage is thermal in nature. According to [127], in the presence of non-thermal beams, which is supported by the HXR emission, the thermal influence on the chromosphere is negligible.

## 5.2 Signature of an Avalanche in Solar Flares as Measured by Photospheric Magnetic Fields

### 5.2.1 Introduction

A solar flare can be regarded as a dissipative process in a nonlinear dynamical system. This approach, which originated from a conjecture by [141], has gained much favor during last decade as a self-organized criticality (SOC) concept. This model is based on the assumption that in an active region there is magnetic coupling between the photosphere and the corona [141] & [142]. Due to photospheric turbulence, random motions of foot-points of magnetic loops [143] and the emergence of twisted and braided magnetic flux tubes [110] & [114] continuously create disturbances in the photospheric magnetic field. These disturbances then propagate into the corona and they create braided and intertwined magnetic flux tubes or numerous tangential discontinuities, thus driving the coronal magnetic field into the SOC state. When the number of discontinuities exceeds a critical level, an avalanche of fast small-scale reconnection events (a flare) occurs [141]. Note that a recent study by [144], based on the comparison of coronal images from SOHO/EIT with photospheric magnetograms from SOHO/MDI in quiet regions of the Sun, strongly suggests that there is magnetic coupling between the photosphere and the corona.

This new paradigm is successful in explaining many observed aspects of solar flares and coronal heating (see [145] for references). This concept also significantly broadens the range of available mathematical tools suitable for the analysis of the dynamics of magnetized solar plasma.

A nonlinear dissipative system can be analyzed by several means: as an attractor of the dynamics of a system (the SOC concept [146] & [145]), as an energy cascade in

fully developed turbulence ([147], [148] & [149]), as a percolation cluster ([150] & [151]) and as a multifractal structure [152]. The behavior of high statistical moments of probability distributions has become vitally important for the study of the evolution of such a system.

In this chapter the turbulence theory has been chosen in order to analyze flare-related changes in the photospheric magnetic field. Random motions of foot-points of magnetic loops and the emergence of new magnetic flux seem to contribute to the turbulent state of the photospheric magnetic field as long as the vertical component of the photospheric magnetic field diffuses in the solar plasma in the same way as scalar field does in a turbulent flow at large magnetic Reynolds numbers [142] & [153].

In general, an increase (decrease) in the turbulence implies that the turbulence becomes more (less) intermittent. Intermittency characterizes a tendency of a turbulent field to concentrate into widely spaced very intense small-scale features [154] & [155]. The degree of intermittency may be estimated quantitatively, in particular, by determining structure functions of high statistical orders [155]. Here methods of the theory of turbulence will be applied to the longitudinal magnetic field in an active region measured near the center of the solar disk. In particular, a scaling exponent,  $\beta$ , obtained from sixth-order [156] will be analyzed as a measure of the degree of intermittency. The correlation length,  $\lambda$ , of the magnetic energy dissipation field will also be calculated and analyzed.

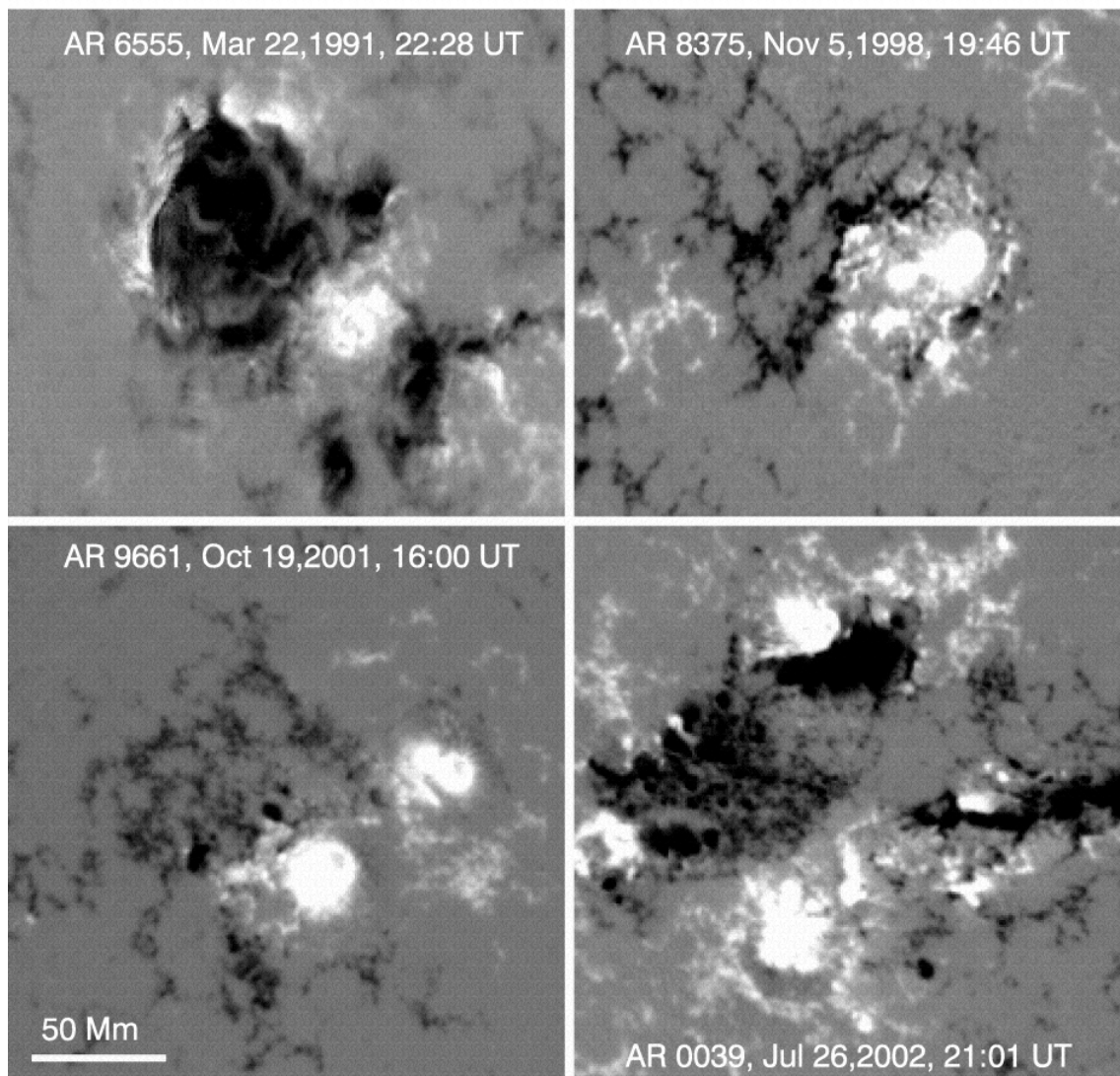
It should be emphasized that the current study is based on an analysis of high statistical moments of the magnetic field. Thus, time variations of these statistical moments reflect subtle small-scale rearrangements in the magnetic field, which usually

cannot be detected by visual inspections of magnetograms and by traditional methods, where only the first and the second moments are analyzed. The method applied here does not allow any estimations to be made of the magnetic energy released during a flare and it is only restricted to the structural rearrangement analysis.

### **5.2.2 Observations**

When data for the purposes mentioned above was selected, the following criteria was used. Namely, in order to reduce projection effects, only those active regions that were located near the central meridian of the Sun (no more than  $40^\circ$  away from disk center) were used.

The observations should also cover time periods before, during and after a major flare (GOES M class and higher) with an appropriate time cadence and excellent seeing. For this purpose, the Big Bear Solar Observatory (BBSO) archive of magnetic field measurements acquired between 1991 and 2002 were used. Four cases that satisfied all of the above requirements were found. The selected active regions are listed in Table 5.1 (in order of increasing X-ray class) and the corresponding longitudinal magnetograms are shown in Figure 5.10.



**Figure 5.10** Maps of the longitudinal magnetic field of the four active regions under study. Images are scaled with a range of  $\pm 500$  Gauss. West is to the right and north is to the top.

NOAA active regions 6555 and 8375 were observed with the BBSO Video Magnetograph system [137]. The dimension of the CCD array was 481 x 512 pixels and the scale of each pixel was 0.776 arc-sec x 0.60 arc-sec. Observations for NOAA AR 9661 and AR 0039 were carried out with the BBSO Digital Magnetograph system ([84]

& the primary subject of this thesis) by a 512 x 512 pixel CCD camera with a pixel scale of 0.6 arc-sec. All magnetograms were taken with the Ca I 610.3 nm spectral line.

0.1 to 0.8 nm GOES X-ray data and BBSO full-disk H $\alpha$  images were also used. Unfortunately, for NOAA AR 6555 the latter was not available. All flares analyzed here were of the two-ribbon type and were followed by coronal mass ejections (CME).

The M8.4 flare, which occurred on 1998 November 5 in NOAA AR 8375, was analyzed in detail by [157] and by [158]. This was the only case, of the four flares considered in this chapter, when the seeing and instrumental conditions were very good for more than the 2 hour period covering the entire flare. 94 magnetograms, acquired between 18:54 and 20:54 UT, were used in order to analyze the variations in  $\lambda$  and  $\beta$ .

For the M8.7 flare, in NOAA AR 0039 on 2002 July 26, the seeing conditions allowed a choice of only 13 magnetograms covering a time interval of about 1 hour 15 minutes, which included the flare.

The X1.6 flare, on 2001 October 19 in NOAA AR 9661, was studied by [94], where they paid special attention to variations in the magnetic flux and shear inside a small area that contained the brightest H $\alpha$  kernels. Note that this chapter, parameters calculated over the entire active region were analyzed. The 24 magnetograms of the highest quality were used.

The X9.4 flare occurred on 1991 March 22 in NOAA AR 6555. This event was discussed in detail by [68] and [94]. It was the most powerful, and impulsive, flare among the four analyzed in this chapter. Only the nine best magnetograms, covering a half-hour interval, centered on the flare maximum were used for this event.



In order to follow the evolution of each solar flare, 0.1 to 0.8 nm X-ray flux measurements, obtained from the GOES satellite, and H $\alpha$  flux data from BBSO full-disk H $\alpha$  observations were used. These data are shown in Figures 5.16 to 5.19 (upper panels).

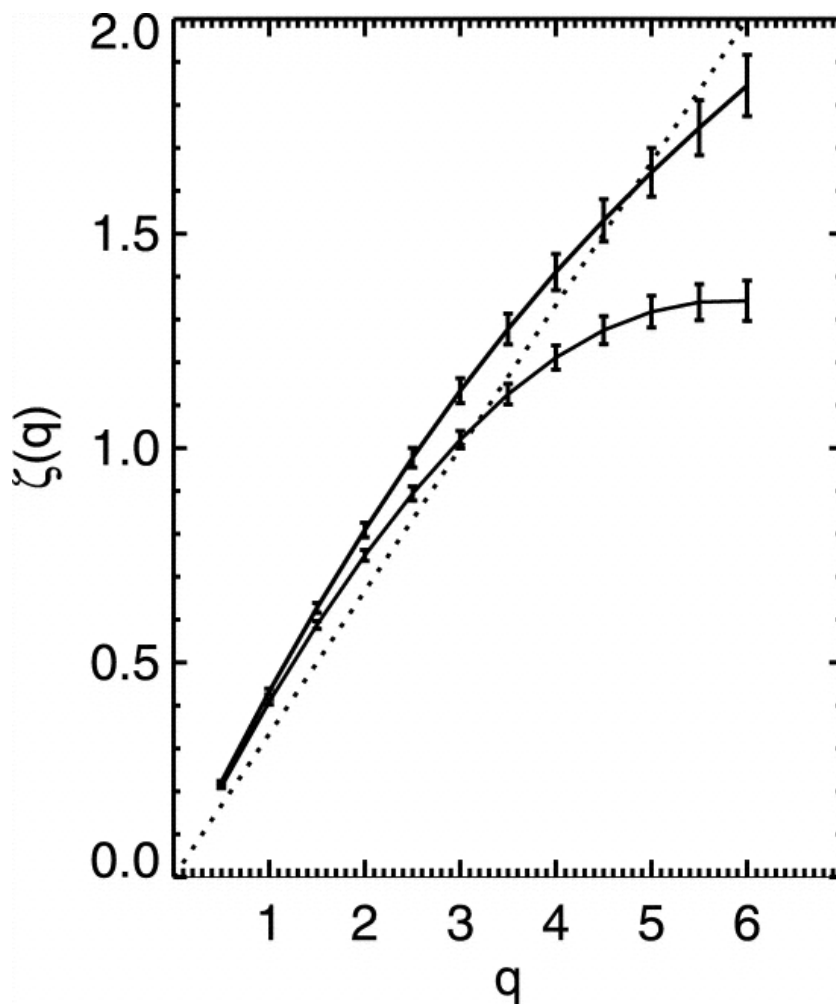
### 5.2.3 Methods

#### 5.2.3.1. Measure of Intermittency of the Magnetic Field.

According to Parker's conjuncture [141], the intensity of tangential discontinuities of the magnetic field is reduced in the course of a solar flare. The higher the intensity of the discontinuities, the more intermittent the magnetic field is (E. N. Parker 2002, private communication). One way to analyze the measure of intermittency of a turbulent field is to calculate its structure functions [155]:

$$S_q(r) = \langle |B_Z(x+r) - B_Z(x)|^q \rangle \sim (r)^{\zeta(q)}. \quad (5.1)$$

Here,  $q$  is an order of a statistical moment (generally, a real number),  $r$  is a separation vector,  $x \equiv (x, y)$  is the current point on a magnetogram and  $B_Z$  is the observed longitudinal magnetic field. Angle brackets denote the average over the area. The rightmost expression in equation (1) holds in the inertial range separations. The values  $\zeta(q)$  can be determined as a slope of  $\log S_q(r)$  versus  $\log r$  within the inertial range separations. A routine used here for the calculation of  $\zeta(q)$  is described in detail by [156]. As an example, Figure 5.9 shows two functions of  $\zeta(q)$ . (See also Figs. 5.2.4 and 5.2.8 in [156].)



**Figure 5.11** Exponents  $\zeta(q)$  of structure functions of order  $q$  vs.  $q$ , calculated for two magnetograms of NOAA AR 0039. The Kolmogorov's straight line K41 corresponding to non-intermittent turbulence is shown with the dotted line. The thin solid line denotes the scaling exponents before the onset of the flare at 20:28 UT (small deviations from the K41 line, low degree of intermittency). The thick solid line shows the scaling exponents during the rising phase of the flare, at 20:57:40 UT (this moment of the maximum  $\beta$  is denoted as  $t_1$  in Figure 5.17; large deviation from the K41 line, high degree of intermittency).

The scaling behavior of structure functions was studied previously in different applications by many authors [159], [160], [161] & [162]. See also [155]. Recently, the scaling behavior of structure functions of solar magnetic fields was considered by [156].

For non-intermittent classical Kolmogorov turbulence,  $\zeta(q) = q/3$  ([163], see the dotted straight line in Figure 5.11, hereafter the K41 line). Whereas for highly intermittent turbulence,  $\zeta(q)$  deviates from the K41 line: as the degree of intermittency increases,  $\zeta(q)$  becomes more saturated (see Figure 5.11). Deviations from the K41 line are more pronounced at high ( $q > 3$ ) statistical moments. In general, the higher the value of  $q$  used in calculations of structure functions, the more reliable the diagnostics of intermittency is. However, the upper limit for  $q$  is set by the number of nodal points,  $N$ , in the area under study:  $10^q \sim N$ . With the data,  $\zeta(q)$  can be estimated for all values of  $q \leq 6$ .

For non-intermittent fields,  $\zeta(6) \sim 2$ , while it decreases in the case of highly intermittent structures (see Figure 5.11). After  $\zeta(6)$  is calculated from the observed  $B_z$ , one can easily acquire a scaling exponent,  $\beta$ , of a power spectrum of magnetic energy dissipation [156] using:

$$\beta = 1 - \zeta(6) \quad (5.2)$$

Thus,  $\beta$  is close to -1 in the case of non-intermittent turbulence and increases up to zero as the measure of intermittency rises (the strength of the discontinuities of magnetic field increases).

There are several numerical methods proposed to calculate  $\beta$ . In the present study, a self-similarity code (SS), described in [156], was applied to three out of the four active regions. In the case of NOAA AR 9661, another method was used, namely, the extended self-similarity code (ESS; see [164], [165] & [162]). This code allows the reduction of ambiguities caused by poor linearity of the spectrum  $\log Sq(r)$  versus  $\log r$ . According to

the research, the ESS method produces values for  $\beta$  slightly lower when compared to the SS code. However, gradients in the time profile of  $\beta$  are the same. Values of  $\beta$  obtained by the ESS method for NOAA AR 9661 are denoted by stars in Figures 5.15 and 5.18 and in Table 5.1.

**Table 5.1** Relative Changes of the Magnetic Field Parameters

NOAA AR	Date	Flare	$\Delta\lambda$ (%) <sup>a</sup>	$\Delta\beta$ (%) <sup>b</sup>	$\Delta F^+$ (%) <sup>c</sup>	$\Delta F^-$ (%) <sup>c</sup>	$\Delta c$ (%) <sup>c</sup>
8375 .....	1998 Nov 5	M8.4	+13	-45	-2.5	-3.9	+4.8
0039 .....	2002 Jul 26	M8.7	+6.0	-63	1.0	-1.0	2.0
9661 .....	2001 Oct 19	X1.6	+11	-15*	4.9	0.5	4.2
6555 .....	1991 Mar 22	X9.4	+46	-81	+2.6	-1.0	+2.9

<sup>a</sup> Changes in the correlation length,  $\lambda$ .

<sup>b</sup> Changes in the scaling exponent,  $\beta$ . The asterisk indicates the value of  $\Delta\beta$ , obtained by the ESS routine.

<sup>c</sup> Changes in the total positive magnetic flux, the total negative magnetic flux, and the image contrast during the period  $\tau_\lambda$ .

### 5.2.3.2. Correlation Length of the Magnetic Energy Dissipation Field. For

some turbulent field,  $u \equiv (u_1, u_2, u_3)$ , the energy dissipation, per unit mass in a unit of time, is defined by [154] as:

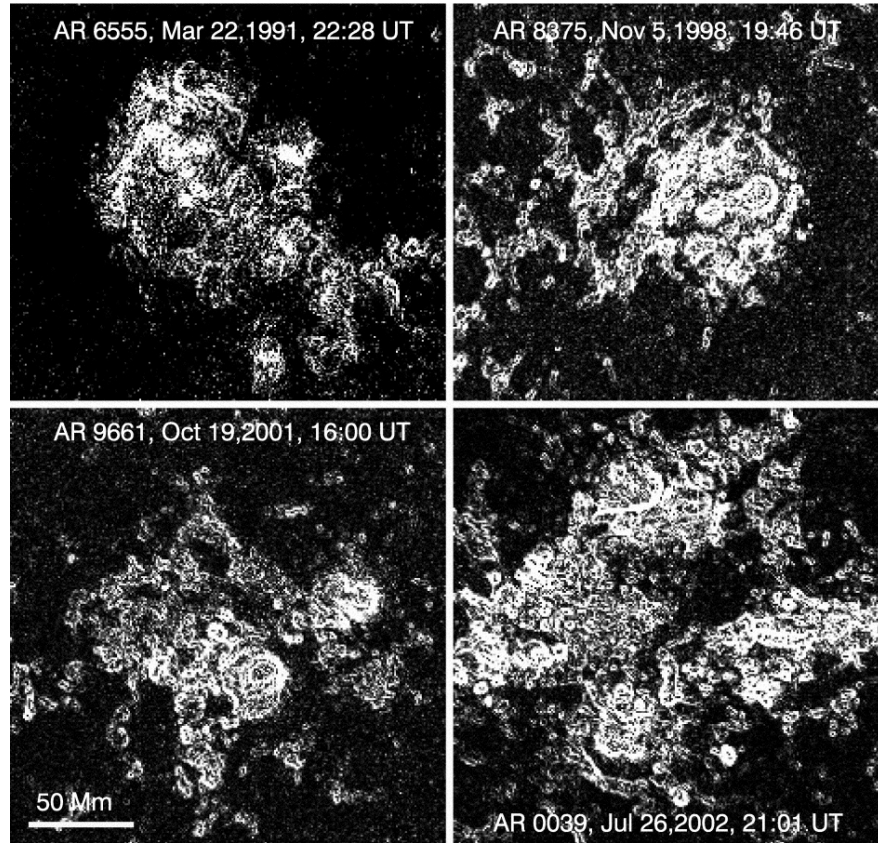
$$\varepsilon(x) = (\nu/2) \sum (du_i/dx_j + du_j/dx_i)^2, \quad (5.3)$$

where  $\nu$  is the viscosity coefficient.

To calculate the magnetic energy dissipation field in the photosphere using equation (5.2.3), one needs simultaneous measurements of the magnetic vector field inside a volume, which are not, as yet, available. For this reason, the dissipation of the longitudinal component,  $B_z$ , of the photospheric magnetic field for which:

$$\varepsilon ( B_Z ) = \nu_m \{ 4 [ ( dB_Z / dx )^2 + ( dB_Z / dy )^2 ] + 2 (dB_Z / dx + dB_Z / dy)^2 \}. \quad (5.4)$$

Assuming the magnetic viscosity,  $\nu_m$ , is spatially uniform and equal to unity, the two-dimensional magnetic energy dissipation,  $\varepsilon(B_Z)$ , can be calculated using equation (5.2.4). These structures, for each active region in this study, are shown in Figure 5.12. One can see that these structures are very jagged and intertwined and resemble percolation clusters (Feder 1988). The next aim is to define the correlation length of these clusters. Following [154], a method of the turbulence theory to calculate the correlation length of the energy dissipation field was used.



**Figure 5.12** Structures of magnetic energy dissipation,  $\varepsilon(B_z)$ , shown in arbitrary units, were calculated by using eq. (4) for the magnetograms shown in Figure 5.10.

First denote that  $\varepsilon(B_z) = \varepsilon$ . Then, a correlation function  $B(r)$ :

$$B(r) = \langle \langle \varepsilon(x+r) - \langle \varepsilon \rangle \cdot (\varepsilon(x) - \langle \varepsilon \rangle) \rangle \rangle \quad (5.5)$$

Is defined, where  $r$  is a separation vector and  $x \equiv (x,y)$  is the current point on a magnetogram. Angle brackets denote the average over the area.

In order to obtain a correlation length  $B(r)$  must be normalized by the variance of dissipation,  $B(0)$ :

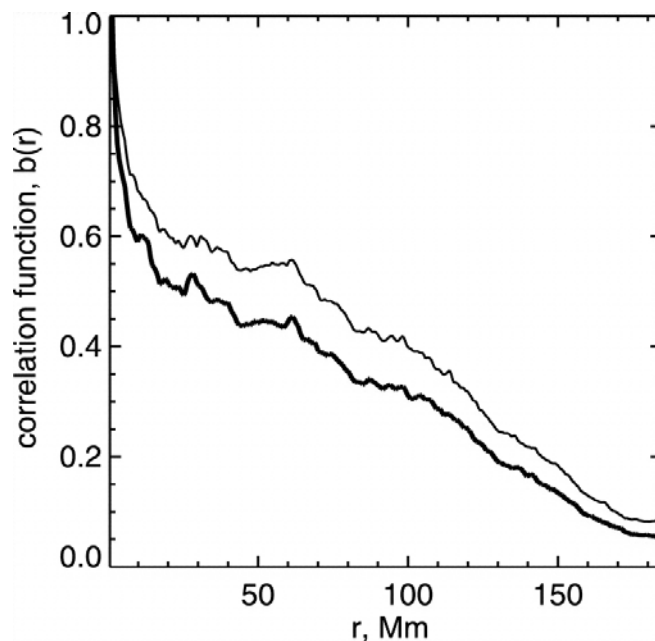
$$b(r) = B(r) / B(0) \quad (5.6)$$

By integrating the normalized correlation function,  $b(r)$ , over all scales  $r$ , a correlation length of the energy dissipation field,  $\lambda$  [154], can be calculated as:

$$\lambda = \int_0^{r_{\max}} b(r) dr \quad (5.7)$$

Note, that  $\lambda$  calculated by using equations (5.2.5), (5.2.6), and (5.2.7) does not depend on the assumption that  $v_m = 1$ .

Examples of  $b(r)$ , calculated from two magnetograms of NOAA AR 9661, are plotted in Figure 5.13. One can see that the two curves are noticeably different and the difference in the area under the curves of  $b(r)$  can not be neglected. Therefore, by calculating  $\lambda$  for a sequence of magnetograms, its evolution can be analyzed. In the percolation theory [166] & [167] an avalanche event corresponds to a state of percolation of a cluster of energy dissipation when the characteristic size (the correlation length) of the cluster grows up to size of the entire system. The correlation length is a very convenient geometrical parameter for detecting an avalanche event in the photosphere, where any direct estimations of the amount of magnetic energy released during a flare are rather problematic.



**Figure 5.13** Photos of the normalized correlation function,  $b(r)$ , of magnetic energy dissipation calculated by using eqs. (5) and (6) for two magnetograms of NOAA AR 9661. The areas under the curves are equal to the correlation length  $\lambda$  of the magnetic energy dissipation at two different times. The thick line correspond to the moment of the minimum correlation length near the beginning of the flare (16:19:37 UT). The thin line shows the correlation function when  $\lambda$  was at its maximum near the peak of the flare (16:27:04 UT).

#### 5.2.4 Data Processing and Results

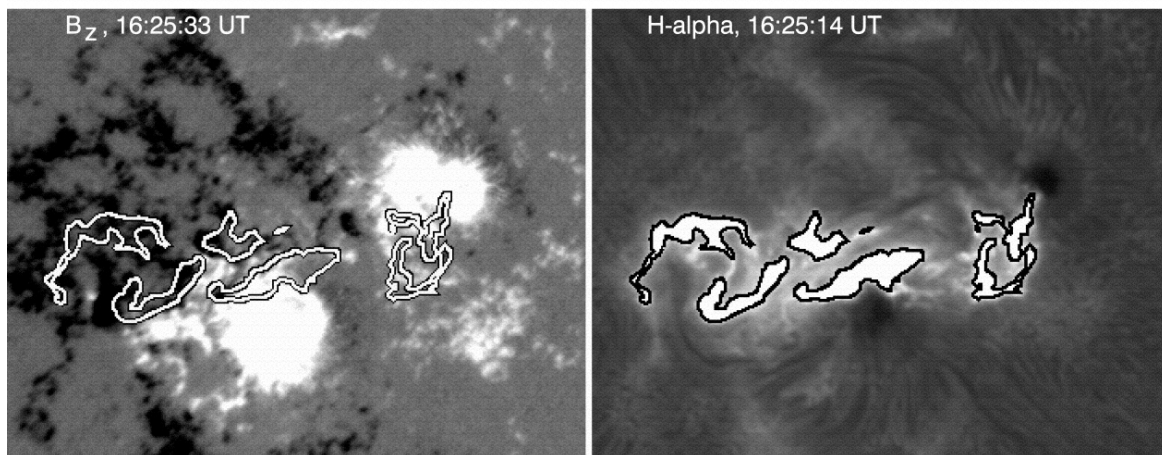
The main results of this study are presented in Figures 5.16 to 5.19. The most important parameters are organized in Tables 5.1 and 5.2, where the flares are arranged in the order of increasing magnitude.

Before the results are presented, the reliability of the determination of the parameters  $\beta$  and  $\lambda$  will be discussed (see chapters 5.2.4.1 and 5.2.4.2).



#### 5.2.4.1 An Effect of Distortion of the Magnetic Field Measured in Areas of H $\alpha$

**Ribbons.** Generally, during a strong flare, measurements of the longitudinal magnetic field can be affected by changes in the spectral line profile due to photospheric heating near the flare. A small area of an active region is usually affected by these changes, namely, the area coincident with H $\alpha$  ribbons. In order to estimate the effect that the line profile change, due to the photospheric heating, has on the calculations of the parameters  $\beta$  and  $\lambda$  in each magnetogram, the area occupied by bright H $\alpha$  ribbons was blocked out and recalculated  $\beta$  and  $\lambda$ . This was done for the 2B/X1.6 flare on 2001 October 19 in NOAA AR 9661. For each magnetogram the H $\alpha$  image, obtained with the same telescope, that was obtained immediately (within 1 minute) before or after the magnetogram was selected. The locations of the H $\alpha$  flare ribbons to be enclosed by a contour which was set to be double the intensity level of the undisturbed chromosphere (hereafter referred to as the H $\alpha$  contour) were defined. An example of this H $\alpha$  contour, overlaid on a magnetogram (obtained at 16:25:14 UT, near the maximum emission in H $\alpha$ ) and an H $\alpha$  image, is shown in Figure 5.14. The area inside the contour was excluded from the calculations of  $\beta$  and  $\lambda$ .



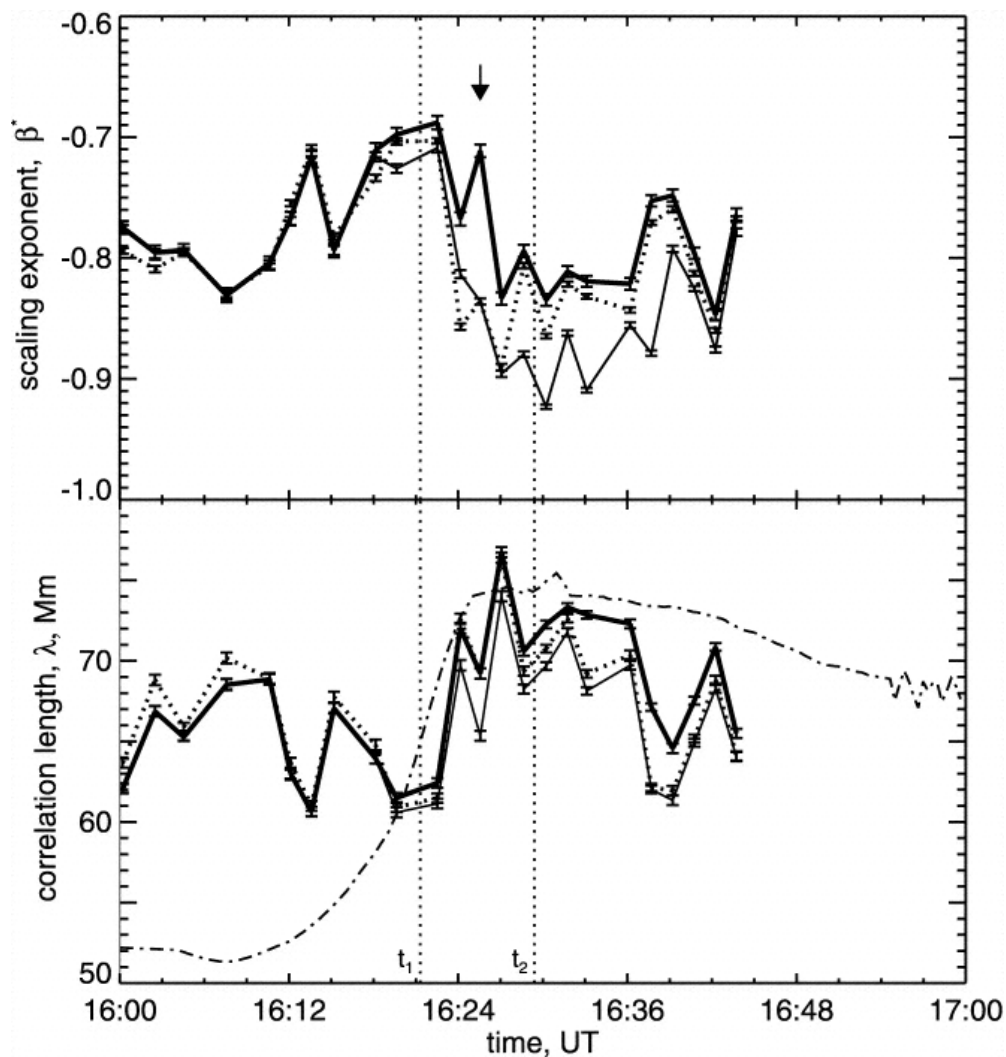
**Figure 5.14** Map of the longitudinal magnetic field for NOAA AR 9661 (left panel, the intensity of the I mage is scaled within a range of  $\pm 250$  Gauss), and an  $H\alpha$  image of the X1.6 flare (right panel) shown at 16:25:33 UT (also denoted by the arrow in Figure 5.15). The contours enclose the area within an  $H\alpha$  intensity twice that of the intensity of the undisturbed chromosphere. The area inside the contours was excluded from the calculation of the  $\beta$  and  $\lambda$  parameters. West is to the right and north is to the top.

The bright  $H\alpha$  ribbons were blocked in two ways:

1) Individual blocking.- The  $H\alpha$  contour was determined individually for each magnetogram by using the  $H\alpha$  image taken closest in time to the magnetogram.

2) Common blocking.-Only one  $H\alpha$  contour (shown in Figure 5.2.5) was determined, at the maximum of the  $H\alpha$  emission (16:25:14 UT) and was applied to all of the magnetograms.

Figure 5.15 represents variations of  $\beta$  and  $\lambda$  (thick solid line), calculated from the magnetograms without blocking the regions susceptible to photospheric heating. The results obtained by the individual (common) blocking are shown by the thin solid (thick dotted) line. One can conclude from comparing the three time profiles that before the flare the differences in the time profiles can be neglected.



**Figure 5.15** Time variations of the parameters for the X1.6 flare on 2001 October 19 in NOAA AR 9661: the scaling exponent,  $\beta$  (top panel), and the correlation length,  $\lambda$  (bottom panel). The thick lines represent the data calculated from the entire magnetogram, whereas the thin solid lines show the data calculated with the individual blocking of the bright H $\alpha$  areas, and the thick dotted lines represent the result of the common blocking of the bright H $\alpha$  ribbons. The arrow indicates the moment at which the magnetogram and H $\alpha$  image used in Figure 5.14 were obtained. The flux of H $\alpha$  emission, in arbitrary units, is shown in the bottom panel by the dash-dotted line. The vertical dotted lines denoted as  $t_1$  and  $t_2$  are the same as in Figure 5.18.

Gradients of  $\beta$  and  $\lambda$ , during the time interval near the flare maximum (between  $t_1$  and  $t_2$ ), are the most important in the present study. One can see that the decrease in  $\beta$  and the increase in  $\lambda$  are still present after disregarding the regions susceptible to photospheric heating. Moreover, the decrease in  $\beta$  and the increase in  $\lambda$  became even more pronounced. This means that the conclusions, which will be discussed in detail later in this chapter, about the decrease in  $\beta$  and the increase in  $\lambda$  during the flare maximum are not affected by the distortion of the magnetic field measurements inside the bright  $H\alpha$  ribbons. Note that the pre-flare increase in  $\beta$  is not affected by this process. Hereafter, in this chapter the time profiles of  $\beta$  and  $\lambda$ , calculated from the entire magnetogram, will be analyzed.

**5.2.4.2 Magnetic Flux Changes and Seeing Variations.** It should be emphasized that the parameters  $\lambda$  and  $\beta$ , discussed in Chapter 5.2.3, are structural parameters of a two-dimensional field. Therefore, they are not affected by the calibration coefficient of the instrument or other uniform changes in the measured signal. Also, it is not required to specify any thresholds for the calculation of these parameters (as opposed to the calculations of the fractal dimension). However, non-uniform changes in magnetograms induced, for example, by seeing variations may affect the values of  $\lambda$  and  $\beta$ . To reduce the influence of seeing, magnetograms of good quality were chosen, which were controlled, quantitatively, by determining the image contrast:

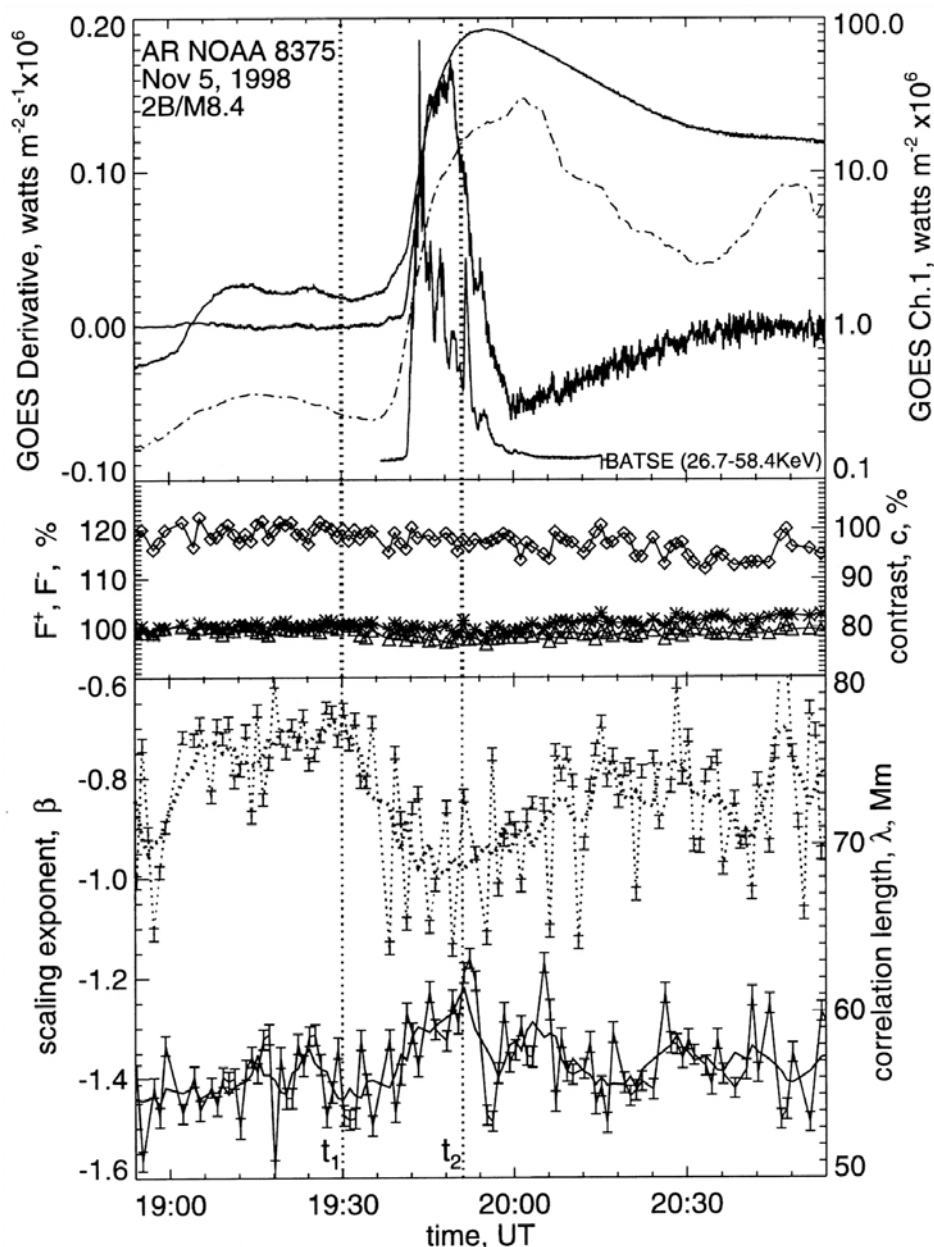
$$c = \sigma ( | B_Z | ) / \langle | B_Z | \rangle. \quad (5.8)$$

Here,  $\sigma ( | B_z | )$  is the standard deviation of the absolute value of the longitudinal magnetic field. The image contrast was calculated over areas located far away from the main sunspots. Variations of  $C$ , normalized to the value of  $C_1$  for the first magnetogram in a set, are shown in Figures 5.16 to 5.19 (middle panels, squares).

To ensure that the longitudinal magnetic field measurements were carried out under steady instrumental conditions, the total positive,  $F^+$ , and total negative,  $F^-$ , magnetic flux over the entire magnetogram were calculated. Their time variations, normalized to the value of  $F^+_{1}$  ( $F^-_{1}$ ) of the first magnetogram in a set, are shown in Figures 5.16 to 5.19 (middle panels, stars and triangles, respectively).

One can see that in all of the cases during the time intervals under study, there were no drastic changes in either the total magnetic flux or the contrast.

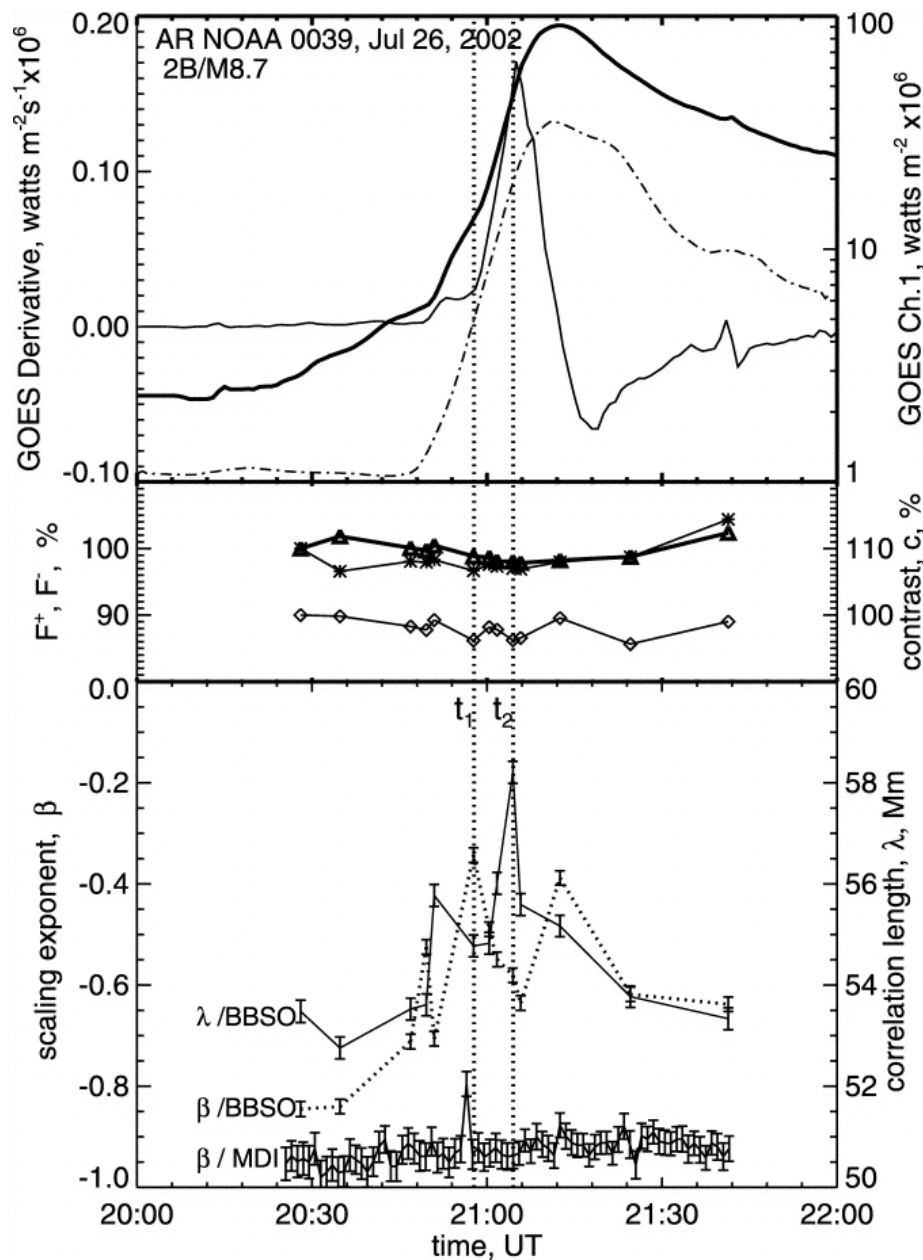
Comparison of the upper and middle panels of Figures 5.16 to 5.19 shows that from the beginning to the end of each flare, there were no correlated changes between the seeing and instrumental parameters ( $c$ ,  $F^+$ ,  $F^-$ ) and  $H\alpha$  and X-ray flux. Therefore, it has been concluded that the turbulence parameters,  $\lambda$  and  $\beta$ , which will be discussed further in this chapter, do not seem to be affected by seeing and instrumental problems.



**Figure 5.16** Time variations of the parameters for the M8.4 solar flare on 1998 November 5 in NOAA AR 8375. The upper panel shows the 0.1 to 0.8 nm GOES X-ray flux (thin line), its time derivative (thick line), the H $\alpha$  flux in arbitrary units (dash-dotted line) and the BATSE X-ray flux, in arbitrary units. In the middle panel the relative variations of the contrast,  $c$  (diamonds), and total positive  $F^+$  (stars) and negative  $F^-$  (triangles) magnetic flux are plotted. The bottom panel shows the variations of the correlation length (solid lines) and the scaling exponent,  $\beta$  (dotted lines). The thin lines are the original values, and the thick lines are their smoothed values. The left vertical dotted line marks the moment of maximum  $\beta$ ,  $t_1$ . The right vertical dotted line indicates the moment when  $\lambda$  is maximum,  $t_2$ . The time interval between the two vertical lines is defined as  $T_\lambda$ , (see text, § 5.4.4).

**5.2.4.3 Proxy for Hard X-Ray Emission.** It is well known that there is a temporal correlation between thermal soft X-ray emission and the integral of the non-thermal hard X-ray emission. This relation is called the Neupert effect and is based on an assumption that all of the energy deposited by precipitating electrons is converted into heat in the chromosphere by trapping [168] & [169]. Thus, the derivative of the soft X-ray emission, which displays the rate of its growth and/ or decline, can serve as a proxy for the hard X-ray emission time profile as well. Note that the maximum of the hard X-ray emission is thought to coincide with the peak in the energy dissipation rate in the corona [170].

In this paper the derivative of soft X-ray emission were used, which is shown in Figures 5.16 to 5.19 (upper panels) to estimate the moments of the peaks in the energy dissipation rate in the corona. Hereafter, unless otherwise noted, the term "HXR emission" will refer to the time derivative of soft X-ray emission.



**Figure 5.17** Time variations of parameters for the M8.7 flare on 2002 July 26 in NOAA AR 0039. The notations for the top and middle panels are the same as in Figure 5.16. The bottom panel shows the non-smoothed values for the scaling exponent,  $\beta$  (dotted line), and correlation length,  $\lambda$  (bold solid line), calculated for each magnetogram. The thin solid line in the lower part of the bottom panel shows the values of  $\beta$  (left axis) calculated by using the full-disk MDI magnetograms.



**5.2.4.4 Variation of  $\lambda$  and  $\beta$  During a Flare.** The lower panels in Figures 5.16 to 5.19 display the time variations of the correlation length,  $\lambda$ , of the magnetic energy dissipation and the scaling exponent,  $\beta$ , which characterizes a measure of intermittency of a Bz structure.

For the M8.4 and X1.6 solar flares (Figures. 5.16 and 5.19), the cadence of the observations was sufficient enough to allow the averaging of the parameters by using five-point (M8.4 flare) and three-point (X1.6 flare) running means. The smoothed time profiles are shown by bold lines in the bottom panels of Figures 5.16 and 5.19. For these two flares, the magnitude of changes in  $\lambda$  and  $\beta$  were determined by these smoothed time profiles.

For each flare, a time period,  $\tau_\beta$ , was identified when there was a gradual pre-flare increase in the parameter  $\beta$ . The left vertical dotted line in Figures 5.16 to 5.19 marks the end of  $\tau_\beta$  (the moment,  $\tau_1$ , of maximum  $\beta$  and the beginning of its rapid decrease). For example, in the case of the M8.4 flare (Figure 5.16),  $\tau_\beta \sim 33$  minutes and lasted from 18:57 UT to  $\tau_1 = 19:30$  UT. In the third column of Table 5.2,  $\tau_\beta$  for all of the flares is listed.  $\beta$  will referred to as the growth time of  $\tau_\beta$ .

**Table 2** Time Intervals

NOAA AR	Flare	$\tau_\beta$ (minutes) <sup>a</sup>	$\tau_\lambda$ (minutes) <sup>b</sup>	$\Delta t_\beta$ (minutes) <sup>c</sup>	$\tau_{\text{dur}}$ (minutes) <sup>d</sup>	$\Delta t_\lambda$ (minutes) <sup>e</sup>
8375 .....	M8.4	$33 \pm 5$	$21 \pm 2.5$	$+14 \pm 5^f$	$15.0 \pm 2.0$	$-6.8 \pm 2.5^f$
0039 .....	M8.7	$25 \pm 7$	$6.7 \pm 3.0$	$+6 \pm 3$	$13.1 \pm 0.7$	$+0.5 \pm 1.8$
9661 .....	X1.6	$15 \pm 3$	$8.1 \pm 1.5$	$+3 \pm 2$	$5.2 \pm 0.6$	$-4.8 \pm 2.6$
6555 .....	X9.4	$6.3 \pm 3.1$	$3.6 \pm 2.9$	$+7 \pm 3$	$2.4 \pm 0.5$	$+3.1 \pm 3.9$

<sup>a</sup> Growth time of  $\beta$ .

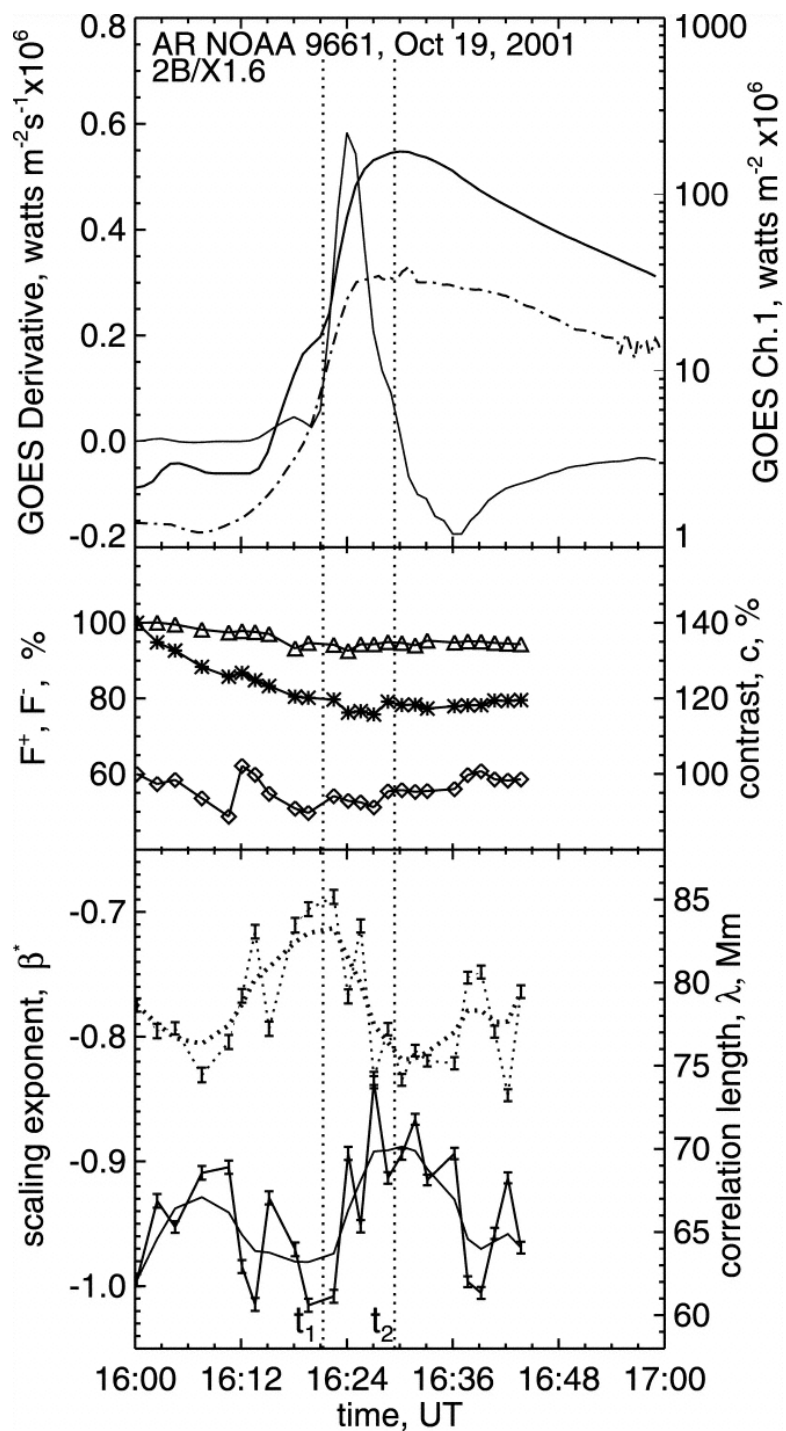
<sup>b</sup> Growth time of  $\lambda$ .

<sup>c</sup> Delay of the hard X-ray peak, as defined from the SXT derivative, relative to the maximum of  $\beta$ . A positive delay indicates that the maximum in  $\beta$  occurs earlier than the peak of the HXR emission.

<sup>d</sup> Duration of the HXR emission, as defined as the FWHM of the time derivative of the SXR emission.

<sup>e</sup> Delay of the hard X-ray peak, as defined from the SXT derivative, relative to the maximum of  $\lambda$ . A negative delay indicates that the maximum in  $\lambda$  occurs later than the peak of the HXR emission.

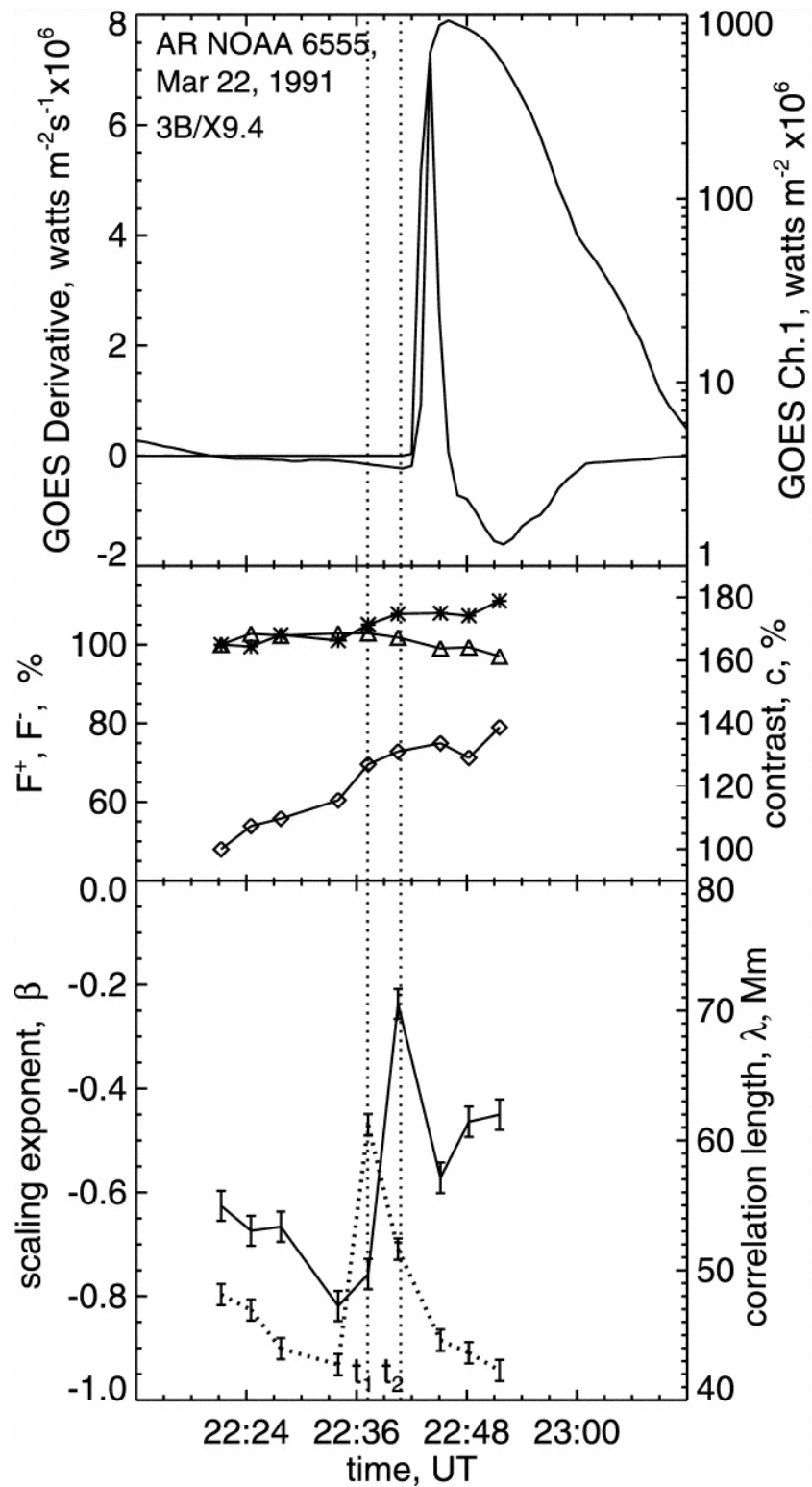
<sup>f</sup> Delays defined from the first peak in the BATSE data.



**Figure 5.18** Time variations of parameters for the X1.6 flare on 2001 October 19 in NOAA 9661. The notations are the same as in Figure 5.16.

The moment  $\tau_1$  corresponds to the primary (over the period under study) maximum of  $\beta$  in all cases. In the case of AR 0039 there was a secondary maximum at 20:12 UT (see Figure 5.2.8). To understand its origin, full-disk MDI magnetograms with high time cadence and a resolution of 4 arc-sec were used. The time profile of  $\beta$  as determined from the MDI data is shown in Figure 5.2.8 (bottom panel). The primary pre-flare peak in  $\beta$  is clearly visible, though due to the coarse spatial resolution of the full-disk data (as compared to the BBSO data), the values of  $\beta$  are smaller and the errors are larger. Comparison of the  $\beta$ /MDI and the  $\beta$ /BBSO time profiles in Figure 5.2.8 shows that the primary maximum in  $\beta$  occurred before  $\tau_1$  (it was missed in the BBSO data because of the poor time cadence of the selected BBSO magnetograms). Also, the secondary peak in  $\beta$ , which was clearly visible in the BBSO data at 20:12 UT, did not appear above the noise level in the MDI data, which indicates that the secondary peak in the BBSO data may be related to increased image contrast (see the middle panel in Figure 5.17) at 20:12 UT.

One can see from Figures 5.16 to 5.19 that in all of the cases the amplification of the correlation length,  $\lambda$ , began near  $\tau_1$ , when  $\beta$  started to decrease. The growth of  $\lambda$  lasted until  $\tau_2$  (right vertical dotted lines in Figures 5.16 to 5.19). In all of the cases, the maximum of  $\beta$  preceded the maximum of  $\lambda$ . The time interval between the  $\beta$  and  $\lambda$  maxima will be denoted as  $\tau_\lambda = \tau_2 - \tau_1$ .  $\tau_\lambda$  will be referred to as the growth time of  $\lambda$  and their values, determined for all of the flares, listed in the fourth column of Table 5.2.



**Figure 5.19** Time variations of parameters for the X9.4 flare on 1991 March 22 in NOAA 6555. The notations are the same as in Figure 5.17.

From Figures 5.16 to 5.19 the relative changes  $\Delta\lambda$  and  $\Delta\beta$ , in percent, during time  $\tau_\lambda$  are estimated. These estimations are shown in the fourth and fifth columns of Table 5.1. One can see that there is an obvious tendency for  $\Delta\lambda$  and  $\Delta\beta$  to be large as the X-ray flux of a flare increases.

The X9.4 flare was the only case in which  $\beta$  did not finish its rapid descent by the moment  $\tau_2$ , when  $\lambda$  was at its maximum (Figure 5.19). For this flare, it was determined that  $\Delta\beta \sim 81\%$  between times  $\tau_1$  and 22:45 UT, when  $\beta$  ceased its rapid decrease. During  $\tau_\lambda$  the correlation length increased by 46%. These relative increments of both  $\lambda$  and  $\beta$  are the largest among the four flares studied here (see Table 5.1).

According to the upper panels of Figures 5.16 to 5.19, the M8.4, M8.7, and X1.6 flares had increased in soft X-ray and H $\alpha$  emissions and had almost reached their peaks during the growth time of  $\lambda$ . However, in the case of the X9.4 flare (Figure 5.19),  $\tau_\lambda$  ended shortly ( $1.5 \pm 2.9$  minutes) before the beginning of the enhancement of the soft X-ray emission. (Unfortunately, H $\alpha$  data are not available for this event.) This difference in timing may be due to the insufficient temporal resolution in the magnetograph data (see Figure 5.19, bottom panel).

In the last three columns of Table 5.1, the relative changes of magnetic flux,  $\Delta F^+$ ,  $\Delta F^-$  and image contrast,  $\Delta c$  (the seeing and instrumental parameters) during the same period of time  $\tau_\lambda$  (persistent changes are denoted by their sign) are shown. One can see that there are no systematic tendencies in the changes of the seeing and instrumental parameters, which are all less than 5%. However, the values of  $\Delta\beta$  and  $\Delta\lambda$  are large enough that there is confidence that they are reliable. Therefore, it is unlikely that the

observed growth in  $\lambda$  and the decrease in  $\beta$  during  $\tau_\lambda$  can be caused by changes in seeing and instrumental conditions.

**5.2.4.5 Timescale Comparison.** Table 5.2 provides a comparison between different time intervals and the X-ray class of each flare. As was mentioned above, the third and fourth columns in Table 5.2 show the growth times,  $\tau_\beta$  and  $\tau_\lambda$ . Comparison of these values shows their nearly synchronous flare-to-flare changes (a decrease of  $\tau_\beta$  is always accompanied by a shortening of  $\tau_\lambda$ ).

For all of the flares discussed in this chapter, the bulk of the hard X-ray emission (as estimated by the time derivative of the SXR emission) occurred after the maximum of  $\beta$  (the maximum of the degree of intermittency). The time delay,  $\Delta\tau_\beta$ , of the HXR peak, relative to the maximum of  $\beta$ , as determined for each of the flares studied here, is shown in the fifth column of Table 5.2. Positive delays indicate that the maximum observed value of  $\beta$  occurred earlier than the hard X-ray peak. For the M8.4 flare the delay was determined by the first burst in the BATSE flux data in the 26.7 to 58.4 keV channel, a flare N5293.

The duration of the HXR emission is defined,  $\tau_{\text{dur}}$ , as the full width at the half-maximum of the time derivative of the soft X-ray emission time profile. Values of  $\tau_{\text{dur}}$  are shown in the sixth column of Table 5.2. Comparison between the X-ray class (second column of Table 5.2) and  $\tau_{\text{dur}}$  shows that, for all four flares selected for the present study, the duration of the HXR emission,  $\tau_{\text{dur}}$ , is inversely proportional to the peak intensity of the SXR emission. This might not be a coincidence. Indeed, [171] and [172] reported on a statistical relationship between the peak electron energy flux,  $F$ , the total flare duration,

D, and the total energy of non-thermal electrons, W:  $FD \sim W^{1.18}$ . This relation holds with high correlation over more than four orders of magnitude. According to [171], the correlation coefficient is approximately 0.93. By using the HXR emission time profiles, the total energy, W, for each of the four events has been estimated. The conclusion is that these total energies are well within one order of magnitude range. Therefore, according to Figure 11 in [171], the corresponding products FD also vary in a narrow range (are nearly constant), or, in other words, the peak intensity of the HXR emission, F, is inversely proportional to its duration, D. This may be the reason for the observed inverse proportion between the X-ray class and the duration of the HXR emission for the four flares discussed here.

Comparison of the third and fourth columns on the one hand, and the second and sixth columns on the other hand, shows that at least for the four flares under this study, the growth time of  $\beta$  and the growth time of  $\lambda$  tend to become shorter as the X-ray class increases and the duration of the HXR emission decreases.

The last column in Table 5.2 shows a time interval,  $\Delta t_\lambda$ , which is defined to be the delay between the maximum of the HXR emission and the peak of  $\lambda$ . A negative  $\Delta t_\lambda$  indicates that the peak in  $\lambda$  occurred later than the peak in the HXR emission. In two of the cases (the M8.4 and X1.6 flares), the HXR peak preceded the maximum of the correlation length. In the other two of the cases, the delay between these maxima was nearly zero (within the errors of calculation).

For the X1.6 flare, a Yohkoh/HXR time profile was analyzed, from which it was determined that  $\Delta t_\lambda \sim -4.4$  minutes. This is very close to the estimation of  $-4.8 \pm 2.6$



minutes by using the time derivative of the SXR emission as a proxy for the HXR emission.

### 5.2.5 Summary and Discussion

In the present study turbulence (fractal) parameters of the longitudinal magnetic field,  $B_z$ , for four major solar flares were analyzed. In particular, the correlation length,  $\lambda$ , of the magnetic energy dissipation field and the scaling exponent,  $\beta$ , which characterizes the measure of intermittency (multifractality) of the  $B_z$  structure were discussed. The time variations of  $\lambda$  and  $\beta$ , during the course of a flare, were the focus of the current discussion. The following conclusions have been made:

1. In all cases, a peak in  $\beta$ , which was followed by a peak in  $\lambda$ , was found. These two peaks were separated by the time interval,  $\tau_\lambda$ , during which a rapid growth of the soft X-ray and  $H\alpha$  flux occurred. The changes in the scaling exponent and correlation length seem not to be caused by variations of seeing and/or instrumental problems.

2. The peak in  $\beta$  was preceded by a period of gradual growth of  $\beta$ ,  $\tau_\beta$ , which was longer than the time interval  $\tau_\lambda$ . The maximum of  $\beta$  occurred earlier than the peak of the hard X-ray emission.

3. The maximum of  $\lambda$  tends to follow, or to occur nearly simultaneously with (within the accuracy of approximately 2 to 4 minutes), the maximum of the hard X-ray emission.

4. On the basis of the limited examples studied here, it has been concluded that the time intervals  $\tau_\beta$  and  $\tau_\lambda$  are inversely proportional to the impulsiveness and the intensity of flares.

The observational and modeling aspects of these conclusions will now be discussed. Intermittency of the photospheric structures is well known in solar physics. Lawrenec et al. [152] have shown that the photospheric longitudinal magnetic field displays multi-fractality (intermittency in terms of the theory of turbulence). Consolini et al. [162] analyzed photospheric velocity fields and found the intermittent turbulent dynamics of photospheric plasma fluid. They concluded that intermittency must play a relevant role in photospheric convection. Abramenko et al. [156] analyzed the degree of intermittency in eight active regions and found that the greater the flare productivity of an active region, the more intermittent the photospheric magnetic field is. No study of photospheric intermittency, before and during solar flares, has been performed, as of yet.

The pre-flare increase in the intermittency of the photospheric magnetic field observed here may be explained, presumably, as the existence of a phase of enhancing turbulence prior a solar flare. Note that similar conclusions were made for the corona by using Yohkoh/BCS data [173] & [174]. The observed pre-flare increases in the non-thermal velocity measured in the S xv spectral line, were interpreted as an increase in the turbulence due to small-scale magnetic reconnections and as a manifestation of a pre-flare turbulent phase. Analyzing the data for ten solar flares, [173] reported that for eight of them, the peak of the non-thermal velocity occurred prior to the first significant burst of the hard X-ray emission, which is in agreement with the findings presented here, though [175], analyzing another spectral line, Ca XIX by using BCS/Yohkoh data, concluded that the peak in the non-thermal broadening occurred more frequently after the first significant hard X-ray peak.

The above results can be understood in the framework of Parker's conjecture. The growth in  $\beta$  indicates the pre-flare increase of the degree of intermittency of the magnetic field. The higher the degree of intermittency, the stronger and the more numerous spontaneous discontinuities of the magnetic field are (E. N. Parker 2002, private communication), which are thought to be reduced in the course of the flare [141]. Then, the decrease in  $\beta$  during a flare onset may be caused by the exhaustion of small-scale discontinuities in the magnetic field, and it may be a trace of a coronal avalanche of reconnection events. This process can be detected in the photosphere on account of the magnetic coupling between the photosphere and the corona [142] and on account of the high propagation speed of magnetic field disturbances. TRACE data acquired during a major flare [176] showed that disturbances propagate from the central flare site outward with a radial speed of about 700 km/sec, which can be considered as the response of a system of magnetic loops to changes in the magnetic field. Thus, these magnetic field disturbances (an avalanche), being spawned in the corona, may reach down into the photosphere within several tens of seconds, though, the problem of whether the photospheric magnetic field responds to the rearrangements in a magnetic structure in the corona is not trivial due to the different ratio of the gas pressure to magnetic pressure in the corona and in the photosphere. The results seem to suggest that a subtle response in the structural organization of the photospheric magnetic field exists and may be detected during the course of a flare.

On the basis of Parker's conjecture, [177] recently elaborated the minimum current corona model of a solar flare. This model assumes that the entire magnetic field

of an active region arises from isolated photospheric sources and is driven to a critical state with avalanches of small-scale energy release events (flares).

Recent numerical modeling of a nonlinear dissipative process in the framework of the SOC concept [178] suggests that before an avalanche, statistical distributions deviate significantly from Gaussian, which indicates the high degree of intermittency of the turbulence. Whereas, after the avalanche event, the distributions are closer to Gaussian. These theoretical findings agree with these results.

In summary, the results presented here seem to suggest the existence of a pre-flare turbulent phase in an active region and are in agreement with the self-organized criticality concept of a solar flare. They also demonstrate that the photospheric magnetic field of an active region can be used to analyze statistical properties of a flare-related nonlinear dissipative process in the entire magnetic field.

## CHAPTER 6

### CONCLUSIONS

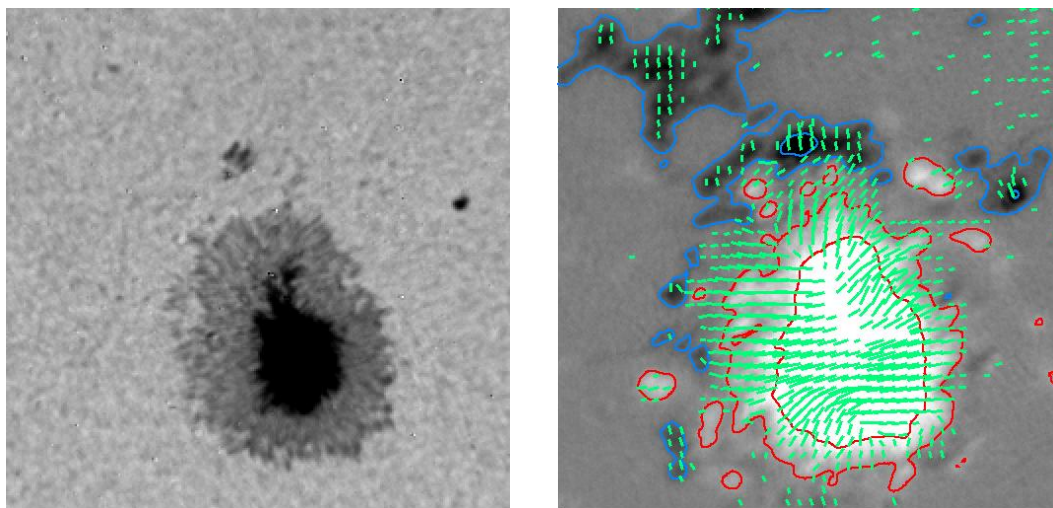
In this thesis work, a new Digital Vector Magnetograph (DVMG) was developed, for the 25 cm vacuum-refractor at the Big Bear Solar Observatory. The DVMG uses the wavelength shift and Stokes polarization components (I, U, Q & V), of the Ca I line at 610.3 nm, as described by the Zeeman effect (Section 1.3) for light emitted by a hot gas in a magnetic field, to measure the magnitude and direction of the magnetic field on the surface of the Sun.

#### **6.1 Digital Vector Magnetograph Characterization and Data Quality**

The DVMG combines three aspects that are required to properly study the dynamics of the solar magnetic field that have not been readily available in past magnetographs. A high time cadence (1 minute), high spatial resolution (1 arc-sec / pixel) over a field of view large enough to cover a typical active region (300 arc-sec x 300 arc-sec) and high quality. Measurements of the longitudinal magnetic field acquired with a cadence of 1 minute have a noise level of ~10 Gauss while measurements of the transverse magnetic field have a noise level of ~100 Gauss (Section 3.7.1). The noise level in longitudinal magnetograms can be reduced to below 5 Gauss, if the integration time is increased to ~5 min, especially when using post-processing techniques such as image selection and alignment (Section 3.7.3).

## 6.2 Testing the DVMG on a Simple Round Sunspot

The final test as to whether the instrument is functioning correctly is to obtain vector magnetograms of a simple round sunspot near the center of the solar disk (Section 3.9.1). Theory and experience indicate that the magnetic field in a simple round sunspot, when viewed near the center of the solar disk (to avoid projection effects such as the limb or canopy effect as shown in Section 3.8.3) should be approximately radial. An example of a vector magnetogram of simple round sunspot is shown in Figures 6.1 (copied here from Section 3.9.1 for convenience).



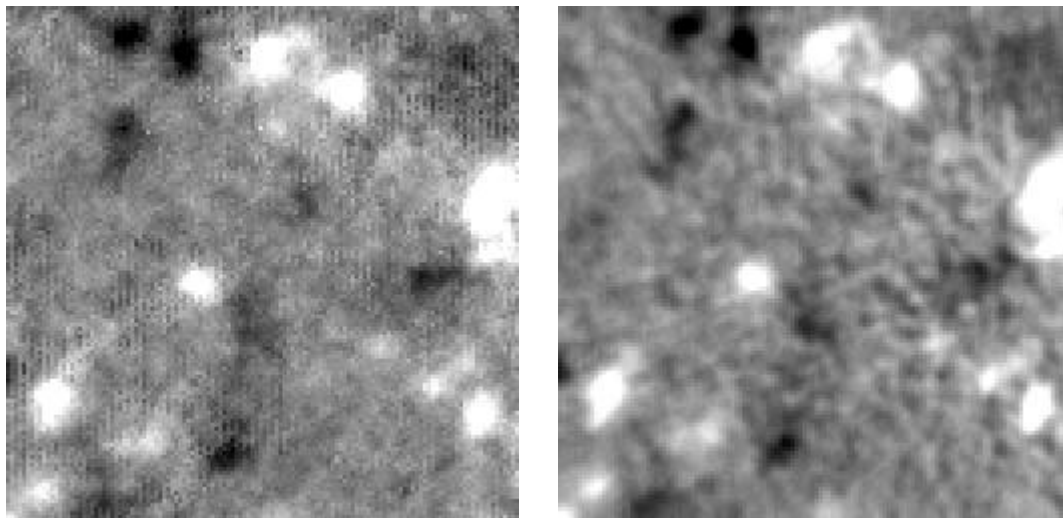
**Figure 6.1** Vector magnetogram of a simple round sunspot.

From an inspection of the vector magnetograms, one can see that the direction of the transverse magnetic field (green lines) in the primary sunspot are radial. When there is confidence in the vector magnetograms produced from a simple round sunspot and are sure that the instrument is working properly, there will then be confidence in the vector magnetograms produced from a more complex active region (Section 3.9.2).

### 6.3 Image Post Processing (Alignment & Selection)

Due to the continual blurring effects of the atmosphere of the Earth (seeing), the contrast and position of images produced by ground-based telescopes are continually, and rapidly, changing (on the order of a few tens of milli-seconds). When averaging a large number of images that are obtained over many seconds, these changes in contrast and position accumulate and degrade the quality of the final integrated image.

To minimize this effect, the images with the highest contrast in the data set can be selected and aligned. The improvements gained from this procedure can be seen in Figure 6.2 (copied here from Section 3.7.3 for convenience). Figure 6.2 shows two quiet-Sun longitudinal magnetograms. The image on the left was created without image selection and alignment and the image on the right was created with selection and alignment. One can see that, in the magnetogram using selection and alignment, the features are more sharply defined.



**Figure 6.2** Example of the improvements gained when using image selection and alignment.

#### **6.4 Rapid Changes in the Solar Magnetic Field**

It has been long thought in the solar community that the strong photospheric magnetic fields can not significantly change rapidly (on the order of minutes or hours). Part of the reason for this conjecture is that, up until recently, solar magnetographs could not measure the photospheric magnetic field with sufficient cadence, spatial resolution over an entire active region and with high quality have not been available. The purpose of developing the DVMG was to provide data to specifically address these issues.

Three examples of where significant changes in strong photospheric magnetic fields associated with solar flares are addressed in detail in Chapters 4.1, 4.2 & 4.3. DVMG observations used in these three research projects have shown that there are significant changes in the photospheric magnetic field, which can occur on the order of tens of minutes, associated with solar flares. These findings are contrary to the long-held belief that the photospheric magnetic field is strongly locked in place by the solar material and can not change in this short time scale. It has been determined that the magnitude of the overall magnetic field of the leading polarity tends to increase while the magnitude of the overall magnetic field of the following polarity tends to decrease, but by a smaller amount.



## **6.5 Limitations of Current Observations and Motivation for Improvements**

As can be seen from Chapters 5.1 and 5.2, data from solar instrumentation currently available are insufficient to completely answer many of the questions under study.

### **6.5.1 Desired Improvements to Magnetographs in General**

There are many ways in which improved magnetograph instrumentation will provide better, and thus far unavailable, data which can answer many important questions about the solar magnetic field and its effect on the dynamics of the Sun. 1) Improved sensitivity in general, and 2) more accurate vector magnetograms specifically, will provide better information on both small scale magnetic features and the actual structure of strong magnetic fields in active regions. 3) Higher spatial resolution (provided by larger aperture telescopes equipped with adaptive optics) will allow the study of the fundamental structures of the solar magnetic field and 4) scanning of the entire absorption line (with the use of Fabry-Perot filters) will allow the calculation of the specific conditions in the solar atmosphere where the magnetically sensitive absorption line was formed. These new data will provide critical information about both the small scale structure of the solar magnetic fields and the dynamics of solar flares which can negatively effect the near earth environment (Section 1.1). This list is, by no means, exclusive

### **6.5.2 Desired Improvements to the DVMG Specifically**

Following is a brief list of improvements one might imagine to a DVMG. Many points on this list were discussed above, in the discussion about the details of the instrumentation in Section 2.1) More light - larger telescope, filters with greater light throughput, camera with higher quantum efficiency, 2) More accurate magnetic field measurements -

narrower filter, use fewer integrations to reach the desired noise level, 3) Instrument stability – better temperature and mechanical stability of instrument, 4) Greater resolution – larger telescope, greater image scale, adaptive optics & 5) Real-time image processing – alignment and selection of many short integrations

It must be noted, however, that while some of these improvements are desired they are not necessarily practical. For example, a refractor with an aperture much greater than 25 cm would provide greater resolution and more light but is very difficult and expensive to build. Also, sometimes improving one characteristic of an instrument might actually degrade the quality of an instrument in other ways. Using a filter with a narrower band-pass would increase the accuracy of the measurements of the magnetic field by reducing contamination from the continuum and the line center but would also reduce the overall light throughput of the instrument requiring more integrations which would allow seeing to degrade the image. As with everything, the construction of a magnetograph is an exercise in compromise. All components must be used in coordination with each other in such a way that their specific characteristics are used most efficiently that the instrument will accomplish its design goals.

## **6.6 Future Instrumentation**

In general, all instrument projects at BBSO not only provide a new and improved instrument but also serve as a learning experience for building the next generation of instruments (as can be seen from the discussion of the evolution of magnetographs at BBSO in Section 1.9). The DVMG is no exception. Over the next several years, the primary goal of BBSO will be the construction of the New Solar Telescope (NST) [179].

A primary goal of the NST is to address many of the problems and limitations addressed above.

Possibly of greatest importance is that the NST will be equipped with a high order adaptive optics system which can correct the distorting effects of the atmosphere of the Earth (seeing) in real time [180]. As of this writing, the adaptive optics instrument is completed and operational in the optics room of the 65 cm vacuum-reflector. This adaptive optics system will allow the NST to operate at or near its diffraction limit (0.07 arc-sec at 500 nm). In addition, the use of real time image reconstruction, which uses a few hundred direct images taken in rapid succession to create a single diffraction limited image, will allow for additional improvements to the quality of the images that are beyond the capabilities of the adaptive-optics system.

The NST will be equipped with a new array of instruments, using the experience gained from previous and current instrument projects, to answer the questions addressed above, among others [179]. The Visible Light and Infrared Imaging Vector Magnetographs (VIM & IRIM respectively) will be the direct descendants of the DVMG and will serve as the basic model for these two instruments [181]. The most obvious improvement of the VIM and IRIM will be the use of Fabry-Perot filters, which will be able to scan the magnetically sensitive line and thus providing the complete Stokes profiles. By the method of Stokes inversion (mentioned above) the local characteristics of the solar atmosphere where the magnetically sensitive line was formed can be determined in addition to the strength and direction of the magnetic field.

Magnetograms with greater resolution and sensitivity (especially in the Stokes-U and Q components), availability of the Stokes profiles (by scanning the magnetically

sensitive absorption line) will enable the NST to address the questions of the size and nature of flux tubes, the formation and dynamics of weak solar magnetic fields and the structure of electric currents in active regions (all which have been address above).

The NST will also be equipped with Fabry-Perot filters for direct imaging (H-alpha filtergrams, for example) in the visible and near infrared spectrum. Used with adaptive optics, and supplemented by real time image reconstruction, these instruments will provide images with unprecedented resolution. Used together with magnetograms, these new images will provide a better understanding of the issues discussed in Section 5.3, as well as other important questions in solar physics, which will lead to a better understanding of the dynamics of the solar magnetic field and the resulting negative effects on the near Earth environment.

## APPENDIX A

### MUELLER MATRICES

Mueller matrices for the polarization optics used in the DVMG and for the polarizations of light of the several Stokes parameters analyzed by the DVMG are shown below. Note that the vertical direction is referenced to be  $0^\circ$ .

#### A.1 MUELLER MATRICES OF RETARDERS

$$\frac{1}{4} \lambda, 0^\circ \quad \begin{vmatrix} 1 & 0 & 0 & 0 \\ 0 & 1 & 0 & 0 \\ 0 & 0 & 0 & -1 \\ 0 & 0 & 1 & 0 \end{vmatrix}$$

$$\frac{1}{4} \lambda, 45^\circ \quad \begin{vmatrix} 1 & 0 & 0 & 0 \\ 0 & 0 & 0 & -1 \\ 0 & 0 & 1 & 0 \\ 0 & 1 & 0 & 0 \end{vmatrix}$$

$$\frac{1}{4} \lambda, 90^\circ \quad \begin{vmatrix} 1 & 0 & 0 & 0 \\ 0 & 1 & 0 & 0 \\ 0 & 0 & 0 & 1 \\ 0 & 0 & -1 & 0 \end{vmatrix}$$

$$\frac{1}{2} \lambda, 0^\circ \text{ \& } 90^\circ \quad \begin{vmatrix} 1 & 0 & 0 & 0 \\ 0 & 1 & 0 & 0 \\ 0 & 0 & -1 & 0 \\ 0 & 0 & 0 & -1 \end{vmatrix}$$

$$0\lambda \quad \begin{vmatrix} 1 & 0 & 0 & 0 \\ 0 & 1 & 0 & 0 \\ 0 & 0 & 1 & 0 \\ 0 & 0 & 0 & 1 \end{vmatrix}$$

## A.2 MUELLER MATRICES OF POLARIZATIONS OF LIGHT

$$\text{Linear Polarization } 0^\circ \quad \begin{vmatrix} 1 \\ -1 \\ 0 \\ 0 \end{vmatrix}$$

$$\text{Linear Polarization } 90^\circ \quad \begin{vmatrix} 1 \\ 1 \\ 0 \\ 0 \end{vmatrix}$$

$$\text{Linear Polarization } +45^\circ \quad \begin{vmatrix} 1 \\ 0 \\ 1 \\ 0 \end{vmatrix}$$

$$\text{Linear Polarization } -45^\circ \quad \begin{vmatrix} 1 \\ 0 \\ -1 \\ 0 \end{vmatrix}$$

$$\text{Right Circular Polarization} \quad \begin{vmatrix} 1 \\ 0 \\ 0 \\ 1 \end{vmatrix}$$

$$\text{Left Circular Polarization} \quad \begin{vmatrix} 1 \\ 0 \\ 0 \\ -1 \end{vmatrix}$$

## APPENDIX B

### TEMPERATURE CONTROL AND OPTICS MOUNTING COMPONENTS

The photo shown below is of the liquid crystal variable retarder and its temperature control and mounting hardware.





## APPENDIX C

### CN76000 TEMPERATURE CONTROLLER

The image shown below is of the specifications of the CN 76000 Temperature Controller.

# 1/16 DIN Auto-Tune Controller Universal Input

**Very High  
Performance  
in a Very  
Small  
Package**



- ✓ Dual 4-Digit Display
- ✓ Auto-Tune PID, PID or On-Off Control
- ✓ Thermocouple Input with 1° or 0.1° Resolution
- ✓ RTD Input with 1° or 0.1° Resolution
- ✓ Scalable Voltage and Current Inputs
- ✓ °F, °C or Engineering Unit Display
- ✓ Password Protection
- ✓ Front Panel Programming
- ✓ Relay, dc Pulse, ac SSR, Voltage or Current Output(s)

**Additional Features:**

- ✓ Loop Break Protection
- ✓ Min/Max Indication
- ✓ Auto/Manual Operation
- ✓ Percent Output Indication
- ✓ Single Segment Ramp and Soak



**KMTSS-125G-6  
Thermocouple Sold  
Separately, \$24.**

Shown Larger than Actual Size

Compact, 1/16 DIN Size,  
with NEMA 2, 3R and 12  
Rated Front Panel



Single Output  
**\$189**

Dual Output  
**\$199**

P-94

## APPENDIX D

### 100Ω Pt RTD-850 TEMPERATURE PROBE


The image shown below is of the specifications of the 100Ω Pt RTD-850 temperature probe.

## Precision RTD Probes For Laboratory Applications

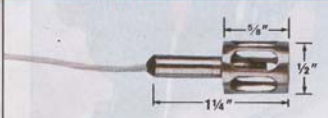

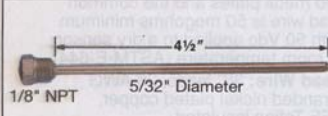
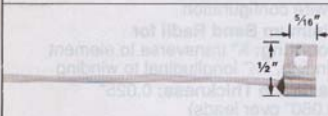
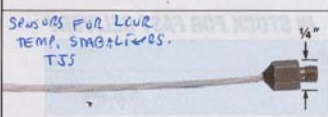
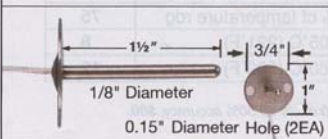
### RTD-800 Series

- ✓ 100Ω Pt RTD Sensor
- ✓ 3' Teflon® Coated Lead Wires
- ✓ Subminiature MTP Series Connector

*In-Stock for Fast Delivery*



MADE IN USA

To Order (Specify Model Number)					
Configuration	Model No.	Description	Temp. Range	Applications	Price
	RTD-805  RTD-806	RTD element mounted in open-end stainless steel housing with Teflon insulated leads. Designed for air temperature measurement and monitoring of gas streams. 3' lead wires. RTD-806 features economical plastic housing.	-200 to 230°C	Gas and Air	\$86  81
	RTD-809	Encapsulated sensor in stainless steel housing with Teflon insulated leads. Surface temperature measurement design, ideal for heat loss or compressor efficiency measurement. 3' lead wires.	-200 to 230°C	Surface	83
	RTD-810	Closed-end stainless steel tube with Teflon insulated leads. Rugged design is ideally suited for fluid measurement. Also for use in a wide variety of pressurized systems applications. 3' lead wires	-200 to 750°C	Gas and Liquid	79
	RTD-830	Encapsulated sensor in screw-mounted Aluminum housing with Teflon insulated leads. Sensor design provides low cost, fast response, and is designed for easy mounting on flat surfaces. 3' lead wires.	-200 to 230°C	Flat Surface	64
 <p style="font-size: small; margin-top: 5px;">Sensors For LCR TEMP. SMO. LIQ. TJS</p>	RTD-850	Stainless steel housing with 1/4" hex head and #8-32 NC-2A threaded body. RTD sensor encapsulated in housing with Teflon insulated leads. Designed for applications requiring vibration & shock resistance. 3' lead wires.	-200 to 230°C	Surface	64
	RTD-860	Closed-end stainless steel tube with sensor mounted in tip. Stainless steel mounting plate with two (2) mounting holes welded to tube. Teflon insulated 3' lead wires.	-200 to 230°C	Gas and Air	83

C-13





## APPENDIX E

### FLEXIBLE SILICON RUBBER FIBERGLASS INSULATED HEATERS

The image shown below is of the specifications of the flexible silicon rubber fiberglass insulated heaters.

## FLEXIBLE SILICONE RUBBER FIBERGLASS INSULATED HEATERS

- ✓ **Lightweight, Thin, Flexible**
- ✓ **UL Recognized and CSA Certified**
- ✓ **Available in 2.5, 5 and 10 W/in<sup>2</sup>**
- ✓ **-112°C (-170°F) to 232°C (450°F) Operating Temperature**
- ✓ **Etched Foil and Wire Wound Design**
- ✓ **Round or Rectangular Shapes**
- ✓ **Available in 115 Vac**
- ✓ **Optional Pressure Sensitive Adhesive (PSA)†**

OMEGALUX® silicone rubber fiberglass insulated flexible heaters can improve heat transfer and speed warm-ups where controlled heating is required in confined areas. Two circuit designs are available: etched foil or wire wound. Heaters with etched foil designed elements are available where the length or width dimension is less than 12" (305 mm). All other heaters where both the length and the width dimensions exceed 12" (305 mm) use the wire-wound element design.

Effect of power density: gentle warming is best done with 2.5 W/in<sup>2</sup>. A good all-purpose unit is the 5 W/in<sup>2</sup>. Rapid warm-up and high temperature are achieved with the 10 W/in<sup>2</sup>; however, temperature must be controlled as the safe maximum operating temperature limit of 450°F (232°C) may be exceeded.

<b>To Order (Specify Model Number) Round Silicone Rubber Heaters</b>							
Diameter (in.)	Total Wattage for Watt Density			Without PSA Model No.	Price	With PSA Model No.	Price
	2.5W/in <sup>2</sup>	5W/in <sup>2</sup>	10W/in <sup>2</sup>				
3	17.5	35	70	SRFR-3/*	\$19	SRFR-3/*-P	\$20.90
4	31.4	62.8	125.6	SRFR-4/*	23	SRFR-4/*-P	25.30
5	49.0	98.15	196.3	SRFR-5/*	28	SRFR-5/*-P	30.80
6	70.67	141.3	282.7	SRFR-6/*	29	SRFR-6/*-P	31.90
7	96.2	192.4	384.8	SRFR-7/*	32	SRFR-7/*-P	35.20
8	125.65	251.3	502.6	SRFR-8/*	35	SRFR-8/*-P	38.50
9	157.9	315.8	631.7	SRFR-9/*	39	SRFR-9/*-P	42.90
10	196.25	392.5	785	SRFR-10/*	43	SRFR-10/*-P	47.30
11	237.45	474.9	949.8	SRFR-11/*	48	SRFR-11/*-P	52.80
12	376.8	753.6	1507.2	SRFR-12/*	53	SRFR-12/*-P	58.30

Comes with complete operator's manual.

/\* Insert watt density: 2 for 2.5 W/in<sup>2</sup>, 5 for 5W/in<sup>2</sup> or 10 for 10 W/in<sup>2</sup>.

**Ordering Example:** SRFR-3/10 is a 3 in diameter heater with a watt density of 10 W/in<sup>2</sup> and 70 watts of total power, \$19.

† Note: Heaters with pressure sensitive adhesive: max. operating temperature is 250°F (120°C).

M-5

## **APPENDIX F**

### **USING THE INSTRUMENT**

The DVMG is controlled by a Visual C++ program that was purchased from the camera manufacturer and highly edited to specifically control the DVMG. The Graphical User Interface nature of the program makes the operation of the DVMG quite easy. In addition, the typical instrument settings are saved on disk and automatically restored when the DVMG control program is executed at the beginning of each observing day. Thus making routine instrument setup automatic.

#### **Appendix F.1 Camera Initialization**

The SMD 1M15 CCD camera that is used in the DVMG is automatically initialized, via the serial port on the control computer, when the DVMG control program is executed. The frame rate is set to 7.5 frames/second, the shutter speed is set to the “off” setting (the beginning of each exposure is triggered by a TTL signal provided via the parallel port of the control computer). The camera gain is set to “1” to minimize noise and the camera binning is set to the 2 x 2 mode. The reasons for choosing each particular value listed here was discussed in detail in Section 3.2. All of these settings are typically used during the operation of the DVMG, are saved on disk and loaded automatically when the DVMG control program is executed.

## Appendix F.2 Live Images

The control program provides a live display so the field of view of the telescope can be properly positioned on the Sun. In addition, the observer must ensure that the instrument is properly focused. (Automatic focusing is an extremely difficult technical problem. Atmospheric turbulence creates continuous small scale changes in the clarity of the image. Thus, focusing ground-based telescopes is still best accomplished by the human eye). Telescope flexure and long-term temperature changes in the atmosphere require that the focus of the instrument must be checked from time to time (~30 min). It is therefore important that a real-time display of the image be easily.

The contrast settings of the live image display can be accessed and changed via the “Edit / Live Display Settings” pull-down menu. The observer can change the maximum and minimum values of the live display settings to best accommodate the specific requirements of the live image at any time. This can depend on the opacity of the atmosphere, the contrast of the solar features and the location on the Sun that is being imaged. (The apparent brightness of the solar surface is a function of the observed position on the Sun relative to the center of the solar disk. As we observe locations on the Sun that are closer to the solar limb, we are looking through more of the solar atmosphere so we see light emanating from higher in the solar atmosphere (chromosphere) where it is cooler and, therefore, dimmer, relative to the surface we see near disk center.) It is therefore important that the contrast of the live image be easily set to the requirements dictated by the target of the observations and the observing conditions.

### **Appendix F.3 Instrument Settings**

Four pull-down menus enable the observer to easily setup the instrument to perform the observing requirements of the day: Edit/Sequence Configuration, Edit/Display Settings, Edit/I-Region and Edit/Object Type. These menus allow the observer to change the way the instrument is used, the way that real-time data is displayed on the monitor of the control computer and the information that is stored in the FITS header of each saved image. Experience in using the instrument during a typical day of observations has determined standard settings for each of these four pull-down menus. These values are saved to disk, and the pull-down menus are automatically initialized to these values when the DVMG control program is executed. The details of the settings of each of the four pull-down menus will now be discussed in turn.

#### **Appendix F.3.1 Edit/Sequence Configuration**

The Edit/Sequence Configuration pull-down menu controls the basic operating of the instrument. The settings that are controlled from the other three pull-down menus all work to supplement the instrument settings from this main control pull-down menu.

#### **Contents of Data Set**

##### **Vector or Longitudinal Magnetograms or 601.3 nm Intensitygrams**

The most basic determination that must be made when setting up how the DVMG will be used during any particular observing run is to decide exactly which types of images will be taken. The DVMG can take three basic types of data: vector magnetograms, longitudinal magnetograms or 610.3 nm intensitygrams. Which type of observation is made is controlled with the appropriate radio-button.

The primary purpose of the DVMG is to monitor the dynamics of the magnetic fields in active regions on the surface of the Sun. This requires the full set of Stokes-I, V, Q and U images. Therefore, vector magnetograms are, by far, the most common type of observations made with the DVMG. However, if the goal of the observations is to study, for example, the dynamics of quiet-Sun small scale magnetic fields, only the Stokes-I and Stokes-V parameters are required. In this case, not acquiring the Stokes-Q and U parameters will allow more time to be devoted to collecting more accurate longitudinal magnetograms than typical (which require additional integration time) or to acquire typical longitudinal magnetograms at a higher cadence. The instrument can also take a series of Stokes-I images (610.3 nm intensitygrams) if magnetic field measurements are not required by the current observations.

#### Number of Stokes-I Images To Be Tested

The DVMG saves a 610.3 nm intensitygram which is to be used as the Stokes-I image. However, the DVMG does not simply take a single 610.3 nm intensitygram during each Stokes set. Many 610.3 nm intensitygrams are rapidly taken and the single image with the best contrast is saved as the Stokes-I image. The rest of the 610.3 nm intensitygrams are simply discarded.

Real-time images produced by ground-based telescopes are continually shimmering due to the turbulent effects of the atmosphere of the Earth. This effect is referred to as “seeing” and the turbulence acts on the order of a few tens of milli-seconds with the overall seeing often showing apparent variations on timescales of a few tens of seconds (yielding images that appear to drift in and out of focus). The quality of the seeing at any particular time is a function of the weather and the general environmental

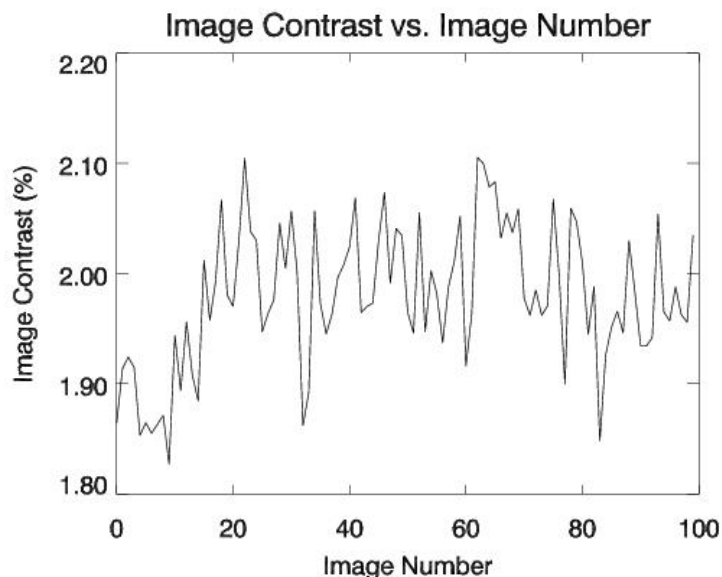
conditions at the location of the observations and the specific environmental technical aspects in the vicinity of the telescope as patches of more and less stable skies drift by. Good seeing occurs when the turbulent effects of the atmosphere are at a minimum.

The size of the smallest detail that can be resolved in any individual image is not only a function of the aperture of the telescope but it is also strongly depends on the quality of the seeing at the moment the observation is made. In fact, the quality of the seeing is quantified by the apparent size, in seconds-of-arc, of the smallest details that can be resolved in an image. To increase the probability of recording an image that was taken during a moment of good seeing, the DVMG takes a sequence of identical 610.3 nm intensitygrams as rapidly as possible (7.5 frames/sec). These images are temporarily stored in the RAM of the DVMG control computer. When the sequence is complete, the control computer calculates the contrast of each image and saves the single image with the highest contrast to be used as the Stokes-I component.

The chances of capturing an image during a moment of good seeing increases as the number of individual 610.3 nm intensitygrams that are to be tested increases. Of course, acquiring a large number of 610.3 nm intensitygrams takes integration time away from other observations that are also being conducted with the 25 cm vacuum-refractor (longitudinal or vector magnetograms, H $\alpha$  and Ca I intensitygrams, etc.) The number of 610.3 nm intensitygrams that are to be tested in a single sequence is set by the observer in the upper-left section of the Sequence Configuration GUI. This value is typically set to 100 images. Experience has shown that this number of images tends to be enough to make it likely to capture an image during a moment of relatively good seeing while not taking too much time away from the other observations being conducted by the 25 cm



vacuum-refractor. The entire process of image acquisition, the selection of the 610.3 nm intensitygrams with the highest contrast and saving that image as a 512 x 512 FITS file takes approximately 15 seconds.



**Figure F.1** Variation in the seeing, as measured by the contrast, of a sequence of 100 610.3 nm intensitygrams.

The variation of the local seeing, as measured by the contrast of the images, is shown as a function of time in Figure 3.23. For this example, all of the individual 610.3 nm intensitygrams in the sequence were saved and the contrast of each individual image is plotted vs. image number. The contrast of each image is determined by:

$$c = ( S_I / M_I ) * 100\%$$

where  $c$  is the contrast,  $S_I$  is the standard deviation of the image and  $M_I$  is the mean value of the image. One can see that, in this example, the contrast can vary on the order of 10% between consecutive images.

If desired, however, the observer can specify that more than the single image with the best contrast be saved. The control computer can save the  $n$  best 610.3 nm intensitygrams as specified in the lower right section of the Sequence Configuration GUI. The selected intensitygrams are saved as a  $512 \times 512 \times n$  FITS file.

#### Number of Stokes-V, Q and U Images to be Summed

Three components are required to completely reconstruct the solar magnetic field. The Stokes-V component, which represents the longitudinal magnetic field, and the Stokes-Q and Stokes-U components which, taken together, represent the transverse magnetic field. A Stokes parameter is generated from a set of two images, each taken at opposite polarizations within their respective Stokes set (Q, U or V). To increase the signal-to-noise ratio of the magnetograms, each of the two images used to create each Stokes component is the summation of many individual images.

The observer can easily input the desired number of integrations that will be used to create each respective Stokes component in the Edit/Sequence Configuration pull-down menu. Experience has shown that, for observations of a typical active region, 32 integrations for each image that will be used to create the Stokes-V component (for a total integration of 7.68 seconds) and 64 integrations for each image that will be used to create both the Stokes-Q and Stokes-U components (for a total integration of 15.36 seconds each) provide a good signal-to-noise ratio (the exact signal-to-noise ratio of these typical images will be discussed in Section 3.7.1).

Typically, twice the number of integrations are used to generate the Stokes-Q and U parameters as is used to generate the Stokes-V parameter. However, the observer can easily change the number of integrations that are used to create each Stokes component

depending on the goal of the observations and/or the observing conditions at any particular time. For example, if the goal of the observations is the study of the dynamics of quiet-Sun small scale magnetic fields, the observer will not acquire Stokes-Q or Stokes-U images (as previously discussed). Quiet-Sun magnetic fields tend to be mostly vertical with respect to the solar surface. Observations of the quiet-Sun tend to be at, or near, the center of the solar disk thus making the transverse components of the quiet-Sun magnetic fields approximately zero.

Another example in which the number of integrations that are to be used to create each of the Stokes components needs to be changed from the typical values is when the observations are being conducted under relatively poor seeing conditions. A disadvantage to taking the long integrations that are required to construct magnetograms is that the blurring effects of the atmosphere during poor seeing conditions tend to smear out the fine details in the images. However, many integrations are still required to acquire an adequate signal-to-noise ratio. The solution to this problem is to acquire more individual Stokes images, each with less integrations per image. Images that were acquired during moments of good seeing can then be selected, aligned and averaged, thus reaching the desired signal-to-noise ratio and avoiding the long individual integrations that will smear out the small details in the images. Of course, the tradeoff for this gain in image resolution is that more disk space is used to store the greater number of images and the additional post-processing work of selecting, aligning and averaging the images. However, this method is an excellent way of making good observations under less than ideal seeing conditions and tends to be worth the extra effort. This technique can also be used under normal seeing conditions to obtain higher quality data that might otherwise be

acquired. Examples of quiet-Sun and vector magnetograms, the results of image alignment and how the signal-to-noise ratio of the magnetograms increases with the number of integrations will be presented and discussed in Section 3.7.3.

### Light Beam Control

The observer also needs to determine if the DVMG will operate under the direction of the telescope control computer. There are three individual instruments mounted on the 25-cm vacuum refractor. In addition to the DVMG, there are instruments that acquire intensitygrams in the light of the H $\alpha$  spectral line (656.3 nm) and in the light of the Ca II K spectral line (393.3 nm). The light from the telescope is directed to each instrument, in turn, by a set of small plane mirrors, controlled by the telescope control computer. Thus, the telescope control computer must inform the control computer of each instrument when the light is available and data may be acquired. In addition, information such as the coordinates of the location on the Sun that is being observed is passed to the individual control computers of each instrument which is written in the FITS header of each saved image.

The DVMG can also operate in what is basically a free-run mode (not under the direction of the telescope control computer) if the other two instruments on the 25 cm vacuum-refractor are not to be used and the light will be exclusively directed to the DVMG. The advantage of operating in this free run mode is that the instrument can take data at its maximum rate (beginning an observation immediately after the previous observation is complete). However, when operated in this mode the instrument does not receive the pointing information from the telescope control computer and the coordinates of the location on the Sun that is being observed must be input manually via the

Edit/Object Type dialog box (which will be discussed in Section 3.1.3.4) and will not be automatically updated as the Sun rotates over the course of the day. Therefore, the DVMG is typically under the direction of the telescope control computer except on rare occasions when test images are being taken or when routine maintenance is being performed on the instrument (tuning of the birefringent filter, calibration of the liquid crystals, etc.).

#### Use a Sub Region of the Stokes-I Image for Contrast Testing

The observer has the option to specify if a sub-region of the 610.3 nm intensitygrams be used to select which individual intensitygram has the best contrast and will be saved as the Stokes-I image from the set of many individual intensitygrams acquired (as discussed previously) by selecting the appropriate check-box in the Sequence Configuration GUI. When this option is not selected, the contrast of the entire 610.3 nm intensitygrams is used to determine which image is to be saved. However, using the entire image to determine the contrast might not always be desired. For example, in the case when there is a sunspot near the edge of the field-of-view, real-time motions of the image, produced by seeing, may cause part of the Sunspot to leave the field-of-view and an area of quiet-Sun to enter the field-of-view on the opposite side of the image. Since the contrast of a Sunspot is greater than the contrast of the quiet-Sun, this will cause the overall contrast of the image to decrease. However, this may not represent a real degradation in the seeing. To solve this problem, the observer should select a sub-region of the image to be used for the contrast calculations, thus avoiding the motion of high contrast solar features in and out of the area used to calculate the quality of the seeing in the image.

Using only a sub-region of the images to calculate the contrast has the added advantage of taking less time than using the entire image. The contrast of more individual images can be checked, thus increasing the probability of capturing an image that was acquired during a moment of good seeing.

The exact sub-region is set by the observer using the Edit/I Region dialog box. The lower left corner of the sub-region is input as (x1:y1) and the upper right corner of the sub-region is input as (x2:y2). For the full size image, the coordinates of the lower left corner are (0:0) and the coordinates of the upper right corner are (511:511).

### **Appendix F.3.2 Edit/Display Setting Pull Down Menu**

The observer can set the display level at which the real-time magnetograms are viewed on the monitor of the DVMG control computer using the Edit/Display Setting pull down menu. The settings in this pull down menu, only effect the level at which the magnetograms are displayed and does not effect the data that are saved in the FITS files.

It is important that the observer be able to change the level at which the magnetograms are displayed because of the wide spectrum of magnetic field strengths that are found on the Sun. A large, complex active region can have magnetic fields that are a few thousand Gauss, while the quiet-Sun typically is dominated by magnetic fields that are on the order of a few tens of Gauss, or less.

To determine this level, the observer inputs the calibration constant for each Stokes component, which have been previously determined. This level is specific to the characteristics of the instrument and, in general, does not change with time. The observer also inputs the strength level, in Gauss, at which the display will saturate. All locations in the image that have a positive magnetic field that is stronger than the saturation value will

appear as solid white while all locations in the image that have a negative magnetic field that is stronger than the negative of the saturation value will appear as solid black. All locations in the image that have magnetic fields that fall within these limits will appear as a level of gray that is commensurate to the strength of the magnetic field at that location.

### **Appendix F.3.3 Edit/Object Type Pull Down Menu**

The observer also needs to input important information about the observations that will be stored in the FITS header of the data files. This is accomplished by the Edit/Object Type Pull Down Menu pull down menu. The type of data that will be taken (observations of an active region, the quiet-Sun, flat-fields, dark images or line profiles, etc.) is selected with the appropriate radio button. With each type of observation that is selected, the typical instrument settings are automatically input into the Edit/Sequence Configuration pull down menu. Also, the appropriate NOAA active region number is input, if applicable.

The other information that is saved in the FITS headers are the initials of the observer and the seeing conditions, on a scale of 0 being the poorest seeing to 4 being the best seeing, as estimated by the observer. Also, when the DVMG is not under the control of the telescope control computer (Section 3.1.3.1) in concert with the other instruments on the 25-cm vacuum refractor, the observer manually inputs the right ascension and declination of the center of the field of view on the Sun. When the DVMG control computer is under the direction of the telescope control computer, it will receive the coordinates of the center of the field of view at the start of each integration. Therefore, these input boxes are grayed-out when the light beam control option is selected.

### **Appendix F.3.4 Edit/Crystal Voltage Pull Down Menu**

The final menu which controls the operation of the instrument is the Edit/Crystal Voltage pull down menu. The values input in this menu control the voltages, and therefore the retardance settings, of the Liquid Crystal Variable Retarders that are used to select which Stokes component is to be imaged. The process of calibrating the crystals was discussed, in detail, in Section 2.6.6. These values are only adjusted during the calibration of the polarization optics of the instrument and are not edited on a daily basis.

### **Appendix F.4 File/Start & File/Acquire Pull Down Menus**

After the instrument has been set up to acquire the desired type of data, observations are ready to begin. The observer then selects File/Start from the main menu which initializes the display and then File/Acquire which begins the observations. If the instrument is to be used to observe in concert with the telescope control computer, it will inform the telescope control computer, via the serial port, that it is ready to observe and will wait for the telescope control computer to inform it that light is available and that observations can begin. If the instrument is to observe independently, in the free run mode, it will simply begin observations.

Each Stokes component will then be displayed, as it is acquired, on the monitor of the DVMG control computer as shown in Appendix 1.10. The images displayed are as follows: upper left is the Stokes-I image, upper right is the Stokes-V image (longitudinal magnetogram), lower left is the Stokes-Q image and the lower-right is the Stokes-U image. Note that, while the Stokes-Q and U images are used to determine the transverse magnetic field, the nature of the transverse field is not readily apparent via visual inspection of the Stokes-U and Q components in the same way that the nature of the



longitudinal magnetic field can be easily determined via visual inspection of the Stokes-V image. To understand the nature of the transverse magnetic field, the Stokes-Q and U images must be processed and displayed in conjunction with the longitudinal magnetic field as will be discussed in Chapters 3.4.2, 3.4.4 and 3.9. All images displayed are raw (not corrected with the flat field or dark frame images as will be discussed in Section 3.2).

### **Appendix F.5 Telescope Control Computer**

In addition to preparing the DVMG for observations, the telescope control computer must also be configured to properly direct the telescope and the instruments mounted on the 25 cm vacuum-refractor. There are two GUIs that are of concern when operating the DVMG.

The first is the GUI that controls the pointing of the 25 cm vacuum-refractor. In addition to providing some basic information such as the time, the radius and position angle of the Sun, etc., this GUI indicates exactly where on the Sun the telescope is pointed, which is indicated by the yellow “x” on the solar image. The telescope control computer continuously updates the pointing of the telescope to take into account the rotation of the Sun.

The apparent rotation rate of the Sun, at the equator near the central meridian, is ~10 arc-sec per hour, which translates to ~80 arc-sec over the course of a typical observing day, which is a significant fraction of the field of view of the telescope (300 x 300 arc-sec). The telescope control computer takes the rotation of the Sun into account by moving the telescope to the west (the direction of the rotation of the Sun) at the

appropriate rate to keep the center of the field of view centered on the same position on the Sun through out the day.

The second GUI on the telescope control computer which concerns us here is that which controls the instruments mounted on the telescopes. The upper portion of this GUI controls the instruments mounted on the 65 cm vacuum-reflector and need not concern us here. The central portion of this GUI determines which instruments, that are mounted on the 25 cm vacuum-refractor, will be used in the observing cycle and the total time of one cycle (a cycle is defined by every selected instrument taking its appropriate images).

All three instruments will take data, the Ca II K (393.3 nm), the H $\alpha$  (656.3 nm) intensitygram instruments and the DVMG and cycle time is set to 60 seconds. This cycle time is sufficient to take the two intensitygrams and the DVMG data (Stokes-I, V, Q and U) and leaves enough time to actuate the plane mirrors on the 25 cm vacuum-refractor to direct the light to the appropriate instrument.

When the position of the telescope is correct and the desired instruments and cycle time are selected then observations are ready to begin. The observation cycle is started by simply clicking "Start 10" in the lower section of this telescope GUI. Of course, each instrument must be prepared and started before the cycle can be started with the telescope control computer. This is accomplished with the DVMG using the appropriate pull down menus as was be discussed in Section 3.1.5.

## REFERENCES

- [1] Gallagher, P. T., Denker, C. Yurchyshyn, V., Spirock, T., Qiu, J., Wang, H., & Goode, P. R., 2002, *Annales Geophysicae*, Vol. 20, p. 1105.
- [2] Shea, M. A. & Smart, D. F., 1998, *Advanced Space Research*, Vol. 22, No. 1, p. 29.
- [3] L. J. Lanzeretti, Distinguished Research Professor, Center for Solar-Terrestrial Research, New Jersey Institute of Technology.
- [4] SOHO, operated by the European Space Agency and NASA, <http://sohowww.nascom.nasa.gov>, retrieved January, 2005.
- [5] Hudson, H., Fletcher, L., Kahn, J. I. & Kosugi, T., 2004, in “Solar and Space Weather Radiophysics”, (eds. Gary, D. E. & Keller, C. U.), *Astrophysics and Space Science Library*, Kluwer Academic Publishers, Dordrecht, Holland.
- [6] Kahler, S. W., 1992, *Annual Review of Astronomy and Astrophysics*, Vol. 30, p. 113.
- [7] Yurchyshyn, V., Wang, H. & Abramenko, V., 2004, *Space Weather*, Vol. 2, S02001, doi:10.1029/2003SW000020.
- [8] Low, B. C., 2001, *Journal of Geophysical Research*, Vol. 106 No. A11, p. 25141.
- [9] BBSO, <http://www.bbso.njit.edu>, retrieved January, 2005.
- [10] SOHO, operated by the European Space Agency and NASA, <http://sohowww.nascom.nasa.gov>, retrieved January, 2005.
- [11] Fox, N. J., Peredo, M. & Thompson, B. J., 1998, *Geophysical Research Letters*, Vol. 25, No. 14, p. 2461.
- [12] Kubo, Y. & Akioka, M., 2004, *Space Weather*, Vol. 2, S01002, doi:10.1029/2003SW000022.
- [13] Stassinopoulos, E. G., Stauffer, C. A. & Brucker, G. J., 2003, *Space Weather*, Vol. 1, No. 1, 1005, doi:10.1029/2003SW000011.
- [14] Lanzerotti, L. J., 2004, in “Solar and Space Weather Radiophysics”, (eds. Gary, D. E. & Keller, C. U.), *Astrophysics and Space Science Library*, Kluwer Academic Publishers, Dordrecht, Holland.
- [15] Love, D. P., Toomb, D. S., Wilkinson, D. C. & Parkinson, J. B., 2000, *IEEE Transactions on Plasma Sciences*, Vol. 28, No. 6, p. 2075.

- [16] Andersson, L., Norberg, O. & Eliasson, L, 2000, 6<sup>th</sup> Spacecraft Charging Technology Conference, AFRL-VS-TR-20001578.
- [17] Forbes, K. F., 2004, Space Weather, Vol. 2, S1003, doi:10.1029/2003SW000005.
- [18] Iniversitetet I Oslo, <http://www.astro.uio.no/~viggoh/ast1100/solatm/1/page1.html>, retrieved January, 2005.
- [19] Global Oscillation Network Group, National Solar Observatory, <http://gong.nso.edu>), retrieved January, 2005.
- [20] Marshall Space Flight Center, NASA, <http://science.msfc.nasa.gov/ssl/pad/solar/images/bfly.gif>, retrieved January, 2005.
- [21] Steward Observatory, Univ. of Arizona, [http://atropos.as.arizona.edu/aiz/teaching/a250/em\\_and\\_spectra.html](http://atropos.as.arizona.edu/aiz/teaching/a250/em_and_spectra.html), retrieved January, 2005.
- [22] Zeeman, P., 1897, Nature, Vol. 55, p. 347.
- [23] <http://csep10.phys.utk.edu/astr162/lect/light/zeeman-split.html>, retrieved January, 2005.
- [24] Young, C. A., 1892, Astrophysical Journal, Vol. 6, p. 115.
- [25] Mitchell, W. M., 1904, Astrophysical Journal, Vol. 19, p. 357.
- [26] Hale, G. E., 1908a, Astrophysical Journal, Vol. 28, p. 315.
- [27] Kitt Peak Vacuum Telescope, Kitt Peak Observatory, National Solar Observatory, [http://eo.nso.edu/dasl/dasl\\_data.html](http://eo.nso.edu/dasl/dasl_data.html), retrieved January, 2005.
- [28] Hale, G. E., 1908b, Astrophysical Journal, Vol. 28, p. 100.
- [29] Babcock, H. W. & Babcock, H. D., 1952, Publications of the Astronomical Society of the Pacific, Vol. 64, p. 282.
- [30] Babcock, H. W., 1953, Astrophysical Journal, Vol. 118, p. 387.
- [31] Leighton, R. B., 1959, Astrophysical Journal, Vol. 130, p. 366.
- [32] Smithson, R. C. & Leighton, R. B., 1971, International Astronomical Union, Vol. 42, p. 76.
- [33] Mosher, J., 1976, "The Caltech Videomagnetograph", PhD Thesis, BBSO Preprint 159.

- [34] Goode, P. R., Denker, C. J., Didkovsky, L. I., Kuhn, J. R. & Wang, H., 2003, *Journal of the Korean Astronomical Society*, Vol. 36, p. 125.
- [35] Denker, C., Ma, J., Wang, J., Didkovsky, L., Varsik, J., Wang, H. & Goode, P., 2002, *SPIE Conference Proceedings*, pp. 4853-34.
- [36] Mt. Wilson Observatory, <http://www.mtwilson.edu>, retrieved January, 2005.
- [37] Hale, 1908d, p. 205.
- [38] Hale, G. E., 1908d, *Astrophysical Journal*, Vol. 27, p. 204.
- [39] Hale, G. E., 1908c, *Astrophysical Journal*, Vol. 28, p. 244.
- [40] Bruck, H. A. & Phil, D., *Royal Astronomical Society*, Vol. 99, p. 607.
- [41] Van Maanen, A., 1917, *Journal of the Royal Astronomical Society of Canada*, Vol. 11, p. 223.
- [42] Hale, G. E., 1915, *Publications of the Astronomical Society of the Pacific*, Vol. 27, p. 233.
- [43] Varsik, J., 1995, *Solar Physics*, Vol. 161, p. 207.
- [44] The Solar Survey Archive, Observatoire de Paris.
- [45] Meadowlark Optics.
- [46] Wang, J., 2001, "A Near-Infrared Filter System and a Study of Solar Umbral Dots at 1.6 $\mu$ ", PhD Thesis, NJIT, p. 17.
- [47] Mosher, J., 1976, "The Caltech Videomagnetograph", PhD Thesis, BBSO Preprint 159, p. 31.
- [48] Varsik, J. R., 1995, *Solar Physics*, Vol. 161, p. 207.
- [49] Rust, D. M. & O'Byrne, J. W., 1991, November (ed.), *Solar Polarimetry*, National Solar Observatory, Sunspot, NM, p. 74.
- [50] Shi, Z., Wang, J. & Patterson, A., 1986, "The Calibration of Dopplergrams and Magnetograms at BBSO", BBSO Preprint No. 0257.
- [51] Kuhn, J. R., Lin, H. & Lorz, D., 1991, *Publications of the Astronomical Society of the Pacific*, Vol. 103, p. 1097.

- [52] Canfield, R. C., de La Beaujardiere, J. F., Fan, Y., Leka, K. D., McClymont, A. N., Metcalf, T. R., Mickey, D. L., Wuelser, J. P. & Lites, B. W., 1993, *Astrophysical Journal*, Vol. 411, p. 363.
- [53] Gary, G. A. & Demoulin, P., 1995, *Astrophysical Journal*, Vol. 445, p. 982.
- [54] Metcalf, T. R., 1994, *Solar Physics*, Vol. 155, p. 235.
- [55] Moon, Y. J., Wang, H., Spirock, T. J., Goode, P. R. & Park, Y. D., 2003, *Solar Physics*, Vol. 217, p. 79.
- [56] Sevemy, A. B., 1964, *ARA&A*, 2,363.
- [57] Zvereva, A. M. & Sevemy, A. B., 1970, *Izv. Krymskoi Astrofiz. Obs.*, 4142, 97.
- [58] Moore, R. L., Hurford, G. J., Jones, H. P. & Kane, S. R., 1984, *Astrophysical Journal*, Vol. 276, p. 379.
- [59] Kosovichev, A. G. & Zharkova, V. V. 1999, *Solar Physics*, Vol. 190, p. 459.
- [60] Sakurai, T. & Hiei, E., 1996, *Adv. Space Res.*, 17, 91.
- [61] Wang, H., Ewell, M. W., Zirin, H. & Ai, G., 1994, *Astrophysical Journal*, Vol. 424, p. 436.
- [62] Chen, J., Wang, H., Zirin, H. & Ai, G., 1994, *Solar Physics*, Vol. 154, p. 261.
- [63] Ambastha, A., Hagyard, M. J. & West, E. A. 1993, *Sol. Phys.*, 148, 277 Chen, J. 1989, *Astrophysical Journal*, Vol. 338, p. 453.
- [64] Hagyard, M. J., Start, B. A. & Venkatakrisnan, P., 1999, *Sol. Phys.*, 184, 133.
- [65] Kosovichev & Zharkova, 2001, *Astrophysical Journal*, Vol. 550, p. L105.
- [66] Spirock, T. J., Yurchyshyn, V. & Wang, H., 2002, *Astrophysical Journal*, Vol. 572, p. 1072.
- [67] Scherrer, P. H., et al., 1995, *Solar Physics*, 162, 129.
- [68] Wang, H. & Tang, F., 1993, *Astrophysical Journal*, Vol. 407, p. L89.
- [69] Melrose, D. B., 1995, *Astrophysical Journal*, Vol. 451, p. 391.
- [70] Chen, J, 1989, *Astrophysical Journal*, Vol. 338, p. 453.
- [71] Chen, J. & Garren, F., 1993, *Geophys. Res. Lett.*, 20, 2319.

- [72] Krall, J., Chen, J., Duffin, R. T., Howard, R. A. & Thompson, B. J. 2001, *Astrophysical Journal*, Vol. 562, p. 1045.
- [73] Patterson, A. & Zirin, H., 1981, *Astrophysical Journal*, Vol. 243, p. L99.
- [74] Tanaka, K., 1978, *Solar Physics*, Vol. 58, p. 149.
- [75] Kosovichev, A. G. & Zharkova, V. V., 2001, *Astrophysical Journal*, Vol. 550, p. L105.
- [76] Hagyard, M. J., Teuber, D., West, E. A. & Smith, J. B. 1984, *Solar Physics*, Vol. 91, p. 115.
- [77] Falconer, D. A., 1997, *Solar Physics*, Vol. 176, p. 123.
- [78] Ambastha, A., Hagyard, M. J. & West, E. A. 1993, *Solar Physics*, Vol. 148, p. 277.
- [79] Chen, J., Wang, H., Zirin, H. & Ai, G. 1994, *Solar Physics*, Vol. 154, p. 261.
- [80] Wang, H., Ewell, M.W., Jr., Zirin, H. & Ai, G., 1994, *Astrophysical Journal*, Vol. 424, p. 436.
- [81] Cameron, R. & Sammis, I. 1999, *Astrophysical Journal*, Vol. 525, p. L61.
- [82] Scherrer, P. H., et al., 1995, *Solar Physics*, Vol. 162, p. 129.
- [83] Zirin, H. 1985, *Australian Journal of Physics*, Vol. 38, p. 961.
- [84] Spirock, T. J., et al., 2000, in ASP Conference. Ser. 236, *Advanced Solar Polarimetry Theory: Observation and Instrumentation*, ed. M. Sigwarth (San Francisco: ASP), 65.
- [85] Priest, E. R. & Milne, A. M., 1980, *Solar Physics*, Vol. 615, . 315.
- [86] Asai, A., Ishii, T. T. & Kurokawa, H. 2001, *Astrophysical Journal*, Vol. 555, p. L65.
- [87] Kurokawa, H. & Kawai, G., 1993, in ASP Conference Ser. 46, *The Magnetic and Velocity Fields of Solar Active Regions*, (ed. H. Zirin, G. Ai & H. Wang), San Francisco: ASP, 507.
- [88] Severny, A. B., 1964, *ARA&A*, 2, 363.
- [89] Zvereva, A. M., & Severny, A. B., 1970, *Izv. Krymskoi Astrofiz. Obs.*, 4142, 97.

- [90] Moore, R. L., Hurford, G. J., Jones, H. P. & Kane, S. R., 1984, *Astrophysical Journal*, Vol. 276, p. 379.
- [91] Kosovichev, A. G. & Zharkova, V. V., 1999, *Solar Physics*, Vol. 190, p. 459.
- [92] Kosovichev, A. G. & Zharkova, V. V., 2001, *Astrophysical Journal*, Vol. 550, p. LI05.
- [93] Wang, H., Ewell, M. W., Zirin, H. & Ai, G., 1994, *Astrophysical Journal*, Vol. 424, p. 436.
- [94] Wang, H., Spirock, T. J., Qiu, J., Ji, H.-S., Yurchyshyn, V., Moon, Y.-J., Denker, C. & Goode, P. R., 2002, *Astrophysical Journal*, Vol. 576, p. 497.
- [95] van Driel-Gesztelyi, L., Manoharan, P. K., Pick, M. & Dernoulin, P. P. 1997, *Adv. Space Res.*, 19, 1883.
- [96] Aschwanden, M. J., Fletcher, L., Schrijver, C. J. & Alexander, D., 1999, *Astrophysical Journal*, Vol. 520, p. 880.
- [97] Yurchyshyn, V. B., Abramenko, V. I. & Carbone, V., 2000, *Astrophysical Journal*, Vol. 538, p. 968.
- [98] Abramenko, V. I., Yurchyshyn, V., Wang, H., Spirock, T. J. & Goode, P. R., 2003, *Astrophysical Journal*, Vol. 597, p. 1135.
- [99] van Tend, W. & Kuperos, M., 1978, *Solar Physics*, Vol. 59, p. 115.
- [100] van Ballegooijen, A. A. & Martens, P. C. H., 1989, *Astrophysical Journal*, Vol. 343, p. 971.
- [101] Forbes, T. G. & Isenberg, P. A., 1991, *Astrophysical Journal*, Vol. 373, pg. 294.
- [102] Kumar, A. & Rust, D. M., 1996, *J. Geophys. Res.*, 101, 15667.
- [103] Wu, S. T. & Guo, W. P., 1999, *J. Geophys. Res.*, 104, 14, 789.
- [104] Amari, T., Luciani, J. F., Mikic, Z. & Linker, J., 2000, *Astrophysical Journal*, Vol. 529, p. L49.
- [105] Moore, R. L. & LaBonte, B., 1980, in *IAU Symp. 91, Solar and Interplanetary Dynamics*, ed. M. Dryer & E. Tandberg-Hanssen (Boston: Reidel), 207.
- [106] Antiochos, S. K., 1998, *Astrophysical Journal*, Vol. 502, p. L181.



- [107] Antiochos, S. K., DeVore, C. K. & Klimchuk, J. A., 1999, *Astrophysical Journal*, Vol. 510, p. 485.
- [108] Sterling, A. C. & Moore, R. L., 2001, *Astrophysical Journal*, Vol. 560, p. 1045.
- [109] Sterling, A. C., Moore, R. L., Qiu, J. & Wang, H., 2001, *Astrophysical Journal*, Vol. 561, p. 1116.
- [110] Leka, K. D., Canfield, R. C., McClymont, A. N. & van Driel-Gesztelyi, L., 1996, *Astrophysical Journal*, Vol. 462, p. 547.
- [111] Krucker, S., Hurford, G. J. & Lin, R. P., 2003, *Astrophysical Journal*, Vol. 595, p. L103.
- [112] Abramenko, V. I. & Baranovsky, E. A., 2004, *Solar Physics*, in press.
- [113] Heyvaerts, J., Priest, E. R. & Rust, D. M., 1977, *Astrophysical Journal*, Vol. 216, p. 123.
- [114] Wang, T. & Abranlenko, V. I., 2000, *Astronomy & Astrophysics*, Vol. 357, p. 1056.
- [115] Abramenko, V. I. & Yurchishin, V. B., 1996, *Solar Physics*, Vol. 168, p. 47.
- [116] Hurford, G. J., Schwartz, R. A., Krucker, S., Lin, R. P. & Smith, D. M., 2003, *Astrophysical Journal*, Vol. 595, p. L77.
- [117] Sweet, P. A. 1958, in *IAU Symp. 6, Electromagnetic Phenomena in Cosmical*.
- [118] Sturrock, P. A., 1989, in the *Proceedings of the Max '91 Workshop*, (ed. Winglee, R. M. & Dennis, B. R.), Greenbelt, MD, NASA, 1.
- [119] Kiplinger, A. L., Dennis, B. R., Emslie, A. G., Frost, K. L. & Orwig, L. E, 1983, *Astrophysical Journal*, Vol. 265, p. L99.
- [120] Aschwanden, M. J., Wills, M. J., Hudson, H. S., Kosugi, T. & Schwartz, R. A, 1996, *Astrophysical Journal*, Vol. 468, p. 398.
- [121] Brown, J., 1971, *Solar Physics*, Vol. 18, p. 489.
- [122] Emslie, A. J., 1978, *Astrophysical Journal*, Vol. 224, p. 241.
- [123] Canfield, R. C., Gunkler, T. A. & Ricciuzzi, P. J., 1984, *Astrophysical Journal*, Vol. 282, p. 296.

- [124] Fisher, G. H., Canfield, R. C. & McClymony, A. N., 1985, *Astrophysical Journal*, Vol., 289, p. 425.
- [125] Canfield, R. C. & Gayley, K. G, 1987, *Astrophysical Journal*, Vol, 322, p. 999.
- [126] Hawley, S. L. & Fisher, G. H, 1994, *Astrophysical Journal*, Vol., 426, p. 387.
- [127] Abbett, W. P., & Hawley, S. L., 1999, *Astrophysical Journal*, Vol, 512, p. 906.
- [128] Svestka, Z., 1976, *Solar Flares* (Dordrecht: Reidel).
- [129] Fang, C. Henoux, J. C. & Gan, W., 1993, *Astronomy & Astrophysics*, Vol. 274, p. 917.
- [130] Wulser, J. P. & Marti, H., 1989, *Astrophysical Journal*, Vol. 341, p. 1088.
- [131] de La Beaujardiere, J. F., Kiplinger, A. L & Canfield, R. C., 1992, *Astrophysical Journal*, Vol., 401, p. 761.
- [132] Kiplinger, A. L., Dennis, B. R. & Orwig, L. E., 1989, in the *Proceedings of the Max '91 Workshop*, (ed. Winglee, R. M. & Dennis, B. R.), Greenbelt, MD, NASA, 346.
- [133] Kaempfer, N. & Magun, A., 1983, *Astrophysical Journal*, Vol., 274, p. 910.
- [134] Goode, P. R., Wang, H., Marquette, W. H. & Denker, C., 2000, *Solar Physics*, Vol, 195, p. 421G.
- [135] Lin, R. P, et al., 1998, *SPIE Proceedings*, 3442, 2.
- [136] Denker, C., Johannesson, A., Marquette, W. H., Goode, P. R., Wang, H. & Zirin, H., 1999, *Solar Physics*, Vol., 184, p. 87.
- [137] Varsik, J. R., 1995, *Solar Physics*, Vol., 161, p. 207.
- [138] Kiplinger, A. L., Dennis, B. R., Frost, K. L. & Orwig, L. E, 1984, *Astrophysical Journal*, Vol., 287, p. L105.
- [139] Neidig, D. F., Kiplinger, A. L, Cohl, H. S. & Wiborg, P. H., 1993, *Astrophysical Journal*, Vol., 406, p. 306.
- [140] Benz, A. O., Kosugi, T., Aschwanden, M. J., Benka, S. G., Chupp, E. L., Enome, S., Garcia, H., Holman, G. D., Kurt, V. G., Sako, T., Stepanov, A. V. & Volwerk, M, 1994, *Solar Physics*, Vol. 153, p. 33.

- [141] Parker, E. N., 1979, *Cosmical Magnetic Fields* (Oxford: Clarendon Press), 1987, *Solar Physics*, Vol. 111, p. 297.
- [142] Parker, E. N., 1979, *Cosmical Magnetic Fields* (Oxford: Clarendon Press), 1996, *Solar Physics*, Vol. 169, p. 327.
- [143] Berger, T.E. & Title, A.M., 1996, *Astrophysical Journal*, Vol. 463, p. 365.
- [144] Moore, R. L., Falconer, D. A., Porter, J. G. & Hathaway, D. H., 2003, AASSPD Meeting, 34, 10.10.
- [145] Charbonneau, P., McIntosh, S. W., Liu, H. L. & Bogdan, T. J., 2001, *Solar Physics*, Vol. 203, p. 321.
- [146] Lu, E. T., & Hamilton, R. J., 1991, *Astrophysical Journal*, Vol. 380, p. L89.
- [147] Einaudi, G., Velli, M., Politano, H., & Pouquet, A., 1996, *Astrophysical Journal*, Vol. 457, p. L113.
- [148] Boffetta, G., Carbone, V., Giuliani, P., Veltri, P., & Vulpiani, A., 1999, *Phys. Rev. Lett.*, Vol. 83, p. 4662.
- [149] Cattaneo, F., Lenz, D. & Weiss, N., 2001, *Astrophysical Journal*, Vol. 563, p. L91.
- [150] Wentzel, D. G. & Seiden, P. E., 1992, *Astrophysical Journal*, Vol. 390, p. 280.
- [151] Pustil'nik, L. A., 1999, *Ap& SS*, Vol. 264, p. 171.
- [152] Lawrence, J. K., Ruzmaikin, A. A. & Cadavid, A. C., 1993, *Astrophysical Journal*, Vol. 417, p. 805.
- [153] Petrovay, K. & Szakaly, G. 1993, *Astronomy & Astrophysics*, Vol. 274, p. 543.
- [154] Monin, A. S. & Yaglom, A. M. 1975, *Statistical Fluid Mechanics: Mechanics of Turbulence*, Vol. 2, ed. J. Lumley (Cambridge: MIT Press).
- [155] Frisch, U. 1995, *Turbulence, The Legacy of A. N. Kolmogorov* (Cambridge: Cambridge Univ. Press).
- [156] Abramenko, V. I., Yurchyshyn, V. B., Wang, H., Spirock, T. J. & Goode, P. R. 2002, *Astrophysical Journal*, Vol. 577, p. 487.
- [157] Wang, H., Goode, P. R., Denker, C., Yang, G., Yurchyshyn, V., Nitta, N., Gurman, J. B., Cyr, C. St., & Kosovichev, A. G., 2000, *Astrophysical Journal*, Vol. 536, p. 971.

- [158] Yurchyshyn, V. B., Wang, H., Goody, P. R. & Abramenko, V. I. 2000, *Astrophysical Journal*, Vol. 540, p. 1143.
- [159] Stolovitzky, G. & Sreenivasan, K. R., 1993, *Phys. Rev. E*, Vol. 48, p. 33.
- [160] Vainshtein, S. I., Sreenivasan, K. R., Rierrehumbert, R. T., Kashyap, V. & Juneja, A. 1994, *Phys. Rev. E*, Vol. 50, p. 1823.
- [161] She, Z. H. & Leveque, E., 1994, *Phys. Rev. Lett.*, Vol. 72, p. 336.
- [162] Consolini, G., Berrilli, E., Pietropaolo, E., Bruno, R., Carbone, V., Bavassano, B. & Ceppatelli, G., 1999, in *Magnetic Fields and Solar Processes*, ed. A. Wilson (ESA SP-448; Paris: ESA), 209.
- [163] Kolmogorov, A. N. 1941, *C. R. Acad. Sci. USSR*, Vol. 30, p. 301.
- [164] Benzi, R., Ciliberto, S., Tripiccion, R., Baudet, C., Massaioli, F. & Succi, S. 1993, *Physics Review*, Vol. 48, p. 29.
- [165] Briscolini, M., Santangelo, P., Succi, S. & Benzi, R., 1994, *Physics Review E*, Vol. 50, p. 1745.
- [166] Feder, J., 1988, *Fractals* (New York: Plenum), chap. 7.
- [167] Schroeder, M. R. 2000, *Fractals, Chaos, Power Laws* (New York: W. H. Freeman).
- [168] Dennis, B. R., & Zarro, D. M., 1993, *Solar Physics*, Vol. 146, p. 177.
- [169] Veronig, A., Vrsnak, B., Dennis, B. R., Temmer, M., Hanslmeier, A. & Magdalenic, J., 2002, *Astronomy & Astrophysics*, Vol. 392, p. 699.
- [170] Aschwanden, M. J., Dennis, B. R. & Benz, A., 1998, *Astrophysical Journal*, Vol. 497, p. 972.
- [171] Crosby, N. B., Aschwanden, M. J. & Dennis, B. R., 1993, *Solar Physics*, Vol. 143, p. 275.
- [172] Bromund, K. R., McTieman, J. M. & Kane, S. R., 1995, *Astrophysical Journal*, Vol. 455, p. 733.
- [173] Alexander, D., Harra-Mumion, L. K., Khan, J. I. & Matthews, S. A., 1998, *Astrophysical Journal*, Vol. 494, p. L235.
- [174] Harra, L. K., Matthews, S. A. & Culhane, J. L., 2001, *Astrophysical Journal*, Vol. 549, p. L245.

- [175] Mariska, J. T. & McTiernan, J. M., 1999, *Astrophysical Journal*, Vol. 514, p. 484.
- [176] Aschwanden, M. J., Fletcher, L., Schrijver, C. J. & Alexander, D., 1999, *Astrophysical Journal*, Vol. 520, p. 880.
- [177] Longcope, D. W. & Noonan, E. J., 2000, *Astrophysical Journal*, Vol. 542, p. 1088.
- [178] Krasnoselskikh, V., Podladchikova, O., Lefebvre, B., & Vilmer, N. 2002, *Astronomy & Astrophysics*, Vol. 382, p. 699.
- [179] Goode, P. R., Denker, C. J., Didkovsky, L. I., Kuhn, J. R., & Wang, H., 2002, *Journal of the Korean Astronomical Society*, Vol. 36, S1, pp. S125-S133.
- [180] Didkovsky, L. V., Denker, C., Goode, P. R., Wang, H. & Rimmele, T. R., 2003 *Astronomische Nachrichten*, Vol. 324, No. 4, pp. 297-298.
- [181] Denker, C., Yang, G. & Wang, H., 2001, *Solar Physics*, Vol. 202, p. 63D.